Université de Liège

Faculté des Sciences Appliquées

Collège de doctorat en Electricité, Electronique et Informatique

Investigation of methods for combining several trapped field superconducting magnets to obtain large magnetic field gradients

Doctoral dissertation presented by

Houbart Michel

Submitted in partial fulfillment of the requirements for the degree of
Doctor of Philosophy (PhD) in Engineering Sciences

January 2024

Thesis committee

Prof. Christophe Geuzaine (Université de Liège), President

Prof. Philippe Vanderbemden (Université de Liège), Supervisor

Prof. Benoît Vanderheyden (Université de Liège)

Prof. Bruno Douine (Université de Lorraine)

Prof. John Durrell (University of Cambridge)

Prof. Frédéric Sirois (Polytechnique Montréal)

Author contact information

Michel Houbart

Sensors and electrical measurement systems
Dept. of Electrical Engineering and Computer Science
Université de Liège

Montefiore Institute B28
Quartier Polytech 1
Allée de la Découverte 10
4000 Liège, Belgium

Email: michel.houbart@uliege.be

Funding

This thesis was funded by the Fonds de la Recherche Scientifique (F.R.S.-FNRS).

 This version was generated on January 25, 2024

Acknowledgements

First of all, my deepest gratitude goes to my supervisor Prof. Philippe Vanderbemden. I feel extremely lucky and honoured that such a passionate person introduced me to the world of superconductivity and offered me the opportunity to work and learn so much alongside with him. I am immensely grateful for his unwavering dedication and availability for answering my questions, offering me precious advice and shaping collaboratively the direction of the project. I would also like to thank him for all the time spent meticulously reviewing and enhancing my scientific work including articles, presentation and of course this manuscript. His dynamism and cheerful mindset kept me motivated and inspired throughout this enriching experience.

I would also like to thank Prof. Benoît Vanderheyden for his precious guidance, thorough proofreading, and crucial assistance with certain theoretical aspects, particularly regarding the modelling of moving superconductors. Furthermore, I express my gratitude to Prof. Christophe Geuzaine for all the enlightening conversations we shared as well as for his assistance and insights which were essential for the modelling aspects of this thesis.

I thank Prof. Bruno Douine, Prof. John Durrell and Prof. Frédéric Sirois for accepting to be part of my jury, for taking the time and energy to read throughout the manuscript and for attending to my defence.

Then, I extend my sincere thanks to Jean-François Fagnard for his systematic availability and his invaluable assistance with the practical aspects of the work conducted in this thesis. I cannot remember a single instance when I sought his help and he did not come forward with imaginative and effective ideas to address the challenges I faced. Additionally, I want to thank him for his detailed proofreading work and for his unrivalled ability to spot errors and typos.

Next, I thank Pascal Harmeling without whom none of the experiments performed in this work would have been possible. I warmly thank him for his extremely precious help in conceiving and implementing all the necessary electronics for controlling the experimental setups used in this thesis. He consistently demonstrated his expertise, always managing to guide me towards realistic and efficient designs, even when dealing with my requests that sometimes approached the seemingly impossible.

Furthermore, I want to thank Anthony Dennis, Devendra Kumar Namburi, Yunhua Shi and

John Durrell, i.e. the members of the Bulk Superconductivity Group of Cambridge University for the fruitful collaboration over the past four years. More precisely, I thank them for their generous efforts in proofreading all my articles as well as for providing me with the opportunity to measure some of the best bulk superconducting samples manufactured.

I express my gratitude to the F.R.S.-FNRS for providing me with the opportunity to engage in the study of gradient-generating superconducting assemblies.

I realise that I had the chance to be surrounded by wonderful colleagues without whom my PhD journey would definitely not have been the same. In particular, I want to thank Sébastien and Clara for their positive mindset and their "willing to help" attitude which made the working atmosphere truly uplifting. I would also like to acknowledge Julien, who initially implemented the Life-HTS toolkit. His willingness to assist, whether in adjusting, debugging, or optimizing the numerical models within the toolkit, has been a precious contribution to this research. I also thank Thomas and Nicolas for the numerous enhanced coffee breaks spent together. Beyond providing me energy for the rest of the day, these moments have, on more than one occasion, offered me a fresh perspective on my research. Furthermore, I also thank Nicolas for his help during the measurements carried out on the truncated Halbach array. My gratitude next goes to Sami and Alanis, all these discussions about sciences, sometimes, and other subjects, more often, really motivated me on a day-to-day basis and fully disserve their place in these acknowledgements. I also strongly thank Thor and Arthur for deciding to share their office with me and for these unique focaccia lunch breaks.

I also want to thank my circle of friends for the countless enjoyable evenings we shared. Your company provided me with a welcomed break from the demands of my thesis, and the laughter and support were extremely precious. I would also like to express my gratitude to my brother, my sisters, their companions and my parents for their unconditional support throughout this journey. Their constant encouragement, understanding and belief in my abilities have been the pillars that sustained me in the challenge of undertaking this thesis.

Finally, I cannot close these acknowledgements without a special tribute to my father. Among so many other things, I want to thank him for his passionate assistance, his insightful advice as well as his infectious solution-oriented mindset. His inspiration and encouragement accompanied me at every single step of this enriching experience and I can barely show enough gratitude for that.

I dedicate this work to my father.

Abstract

The unique magnetic and electric properties of type II superconductors make these materials extremely attractive in applications where large magnetic flux density gradients are desired. Indeed, these gradients can be exploited to exert remotely a magnetic force which is of interest for magnetic levitation systems, magnetic drug delivery systems or brake systems to enumerate a few. The ability of type II superconductors to trap permanent superconducting current loops allows them to act as permanent magnets with the significant advantage that they can generate magnetic flux densities up to one order of magnitude larger than the saturation magnetization of conventional ferromagnetic materials. This thesis aims to determine how several trapped-field magnets with non-parallel magnetization directions can be combined efficiently to generate large magnetic field gradients and surpass the limits of ferromagnetic materials. Starting from configurations inspired by those involving conventional magnets, the work elucidates the advantages and potential limitations associated with superconducting assemblies. Then, several modifications, either in the geometry of the assembly or in the combination procedure, are proposed and explored to enhance the performance of the final structure. To this aim, two cryogenic experimental setups are designed, assembled, calibrated and used extensively.

The first setup allows the assembly of up to five pre-magnetized samples arranged linearly through a precisely controlled translation, at liquid nitrogen temperature. This system is used to investigate how superconductors magnetized independently can be efficiently arranged in a Halbach array configuration. Trapped-field measurements show that a superconducting Halbach array of three $YBa_2Cu_3O_{7-x}$ samples produces, at a distance of 20 mm, a magnetic flux density gradient 30% higher than an isolated sample. Since the magnetizations of neighbouring trapped-field magnets are perpendicular in such arrangements, each superconductor of the array inevitably experiences a time-varying field component perpendicular to its main magnetization direction during the assembly process. Considering that magnetized superconductors are prone to partial demagnetization under these circumstances, a specific emphasis is placed on developing methods to mitigate the detrimental impact of such partial demagnetization. To this aim, the use of superconductors with triangular cross-sections as peripheral samples in a three-sample configuration is shown to significantly reduce the demagnetization and to maintain better performances than stand-alone superconductors. Alternatively, using the trapped magnetic field of an additional sample positioned above the central superconductor of the array, and extracted after the assembly process, is found to be an effective re-magnetization technique.

The second setup is an insertion tool compatible with the sample chamber of a *Physical Property Measurement System*. It allows for the in-situ magnetization of two samples and for the controlled rotation of one sample by an angle of up to 190°. With this system, the magnetic flux density gradient achieved with either a single or a pair of magnetized $YBa_2Cu_3O_{7-x}$ superconductors in the presence of a uniform background DC magnetic field is investigated at 59 K, 65 K and 77 K. Although the background field reduces the trapped field ability of individual samples, it is shown that substantial gradients can still be generated in such conditions. This investigation reveals that the distance between the samples is sufficient to avoid any mutual demagnetization effect during the rotational motion. As a result, the combined contribution of each sample generates a higher magnetic flux density gradient in comparison to the one produced with a stand-alone superconductor.

Résumé

Les propriétés magnétiques et électriques singulières des supraconducteurs de type II confèrent à ces matériaux un attrait particulier dans des applications nécessitant d'importants gradients de densité de flux magnétique. En effet, ces gradients peuvent être exploités pour exercer à distance une force magnétique. Ceci est intéressant notamment pour les systèmes de lévitation magnétique, pour les systèmes d'administration magnétique de médicaments ou pour les systèmes de freinage magnétiques. La capacité des supraconducteurs de type II à piéger de manière permanente des boucles de courant leur permet d'imiter le comportement des aimants permanents. L'avantage significatif des supraconducteurs de type II réside dans leur capacité à piéger une densité de flux magnétique jusqu'à un ordre de grandeur supérieure à la magnétisation à saturation des matériaux ferromagnétiques conventionnels. Cette thèse vise à déterminer comment combiner efficacement plusieurs aimants supraconducteurs à champ piégé présentant des directions de magnétisation non parallèles pour générer des gradients de densité de flux magnétique surpassant les limites des matériaux ferromagnétiques. A partir de configurations inspirées de celles impliquant des aimants conventionnels, le travail investigue les avantages et les limitations potentielles associées aux assemblages supraconducteurs. Ensuite, plusieurs modifications, que ce soit dans la géométrie de l'assemblage ou dans la procédure de combinaison, sont proposées et explorées pour améliorer les performances de la structure finale. Dans cette optique, deux dispositifs expérimentaux cryogéniques sont conçus, montés, calibrés et largement utilisés.

Le premier dispositif permet de combiner, à la température de l'azote liquide, jusqu'à cinq échantillons pré-magnétisés disposés linéairement, et déplacés au moyen d'une translation précisément contrôlée. Ce système est utilisé pour étudier comment des supraconducteurs magnétisés de manière indépendante peuvent être efficacement combinés dans une configuration de réseau de Halbach. Les mesures de champ piégé montrent qu'un réseau de Halbach supraconducteur composé de trois échantillons de $YBa_2Cu_3O_{7-x}$ produit, à une distance de 20 mm, un gradient de densité de flux magnétique 30% plus élevé qu'un échantillon isolé. Étant donné que la magnétisation des aimants à champ piégé voisins est perpendiculaire dans de telles assemblages, chaque supraconducteur constituant le réseau subit inévitablement l'influence d'une composante de champ variable dans le temps et perpendiculaire à sa direction de magnétisation principale pendant le processus d'assemblage. Dans de tels circonstances, les supraconducteurs magnétisés sont susceptibles de subir une démagnétisation partielle. Par conséquent, une attention particulière est accordée au développement de méthodes visant à atténuer l'impact préjudiciable de

cette démagnétisation. À cette fin, l'utilisation de supraconducteurs avec des sections droites triangulaires en tant qu'échantillons périphériques dans une configuration à trois échantillons permet de réduire significativement la démagnétisation tout en maintenant de meilleures performances que les supraconducteurs isolés. De plus, l'utilisation du champ piégé d'un échantillon supplémentaire positionné au-dessus du supraconducteur central du réseau, et extrait après le processus d'assemblage, s'avère être une méthode de re-magnétisation efficace.

Le deuxième dispositif est un outil d'insertion compatible avec la chambre expérimentale d'un *Physical Property Measurement System*. Il permet la magnétisation in-situ de deux échantillons et la rotation contrôlée d'un échantillon d'un angle pouvant atteindre 190°. Ce système a rendu possible l'étude du gradient de densité de flux magnétique obtenu à l'aide soit d'un seul, soit d'une paire de supraconducteurs $YBa_2Cu_3O_{7-x}$ magnétisés en présence d'un champ magnétique constant et uniforme à 59 K, 65 K et 77 K. Bien que le champ de background réduise le champ piégé de chaque échantillon individuel, il est démontré que des gradients significatifs peuvent toujours être générés dans de telles conditions. Cette étude révèle que la distance entre les échantillons est suffisante pour éviter tout effet de démagnétisation mutuelle pendant le mouvement de rotation. En conséquence, la contribution combinée de chaque échantillon génère un gradient de densité de flux magnétique plus élevé par rapport à celui produit avec un supraconducteur seul.

Contents

List of Figures

List of Tables

Introduction

Context and motivation

The context of this thesis is the need to elaborate a compact system capable of producing large magnetic forces. The magnetic force that a magnetized material undergoes is proportional to its magnetization and to the gradient of the magnetic density $\nabla||\mathbf{B}||$. Depending on the length scale over which this gradient extends, applications involving such a force range from large lifting electromagnets down to magnetic matrices machined at the micrometre scale to attract fine magnetic particles [1–5].

In this thesis, the focus is directed to the elaboration of a compact system producing a magnetic flux density gradient on the centimetre scale. This centimetre scale is typical of magnetic drug delivery systems [6]. In this application, pharmaceutical agents containing magnetic nanoparticles, commonly superparamagnetic in nature [7, 8], are administered into the vascular system of a patient. Under an external magnetic field, the magnetization of these particles increases until reaching a maximum saturation value, and returns to zero upon removal of the applied magnetic field. This property allows to navigate the pharmaceutical agents in the vascular system remotely by applying an inhomogeneous magnetic flux density to a localized region of the body. Nevertheless, there exist several challenges that must be addressed for the successful implementation of this technique at a human scale [9]: the magnetic flux density in the targeted region has to be large enough to magnetize the superparamagnetic nanoparticles and the gradient has to be sufficient to achieve the needed pulling forces.

The most straightforward approach for producing the desired magnetic field and field gradient involves positioning a permanent magnet in proximity to the patient's body [10–12]. This configuration results in an attractive force close to the magnet. Although a strong magnetic field gradient can be achieved within the immediate vicinity of the magnet, the practical application of this technique is constrained to areas near the surface of the body, due to the rapid decay in field strength with distance from the magnet.

Several methods have been proposed for enhancing the reach of the magnetic force of magnetic drug delivery systems based on permanent magnets. Among them, a promising approach consists of using a particular assembly of permanent magnets called a Halbach array as a source of field and field gradient [13–16]. While several types of Halbach structures exist [17–19], the most

common configuration, corresponding to the one investigated in this thesis, is characterized by a linear arrangement of neighbouring permanent magnets with perpendicular magnetizations as illustrated in Figure 1 (a). This magnetization pattern was initially identified in the early 1970s by John Mallinson [20] and later in the same decade by Klaus Halbach [21–23]. Their research demonstrated that this arrangement results in a phenomenon they referred to as a "magnetic curiosity": an enhancement of the magnetic field on one side of the array, accompanied by a near-nullification of the field on the opposite side. Using this arrangement, the peak field and field gradient can surpass those of the original single permanent magnet, thanks to the superimposition of individual magnetic field contributions. In addition to magnetic drug delivery systems, Halbach arrays find application in various domains, including magnetic levitation systems [24], DC motors [25, 26], brake systems [27] or biomagnetic separation [28].

An alternative actuation technique for magnetic drug delivery systems, recently introduced, is referred to as dipole field navigation [29–32]. In this method, the patient is placed within the strong and homogeneous field of an MRI scanner (1.5−3 T) which ensures the magnetization saturation of all the superparamagnetic particles. The desired magnetic gradient is induced by distorting the initially uniform magnetic field within the scanner through the placement of soft ferromagnetic cores around the patient, as shown in Figure 1 (b). The suitable arrangement of these cores facilitates the creation of a magnetic path that guides the movement of pharmaceutical agents.

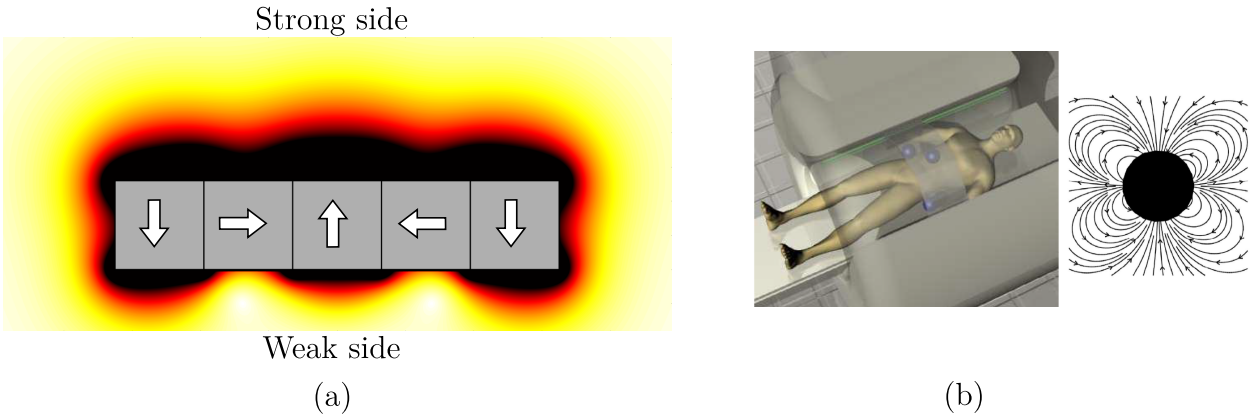

Figure 1: (a) Contour plot of the magnetic flux density amplitude around a linear Halbach array made of 5 permanent magnets. (b) Ferromagnetic cores positioned around the patient inside an MRI scanner (left) and magnetic gradient line around a spherical core (right) © 2018 IEEE [32].

All the methodologies mentioned above require the use of ferromagnetic materials, either hard or soft, in the gradient-generating system. Therefore, the saturation magnetization $\mu_0 M_{sat}$ of these materials (1.4 T for hard Nd-Fe-B permanent magnets [33, 34] and 2.4 T for soft ferromagnetic Fe-Co alloys [35]) is a fundamental limit dictating the maximum attainable field gradient. In this context, there is a need to explore compact solutions that avoid such saturation limitations. The ultimate goal is to achieve higher gradients with a more extensive spatial reach. This thesis addresses this need by using superconductors. Superconducting materials were discovered by Heike Kamerlingh Onnes in 1911 [36]. Onnes demonstrated that, when subjected to cryogenic temperatures, a superconductor can conduct an electrical current with zero DC

electrical resistivity. These materials were subsequently found to display unique magnetic properties, initially by the scientist Walther Meissner and later by the scientist Alexei Abrikosov [37,38].

Since their discovery, a substantial scientific effort has been devoted to advancing the performance and manufacturing processes of these materials. Superconductors have demonstrated utility across a wide range of applications such as rotating electric machines, fault current limiters, tokamak fusion reactors or flywheels for energy storage systems to enumerate a few [39–42]. While these materials are currently produced in various forms such as multifilamentary twisted wires [43, 44], superconducting tapes [45], or thin films [46, 47], the primary emphasis in the context of this thesis is on parallelepipeds or disks with a size of a few centimetres, called "bulk superconductors". Bulk superconducting materials are able to trap substantial magnetic fields [2, 3, 48–50]. Indeed, following an adequate magnetization procedure, persistent, macroscopic superconducting current loops can be induced in the bulk superconductor. The flux lines trapped in the superconductor are generated by these current loops. This property allows such a bulk sample to operate as a compact "trapped-field" magnet, capable of generating several teslas [2, 51]. Although they need to be operated at cryogenic temperature, superconducting trapped-field magnets offer significant advantages over ferromagnetic permanent magnets: the trapped field is not limited by any saturation magnetization and can be increased by either enlarging the geometric dimensions of the sample or reducing the operating temperature. Instead of bulk materials, a stack of thin superconducting coated conductors is also very efficient in trapping a substantial magnetic field. To date, the maximum field trapped within a bulk superconductor or a superconducting stack of tapes is equal to 17.6 T [52] and to 17.7 T [53] respectively, almost one order of magnitude higher than the fundamental saturation limit for pure iron ($\sim$2.15 T [54]).

The goal of this thesis is to determine how several trapped-field magnets with non-parallel magnetization directions can be combined efficiently to generate large magnetic field gradients and to surpass the limits of ferromagnetic materials. The innovative aspect of this research lies in exploiting the benefits of assembling mechanically several superconductors, potentially in the presence of a uniform DC background field, while overcoming the associated forces and torques.

Manuscript outline

This manuscript is divided into five chapters. Chapter 1 is devoted to the presentation of the modelling tools used throughout the thesis for reproducing and interpreting experimental results. The chapter begins by introducing the magnetodynamic approximation of Maxwell's equations and fundamental theoretical concepts related to superconductivity. Next, the widespread finite element method is briefly introduced along with two classical weak formulations of the magnetodynamic problem. Based on these formulations, the method used to model the motion of multiple conductors at different velocities is discussed and the selected formulation used throughout the thesis is exposed. The chapter ends with a description of the analytical model developed in this thesis for calculating the three components of the magnetic flux density produced by either a cubic permanent magnet or a cubic magnetized superconductor. The model is based on Biot-Savart law and can also be used for estimating analytically the field and field gradient generated by various Halbach structures investigated in the following chapters.

Chapter 2 is dedicated to the design, development and calibration of two bespoke experimental setups. The first setup is designed for the assembly and measurement of the magnetic flux

density generated by a superconducting linear Halbach array. The second setup is a custom insertion tool for the *Physical Property Measurement System*, facilitating the insertion and clamping of two superconducting samples, with the capability for controlled rotation of one of the samples.

Chapter 3 focuses on the investigation of the field and field gradient that can be achieved with a superconducting linear Halbach array consisting of 3 magnetized bulk cuboid superconductors. Following the preliminary characterization of the superconducting properties of individual samples, this superconducting Halbach array is experimentally assembled and its properties are investigated at a temperature of 77 K. The measured distribution of the magnetic flux density is compared to predictions from both finite element analysis and analytical models. The detailed analysis suggests that the performance of the array is limited due to an alteration in the current density distribution within the central superconductor.

Addressing this current alteration is the motivation of Chapter 4. In this chapter, three methods are proposed and explored to mitigate the detrimental impact of the current re-organization on the performances of superconducting Halbach arrays. The first method involves substituting bulk superconductors with stacks of coated conductors and taking advantage of the strong anisotropy of these samples to mitigate the alteration of the current density distribution. The second method involves investigating the influence of various geometrical parameters on the demagnetization effect, focusing on the geometrical shape and vertical position of the peripheral samples. The third method introduces an alternative procedure for assembling superconducting Halbach arrays, designed to re-magnetize the central superconductor.

In Chapter 5, the magnetic flux density gradient achievable between two magnetized superconductors in the presence of a uniform DC background magnetic field is investigated. The work includes both experimental and numerical approaches. The arrangement under consideration involves two facing cubic superconductors with anti-parallel magnetization directions. The superconductors are placed in the experimental chamber of a *Physical Property Measurement System*, which is used for magnetizing the samples, producing a background DC field, and investigating how the performances of the assembly are improved when decreasing temperature down to 59 K.

Finally, the manuscript ends with a concluding chapter that summarizes the main outcomes and discusses some perspectives.

1 Modeling techniques

1.1 Magnetodynamic approximation

The set of equations describing the interaction of electromagnetic fields with media is known as Maxwell's equations. These equations write:

$$\nabla \times \mathbf{E} = -\partial_t \mathbf{B}, \tag{1.1}$$
$$\nabla \times \mathbf{H} = \partial_t \mathbf{D} + \mathbf{J}, \tag{1.2}$$
$$\nabla \cdot \mathbf{D} = \rho, \tag{1.3}$$
$$\nabla \cdot \mathbf{B} = 0. \tag{1.4}$$

Equation (1.1) is also known as Faraday's law and expresses that a time-varying magnetic flux density $\mathbf{B}$ (T) generates an electric field $\mathbf{E}$ (V/m). Ampere-Maxwell's law, equation (1.2), states that a time varying electric displacement $\mathbf{D}$ (C/m^2) and a current density $\mathbf{J}$ (A/m^2) contribute to the generation of a magnetic field $\mathbf{H}$ (A/m). Equations (1.3) and (1.4) are referred to as Gauss's electric and magnetic laws respectively. The first expresses that a charge density distribution ρ (C/m^3) generates an electric displacement. The second states that the magnetic flux density is a solenoidal field, i.e. it has no divergence.

When solving a specific problem, Maxwell's equations need to be supplemented by constitutive relations that relate the field quantities expressed in different physical laws to each other. For the material considered in this thesis, the following laws can be used:

$$\mathbf{B} = \mu \mathbf{H}, \tag{1.5}$$
$$\mathbf{D} = \epsilon \mathbf{E}, \tag{1.6}$$
$$\mathbf{J} = \sigma \mathbf{E}. \tag{1.7}$$

These constitutive laws include all the underlying physics into three parameters: the magnetic permeability μ (H/m), the electric permittivity ϵ (F/m) and the conductivity σ (S/m). These parameters are material-dependent and describe the electric and magnetic properties of a specific material in an electromagnetic field. Depending on the considered material, they can be rather complex functions of various physical quantities such as temperature, mechanical stress, etc. In this study, however, it is assumed that these parameters depend on electromagnetic fields only.

Combining Maxwell's equations with the constitutive laws leads to a wave equation including second-order derivatives in both time and space. This equation describes the propagation of an electromagnetic wave in which the energy is stored both in electric and magnetic forms. In several engineering problems, however, the energy can be assumed to be almost completely stored within either the electric field or the magnetic field. More particularly, this assumption is known as the quasistatic assumption and is valid when the dimensions of the studied structure are much less than the wavelength of the electromagnetic wave interacting with it. In that case, the field that predominantly stores the energy depends on whether the structure behaves like a lossy dielectric or as a conductor. Noting l the characteristic dimension of the system, it can be shown that the energy is stored mainly in magnetic form if $\sigma > \frac{1}{l}\sqrt{\frac{\epsilon}{\mu}}$ [55]. This last condition with the quasistatic assumption forms the basis of the magnetodynamic approximation which is used throughout this thesis.

In this approximation, the term $\partial_t \mathbf{D}$ in Ampere-Maxwell's law may be neglected and it may be shown that the resulting governing equation for the magnetic field becomes first-order in time rather than second-order, leading to a diffusion problem.

1.2 Superconducting materials

1.2.1 Phenomenological description of superconductivity

In 1911, the scientist Kamerlingh Onnes and his team made a discovery while conducting experiments on the electrical resistivity of mercury-filled capillary tubes at cryogenic temperatures: superconductivity [36]. This unique physical property is only observed in specific materials that exhibit remarkable magnetic behaviour and carry electrical current without losses. However, these materials, known as "superconductors", can only maintain their distinctive magnetic and electrical characteristics under specific conditions. These conditions involve keeping the temperature, the current density and the magnetic field strength below critical values denoted as T_c, $\mathbf{J}_c$, and $\mathbf{H}_c$ respectively. In general, each of these critical values is interrelated with the other physical parameters, e.g. $\mathbf{J}_c$ depends both on the temperature and the magnetic field. Superconductivity is thus observed below a critical surface in the (T,$\mathbf{H}$,$\mathbf{J}$) space. This critical surface is represented schematically in Figure 1.1 (a) in the case of an isotropic superconductor for which the critical surface is only a function of the norm of $\mathbf{J}$ and $\mathbf{H}$ respectively noted J and H.

Superconducting materials can be classified into two categories, respectively named type I and type II superconductors. The difference between both types appears when examining a phase diagram in the (T,$\mathbf{H}$) space which is represented schematically for the isotropic case in Figures 1.1 (b) and (c).

Type I superconductors (Figure 1.1 (b)) are characterized by a single phase transition that occurs at a critical field $H_c(T,J)$. When the magnetic field experienced by a type I superconductor is below H_c, the material is said to be in the Meissner state [37]. Under such conditions, the superconductor behaves as a perfect diamagnetic material, i.e. it completely expels the magnetic flux from its bulk. The magnetic flux density only penetrates the material over a temperature-dependent characteristic depth known as the London penetration depth λ. This magnetic flux expulsion results from the spontaneous appearance of electrical current at the surface of the

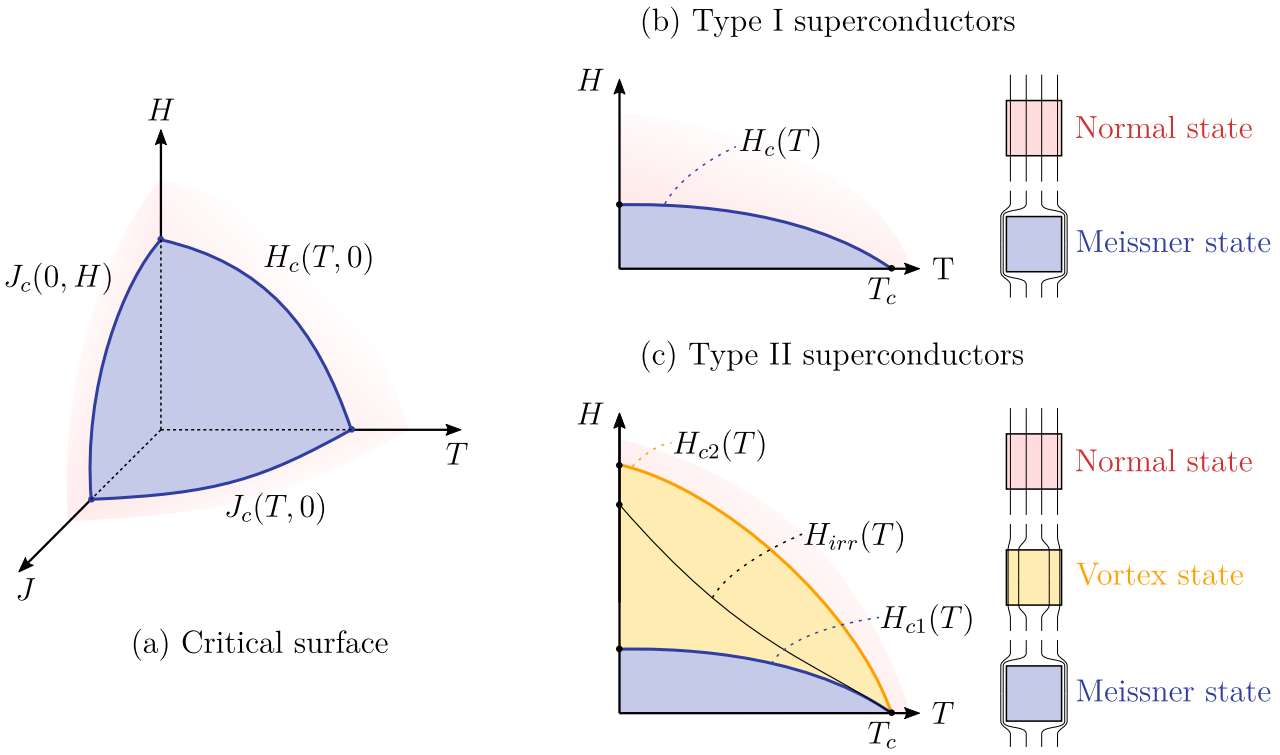

Figure 1.1: (a) Schematic representation of the critical surface separating the superconducting phase, in blue, from the normal phase, in red, for an isotropic superconductor. (b) and (c) Phase diagrams in the principal (T,H) plane, i.e. J=0, for type I and type II superconductors respectively.

superconductor, referred to as supercurrents. No losses are associated with these currents, instead they store kinetic energy within the material. Above H_c, a type I superconductor is in the normal state: it behaves similarly to a resistive conductor with non-negligible resistivity.

Type II superconductors (Figure 1.1 (c)) exhibit an additional phase transition and an intermediate state situated between the Meissner and normal states in the phase diagram: the "mixed state" or "vortex state". Type II superconductors therefore exhibit a lower and an upper critical field noted $H_{c1}(T,J)$ and $H_{c2}(T,J)$ respectively. When the superconductor is in the mixed state, the magnetic flux is observed to penetrate the material in the form of whirlpool-like structures referred to as vortices. These vortices consist of a core in the normal state with a typical size named the coherence length ($\xi \sim$ [1-1000] nm [41]) encircled by supercurrents. It was experimentally shown that the magnetic flux carried by each vortex is the same and corresponds to the flux quantum: $\Phi_0 \simeq 2.07 \cdot 10^{-15}$ Wb [56]. When the magnetic field applied on a type II superconductor is increased above H_{c1}, it initiates the penetration of vortices into the material from its surface. If the applied field is further increased (while remaining below H_{c2}), an increasing number of vortices are pushed into the superconductor.

It can be demonstrated that vortices experience a repulsive force between them [55]. When they are free to move within the material, they tend to organize themselves into a triangular pattern, which is also referred to as the Abrikosov vortex lattice. In that specific case, the superconductor is said to be reversible because the density of vortices decreases to zero reversibly upon removal

of the applied magnetic field.

Type II reversible superconductors, however, are generally considered to have limited practical relevance since it has been shown that Joule losses are associated with the motion of vortices [55]. Consequently, there is an interest in impeding the mobility of these vortices. This is known as "pinning" the vortices and it may be achieved by intentionally introducing defects in the superconductor that are commonly termed "pinning centres" or "pinning sites". These pinning centres attract the vortices so that the pinning strength needs to be overcome to induce their motions. Note that imperfections in the material such as dislocations or grain boundaries can also contribute to this pinning effect.

Under these conditions, when the applied magnetic field exceeds H_{c1} the first vortex penetrates the material from its surface and gets rapidly trapped in a pinning site. This vortex remains anchored until it undergoes an external force (e.g. coming from another vortex entering the material) exceeding the pinning strength. At this point, the vortex detaches from the pinning centre and starts migrating into the superconductor until it gets pinned to another pinning site. Consequently, the density of vortices is higher close to the edges of the material which results in the emergence of a net macroscopic supercurrent loop in the material. Such superconductors exhibit hysteretic behaviour and are qualified as irreversible since some vortices may remain trapped upon removal of the applied field.

When an external current density $\mathbf{J}$ is forced through a type II irreversible superconductor in the vortex state, an additional Lorentz-like force acts on the vortex lattice: $\boldsymbol{F}_l = \mathbf{J} \times \mathbf{B}$, where $||\mathbf{B}|| = n_v \Phi_0$ with n_v the surface density of vortices. As this Lorentz-like force approaches the pinning strength, the probability of vortex unpinning increases. This defines an additional threshold surface in the (T,$\mathbf{H}$,$\mathbf{J}$) space corresponding to $H_{irr}(T,J)$ in Figure 1.1 (c). Above $H_{irr}(T,J)$ and below H_{c2}, the material is still in the vortex state, however, vortices are no longer pinned and consequently the material exhibits losses. This regime in which vortices are in motion and dissipate energy simultaneously is called the flux flow regime. The associated losses can be characterized by a flux flow resistivity that is typically higher than that of a conventional conductor operating at a similar temperature. Therefore, this irreversible critical surface limits the actual useful region for practical applications. Hereafter, when the critical temperature, field, or current density is mentioned, reference is made to the irreversible critical surface unless the contrary is explicitly specified.

Type II irreversible superconductors are the most suitable for practical applications [41]. They can be further categorized into two distinct groups based on whether their critical temperature is higher or lower than 30 K, these groups are presented below:

- **Low-temperature superconductors** (LTS): These materials typically have critical temperatures below 20 K, requiring the use of sophisticated cryocooling systems for their applications [40]. However, they tend to exhibit excellent performance in high magnetic fields. Among the commonly employed low-temperature superconductors are Nb-Ti ($T_c \simeq 9.8$ K) and Nb_3Sn ($T_c \simeq 18$ K).
- **High-temperature superconductors** (HTS): These materials were discovered in 1987 [57–59], most of them exhibit critical temperatures above 77 K, allowing for their convenient

and low-cost maintenance in a superconducting state by submerging them in liquid nitrogen. They typically present a crystalline layered structure consisting of a succession of copper oxide planes CuO_2 referred to as "*ab*-planes", separated by metals and/or other oxide layers. The direction perpendicular to the *ab*-planes is called the *c*-axis. Among the commonly employed high temperature superconductors are $YBa_2Cu_3O_{7-x}$ ($T_c \simeq 92$ K), $Bi_2Sr_2Ca_1Cu_2O_8$ ($T_c \simeq 87$ K) and $Bi_2Sr_2Ca_2Cu_3O_{10}$ ($T_c \simeq 110$ K).

This thesis exclusively focuses on type II irreversible high-temperature superconductors in the mixed state. The Ginzburg-Landau theory is well adapted for investigating the physical characteristics of a limited quantity of vortices within such superconductors. Considering that macroscopic-sized samples (~ 1 cm^3) are investigated in this work, the application of this theory is, however, not manageable since it would necessitate addressing a prohibitively large number of vortices. In this context, macroscopic constitutive laws describing the average response of irreversible type II superconductors are required, two of them are presented in the following two subsections. In both models, the supercurrents caused by the applied field are treated as induced currents and the magnetic field they generate is taken into account through Ampere's law. Therefore, the magnetic constitutive law $\mathbf{B} = \mu_0 \mathbf{H}$ can be used for superconducting materials, where $\mu_0 = \frac{1}{\nu_0} = 4\pi \times 10^{-7}$ H/m is the magnetic permeability of vacuum.

1.2.2 Bean model

The Bean model belongs to a specific family of macroscopic models aiming at understanding the distribution of the magnetic field within type-II superconductors: critical state models. The common feature of these models is that a strong pinning is assumed. This means that, once the external field is maintained constant the pinning is sufficient to prevent any motion of vortices. In other words, the possibility of unpinning through thermal excitation is entirely disregarded. Based on this hypothesis and the discussion of the previous section, it can be deduced that, in an equilibrium state, the non-uniform distribution of vortices arising from the application of a magnetic field higher than H_{c1} (and smaller than H_{irr}) is such that the norm of the current density in the vortex-penetrated region matches exactly the critical value J_c.

In addition to the strong pinning, the Bean model assumes that the pinning landscape in the superconductor is uniform which results in a constant value of the critical current density J_c in the entire material. The model also assumes that H_{c1} is equal to zero and that H_{c2} is infinitely large. In its most simple form, the model also assumes that J_c is field-independent.

Despite these simplifying assumptions the Bean model reproduces several important features of type II superconductors such as the ability of a superconductor to trap significant magnetic flux density [55, 60]. Furthermore, this model can be used to anticipate with relative ease the current density distribution induced in a sample subjected to a specific applied field sequence. This is illustrated in two examples below by applying the model to the simple case of an infinite superconducting slab. Despite their simplicity, these examples serve as a means to introduce two commonly used magnetization procedures known as the "zero-field-cooling" and the "field-cooling" processes.

Zero-field-cooled magnetization (ZFC)

The magnetization of a superconducting slab infinitely long along the y and z-directions and of finite width W parallel to the x-direction is considered in this section. This slab is subjected to an applied field aligned with the z-direction denoted $\mathbf{H}_{app} = H_{app}\,\boldsymbol{e_z}$. In a zero-field-cooled process, the slab is first cooled below the critical temperature in the absence of any applied magnetic field, and then the magnetic field sequence is applied. This sequence consists of increasing at a constant rate H_{app} until it reaches a maximum value H_{max} and then decreasing H_{app} down to 0 at the same rate. The time-dependence of the slab temperature and of the external applied field is illustrated schematically in Figure 1.2 (a).

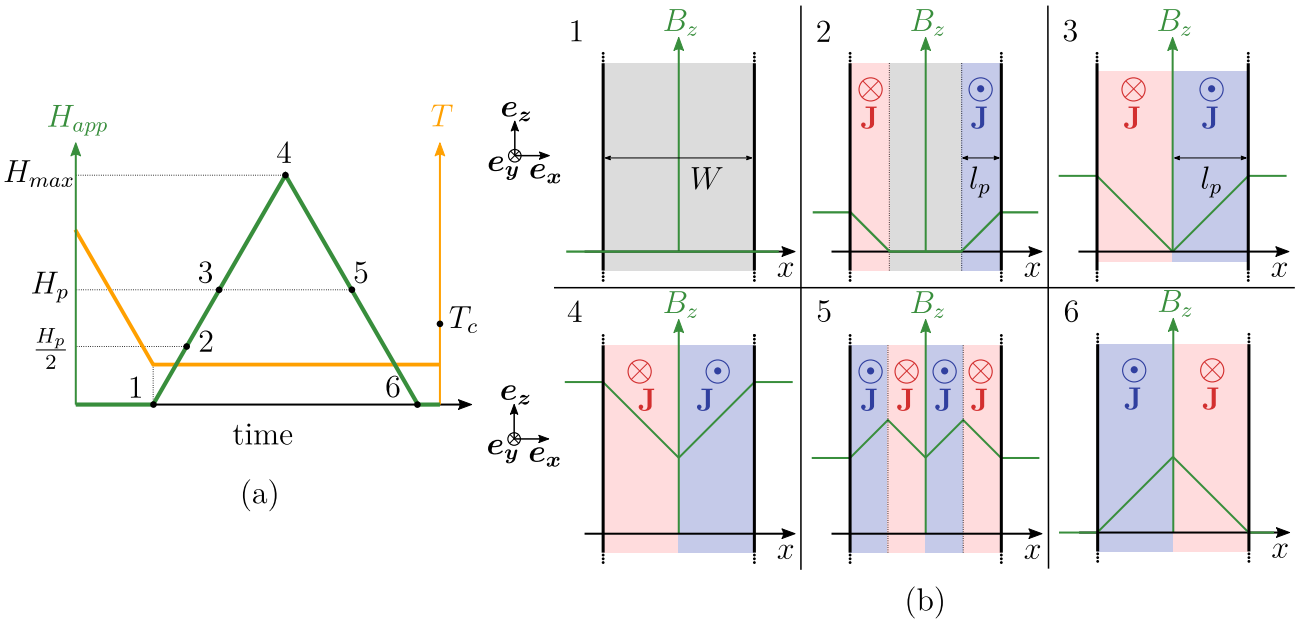

Figure 1.2: Illustration of the Bean model applied to the case of an infinite superconducting slab parallel to the y-z plane and of finite width W parallel to the x-direction. The slab is subjected to a zero-field-cooling process in which the applied field is aligned with the z-direction. (a) Time-dependence of the slab temperature and of the external applied magnetic field. (b) Magnetic flux density profile and current distribution in the slab at different times.

In these conditions, the problem becomes one-dimensional since from Ampere's law it may be deduced that current in the slab will only be induced in the y-direction, i.e. $\mathbf{J} = J(x)\,\boldsymbol{e_y}$. The problem thus amounts to solving Ampere's law that may be written $\partial_x H(x) = J(x)$ while considering that $H = H_{app}$ at $x = \pm W/2$ and that $|J(x)|$ is either 0 or equal to J_c. The resulting magnetic flux profile and current density distribution at different values of the applied field are shown in Figure 1.2 (b). At time instant number 2, it appears that inside the slab, the magnetic flux density decreases linearly (with a slope $\mu_0 J_c$) until it reaches a 0 value at a distance l_p from the edge of the slab. This distance also corresponds to the distance over which supercurrents penetrate the slab and is referred to as the penetration depth. The penetration depth increases with the applied field until it reaches the maximum value $W/2$, this occurs at time instant number 3 in Figure 1.2 (b) for the particular applied field value $H_{app} = H_p = J_c\,W/2$. This specific applied field value is commonly termed the penetration field of the superconducting slab. When the applied field is further increased, the magnetic response of the slab remains

unchanged, and the profile of B_z is simply shifted up.

As the applied field begins to decrease, vortices carrying a magnetic flux of opposite sign enter the slab from its edges and gradually replace the vortices that were previously anchored. This partitions the slab in two distinct regions, in the first $J(x) = -\,\mathrm{sgn}(x)J_c$ while in the second $J(x) = \mathrm{sgn}(x)J_c$ this can be observed at time instant number 5 in Figure 1.2 (b).

Provided that $H_{max} \geq 2\,H_p$, the current density profile at the end of the sequence is the same and is such that: $J(x) = \mathrm{sgn}(x)J_c$ in the whole slab. In such conditions, the slab is considered to be "fully magnetized".

Field-cooled magnetization (FC)

The same infinite slab parallel to the y-z plane submitted to a different magnetizing process is now considered. In field-cooled magnetization, the applied field is increased to H_{max} while the slab is in the normal state. After this, the slab temperature is decreased below the critical temperature and the applied field is removed at a constant rate. The time-dependence of the slab temperature and of the external applied field is illustrated schematically in Figure 1.3 (a).

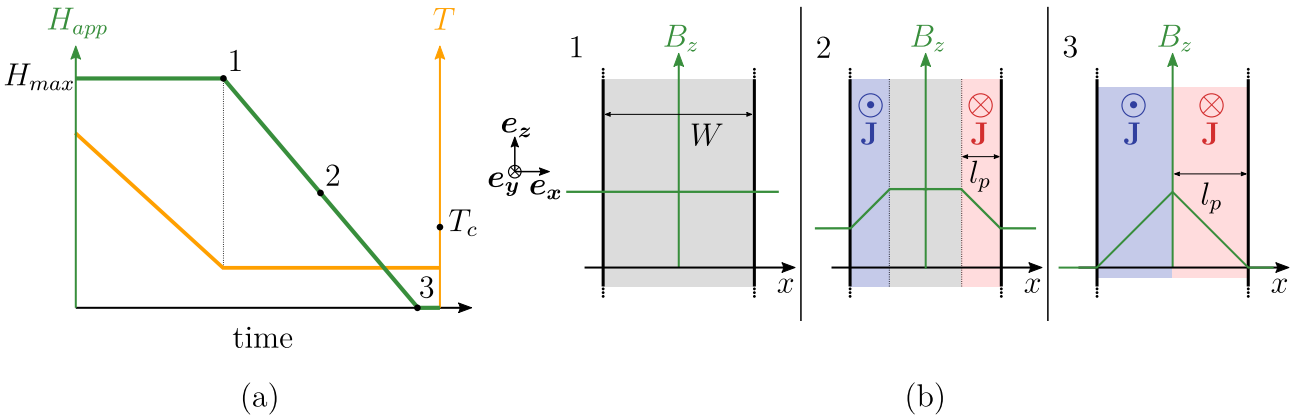

Figure 1.3: Illustration of the Bean model applied to the case of an infinite superconducting slab parallel to the y-z plane and of finite width W parallel to the x-direction. The slab is subjected to a field-cooling process in which the applied field is aligned with the z-direction. (a) Time-dependence of the slab temperature and of the external applied magnetic field. (b) Magnetic flux density profile and current distribution in the slab at different times.

In these conditions, the phase transition towards the mixed state occurs in the presence of a uniform applied field that has already penetrated the whole slab. As a result, at time number 1 in Figure 1.3 (a), the vortices distribution inside the slab is uniform, the flux density profile is flat and no supercurrent is flowing. Considering that the magnetic flux profile in the slab is either linear or flat, the calculations for decreasing applied field are similar to the zero-field-cooling case.

As can be observed at time number 3 in Figure 1.3 (b), the same "fully magnetized" state as with a zero-field-cooling procedure can be achieved provided that the maximum applied field H_{max} is large enough. A major difference, however, is that the minimum required applied field allowing to reach this final state is twice smaller with the present magnetization process.

1.2.3 Power law and flux creep

The strong pinning hypotheses of the Bean model are not necessarily verified when thermal fluctuations are considered. An interesting approach to understand this consists in considering that the pinning centres act locally as potential wells in which vortices remain trapped and that the pinning forces derive from these potential wells. Noting U the activation energy required for one vortex to escape the potential well associated with a specific pinning site, it appears that depending on how the thermal energy compares to U, there is a non-zero probability for this vortex to get unpinned by thermal activation even if $||\mathbf{J}||<J_c$. This thermally activated process is referred to as the flux creep regime and ensures a smooth transition from the flux pinning to the flux flow regime. From a modelling perspective, this phenomenon can be reproduced with the following electric constitutive law, commonly referred to as the power law [61–65]:

$$\mathbf{E} = \frac{E_c}{J_c}\left(\frac{||\mathbf{J}||}{J_c}\right)^{n-1}\mathbf{J} = \rho\left(||\mathbf{J}||\right)\mathbf{J} \qquad \text{or} \qquad \mathbf{J} = \frac{J_c}{E_c}\left(\frac{||\mathbf{E}||}{E_c}\right)^{(1-n)/n}\mathbf{E} = \sigma\left(||\mathbf{E}||\right)\mathbf{E}. \tag{1.8}$$

In this equation, the exponent n is known as the critical exponent of the material and is defined such that $n = U_0/k_bT$, where U_0 is the value of the activation energy in the absence of current and $k_b = 1.38 \times 10^{-23}$ J/K is the Boltzmann constant. The critical exponent characterizes how strong the pinning is in the material. It can be shown that taking the limit $n \to \infty$ leads to the Bean model [62, 66]. The value of E_c can be arbitrarily chosen but it should be pointed out that this choice defines the actual meaning of J_c in the power law. In this work, the widespread value $E_c = 1\,\mu$V/cm is used.

The parameters in equation (1.8) can be determined through experimental characterisation [67–70]. For high-temperature type II irreversible superconductors the critical exponent typically ranges from $n = 20$ to $n = 50$ [71, 72]. The n-value of the superconducting samples can be determined through experimental measurements of the magnetic relaxation. Indeed, at the end of the magnetization process of a superconductor, the total magnetization of the sample is expected to decrease progressively over time since some of the vortices that get thermally activated leave the material. In this thesis, the model used to approximate this magnetic relaxation was proposed by Zeldov [63, 73], it assumes a logarithmic relationship between the activation energy U and the current density. Applying this model to the case of an infinite superconducting slab discussed in the previous section, it can be shown that the time evolution of flux density at any point inside the slab after the magnetization process writes:

$$B_z(t,x) = B_{z,0}(x)\left(1 + \frac{t}{t_0}\right)^{\frac{1}{1-n}}, \tag{1.9}$$

where $B_{z,0}(x)$ is the magnetic flux density initially trapped at the considered point and the time $t = 0$ corresponds to the moment at which the applied field returns to zero during the magnetization process.

1.3 Finite element method

The study of the electrodynamic behaviour of superconducting materials represents a non-linear challenge in physics. Exact analytical solutions of Maxwell's equations in this context are only available for problems exhibiting relatively simple geometries and constraints. When dealing with

more realistic problems, numerical simulations are often required to carry out parametric studies.

Among the various numerical methods available, this thesis employs the finite element method. This approach involves dividing the studied domain into smaller geometric entities and approximating the fields of interest as linear combinations of N_f locally defined basis functions. The unknowns of the problem then become the coefficients within this linear combination. These coefficients are determined by enforcing an integral form of the governing equation, referred to as the weak form, with a set of N_f test functions. This process leads to the formulation of a system of equations in the form of a $N_f \times N_f$ matrix [74].

The simulations conducted in this thesis rely on a mixed **H**-ϕ-**A** formulation developed in [75,76] and made accessible through the Life-HTS toolkit. The meshing of the domain and the numerical calculations are performed using the free and open-source software tools *Gmsh* and *GetDP* respectively. In this section, the formulations available in the Life-HTS toolkit [77] that were used in this study are introduced and a method for modelling the motion of superconducting materials using these formulations is discussed.

1.3.1 Strong form of Maxwell's equations in the magnetodynamic approximation

As presented in section 1.1, addressing a magneto-dynamic problem amounts to solving Faraday's law, Ampere's law and Gauss's law simultaneously, while neglecting the current displacement term, which writes:

$$\nabla \times \mathbf{E} = -\partial_t \mathbf{B}, \tag{1.10}$$

$$\nabla \times \mathbf{H} = \mathbf{J}, \tag{1.11}$$

$$\nabla \cdot \mathbf{B} = 0. \tag{1.12}$$

Let us denote Ω the domain in which the solution is looked for and Γ the piecewise smooth boundary of this domain. To form a closed set of equations, the problem has to be completed with constitutive laws defined on Ω that particularize the electromagnetic response of the medium. Note that the electric displacement has completely disappeared from equations (1.10) to (1.12), only two constitutive laws are therefore needed. First, a magnetic constitutive law relating the fields **B** and **H** can be written in the whole domain:

$$\mathbf{B} = \mu \mathbf{H} \qquad \text{or} \qquad \mathbf{H} = \nu \mathbf{B}, \tag{1.13}$$

in this work, only superconducting materials will be considered. As a result, $\mu = \frac{1}{\nu} = \mu_0 = 4\pi \times 10^{-7}$ H/m in Ω, as discussed in section 1.2.1.

For the second constitutive law, the domain Ω is further divided into two complementary subdomains: the conducting region noted Ω_c and the non-conducting region Ω_c^C. In the conducting region, the fields **E** and **J** are related as follows:

$$\mathbf{E} = \rho \mathbf{J} \qquad \text{or} \qquad \mathbf{J} = \sigma \mathbf{E}. \tag{1.14}$$

In all the simulations of this work, the conducting region is filled with superconducting materials. The resistivity and the conductivity appearing in equation (1.14) thus correspond to the functions

introduced in equation (1.8) and are responsible for the non-linear nature of the problem. In the non-conducting region, the current density vanishes and is no longer related to the electric field:

$$\mathbf{J} = \mathbf{0}. \tag{1.15}$$

It is worth noticing that $\mathbf{E}$ and $\mathbf{J}$ being unrelated in Ω_c^C, adding any vector field $\mathbf{E}^*$ vanishing within Ω_c and that can be expressed as the gradient of a scalar field within Ω_c^C to $\mathbf{E}$ does not alter equations (1.10) to (1.15) in any way so that $\mathbf{E}$ is unknown in Ω_c^C (only its curl is known). As it will become clearer in the following sections, the specific form of the constitutive laws (1.13) and (1.14) depends on the formulation that is used.

To guarantee the uniqueness of the solution, one should also ensure appropriate boundary conditions on Γ, in addition to equations (1.10) to (1.15). In the most general case, Γ can be subdivided in two complementary regions: Γ_h on which the tangential component of $\mathbf{H}$ is imposed and Γ_e on which the tangential component of $\mathbf{E}$ is imposed:

$$\mathbf{H} \times \boldsymbol{n}|_{\Gamma_h} = \bar{\mathbf{H}} \times \boldsymbol{n}|_{\Gamma_h}, \tag{1.16}$$

$$\mathbf{E} \times \boldsymbol{n}|_{\Gamma_e} = \bar{\mathbf{E}} \times \boldsymbol{n}|_{\Gamma_e}, \tag{1.17}$$

where $\boldsymbol{n}$ is the external normal unit vector defined on Γ and $\bar{\mathbf{H}}$ and $\bar{\mathbf{E}}$ are prescribed functions. The strong form of the magnetodynamic problem is established by gathering (1.10) to (1.17) together and adding proper initial conditions.

1.3.2 Weak formulations of magnetodynamics

Three linear differential operators are involved in Maxwell's equation: the gradient operator, the curl operator and the divergence operator. To ensure the well-posedness of the problem, the scalar (or vectorial) fields upon which these operators operate must belong to specific function spaces known as scalar (or vectorial) Sobolev spaces. This prerequisite fundamentally ensures that the fields computed are sufficiently smooth to evaluate all the pertinent physical quantities. While the detailed mathematical framework of the problem is not presented here, certain functional spaces which are useful for deriving the weak formulations are introduced below:

$$F_h^0(\Omega) = \left\{ f \in L^2(\Omega)\,;\, \nabla f \in \boldsymbol{L}^2(\Omega)\,;\, f|_{\Gamma_h} \text{ fixed} \right\}, \tag{1.18}$$

$$F_h^1(\Omega) = \left\{ \boldsymbol{f} \in \boldsymbol{L}^2(\Omega)\,;\, \nabla \times \boldsymbol{f} \in \boldsymbol{L}^2(\Omega)\,;\, \boldsymbol{f} \times \boldsymbol{n}|_{\Gamma_h} \text{ fixed} \right\}, \tag{1.19}$$

$$F_h^2(\Omega) = \left\{ \boldsymbol{f} \in \boldsymbol{L}^2(\Omega)\,;\, \nabla \cdot \boldsymbol{f} \in L^2(\Omega)\,;\, \boldsymbol{f} \cdot \boldsymbol{n}|_{\Gamma_h} \text{ fixed} \right\}, \tag{1.20}$$

where $L^2(\Omega)$ (resp. $\boldsymbol{L}^2(\Omega)$) is the set of scalar (resp. vectorial) fields that are square-integrable over Ω.

The spaces $F_e^0(\Omega)$, $F_e^1(\Omega)$ and $F_e^2(\Omega)$ are defined similarly except that the essential boundary condition is enforced on Γ_e instead of Γ_h. When homogeneous boundary conditions are used, the notation is further particularized: $F_{h0}^0(\Omega)$, $F_{h0}^1(\Omega)$, $F_{h0}^2(\Omega)$, $F_{e0}^0(\Omega)$, $F_{e0}^1(\Omega)$ and $F_{e0}^2(\Omega)$.

At this point, it becomes necessary to make a decision regarding which of Maxwell's equations will be satisfied in a weak sense [74], while the others will be strongly enforced. This choice

amounts to selecting the electromagnetic field that will serve as the primary unknown within the problem, with the remaining fields being derived from the constitutive laws. Depending on this decision, various formulations of the magnetodynamic problem may be obtained, two of them are derived below. Frequently, a single formulation is selected and solved in Ω. Nevertheless, it is sometimes beneficial to use distinct formulations within different subdomains of Ω and to couple them at their common boundary [76].

Magnetic field formulation

The magnetic field formulation is a weak form of Faraday's law in which the unknown field is $\mathbf{H} \in F_h^1(\Omega)$. More precisely, $\mathbf{H}$ being curl-free in the non-conducting region, the space in which the solution is looked for can be further restricted to $\mathbf{H} \in \bar{F}_h^1(\Omega) = \left\{\mathbf{H} \in F_h^1(\Omega); \nabla \times \mathbf{H} = \mathbf{0} \,\text{in}\, \Omega_c^C\right\}$. Using the magnetic constitutive law (1.13), Faraday's law becomes:

$$\partial_t(\mu \mathbf{H}) + \nabla \times \mathbf{E} = \mathbf{0}. \tag{1.21}$$

Multiplying this equation by an arbitrary test function $\mathbf{H}' \in \bar{F}_{h0}^1(\Omega)$ and integrating over the whole domain, one has:

$$\int_\Omega (\partial_t(\mu \mathbf{H})) \cdot \mathbf{H}' \,\mathrm{d}\Omega + \int_\Omega (\nabla \times \mathbf{E}) \cdot \mathbf{H}' \,\mathrm{d}\Omega = 0, \qquad \forall \mathbf{H}' \in \bar{F}_{h0}^1(\Omega). \tag{1.22}$$

Next, applying the curl-curl Green's identity to the second term and exploiting the fact that $\mathbf{H}' \times \boldsymbol{n}|_{\Gamma_h} = 0$ yields:

$$\int_\Omega (\partial_t(\mu \mathbf{H})) \cdot \mathbf{H}' \,\mathrm{d}\Omega + \int_\Omega \mathbf{E} \cdot (\nabla \times \mathbf{H}') \,\mathrm{d}\Omega + \int_{\Gamma_e} (\mathbf{H}' \times \boldsymbol{n}) \cdot \mathbf{E} \,\mathrm{d}\Gamma = 0, \qquad \forall \mathbf{H}' \in \bar{F}_{h0}^1(\Omega). \tag{1.23}$$

Inserting equations (1.11) and (1.14) in (1.23) and exploiting the triple product property, one has:

$$\int_\Omega (\partial_t(\mu \mathbf{H})) \cdot \mathbf{H}' \,\mathrm{d}\Omega + \int_\Omega (\rho \nabla \times \mathbf{H}) \cdot (\nabla \times \mathbf{H}') \,\mathrm{d}\Omega - \int_{\Gamma_e} (\mathbf{E} \times \boldsymbol{n}) \cdot \mathbf{H}' \,\mathrm{d}\Gamma = 0, \forall \mathbf{H}' \in \bar{F}_{h0}^1(\Omega). \tag{1.24}$$

Exploiting the curl-free property of $\mathbf{H}$ in non-conducting regions, one can restrict the integral of the second term to Ω_c. It is worth emphasizing that since the computation of this integral is not required within Ω_c^C, there is no requirement to know the electric field in that specific region. As a result, the field $\mathbf{E}^*$, mentioned in section 1.3.1, does not need to be fixed. The final form of the governing equation solved in this formulation writes:

$$\int_\Omega (\partial_t(\mu \mathbf{H})) \cdot \mathbf{H}' \,\mathrm{d}\Omega + \int_{\Omega_c} (\rho \nabla \times \mathbf{H}) \cdot (\nabla \times \mathbf{H}') \,\mathrm{d}\Omega - \int_{\Gamma_e} (\mathbf{E} \times \boldsymbol{n}) \cdot \mathbf{H}' \,\mathrm{d}\Gamma = 0, \forall \mathbf{H}' \in \bar{F}_{h0}^1(\Omega). \tag{1.25}$$

Note that in this formulation, Faraday's law is solved in a weak sense allowing for the determination of the magnetic field $\mathbf{H}$. The electric field, magnetic induction, and current density values are subsequently derived from the constitutive laws and Ampere's law, which are therefore strongly enforced.

Besides, when modelling superconducting materials, non-linearities are introduced by the second term in equation (1.25) as a result of the dependence of the resistivity on the current density. It has been shown that the shape of the non-linearities introduced allows the treatment of the problem with effective iterative techniques (e.g. Newton-Raphson [78]), this explains why this formulation is often preferred when modelling superconducting materials [75, 79–85].

Vector potential formulation

This formulation uses Ampere's law as governing equation, multiplying equation (1.11) by an arbitrary test function $\mathbf{A}' \in F^1_{e0}(\Omega)$ and integrating over the whole domain, one has:

$$\int_\Omega (\nabla \times \mathbf{H}) \cdot \mathbf{A}' \, \mathrm{d}\Omega - \int_\Omega \mathbf{J} \cdot \mathbf{A}' \, \mathrm{d}\Omega = 0, \qquad \forall \mathbf{A}' \in F^1_{e0}(\Omega). \tag{1.26}$$

Next, applying the curl-curl Green's identity to the first term and exploiting the fact that $\mathbf{A}' \times \boldsymbol{n}|_{\Gamma_e} = 0$ yields:

$$\int_\Omega \mathbf{H} \cdot (\nabla \times \mathbf{A}') \, \mathrm{d}\Omega + \int_{\Gamma_h} (\mathbf{A}' \times \boldsymbol{n}) \cdot \mathbf{H} \mathrm{d}\Gamma - \int_\Omega \mathbf{J} \cdot \mathbf{A}' \, \mathrm{d}\Omega = 0, \qquad \forall \mathbf{A}' \in F^1_{e0}(\Omega). \tag{1.27}$$

Applying the triple product property to the second term and enforcing $\mathbf{J} = \sigma \mathbf{E}$ in Ω_c and $\mathbf{J} = \mathbf{0}$ in Ω_c^C, it comes:

$$\int_\Omega \mathbf{H} \cdot (\nabla \times \mathbf{A}') \, \mathrm{d}\Omega - \int_{\Gamma_h} (\mathbf{H} \times \boldsymbol{n}) \cdot \mathbf{A}' \, \mathrm{d}\Gamma - \int_{\Omega_c} \sigma \mathbf{E} \cdot \mathbf{A}' \, \mathrm{d}\Omega = 0, \qquad \forall \mathbf{A}' \in F^1_{e0}(\Omega). \tag{1.28}$$

Then, considering the divergence-free property of $\mathbf{B}$ imposed by Gauss's law, a magnetic vector potential $\mathbf{A}^*$ can be defined in Ω such that the following relation holds within Ω:

$$\nabla \times \mathbf{A}^* = \mathbf{B}. \tag{1.29}$$

Inserting equation (1.29) in Faraday's law, it comes that a scalar electric potential v can be defined in Ω_c such that the following relation is satisfied within Ω_c:

$$\mathbf{E} = -\partial_t \mathbf{A}^* - \nabla v. \tag{1.30}$$

It can be highlighted that the magnetic vector potential is not uniquely defined since adding any gradient field to $\mathbf{A}^*$ leads to a new vector potential still satisfying Gauss's law. More particularly, a modified vector potential $\mathbf{A}$ can be defined such that: $\mathbf{A} = \mathbf{A}^* + \int_0^t \nabla v \, \mathrm{d}t$. In terms of this modified vector potential, equations (1.29) and (1.30) write:

$$\nabla \times \mathbf{A} = \mathbf{B}, \tag{1.31}$$

$$\mathbf{E} = -\partial_t \mathbf{A}. \tag{1.32}$$

Note that using this modified vector potential amounts to set the electric scalar potential v appearing in equation (1.30) to 0 within the conducting region. In that region, the vector field $\mathbf{A}$ can therefore be interpreted as a primitive of the electric field and is uniquely defined up to a gradient field constant in time. In the non-conducting regions, however, the electric field is not related to the current density and is consequently defined up to a gradient field $\mathbf{E}^*$. As a result, making $\mathbf{A}$ unique in this region requires choosing a gauge condition to fix the field $\mathbf{E}^*$. It can be shown that addressing this gauge condition can be effectively managed during the

spatial discretization phase of the finite element method, as elaborated in [86]. This aspect will however not be discussed in further detail here, instead, the selection of an appropriate gauge for the vector field $\mathbf{A}$ is assumed in the following. The present formulation consists in using as primary unknown this modified magnetic vector potential $\mathbf{A} \in F_e^1(\Omega)$.
Inserting equations (1.13), (1.31) and (1.32) in (1.28), the final form of the weak formulation can be derived:

$$\int_\Omega (\nu \nabla \times \mathbf{A}) \cdot (\nabla \times \mathbf{A}') \, \mathrm{d}\Omega - \int_{\Gamma_h} (\mathbf{H} \times \boldsymbol{n}) \cdot \mathbf{A}' \, \mathrm{d}\Gamma + \int_{\Omega_c} (\sigma \partial_t \mathbf{A}) \cdot \mathbf{A}' \, \mathrm{d}\Omega = 0, \quad \forall \mathbf{A}' \in F_{e0}^1(\Omega). \tag{1.33}$$

This formulation solves Ampere's law in a weak sense while Gauss's law and Faraday's law are strongly enforced through the definition of the modified vector potential $\mathbf{A}$.

When modelling superconducting materials, non-linearities are introduced by the second term in equation (1.33) as a result of the dependence of the conductivity on the electric field. Due to the shape of these non-linearities, the Newton-Raphson method encounters difficulty in converging which forces the use of an iteration technique with a smaller convergence rate: the Picard technique [75, 78]. This explains why the $\mathbf{H}$ formulation is often preferred over the $\mathbf{A}$ formulation for modelling superconducting materials except for some exceptions, e.g. when large time steps are used [87]. As it will become clearer in section 1.3.5, the $\mathbf{A}$ formulation also exhibits a characteristic that may become interesting for modelling specific applications in which superconducting materials are in motion.

1.3.3 Spatial discretization

Up to this point, no assumption has been carried out in the derivation of the weak formulations, rendering it entirely equivalent to solving either the strong or the weak form of the magnetodynamic problem. Nevertheless, the problem is not yet well suited for performing a numerical simulation since the function space within which the solution is sought is of infinite dimension. In this context, the finite element method consists in performing a twofold discretization procedure.

First, the domain Ω is geometrically partitioned into smaller and simpler geometric entities with predefined shapes, referred to as elements. This work addresses three-dimensional problems for which the domain Ω can be subdivided into a combination of tetrahedra, hexahedra and triangular prisms. This geometric partition of the domain constitutes what is commonly referred to as the mesh of Ω and is denoted $\mathcal{M}$. Figure 1.4 schematically depicts the various types of elements employed in this work to construct the mesh. These elements can be qualified as first-order because all their edges correspond to straight lines.

Based on this geometrical discretization, it can be shown that a distinct set of basis functions can be established for each geometric entity that characterizes the elements within $\mathcal{M}$, i.e. one can define volume, facet, edge and nodal basis functions. The basis functions used in this thesis are known as Whitney shape functions [88]. A highly prevalent characteristic of these functions is their compact support. This implies that the basis function associated with a specific element remains non-zero only in the vicinity of that particular element. This property holds significant importance in the context of the finite element method because it implies that the resulting matrix system is sparse, enabling the implementation of efficient numerical algorithms to solve the problem. A finite-element is defined by the combination of an element of $\mathcal{M}$ with the basis

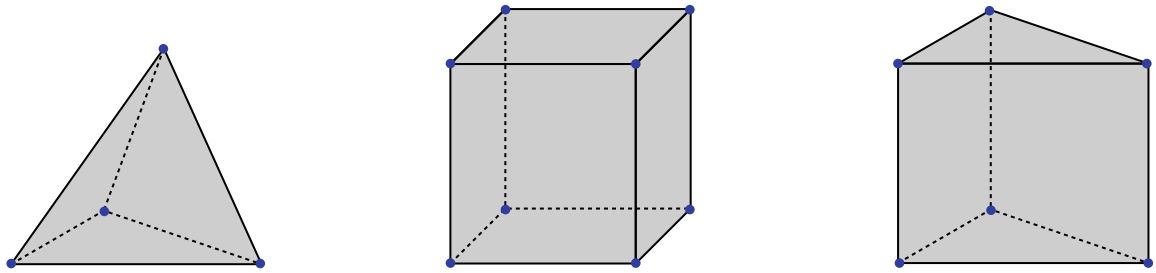

(a) (b) (c)

Figure 1.4: Schematic of the 3D first-order elements used to construct the mesh. (a) Tetrahedra. (b) Hexahedra. (c) Triangular prism.

functions associated with that specific element.

The different sets of basis functions can then be used to perform the second discretization step which takes place within the function spaces in which the solution is sought. Rather than seeking the solution within a function space of infinite dimension, it is assumed that the unknown field can be expressed as a linear combination of the basis functions of a specific basis set. Since this assumption does not necessarily hold true for the exact solution of the problem, the finite element method only yields an approximate solution.

Basis functions

For all the problems addressed in the present work, the definition of only two sets of basis functions is enough to discretize the function spaces of interest. The first set corresponds to nodal basis functions and is used to discretize the function spaces $F_h^0(\Omega)$ and $F_e^0(\Omega)$. Within this particular set, a different function is defined for every node of each element of $\mathcal{M}$. The function s_i is associated with the node n_i and is defined such that s_i is equal to 1 on the node n_i and vanishes on all other nodes. The finite-dimensional function space spanned with the nodal basis functions is denoted $F_\delta^0(\Omega)$ and any scalar field f within this space can be decomposed as:

$$f = \sum_{i=1}^{N_n} a_i s_i, \tag{1.34}$$

where N_n denotes the number of nodes in the mesh. Since only the function s_i does not vanish on the node n_i, the coefficients of this decomposition can be interpreted as the value of the function f at the position of each node. First-order nodal basis functions are used in this work. This implies that the functions s_i are constructed as linear combinations of polynomials that exhibit linear dependencies on the Cartesian coordinates [88–90].

The second set corresponds to edge basis functions and is used to discretize the function spaces $F_h^1(\Omega)$ and $F_e^1(\Omega)$. A distinct function is defined for each edge within the mesh. The function $\boldsymbol{w}_k$ is associated with the edge e_k and is defined in such a way that its circulation is equal to 1 along the edge e_k and to 0 along all other edges. It can be demonstrated that the function $\boldsymbol{w}_k$ can be derived from the nodal functions associated with the nodes situated at the endpoints of the edge e_k [91,92]. The finite-dimensional function space spanned with the edge basis functions

is denoted $F^1_\delta(\Omega)$ and any vectorial field $\boldsymbol{f}$ belonging to this space can be decomposed as:

$$\boldsymbol{f} = \sum_{k=1}^{N_e} a_k \boldsymbol{w}_k, \tag{1.35}$$

where N_e denotes the number of edges in the mesh. Since only the circulation of $\boldsymbol{w}_k$ does not vanish along the edge e_k, the coefficients of this decomposition can be interpreted as the circulation of $\boldsymbol{f}$ along each edge in the mesh $\mathcal{M}$.

Discretization of the electromagnetic fields

In the context of the magnetic field formulation, the unknown field is $\mathbf{H} \in F^1_h(\Omega)$. In the discretized settings, it is thus assumed that $\mathbf{H} \in F^1_\delta(\Omega)$ and can be written:

$$\mathbf{H} = \sum_{k=1}^{N_e} h_k \boldsymbol{w}_k. \tag{1.36}$$

Note that in this general expansion, however, the curl-free property of $\mathbf{H}$ in the non-conducting region has not been enforced yet. Therefore, the discretized function space must be further restricted to ensure this specific constraint. For simply connected non-conducting domains, which is the exclusive case under consideration in this work, the curl-free property implies the existence of a scalar function $\phi \in F^0_h(\Omega^C_c)$ satisfying $\mathbf{H} = \nabla\phi$ in Ω^C_c. Assuming that ϕ belongs to the discretized space function $F^0_\delta(\Omega)$, the expansion (1.36) can be particularized as follows:

$$\mathbf{H} = \sum_{k=1}^{N^c_e} h_k \boldsymbol{w}_k + \sum_{i=1}^{N^{nc}_n} \phi_i \nabla s_i, \tag{1.37}$$

where N^c_e stands for the total number of edges within the conducting region, excluding any edges located on its boundary, and N^{nc}_n denotes the number of nodes within the non-conducting region [93]. The magnetic field formulation used with the discretization (1.37) is H-conform meaning that it ensures the continuity of the tangential components of $\mathbf{H}$.

In the context of the vector potential formulation, the primary unknown field is $\mathbf{A} \in F^1_e(\Omega)$. In the discretized settings, it is thus assumed that $\mathbf{A} \in F^1_\delta(\Omega)$ and can be written:

$$\mathbf{A} = \sum_{k=1}^{N_e} a_k \boldsymbol{w}_k. \tag{1.38}$$

As discussed when deriving the weak formulation, the definition of the vector potential is not unique in the non-conducting region and the use of a gauge that further restricts the decomposition (1.38) is necessary. The gauge selected for the simulation of this work is known as the co-tree gauge and is presented in more detail in [86]. Using this gauge and the discretization (1.38), the vector potential formulation is B-conform meaning that it ensures the continuity of the normal component of $\mathbf{B}$.

For both considered formulations, it appears that the primary unknown field is entirely defined by a finite set of time-dependent coefficients referred to as degrees of freedom. Employing the Galerkin method enables the derivation of a system of non-linear differential equations for the computation of these coefficients. This approach consists in using the same basis functions used

to approximate the unknown field as test functions and enforcing that the weak formulation (either (1.25) or (1.33)) holds for each of these specific test functions. The matrix system obtained at this stage is said to be semi-discrete since temporal discretization is still required to obtain a system that can be solved numerically.

1.3.4 Time discretization

Upon completing the spatial discretization procedure, a system of non-linear, first-order-in-time differential equations is established to describe the degrees of freedom. Numerous time integration methods are available to discretize this system temporally [94, 95]. Among these methods, an implicit Euler method is used throughout this thesis. This time-stepping technique begins with a known initial condition at time $t = t_0$ and then computes successively the value of the degrees of freedom at discrete time instant denoted $t_1, t_2, ..., t_{\mathrm{N}}$. During the calculation of the time instant t_i, $i \in \{1, 2, ..., N\}$, all the terms are assessed at time t_i and the time derivative of any unknown function $y(t)$ is estimated with the following finite difference formula:

$$\left.\frac{\partial y}{\partial t}\right|_{t_i} \simeq \frac{y(t_i) - y(t_{i-1})}{t_i - t_{i-1}}. \tag{1.39}$$

This scheme is termed "implicit" because, at each time step, the resolution of a system of algebraic equations is required to determine the values of the degrees of freedom. Within this time integration scheme, information concerning the value of the degrees of freedom at time t_{i-1} is required only for evaluating the time derivatives as all the other terms are evaluated at time t_i.

1.3.5 Motion of conducting domains

The formulations derived in section 1.3.2 do not account for the potential motion of the conducting domain within Ω. It is, however, highly valuable to incorporate the possibility to model such movements, as it holds significant relevance in various applications, such as calculating the induced current in electric machines involving movable parts [81]. The treatment of these motions is not straightforward, especially when dealing with multiple conductors moving at various speeds [96, 97]. In this section, the modifications made to the governing equations of magnetodynamics when incorporating conductors moving at constant speed are described and a method for addressing the motion of several conductors within the finite element method is proposed.

Modification of the governing equations

First of all, let us consider the most simple case of a single conductor moving at a constant speed $\mathbf{V}$. There are typically two distinct approaches for modelling electromagnetic fields in such a scenario [98]. The first consists in expressing Maxwell's equations in a coordinate system, denoted $\Sigma(\tilde{\boldsymbol{x}}, \tilde{t}\,)$, moving along with the conductor at a velocity noted $\tilde{\mathbf{V}}_f = \mathbf{V}$. In the second approach, the equations are expressed in a fixed coordinate system denoted $\Sigma(\boldsymbol{x}, t)$, i.e. $\mathbf{V}_f = \mathbf{0}$. As an illustration, the moving conductor as well as the two coordinate systems are shown in Figure 1.5.

In the coordinate system $\Sigma(\tilde{\boldsymbol{x}}, \tilde{t}\,)$, there is no motion of the conductor relative to the coordinate system and the governing equations in the conductor are by consequence exactly the same as

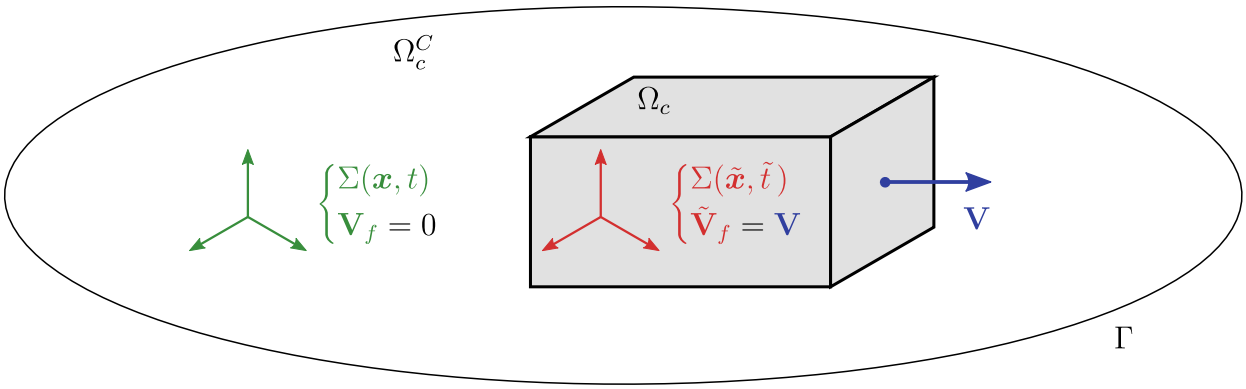

Figure 1.5: Schematic of a conductor moving at a constant velocity $\mathbf{V}$ and of the coordinate systems $\Sigma(\boldsymbol{x}, t)$ and $\Sigma(\tilde{\boldsymbol{x}}, \tilde{t}\,)$.

equations (1.10) to (1.12):

$$\tilde{\nabla} \times \tilde{\mathbf{E}} = -\partial_{\tilde{t}} \tilde{\mathbf{B}}, \tag{1.40}$$

$$\tilde{\nabla} \times (\nu \tilde{\mathbf{B}}) = \tilde{\mathbf{J}} = \sigma \tilde{\mathbf{E}}, \tag{1.41}$$

$$\tilde{\nabla} \cdot \tilde{\mathbf{B}} = 0, \tag{1.42}$$

where the different fields $\tilde{\cdot}$ are evaluated at $\Sigma(\tilde{\boldsymbol{x}}, \tilde{t}\,)$ and the operators $\tilde{\nabla}$ and $\partial_{\tilde{t}}$ are the nabla and the partial time derivatives operators expressed in terms of $\tilde{\boldsymbol{x}}$ and $\tilde{t}$ respectively. Note that the electric and magnetic constitutive laws have already been imposed. The governing equations being identical within the frame of reference moving with the conductor, the same weak formulations as the one derived in section 1.3.2 can be applied to compute the unknown fields $\tilde{\cdot}$.

Provided that the conductor is moving at a speed that is small in comparison with the speed of light, the relationship between $\Sigma(\boldsymbol{x}, t)$ and $\Sigma(\tilde{\boldsymbol{x}}, \tilde{t}\,)$ can be described by a Galilean transformation, i.e.:

$$\tilde{\boldsymbol{x}} = \boldsymbol{x} - \mathbf{V}\, t, \tag{1.43}$$

$$\tilde{t} = t. \tag{1.44}$$

From the chain rule, it comes that the following relation holds between the nabla and the partial time derivative operator expressed in each coordinate system:

$$\tilde{\nabla} = \nabla, \tag{1.45}$$

$$\partial_{\tilde{t}} = \partial_t + \mathbf{V} \cdot \nabla. \tag{1.46}$$

Expressing equations (1.40) to (1.42) in terms of the operators in the fixed coordinate system, one has:

$$\nabla \times \left(\tilde{\mathbf{E}} - \mathbf{V} \times \tilde{\mathbf{B}} \right) = -\partial_t \tilde{\mathbf{B}}, \tag{1.47}$$

$$\nabla \times (\nu \tilde{\mathbf{B}}) = \tilde{\mathbf{J}} = \sigma \tilde{\mathbf{E}}, \tag{1.48}$$

$$\nabla \cdot \tilde{\mathbf{B}} = 0, \tag{1.49}$$

where the following vector formula has been exploited:

$$\nabla \times \left(\mathbf{V} \times \tilde{\mathbf{B}}\right) = \mathbf{V}\left(\nabla \cdot \tilde{\mathbf{B}}\right) - \tilde{\mathbf{B}}\left(\nabla \cdot \mathbf{V}\right) + \left(\tilde{\mathbf{B}} \cdot \nabla\right)\mathbf{V} - \left(\mathbf{V} \cdot \nabla\right)\tilde{\mathbf{B}}, \tag{1.50}$$

$$= -\left(\mathbf{V} \cdot \nabla\right)\tilde{\mathbf{B}}. \tag{1.51}$$

Inspecting equations (1.47) to (1.49), it can be shown that the following relation holds between the electromagnetic fields expressed within the moving and fixed coordinate systems:

$$\mathbf{B} = \tilde{\mathbf{B}}, \tag{1.52}$$

$$\mathbf{E} = \tilde{\mathbf{E}} - \mathbf{V} \times \tilde{\mathbf{B}}, \tag{1.53}$$

$$\mathbf{J} = \tilde{\mathbf{J}}. \tag{1.54}$$

Indeed, when relations (1.52) to (1.54) are substituted in equations (1.47) to (1.49), it can be shown that the vector fields $\mathbf{B}$, $\mathbf{E}$ and $\mathbf{J}$ defined in this manner satisfy Faraday's law, Ampere's law and Gauss's law expressed in $\Sigma(\boldsymbol{x}, t)$:

$$\nabla \times (\mathbf{E}) = -\partial_t \mathbf{B}, \tag{1.55}$$

$$\nabla \times (\nu \mathbf{B}) = \mathbf{J} = \sigma\left(\mathbf{E} + \mathbf{V} \times \mathbf{B}\right), \tag{1.56}$$

$$\nabla \cdot \mathbf{B} = 0. \tag{1.57}$$

In this thesis, the motions modelled consist of either conductors in translation at constant velocities or conductors in rotation at constant angular velocities. For the second case, the rotational movement induces an acceleration, which is omitted in the preceding analysis. It can be shown that this approximation remains valid provided that the angular velocity of the conductor is much smaller than the electronic cyclotron frequency[1] [99], which is the case for all the simulations of this work.

In equation (1.56), it appears that an additional motional-induction term, i.e. $\sigma(\mathbf{V} \times \mathbf{B})$, should be included in the governing equations when describing a conductor in relative motion with respect to the coordinate system. Since the governing equation involves an additional term, it is necessary to modify accordingly the weak formulation derived in section 1.3.2 to obtain a finite element model applicable in the fixed coordinate system. In this particular approach, the relative motion of the conductors with respect to the coordinate system requires to adjust their positions and to re-mesh the domain at each time step. As a result, at each time step, the evaluation of the time derivative of any unknown function $y(t)$ in the conductor within the fixed coordinate system often requires interpolation calculations of the same function computed at the previous time step. These interpolation calculations introduce numerical errors in the scheme at each time step, over time these errors accumulate which degrades the accuracy of the solution [96].

Alternatively, provided that the mesh within the conducting domain is advected with the domain from time step to time step, evaluating the time derivative within the coordinate system moving with the conductor does not require any interpolation calculation. As a result, the progressive accuracy degradation can be avoided by expressing the problem within the coordinate system $\Sigma(\tilde{\boldsymbol{x}}, \tilde{t}\,)$. This allows the weak formulations derived in section 1.3.2 to be applied for computing

[1]The electronic cyclotron frequency is defined as: $(e\,B)/m$, where e and m are the charge and the mass of the electron respectively.

the fields $\tilde{\cdot}$. Then, relations (1.52) to (1.54) can be employed to infer the fields within the stationary coordinate system. As an illustration, Figure 1.6 schematically depicts a 2D scenario illustrating the calculation of the time derivative in both coordinate systems for a scalar function within the conducting domain at the time step t_i. It is assumed that the mesh within the conductor remains unchanged between consecutive time steps.

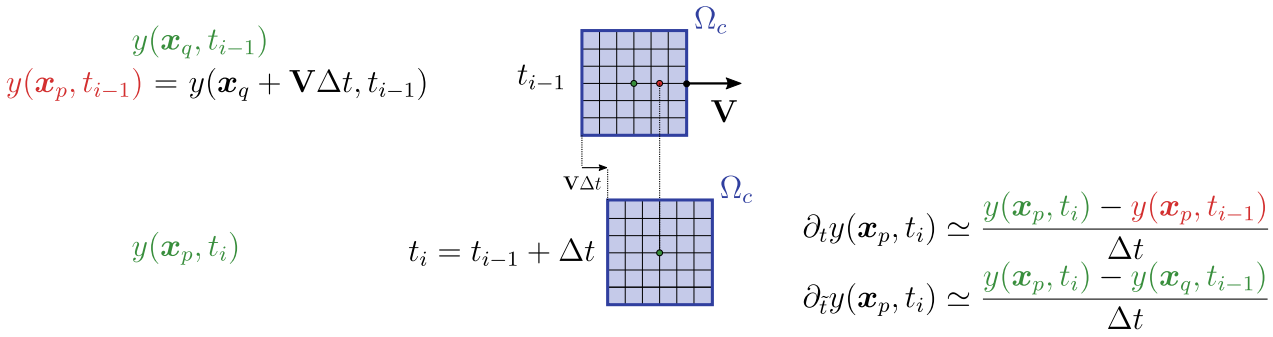

Figure 1.6: Schematic illustration of the quantities involved in the calculation of the time derivatives of a scalar field $y(\boldsymbol{x}, t)$ in the stationary and in the moving coordinate systems. The quantities requiring an interpolation calculation are highlighted in red.

Besides, it was also reported that the results tend to be generally better when the problem is formulated within a moving coordinate system, even in situations where interpolation is unnecessary in the fixed frame [96, 98, 100].

Method for managing multiple mobile conductors

The situation becomes inevitably more complex when several conductors are in motion at various velocities within the domain Ω. The complexity arises because when the velocity of the coordinate system is forced to be equal to the velocity of a specific conductor, it is not identical to the velocity of the other conductors. To illustrate how such situations are addressed in this thesis, let us consider that there are N_{Ω_c} distinct conductors in the domain, each moving at a specific velocity noted $\mathbf{V}_k$ where k ranges from 1 to N_{Ω_c}. A fixed coordinate system $\Sigma(\boldsymbol{x}, t)$ is introduced and is regarded as the standard coordinate system, note that the velocities $\mathbf{V}_k$ correspond to the velocities of the conductors with respect to $\Sigma(\boldsymbol{x}, t)$. Then, for each conducting region a distinct coordinate system $\Sigma(\boldsymbol{x}_k, t_k)$ moving at a velocity $\mathbf{V}_{f,k}$ is defined. This situation is shown graphically in Figure 1.7.
In this work, the method proposed in [96] is used. This approach involves the formulation of governing equations within individual conductors using separate coordinate systems. The equations in conductor k are expressed with respect to the coordinate system $\Sigma(\boldsymbol{x}_k, t_k)$, while the equations in the non-conducting region are formulated in the reference frame. As a result, there is no consideration of motion-induction terms within any conducting region. Equations (1.52) to (1.54) are then exploited to obtain the electromagnetic fields computed within the different coordinate systems in the reference frame $\Sigma(\boldsymbol{x}, t)$.

As can be seen in equation (1.52), the magnetic induction, and hence the magnetic field, defined in a fixed and in a moving coordinate system are identical. As a result, if the magnetic field is

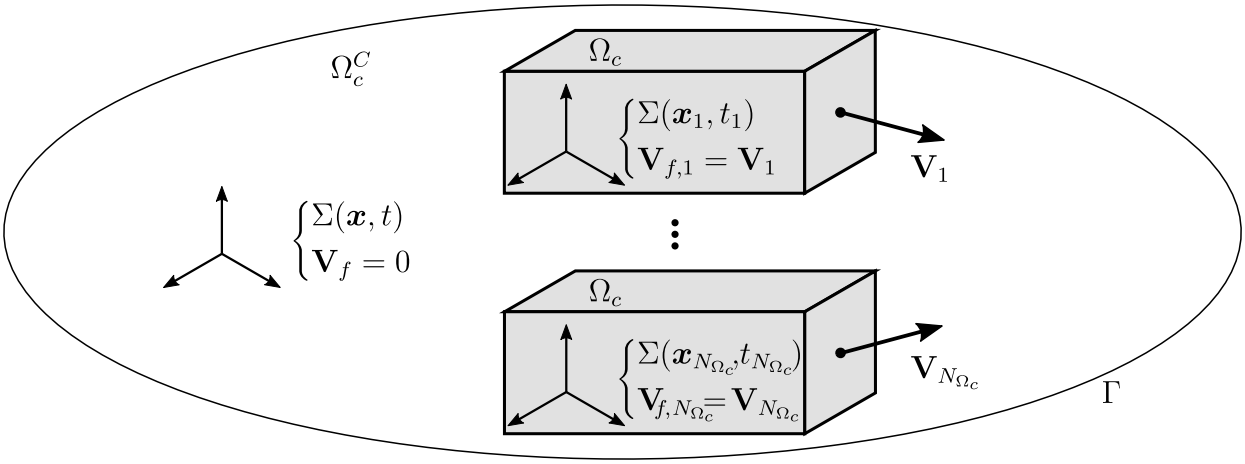

Figure 1.7: Schematic illustration of several conductors moving at distinct velocities $\mathbf{V}_k$ and of the coordinate systems $\Sigma(\boldsymbol{x}, t)$ and $\Sigma(\boldsymbol{x}_k, t_k)$.

selected as the primary unknown, the same unknown field $\mathbf{H}$ can be shared even though the equations in the conducting regions are expressed in coordinate systems moving at distinct velocities. Nevertheless, the potentials introduced in different coordinate systems are not necessarily identical if particular attention is not paid to the gauge condition in each region. In this context, the following discussion considers the alteration of the potential definitions arising from the movement of the coordinate system.

Relation between potentials introduced in different coordinate systems

To clarify the difference between the potentials defined in a fixed and a mobile coordinate system, the simpler case of a single moving conductor shown in Figure 1.5 is considered and the reasoning presented in [96] is applied. Following a procedure similar to the one used for deriving equations (1.29) and (1.30), one can introduce the scalar electric potential and the magnetic vector potential in each coordinate system:

$$\tilde{\mathbf{B}} = \tilde{\nabla} \times \tilde{\mathbf{A}}, \tag{1.58}$$

$$\tilde{\mathbf{E}} = -\partial_{\tilde{t}} \tilde{\mathbf{A}} - \tilde{\nabla} \tilde{v}, \tag{1.59}$$

$$\mathbf{B} = \nabla \times \mathbf{A}, \tag{1.60}$$

$$\mathbf{E} = -\partial_t \mathbf{A} - \nabla v. \tag{1.61}$$

Inserting these definitions in equations (1.41) and (1.56), the governing equation in the fixed and moving coordinate systems respectively writes:

$$\tilde{\nabla} \times \left(\nu \left(\tilde{\nabla} \times \tilde{\mathbf{A}} \right) \right) + \sigma \left(\partial_{\tilde{t}} \tilde{\mathbf{A}} + \tilde{\nabla} \tilde{v} \right) = 0, \tag{1.62}$$

$$\nabla \times \left(\nu \left(\nabla \times \mathbf{A} \right) \right) + \sigma \left(\partial_t \mathbf{A} + \nabla v - \mathbf{V} \times \left(\nabla \times \mathbf{A} \right) \right) = 0, \tag{1.63}$$

where the relationship between the potentials defined in $\Sigma(\tilde{\boldsymbol{x}}, \tilde{t}\,)$ and $\Sigma(\boldsymbol{x}, t)$ can be derived from equations (1.52) to (1.54). Indeed, substituting (1.58) and (1.60) in (1.52), one has:

$$\mathbf{A} = \tilde{\mathbf{A}} + \nabla \xi, \tag{1.64}$$

where ξ is an arbitrary scalar field.

Then inserting equations (1.59), (1.60) and (1.61) in (1.53) yields:

$$-\partial_t \mathbf{A} - \nabla v = -\partial_{\tilde{t}} \tilde{\mathbf{A}} - \tilde{\nabla}\tilde{v} - \mathbf{V} \times (\nabla \times \tilde{\mathbf{A}}), \tag{1.65}$$

$$-\partial_t \tilde{\mathbf{A}} - \partial_t (\nabla \xi) - \nabla v = -\partial_t \tilde{\mathbf{A}} - \mathbf{V} \cdot \nabla \tilde{\mathbf{A}} - \nabla \tilde{v} - \mathbf{V} \times (\nabla \times \tilde{\mathbf{A}}), \tag{1.66}$$

where the relations (1.45), (1.46) and (1.64) have been exploited. Considering that the velocity is homogeneous within the conductor, the following vector identity may be derived:

$$\mathbf{V} \times \left(\nabla \times \tilde{\mathbf{A}}\right) = \nabla \left(\tilde{\mathbf{A}} \cdot \mathbf{V}\right) - (\mathbf{V} \cdot \nabla)\, \tilde{\mathbf{A}} \tag{1.67}$$

Substituting equation (1.67) in (1.66), one has:

$$\nabla \left(v - \tilde{v} - \tilde{\mathbf{A}} \cdot \mathbf{V} + \partial_t \xi\right) = 0. \tag{1.68}$$

If all the potentials vanish at infinite distance, the following relation may be written:

$$v = \tilde{v} + \tilde{\mathbf{A}} \cdot \mathbf{V} - \partial_t \xi. \tag{1.69}$$

As it appears from equations (1.64) and (1.69), the magnetic vector potentials introduced in $\Sigma(\tilde{\boldsymbol{x}}, \tilde{t}\,)$ and $\Sigma(\boldsymbol{x}, t)$ are not necessarily identical and the relationship between them depends on the gauge condition used for the scalar electric potential. A particularly interesting case to discuss is when the electric scalar potential is set to 0 in both coordinate systems since this is the gauge proposed in the derivation of the $\mathbf{A}$ formulation in section 1.3.2. In that specific case, forcing $v = \tilde{v} = 0$ in equation (1.69) and inserting the result in equation (1.64) leads to:

$$\mathbf{A} = \tilde{\mathbf{A}} + \int_0^t \nabla \left(\tilde{\mathbf{A}} \cdot \mathbf{V}\right) \mathrm{d}t. \tag{1.70}$$

Therefore, it can be understood that using this gauge, the magnetic vector potentials defined in coordinate systems moving at distinct velocities are not identical.

Alternatively, the gauge condition $\tilde{v} = -\tilde{\mathbf{A}} \cdot \mathbf{V}$ could be used in the moving coordinate system while conserving the condition $v = 0$ in the stationary one. In that case, equation (1.69) would write $\partial_t \xi = 0$. As a result, with that particular gauge condition, if the initial fields $\mathbf{A}$ and $\tilde{\mathbf{A}}$ are the same, the subsequent magnetic vector potential computed with equations (1.62) and (1.63) are identical.

Now the more elaborated case of several conductors moving at distinct velocities presented in Figure 1.7 is re-considered. Given the discussion above, the most appropriate method for addressing this problem when selecting $\mathbf{A}$ as the primary unknown field consists in formulating the governing equation (1.62) within the conductor k, utilizing the coordinate system $\Sigma(\boldsymbol{x}_k, t_k)$ and applying distinct gauge condition, i.e. $v_k = -\mathbf{A}_k \cdot \mathbf{V}_k$, within each conducting region. This choice ensures that the magnetic vector potential remains consistent across all coordinate systems. In this thesis, a different method is used: the condition $v_k = 0$ is applied in all conductors and a single unknown $\mathbf{A}$-field is used both in the moving and in the fixed coordinate systems, thus assuming $\mathbf{A} = \mathbf{A}_k$. From equation (1.70), this leads to an error in the magnetic vector potential in the moving conductors that can be expressed as the time integral of a gradient field. This error therefore exclusively impacts the non-solenoidal component of the electric field (cf. equation (1.61)) which is not problematic as long as conductors moving at distinct velocities are electrically isolated from one another as discussed in [96]. This last condition holds true for all the simulations conducted in this work which justifies the use of the simpler gauge $v_k = 0$ in all conductors.

Choosing a formulation for modelling mobile superconductors

As pointed out in section 1.3.2, selecting **H** as the primary unknown field is better suited for modelling superconducting materials. Nevertheless, as it appears in equation (1.25), within this formulation, the time derivative of the unknown field needs to be calculated across the entire domain Ω. When the conductors are in movement within Ω, a re-meshing is required at each time step and the mesh cannot be kept identical between consecutive time steps simultaneously in Ω_c and in Ω_c^C. As a result, interpolation calculations between two distinct meshes would be necessary, leading to a progressive deterioration of the solution accuracy. In the framework of the **A** formulation the computation of the time derivative of the unknown field is required only within the conducting regions (cf. equation (1.33)). For moving conductors, the use of this formulation therefore avoids the issue of gradual accuracy deterioration, provided that the mesh in each conducting region remains identical between successive time steps. Therefore, none of these formulations is optimal for modelling mobile superconductors.

In this context, it is proposed to couple these formulations to take advantage of both [76]. More precisely, it is proposed to use the **H**-ϕ formulation in the superconducting regions, the **A** formulation in the non-conducting region and to ensure a proper coupling between them thanks to surface terms.

To illustrate this coupled **H**-ϕ-**A** formulation, let us consider the case of several superconductors moving at distinct velocities presented in Figure 1.7. The domain is partitioned into two distinct regions: the first is noted Ω_H and contains the superconductors and their boundaries while the second is denoted Ω_A and encompasses the non-conducting region along with its boundary, such that $\Omega_\mathrm{H} \cup \Omega_\mathrm{A} = \Omega$. It is assumed that the superconductors remain inside the domain Ω at any instant such that $\Omega_\mathrm{H} \cap \Gamma = \varnothing$. The domain Ω_H is further subdivided into N_{Ω_c} complementary domains noted $\Omega_{\mathrm{H},k}$, where k ranges from 1 to N_{Ω_c}. Each domain $\Omega_{\mathrm{H},k}$ encompasses a single superconductor and its boundary. The shared boundary between each individual superconductor with the non-conducting region is denoted $\Gamma_k = \Omega_{\mathrm{H},k} \cap \Omega_\mathrm{A}$. The domain subdivision is shown schematically in Figure 1.8.

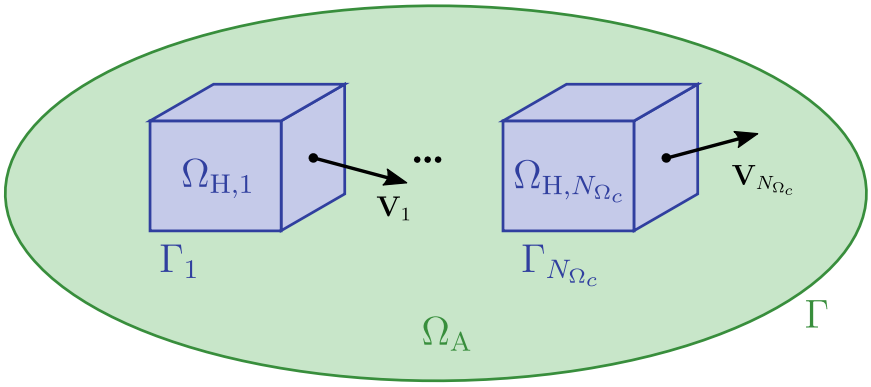

Figure 1.8: Domain partition for the application of the coupled **H**-ϕ-**A** formulation to the problem of N_{Ω_c} moving at distinct velocities. The **A** formulation is used in Ω_A while the **H** formulation is used in $\bigcup_{k=1}^{N_{\Omega_c}} \Omega_{\mathrm{H},k}$.

Solving the **H** formulation expressed in the coordinate systems moving along with the supercon-

ductors amounts to find $\mathbf{H} \in \bar{F}^1_h(\Omega_{\mathrm{H}})$ such that:

$$\begin{aligned}\sum_{k=1}^{N_{\Omega_c}} \int_{\Omega_{\mathrm{H}},k} (\partial_{t_k}(\mu\mathbf{H})) \cdot \mathbf{H}' \,\mathrm{d}\Omega + \int_{\Omega_{\mathrm{H}}} (\rho\nabla\times\mathbf{H}) \cdot (\nabla\times\mathbf{H}') \,\mathrm{d}\Omega \\ - \sum_{k=1}^{N_{\Omega_c}} \int_{\Gamma_k} (\mathbf{E}\times\boldsymbol{n}_{\Omega_{\mathrm{H}}}) \cdot \mathbf{H}' \,\mathrm{d}\Gamma = 0, \quad \forall \mathbf{H}' \in \bar{F}^1_{h0}(\Omega_{\mathrm{H}}),\end{aligned} \tag{1.71}$$

with $\boldsymbol{n}_{\Omega_{\mathrm{H}}}$ the unit external normal vector to the domain Ω_{H}, where the meaning of the partial time derivative ∂_{t_k} is different in each superconductor and where $\mathbf{E} = -\partial_{t_k}\mathbf{A}$ is expressed using the unknown field in domain Ω_{A}.

Then, solving the $\mathbf{A}$ formulation using the method presented in this section amounts to finding $\mathbf{A} \in F^1_e(\Omega_{\mathrm{A}})$ such that:

$$\begin{aligned}\int_{\Omega_{\mathrm{A}}} (\nu\nabla\times\mathbf{A}) \cdot (\nabla\times\mathbf{A}') \,\mathrm{d}\Omega - \sum_{k=1}^{N_{\Omega_c}} \int_{\Gamma_k} (\mathbf{H}\times\boldsymbol{n}_{\Omega_{\mathrm{A}}}) \cdot \mathbf{A}' \,\mathrm{d}\Gamma - \int_{\Gamma_h} \left(\bar{\mathbf{H}}\times\boldsymbol{n}_{\Omega_{\mathrm{A}}}\right) \cdot \mathbf{A}' \,\mathrm{d}\Gamma = 0, \\ \forall \mathbf{A}' \in F^1_{e0}(\Omega_{\mathrm{A}}),\end{aligned} \tag{1.72}$$

with $\boldsymbol{n}_{\Omega_{\mathrm{A}}}$ the unit external normal vector to the domain Ω_{A} and where $\mathbf{H}$ is the unknown field in Ω_{H} and $\bar{\mathbf{H}}$ is a prescribed function.

Gathering equations (1.71) and (1.72) together, the final coupled formulation writes:

$$\begin{aligned}&\sum_{k=1}^{N_{\Omega_c}} \int_{\Omega_{\mathrm{H}},k} (\partial_{t_k}(\mu\mathbf{H})) \cdot \mathbf{H}' \,\mathrm{d}\Omega + \int_{\Omega_{\mathrm{H}}} (\rho\nabla\times\mathbf{H}) \cdot (\nabla\times\mathbf{H}') \,\mathrm{d}\Omega + \int_{\Omega_{\mathrm{A}}} (\nu\nabla\times\mathbf{A}) \cdot (\nabla\times\mathbf{A}') \,\mathrm{d}\Omega \\ &+ \sum_{k=1}^{N_{\Omega_c}} \int_{\Gamma_k} ((\partial_{t_k}\mathbf{A})\times\boldsymbol{n}_{\Omega_{\mathrm{H}}}) \cdot \mathbf{H}' \,\mathrm{d}\Gamma - \sum_{k=1}^{N_{\Omega_c}} \int_{\Gamma_k} (\mathbf{H}\times\boldsymbol{n}_{\Omega_{\mathrm{A}}}) \cdot \mathbf{A}' \,\mathrm{d}\Gamma - \int_{\Gamma_h} \left(\bar{\mathbf{H}}\times\boldsymbol{n}_{\Omega_{\mathrm{A}}}\right) \cdot \mathbf{A}' \,\mathrm{d}\Gamma = 0, \\ &\qquad \forall \mathbf{H}' \in \bar{F}^1_{h0}(\Omega_{\mathrm{H}}) \,\text{and}\, \forall \mathbf{A}' \in F^1_{e0}(\Omega_{\mathrm{A}}).\end{aligned} \tag{1.73}$$

This coupled formulation indeed preserves the individual advantages of the $\mathbf{H}$ and $\mathbf{A}$ formulations since it may be noticed in equation (1.73) that non-linearities are introduced in the formulation through the resistivity only and that time derivatives are evaluated only in the conducting regions.

1.3.6 Modelling scenarios

The finite element model introduced in this section is used throughout the thesis for simulating the responses of superconductors under various sequences of applied fields or movements. The exact geometries and superconducting properties specific to the modelled samples are systematically specified at relevant points in the thesis. Nevertheless, the model is primarily employed to conduct three distinct types of simulations, each characterized by a specific procedure, the parameters of which are outlined below.

Zero-field-cooled magnetization

To model the magnetization of superconducting material in zero-field-cooled conditions, a homogeneous initial condition for all the electromagnetic fields involved in the formulation is

used. The prescribed applied field sequence is imposed by employing a time-varying boundary condition. Sequences involving changes in both the amplitude and direction of the field applied to a stationary superconductor can be effectively simulated using this approach. The **A**-field and **H**-field distributions at the end of the applied field sequence are saved and can be used as initial conditions for subsequent simulations.

Field-cooled magnetization

The modelling of a field-cooled magnetization procedure can be achieved through the execution of two successive simulation processes. In a first simulation, the superconducting regions are substituted with non-conducting regions, homogeneous initial conditions are used and the applied field is ramped up from zero to the initial field of the specified field-cooling process. The **A**-field distribution computed at the end of this first step thus corresponds to a situation in which the magnetic field is uniform and equal to the initial field of the considered field-cooling process and where $\mathbf{J} = \mathbf{0}$ everywhere in Ω. In the second simulation, superconducting regions are considered, the **A**-field and **H**-field distributions computed in the first step are used as initial conditions and the prescribed applied field sequence is imposed by employing a time-varying boundary condition.

Motion of magnetized superconductors

Simulations involving both translations and rotations of multiple magnetized superconductors are conducted in this thesis. In this context, the individual magnetization of each superconductor involved is first simulated to compute the initial **A**-field and **H**-field distributions before any motion. The movement is then handled by either translating or rotating the superconducting regions at each time step. Additionally, the **A**-field and **H**-field computed at the preceding time step are either shifted or rotated appropriately to evaluate the time derivatives.

More specifically, when considering the simulations related to the combination of three magnetized superconductors in Halbach structures, the field distribution of the initial state is evaluated after a 45 min period following the magnetization process. Unless explicitly specified otherwise, the magnetizing process consists in a zero-field-cooled procedure with a maximum applied field of 2.4 T and a field removal rate of 1 mT s^{-1}. During the modelling of the assembly process, the initial distance between neighbouring samples is set to 40 mm. Such a distance is sufficient to consider negligible interactions between the superconductors [101]. The separation distance is then gradually reduced at a rate of 1 mm s^{-1} until it reaches a final value of 0.5 mm.

Regarding the simulations involving a rotational motion, the simulated magnetizing field sequence aligns with the specific experimental conditions outlined in section 2.3.5 and the rotational speed is set to 5° s^{-1}.

1.4 Analytical model

In the previous section, a finite element model solving Maxwell's equations in the magnetodynamic approximation was formulated. This tool holds great interest due to its ability to assess the distribution of electromagnetic fields, even within complex geometrical configurations. Nevertheless, the strong non-linearity of the problem introduced by the superconducting constitutive law may yield a significant computational challenge, especially when three-dimensional problems are considered. To mitigate the numerical cost of the method, it is often necessary to adopt a coarser mesh, which leads to a reduced spatial resolution for the computed electromagnetic fields. Considering these numerical limitations, there remains a great interest in developing simplified analytical models, even though they are based on additional simplifying assumptions.

In this context, assuming the precise knowledge of an electrical current distribution that does not change with time, the Biot-Savart law can be applied to calculate the magnetic flux density produced by this electrical current [102]. As an illustration, the expressions of the Biot-Savart law written for a filamentary, a surface and a volume electrical current are presented in Figures 1.9 (a), (b) and (c) respectively.

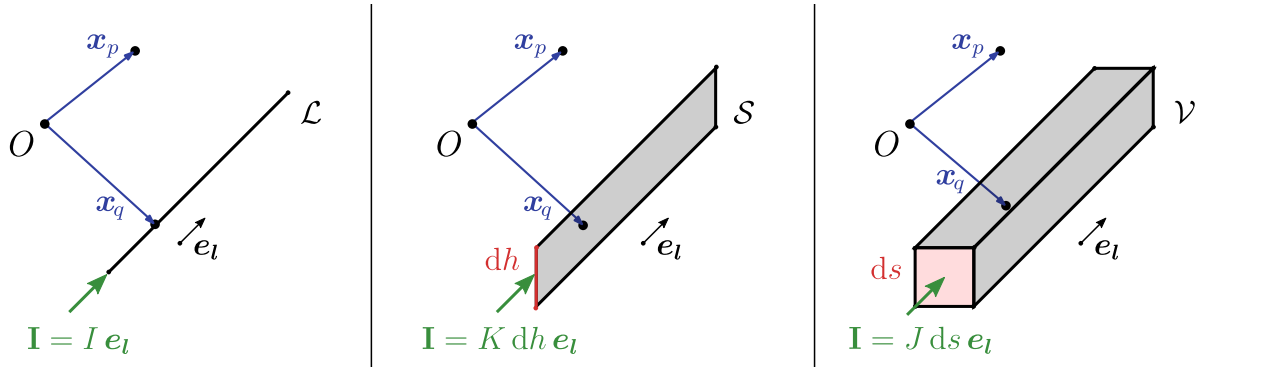

Figure 1.9: Application of the Biot-Savart law to the case of (a) a filamentary, (b) a surface and (c) a volume electrical current. In each case, the conductor carries a total current $\mathbf{I}$ that is directed along the unit vector $\boldsymbol{e_l}$.

In this section the Biot-Savart law is applied to several practical cases in which the current distribution may be assumed. Following mathematical derivations, either an analytical or a semi-analytical model exhibiting a minimal numerical cost is obtained in each case.

1.4.1 Biot-Savart law applied to a cubic permanent magnet

The magnetic flux density produced by permanent magnets can be modelled by a surface current density denoted $\mathbf{K}$ flowing along the surface of the magnet, as reported in [103]. Based on this current distribution, a simple analytical model computing the three components of the magnetic flux density generated by a cubic permanent magnet whose main magnetization direction is

aligned with $\boldsymbol{e_z}$ is derived in this section.

The magnetic flux density produced by one-fourth of a permanent magnet which carries a surface current with an amplitude noted K_c is examined. More particularly, the focus is directed towards two distinct current lines that respectively include the points $\boldsymbol{x}_q$ and $\boldsymbol{x}_q + \mathrm{d}z\,\boldsymbol{e_z}$, both situated on the surface of the magnet. These lines define a surface carrying a total current $\mathbf{I} = K_c\,\mathrm{d}z\,\boldsymbol{e_y}$ as represented in Figure 1.10 (a).

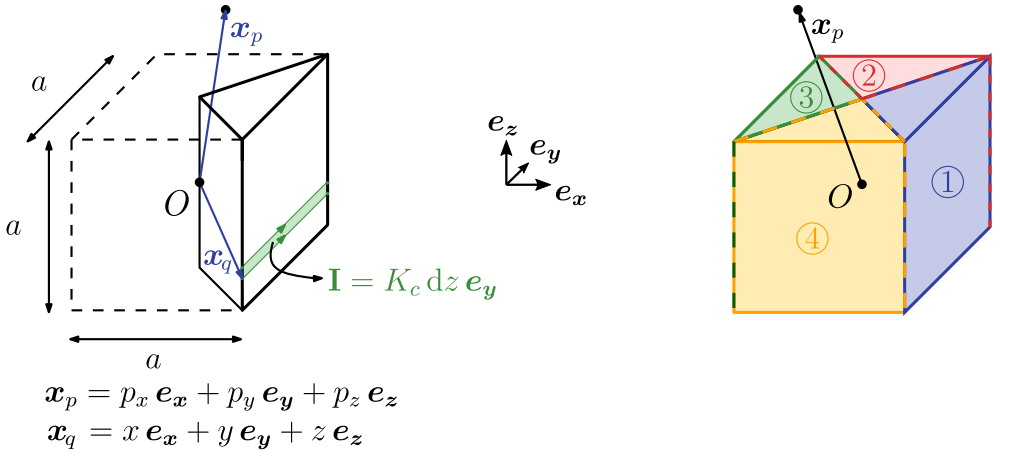

(a) (b)

Figure 1.10: (a) Schematic representation of the analytical model of one-fourth of a permanent magnet. (b) Numbering of the four quarters of the permanent magnet. The origin of the coordinate system is noted O and corresponds to the geometrical centre of the permanent magnet.

The magnetic flux density $\mathrm{d}\mathbf{B}$ generated by the green surface in Figure 1.10 (a) at point $\boldsymbol{x}_p$ can be computed with the Biot-Savart law, which writes:

$$\mathrm{d}\mathbf{B} = \frac{\mu_0\,K_c}{4\pi}\int_{-\frac{a}{2}}^{\frac{a}{2}} \frac{\boldsymbol{e_y}\times(\boldsymbol{x}_p - \boldsymbol{x}_q)}{||\boldsymbol{x}_p - \boldsymbol{x}_q||^3}\,\mathrm{d}y\,\mathrm{d}z. \tag{1.74}$$

The magnetic flux density generated at point $\boldsymbol{x}_p$ by the quarter of the permanent magnet can thus be computed by integrating the expression (1.74) over the height of the cube:

$$\mathbf{B} = \frac{\mu_0\,K_c}{4\pi}\int_{-\frac{a}{2}}^{\frac{a}{2}}\int_{-\frac{a}{2}}^{\frac{a}{2}} \frac{\boldsymbol{e_y}\times(\boldsymbol{x}_p - \boldsymbol{x}_q)}{||\boldsymbol{x}_p - \boldsymbol{x}_q||^3}\,\mathrm{d}y\,\mathrm{d}z. \tag{1.75}$$

Noting $\alpha^2(x,z) = (p_x - x)^2 + (p_z - z)^2$ and solving (1.75) for the x and z-components of $\mathbf{B}$ one obtains:

$$B_x = -\frac{\mu_0 K_c}{4\pi}\left[\left[\frac{p_y - y}{|p_y - y|}\,\text{arctanh}\left(\sqrt{1+\frac{\alpha^2(\frac{a}{2},z)}{(p_y-y)^2}}\right)\right]_{-\frac{a}{2}}^{\frac{a}{2}}\right]_{-\frac{a}{2}}^{\frac{a}{2}} = f(p_x,p_y,p_z), \tag{1.76}$$

$$B_z = -\frac{\mu_0 K_c\left(p_x-\frac{a}{2}\right)}{4\pi|p_x-\frac{a}{2}|}\left[\left[\frac{p_y-y}{|p_y-y|}\arctan\left(\frac{p_z-z}{|p_x-x|\sqrt{1+\frac{\alpha^2(\frac{a}{2},z)}{(p_y-y)^2}}}\right)\right]_{-\frac{a}{2}}^{\frac{a}{2}}\right]_{-\frac{a}{2}}^{\frac{a}{2}} = g(p_x,p_y,p_z). \tag{1.77}$$

The magnetic flux density generated by the full permanent magnet at location $\boldsymbol{x}_p$ can then be computed simply by adding the contributions of each quarter. The number assigned to each quarter and the expression of the total magnetic flux density is presented in Figure 1.10 (b) and in equations (1.78) to (1.82) respectively.

$$\mathbf{B}_1 = f(p_x,p_y,p_z)\boldsymbol{e_x} + g(p_x,p_y,p_z)\boldsymbol{e_z}, \tag{1.78}$$
$$\mathbf{B}_2 = f(p_y,-p_x,p_z)\boldsymbol{e_y} + g(p_y,-p_x,p_z)\boldsymbol{e_z}, \tag{1.79}$$
$$\mathbf{B}_3 = -f(-p_x,-p_y,p_z)\boldsymbol{e_x} + g(-p_x,-p_y,p_z)\boldsymbol{e_z}, \tag{1.80}$$
$$\mathbf{B}_4 = -f(-p_y,p_x,p_z)\boldsymbol{e_y} + g(-p_y,p_x,p_z)\boldsymbol{e_z}, \tag{1.81}$$
$$\mathbf{B} = \mathbf{B}_1 + \mathbf{B}_2 + \mathbf{B}_3 + \mathbf{B}_4. \tag{1.82}$$

A full analytical expression is thus obtained for the magnetic flux density generated by a cubic permanent magnet.

1.4.2 Biot-Savart law applied to a magnetized cubic superconductor

A similar procedure is applied to compute analytically the magnetic flux density generated by a magnetized cubic bulk superconductor whose main magnetization direction is aligned with $\boldsymbol{e_z}$. The model considers a completely magnetized superconductor in the critical state (Bean model [66]) with square current loops strictly perpendicular to $\boldsymbol{e_z}$. The model also assumes that the critical current density is a constant, field-independent value equal to J_c over the whole superconductor. With such assumptions, the flux density produced by one-fourth of a magnetized cubic superconductor is examined, as shown schematically in Figure 1.11 (a). More particularly, four different current lines containing respectively the points $\boldsymbol{x}_q$, $\boldsymbol{x}_q + \mathrm{d}x\,\boldsymbol{e_x}$, $\boldsymbol{x}_q + \mathrm{d}z\,\boldsymbol{e_z}$ and $\boldsymbol{x}_q + \mathrm{d}x\,\boldsymbol{e_x} + \mathrm{d}z\,\boldsymbol{e_z}$ are considered. These lines define a volume carrying a total current $\mathbf{I} = J_c\,\mathrm{d}x\,\mathrm{d}z\,\boldsymbol{e_y}$ as represented in Figure 1.11 (a).

The magnetic flux density $\mathrm{d}\mathbf{B}$ generated by the volume shown in green in Figure 1.11 (a) at the point $\boldsymbol{x}_p$ can be computed with the Biot-Savart law. Similarly to the calculation carried out for permanent magnets, this expression can be integrated over the quarter of the superconductor to compute the flux density at point $\boldsymbol{x}_p$, which writes:

$$\mathbf{B} = \frac{\mu_0}{4\pi}\int_0^{\frac{a}{2}}\int_{-\frac{a}{2}}^{\frac{a}{2}}\int_{-\frac{L(x)}{2}}^{\frac{L(x)}{2}} J_c\,\frac{\boldsymbol{e_y}\times(\boldsymbol{x}_p-\boldsymbol{x}_q)}{||\boldsymbol{x}_p-\boldsymbol{x}_q||^3}\,\mathrm{d}y\,\mathrm{d}z\,\mathrm{d}x, \tag{1.83}$$

where $L(x)$ is the length of the current line containing the point $\boldsymbol{x}_q$. In the case of a cubic superconductor in the critical state, $L(x) = 2x$.

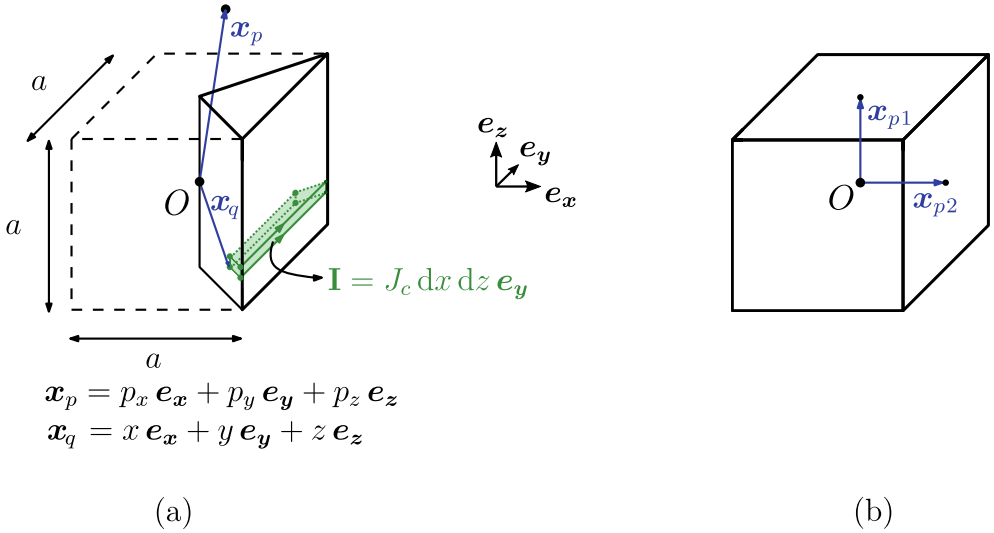

(a) (b)

Figure 1.11: (a) Schematic representation of the analytical model of a quarter of completely magnetized cubic superconductor. (b) Position of the point $\boldsymbol{x}_{p1}$ and $\boldsymbol{x}_{p2}$. The origin of the coordinate system is noted O and corresponds to the geometrical centre of the superconductor.

The first two integrals appearing in equation (1.83) are similar to those for permanent magnets. The x and z-components of the magnetic flux density thus take the following integral form:

$$B_x = -\frac{\mu_0 \, J_c}{4\pi} \int_0^{\frac{a}{2}} \left[\left[\frac{p_y - y}{|p_y - y|} \operatorname{arctanh} \left(\sqrt{1 + \frac{\alpha^2(x,z)}{(p_y - y)^2}} \right) \right]_{-\frac{L(x)}{2}}^{\frac{L(x)}{2}} \right]_{-\frac{a}{2}}^{\frac{a}{2}} \mathrm{d}x = f^*(p_x, p_y, p_z), \quad (1.84)$$

$$B_z = -\frac{\mu_0 \, J_c}{4\pi} \int_0^{\frac{a}{2}} \frac{p_x - x}{|p_x - x|} \left[\left[\frac{p_y - y}{|p_y - y|} \arctan \left(\frac{p_z - z}{|p_x - x| \sqrt{1 + \frac{\alpha^2(x,z)}{(p_y - y)^2}}} \right) \right]_{-\frac{L(x)}{2}}^{\frac{L(x)}{2}} \right]_{-\frac{a}{2}}^{\frac{a}{2}} \mathrm{d}x = g^*(p_x, p_y, p_z). \quad (1.85)$$

The integrals appearing in equations (1.84) and (1.85) are numerically evaluated in this work, thus making the model for the magnetic flux density produced by a cubic superconductor semi-analytical. The magnetic flux density generated by the complete superconductor can be computed by applying the equations (1.78) to (1.82) with the functions f^* and g^* instead of f and g.

Equations (1.84) and (1.85) are further particularized at two specific points exploiting the different symmetries of the generated flux density. The first point $\boldsymbol{x}_{p1}$ corresponds to the geometrical centre of the top surface of the cube; the second point $\boldsymbol{x}_{p2}$ corresponds to the geometrical centre of a lateral surface. At these points, only the z-component of the flux density does not vanish and its value can be computed semi-analytically as follows:

$$B_z^{\boldsymbol{x}_{p1}} = \frac{\mu_0 J_c a}{\pi}\left[\arctan\left(\sqrt{\frac{2}{3}}\right) - \ln\left(\frac{\sqrt{6}+1}{\sqrt{6}-1}\right) + \sqrt{2}\ln\left(\frac{1+\sqrt{3}}{\sqrt{2}}\right)\right] \simeq 0.2384 \times \mu_0 J_c a, \quad (1.86)$$

$$B_z^{\boldsymbol{x}_{p2}} = \frac{\mu_0 J_c a}{2\pi}\int_{-1}^{1} \arctan\left(\frac{\sqrt{2}\sqrt{x^2+x+1}}{x\,(x+1)}\right) \mathrm{d}x \simeq 0.0375 \times \mu_0 J_c a. \quad (1.87)$$

Interestingly, it appears from equations (1.86) and (1.87) that the ratio $B_z^{\boldsymbol{x}_{p2}}/B_z^{\boldsymbol{x}_{p1}}$ does not depend on the critical current density of the sample nor on its size. It only depends on the aspect ratio of the superconductor, for a cube, $B_z^{\boldsymbol{x}_{p2}}/B_z^{\boldsymbol{x}_{p1}}$ is equal to $0.16 \simeq 1/6$.

The model presented in this section can easily be extended to parallelepiped samples by using integration bounds that are not equal to each other, i.e. $a_x \neq a_y \neq a_z$, in equations (1.75) or (1.83). Also, it is possible to take into account a possible variation of the critical current density along the c-axis of the superconductor by incorporating this dependence $J_c(z)$ in equation (1.83). Depending on the considered dependence, however, calculating the integral along the z-direction in equation (1.83) can become complex, and it might be more practical to perform a numerical evaluation for this integral as well.

1.4.3 Biot-Savart law applied to superconductors with complex shape

The magnetization of superconductors exhibiting more elaborated shapes is also considered in this thesis. More particularly, the magnetic flux density generated by two superconducting triangular prisms magnetized along specific directions is considered in this section. Similar to the model used for superconducting cubes, this approach assumes complete penetration of the superconductor and that the current loops are strictly perpendicular to the primary magnetization direction. The model further assumes a constant and field-independent critical current density denoted as J_c in the entire superconductor. Considering these assumptions, the supercurrent penetrates the superconductor equally from all sides during the magnetization, which allows us to predict the expected current density distribution once the superconductor is magnetized. The exact geometry and the current density distribution theoretically expected within these superconductors of triangular cross-section are schematically represented in Figure 1.12. Note that the main magnetization direction is aligned with $\boldsymbol{e_z}$.

As shown in Figures 1.12 (b) and (d), in both cases, the superconductor can be partitioned in four distinct and complementary regions within which the current density is homogeneous and flows in the same direction. Similarly to the calculations of the preceding section, the Biot-Savart law for a volume current (presented in Figure 1.9 (c)) can be employed to compute the individual contribution of each quarter of superconductor shown in Figures 1.12 (b) and (d). The total magnetic flux density can then be determined by adding up all the contributions together. Given the geometrical shape of the superconductor, however, the integrals are not solved analytically but are evaluated numerically instead for these superconductors of triangular cross-section.

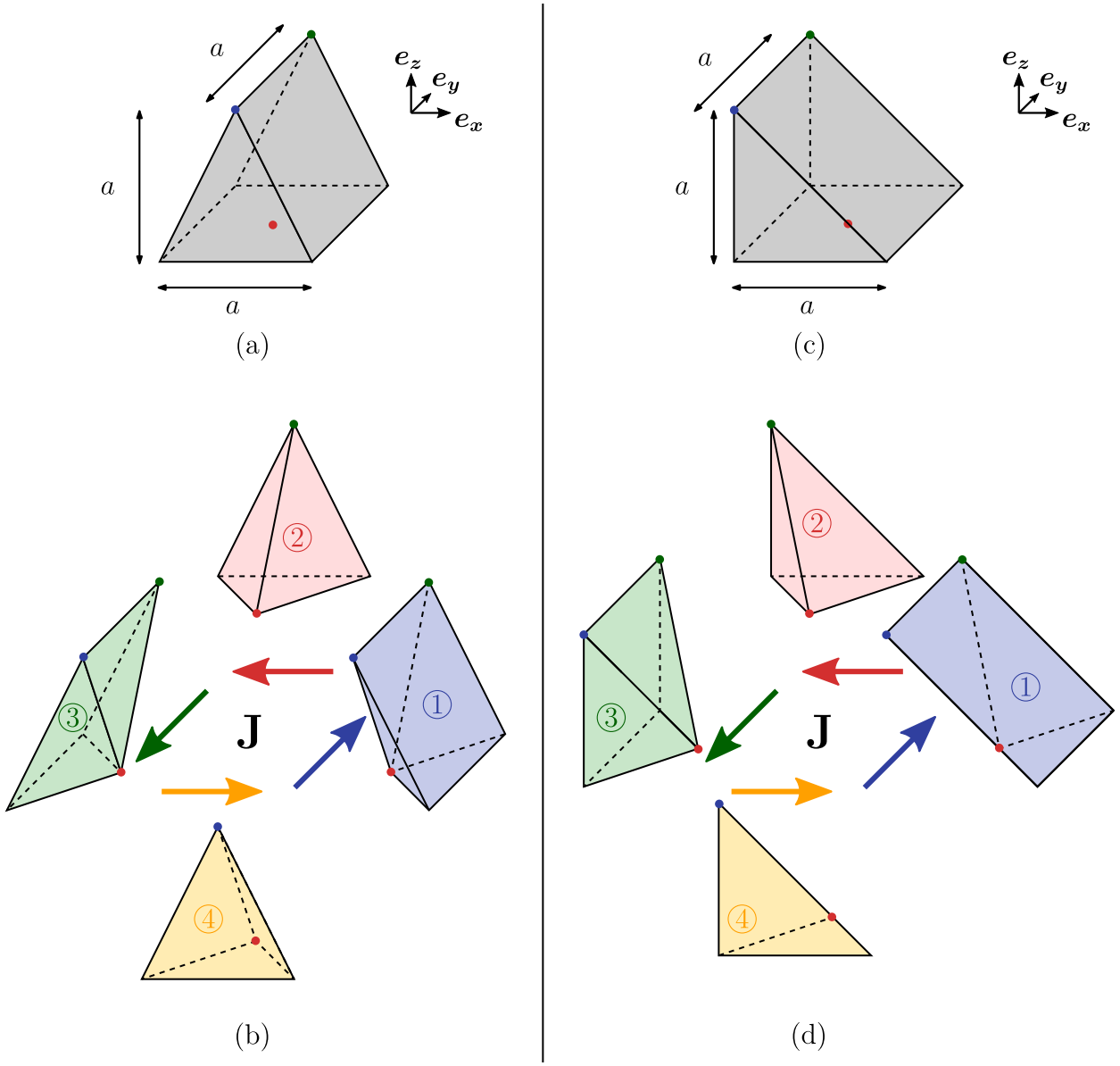

Figure 1.12: (a) and (c) Schematic representation of the geometry of two superconducting triangular prisms magnetized along the z-direction. The red dot coincides with the geometrical centre of the bottom face. (b) and (d) Schematic illustration of the expected current density distribution within the magnetized sample. In the blue and green regions, the current flows strictly along $+\boldsymbol{e_y}$ an $-\boldsymbol{e_y}$ respectively while in the yellow and red volumes the current flows strictly along $+\boldsymbol{e_x}$ an $-\boldsymbol{e_x}$ respectively.

1.5 Magnetic force acting on a particle

The magnetic force experienced by a magnetized particle depends both on the particle dipolar moment $\mathbf{m}$ and on the magnetic flux induction $\mathbf{B}$. This relationship can be expressed as:

$$\mathbf{F} = (\mathbf{m} \cdot \nabla)\, \mathbf{B}. \tag{1.88}$$

This thesis aims to maximize the amplitude and the spatial reach of such a magnetic force by combining several magnetized superconductors. In this section, the expression (1.88) is further developed to point out the physical parameters impacting the value of the magnetic force. Three distinct scenarios are considered below [7, 104–106]:

(a) The magnetic flux density is sufficient to magnetize particles to saturation. In that case, the magnetic moment of the particle is proportional to its volume and spontaneously orientates along the field lines. This can be expressed as:

$$\mathbf{m} = M_s\, V\, \frac{\mathbf{B}}{B}, \tag{1.89}$$

where M_s and V denote the saturation magnetization and the volume of the particle respectively while B refers to the amplitude of the magnetic flux density at the location of the particle.

Inserting equation (1.89) in (1.88) the expression of the force becomes:

$$\mathbf{F} = M_s\, V\, \nabla B. \tag{1.90}$$

(b) The particles are not saturated and contain cores of magnetite material over 30 nm in diameter. In that case, the particles exhibit a permanent magnetic moment which can be assumed to be proportional to the external magnetic field strength and to align rapidly with its direction [7]. Taking the demagnetization effect into account, it can be expressed as follows:

$$\mathbf{m} = \frac{V}{\mu_0} \left(\frac{\chi}{1 + D\chi} \right) \mathbf{B}, \tag{1.91}$$

where D is the demagnetization factor and χ is the magnetic susceptibility.

It follows that the force exerted on the particles writes:

$$\mathbf{F} = \frac{V}{\mu_0} \left(\frac{\chi}{1 + D\chi} \right) B\, \nabla B. \tag{1.92}$$

(c) The particles are not saturated and exhibit diameters smaller than 30 nm. In this case, each particle behaves as a superparamagnetic single domain whose magnetic moment can fluctuate because of thermal agitation [7, 8]. For such particles, it is common to use the Langevin function to compute the average projection of the moment in the direction of $\mathbf{B}$ [106, 107]:

$$\mathbf{m} = \frac{V\, M_s}{B}\, L\left(\frac{V\, M_s\, B}{k_b T} \right) \mathbf{B}, \tag{1.93}$$

where $L(x) = \coth(x) - \frac{1}{x}$ is the Langevin function while k_b and T are respectively Boltzmann's constant and the absolute temperature.
Inserting equation (1.93) in (1.88), the expression of the force writes:

$$\mathbf{F} = \frac{V\,M_s}{B}\,L\left(\frac{V\,M_s\,B}{k_bT}\right)B\,\nabla B. \tag{1.94}$$

For sufficiently weak fields, the Langevin function can be linearized which leads to the following approximation of the magnetic force:

$$\mathbf{F} \simeq \frac{(V\,M_s)^2}{3\,k_bT}\,B\,\nabla B. \tag{1.95}$$

In all three cases, the optimization of the magnetic force acting on a specific particle requires the maximization of the gradient of the magnetic flux density amplitude. Equations (1.92) and (1.95) show that there is also an interest in increasing the amplitude of the magnetic flux density when dealing with non-saturated particles. It is important to note that, in the magnet design, the field and field gradient are the only parameters that can be controlled, as the other terms present in equations (1.90), (1.92), and (1.95) are dictated by the size and physical characteristics of the particles. In this thesis, the nature of the particles on which the force is exerted is not specified. The focus is therefore the maximization of the field gradient generated, driven by the observation that the force is proportional to this gradient under all circumstances. In chapters 3 and 4, a threshold of 1 T m^{-1} is employed for visual performance comparisons among different assemblies.

2 Experimental techniques

The experimental study of this thesis is entirely conducted within the Electrical Measurement Laboratory at the University of Liege. The laboratory is equipped with resources tailored for magnetizing and characterizing the properties of superconducting materials. The present chapter essentially focuses on the presentation of the instruments and the experimental procedures used and/or developed in the framework of this thesis.

More precisely, the chapter is structured as follows. The first section provides a concise overview of three essential pieces of equipment present in the research laboratory and extensively used throughout this work. The second section details the design of a bespoke experimental setup that allows the experimental assembly and the measurement of a linear superconducting Halbach array. The discussion includes practical challenges associated with assembling such a superconducting system, the development of a translational mechanism, and its integration into an existing 3D x, y, z micropositioning system for the measurement of the magnetic flux density distribution. The third section outlines the versatile experimental capabilities provided by the *Physical Property Measurement System*, another equipment available in the laboratory. Following a brief introduction, the design of a bespoke experimental instrument compatible with this equipment is presented. The discussion related to this second setup includes the implementation of a rotational mechanism in a sealed experimental chamber as well as the development of a bespoke probe for measuring a gradient of magnetic flux density using stationary Hall sensors.

2.1 Available experimental equipment

2.1.1 Electromagnet

The laboratory houses an electromagnet with a B/I ratio of 32.5 mT/A and capable of producing magnetic fields of up to 1.5 T. A photograph of this electromagnet is shown in Figure 2.1 (a). As highlighted in this illustration, the airgap between the magnet poles is 30 mm. In the framework of this thesis, the electromagnet is used to generate the applied field sequence necessary for magnetizing $YBa_2Cu_3O_{7-x}$ superconducting samples. Considering that such samples have to remain fully immersed in liquid nitrogen during the whole magnetization procedure, the available space for the sample located in the airgap is constrained by the internal dimensions of the cryostat. A picture of the cryostat is shown in Figure 2.1 (b). It can be noticed that the cryostat can accommodate samples with dimensions parallel to the applied field smaller than 26.5 mm. The magnet is powered with a DC *BK Precision 9117* current supply [108] connected to a

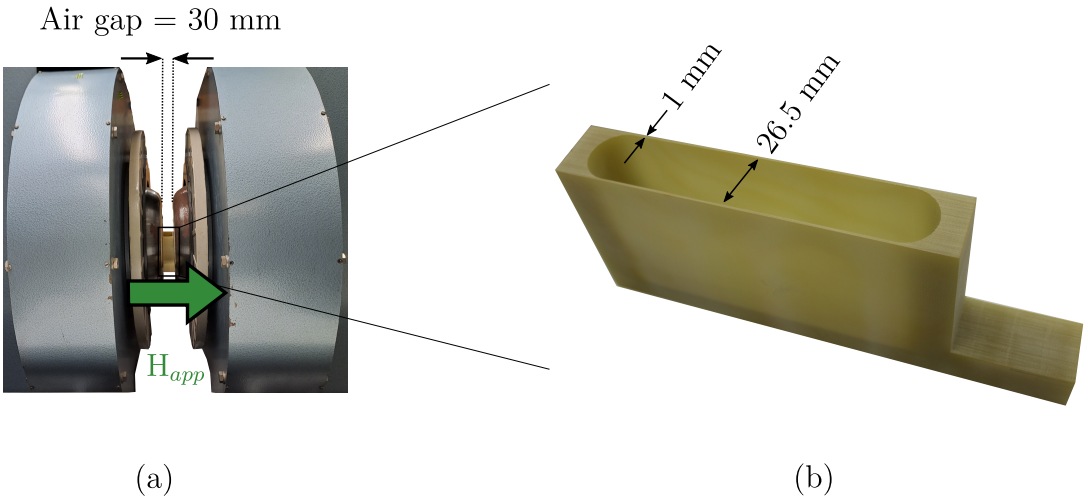

Figure 2.1: (a) Photograph of the electromagnet capable of generating up to 1.5 T within an air gap of 30 mm. (b) Photograph of the cryostat made of Permaglas® used for the magnetization procedure.

computer through a *GPIB* interface. This interface enables the control of the magnet current by using a software developed in *LabVIEW*.

2.1.2 3D Mapping system

As illustrated in Figure 2.2 (a), the laboratory is also equipped with a 3D $x\,y\,z$ micropositioning system from Thorlabs® [109]. This equipment facilitates the precise displacement along three mutually orthogonal directions over a range of 50 mm and with a minimum step size of 5 μm. Attaching a Hall probe to this displacement system allows the implementation of a Hall probe mapping technique, a widely used method to measure the distribution of the trapped flux density of superconducting bulks [103, 110–115] and staked tapes [116–118]. This technique can be used to estimate the critical current density based on the mapping measurements and a pre-supposed distribution of supercurrent loops within the sample. It should be emphasized that this measurement technique is primarily sensitive to the supercurrents flowing close to the measured surface.

Two different cryogenic Hall sensors are used with the 3D mapping system. The first sensor is shown in Figure 2.2 (b). It consists of a single-axis Hall sensor manufactured by Arepoc® (model HHP-MP [120]). This sensor exhibits a sensitivity of 0.2 mV/mT, the active area size is equal to 0.1×0.1 mm^2 and the distance between the active area and the sensor's upper surface is 0.150 mm. This probe is used to perform all the mapping measurements shown in chapter 3 and part of the mapping of chapter 4. The second probe consists of a bespoke 3-axis Hall sensor that can be operated in cryogenic conditions. The active surface is located at 2.2 ± 0.25 mm from the bottom of the probe. This tool was developed only recently within our research group [119] and is used to perform part of the measurements presented in chapter 4. The significant advantage of this customized probe over the Arepoc® sensor resides in its ability to acquire simultaneously the 3 components of $\mathbf{B}$. This characteristic is extremely useful in situations where lateral components cannot be easily deduced from the axial one, a situation that is encountered when investigating superconducting linear Halbach arrays.

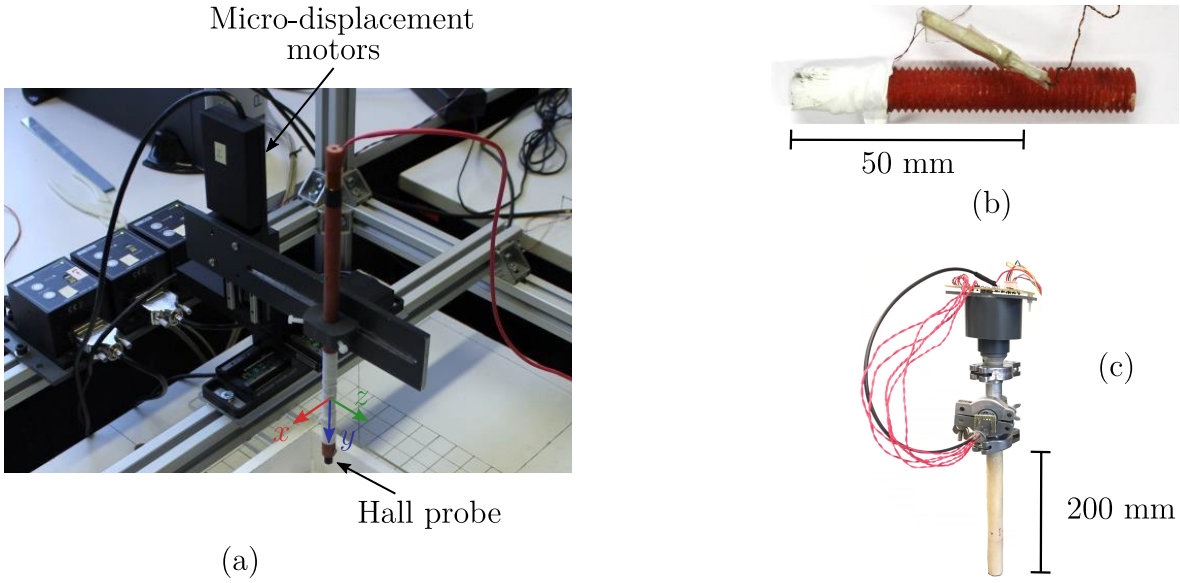

Figure 2.2: (a) Picture of the 3D Hall probe mapping system. (b) Single-axis cryogenic Hall sensor Arepoc® HHP-MP fixed at the end of a Permaglas screw. (c) Bespoke 3-axis cryogenic Hall sensor [119].

2.1.3 Extraction magnetometer

A flux extraction magnetometer previously developed in our research laboratory [121] is used to measure the dipole magnetic moment of large grain, bulk samples which cannot be accommodated in commercial magnetometers, such as the $YBa_2Cu_3O_{7-x}$ samples described in section 2.9. This magnetometer includes two pick-up coils that are wound in series opposition. The sample to be measured is placed in a liquid nitrogen cryostat located in the bore of the pick-up coils. The sample is stationary. These coils move vertically at a constant velocity of 0.5 m/s, covering a distance of 75 cm. The relative motion between the sample and the sensing coils leads to a change in magnetic flux within the coils, resulting in the generation of a voltage signal, that can be calculated using Faraday's law. This signal is measured and integrated to derive the dipole magnetic moment of the sample. It has been shown in [121] that the contributions of the quadrupole and octupole component of the flux generated by the measured sample to the acquired signal remain smaller than 0.1% provided that the diameter of the measured sample (assumed to here to have a circular cross-section) is smaller than 17 mm. A photograph of this magnetometer is shown in Figure 2.3.

One of the significant advantages of this measuring technique is that the measured signal is sensitive to the volume dipole magnetic moment of the sample. Unlike the Hall probe mapping, therefore, this measurement provides information related to the superconducting properties averaged over the whole sample volume.

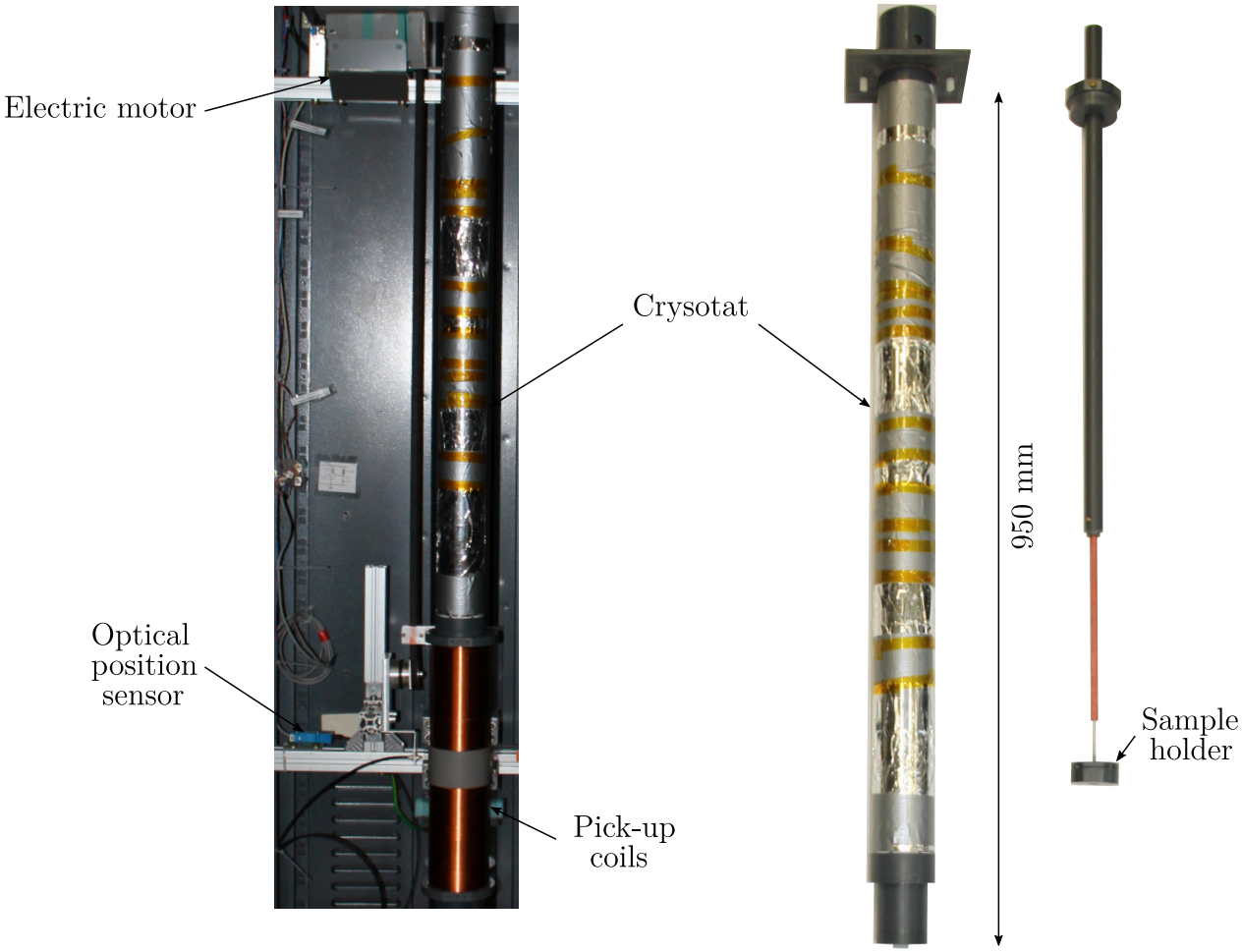

Figure 2.3: Photograph of the extraction magnetometer [121] together with the cryostat and the sample holder. The magnetometer is used for characterizing the dipole magnetic moment of superconducting samples.

2.2 Experimental setup for assembling and measuring linear Halbach arrays

In the context of this thesis, the performance of a linear Halbach array made of magnetized superconductors is investigated in chapters 3 and 4. Although the magnetization and characterization of individual superconductors can be carried out with the existing devices described in the previous section, there were no existing facilities dedicated to the controlled assembly and systematic measurement of multiple magnetized superconducting samples arranged in a Halbach configuration. The full development of such an experimental system is part of the work carried out in this thesis. The focus of this section is to describe the most crucial steps involved in the development of this bespoke experimental setup.

The section is structured as follows. The specifications and requirements for the experimental system are presented first. Then, the design of both the sample holding system and the translational mechanism is discussed. Next, the motorization and the integration of the experimental setup into the existing 3D mapping system are described. Finally, the samples used with this system and the experimental procedure are presented.

Specifications and constraints

The experimental rig has to fulfil the mechanical operations shown schematically in Figure 2.4. The direction of the axes employed throughout the design and the experimental investigations are also defined in Figure 2.4: the x-direction aligns with the axis of the array and the z-direction corresponds to the main magnetization direction of the central sample of the Halbach array.

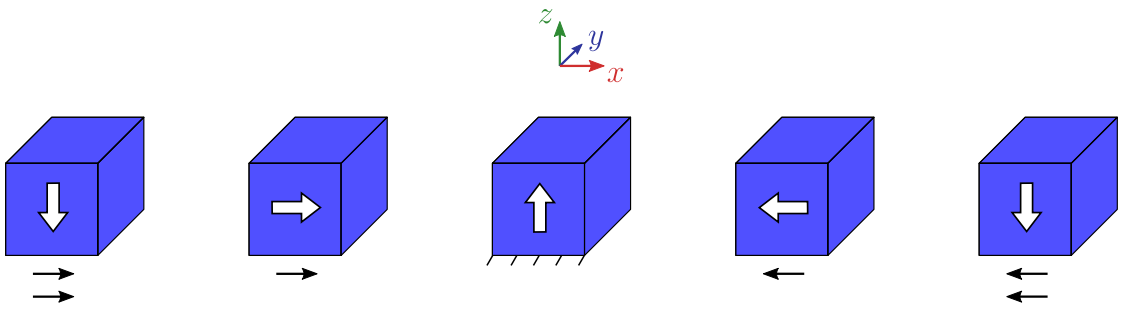

Figure 2.4: Schematic illustration of the assembly process of a Halbach array together with the definition of the axes used in this work. The white arrows represent the main magnetization direction of each sample, and the black arrows show the required displacement for assembling the array.

Since the motion of magnetized superconductors shown in Figure 2.4 may yield significant forces and torques, the setup should also ensure the secure clamping of up to five superconducting magnets. The central sample has to be held stationary while a mechanism should allow for the precise translational approach of peripheral samples from left and right until contact between the samples is achieved. Note that the most external samples have to move twice as fast as the intermediate samples to reach the contact between all samples simultaneously. The system is designed to accommodate primarily samples of parallelepiped shape, characterized by side lengths within the range of 12 - 16 mm. The operation of the device is constrained by further requirements listed below:

- **Mechanical constraints**: Due to the interplay between the magnetic flux density trapped in the superconductors, significant magnetic forces are expected to develop within the array. The system, therefore, has to generate a translational motion of trapped-field superconducting magnets over a range of ∼20 cm while handling safely the significant repulsive forces between the superconductors. These forces are evaluated numerically not to exceed 15 N for an array of cubic superconductors with a 14 mm side and characterized by a homogeneous and field-independent critical current density of 2×10^8 A m^{-2}. These repulsive forces develop mainly in a direction perpendicular to the axis of the array.

- **Magnetic constraints**: Since the experimental system is intended to be used to carry out magnetic measurements, a low magnetic susceptibility is required for the structure, so to avoid any magnetic interaction aside from that occurring between the superconducting samples. For this reason, the sample holders are machined in aluminium ($\chi \sim 10^{-5}$).

- **Cryogenic constraints**: The cryogenic temperature required for maintaining the superconducting state of the samples is achieved by fully immersing the samples in a liquid nitrogen bath. For user safety and to mitigate the problems related to thermal expansion of the precise translation and positioning mechanism, most of the components, including the motor, mechanical guides, and position sensors, are kept above the cryogenic bath, close to room temperature. As a result, some mechanical parts are partially immersed in the cryostat, these parts are machined in Permaglas M730. The selection of this material is motivated by two primary factors. First, it exhibits a low thermal conductivity, i.e. within the range of 0.3 to 0.5 W/m K at temperatures ranging from 50 to 77 K [122]. This ensures an effective thermal insulation between the inside of the cryostat and the translation mechanism. Second, this material exhibits a relatively small thermal expansion coefficient, i.e. $\sim 4.4 \times 10^{-5}$ between 300 K and 77 K [122].

Sample holding system

The assembly procedure for a superconducting Halbach array includes two steps described in more detail later. The first step involves the individual magnetization of the samples in appropriate directions. During this phase, it is essential that the samples can be conveniently and safely handled within a liquid nitrogen cryostat. For this purpose, the sample holder shown in Figure 2.5 (a) is employed. Certain dimensions are deliberately omitted in Figure 2.5 (a) for the sake of clarity. The comprehensive mechanical drawings of all mechanical parts designed for this setup are shown in Appendix C.1. The sample holder consists of a rectangular block with a recess where the sample can be secured thanks to a set screw. A rod made of Permaglas is tightened in the sample holder, ensuring safe manipulation even when the samples are immersed in liquid nitrogen. The dimensions of this holder allow its insertion into the air gap of the electromagnet presented in section 2.1 for magnetizing the sample either in the x or in the z-direction. The same sample holder design can therefore be used for all samples involved in the Halbach array. The second step consists in controlling the approach of the samples. For this step, the sample holders are inserted and attached within sample mounting frames made of Permaglas shown in Figure 2.5 (b). These frames are mounted on distinct carriages. Their translational displacement is measured and controlled as described in the following section.
Examining Figure 2.5 (b), it should be noted that the x dimension of the sample has to be at least equal to the width of both the sample holder and the sample mounting frame (12 mm) to reach contact between samples.

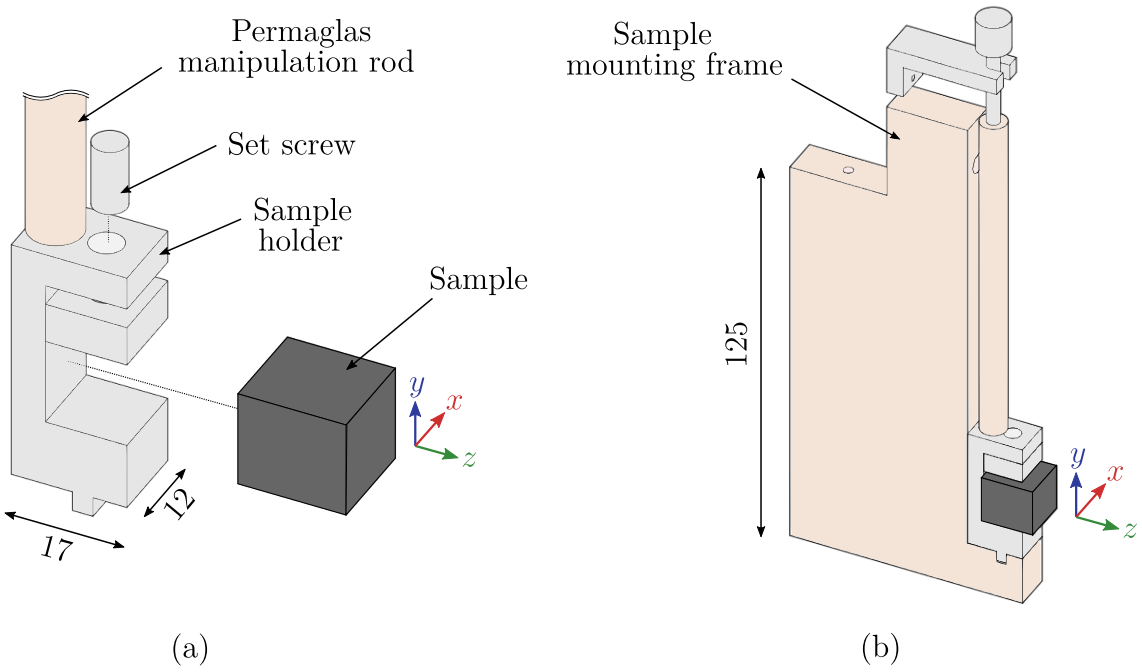

Figure 2.5: Design of the sample holding system. (a) Sample holder as used for the magnetization phase. (b) Sample holder secured in a mounting frame for the approach phase. All dimensions are in mm.

Displacement mechanism

The displacement mechanism is based on a screw and nut system which facilitates the conversion of a rotational motion into a linear one. In the present case, the translation of the screw along its axis is blocked, and the rotational degree of freedom of the nut is also locked. The rotation of the screw is set and controlled by a motor generating the linear displacement of the nut along the lead screw. This working principle is shown in Figure 2.6 (b). Two distinct nuts are employed on each lead screw, causing the simultaneous translation of both nuts at an equal speed when the screw is rotated. As shown in Figure 2.6 (c), the lead screws exhibit one additional feature: one half of the thread is right-handed, while the other half is left-handed. Consequently, when one nut is engaged on each half, the rotation of the screw results in the linear motion of the two nuts in opposite directions.

The practical implementation of this mechanism is schematically illustrated in Figure 2.6 (a). The system includes five distinct carriages: a central one remains stationary and four others are allowed to slide along two guiding rods. A nut is threaded into the movable carriages which enables their displacements through the rotation of two distinct lead screws. The nuts of the intermediate carriages engage with the first screw, while those of the outer carriages engage with the second one.

The nuts and the screws selected for the setup are characterized by a trapezoidal thread Tr10 $\times$ 2 [123,124]. This choice determines the resolution of the rotation to translation mechanism: 2 mm/turn. Although not represented in Figure 2.6 (a) for clarity, 4 linear resistive position sensors are integrated into the motion system for measuring precisely the position of each

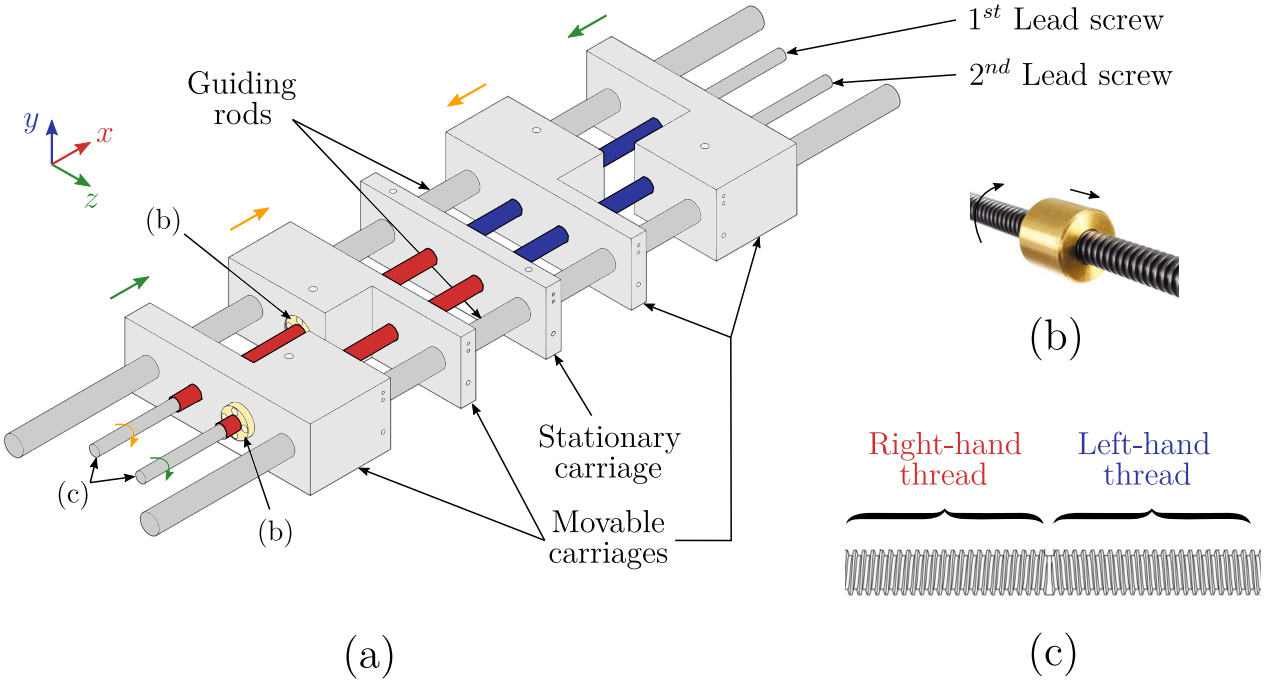

Figure 2.6: (a) Schematic illustration of the displacement mechanism. (b) Screw and nut working principle. (c) Schematic representation of a dual-handed lead screw.

movable carriage [125].

Motorization

According to the design illustrated in Figure 2.6 (a), the motion of the carriage can be initiated by activating two lead screws. The next step in the design therefore involves motorizing these lead screws. For this purpose, the design of a gearbox facilitating the transmission of the torque from a single motor to both screws is presented in Figure 2.7.

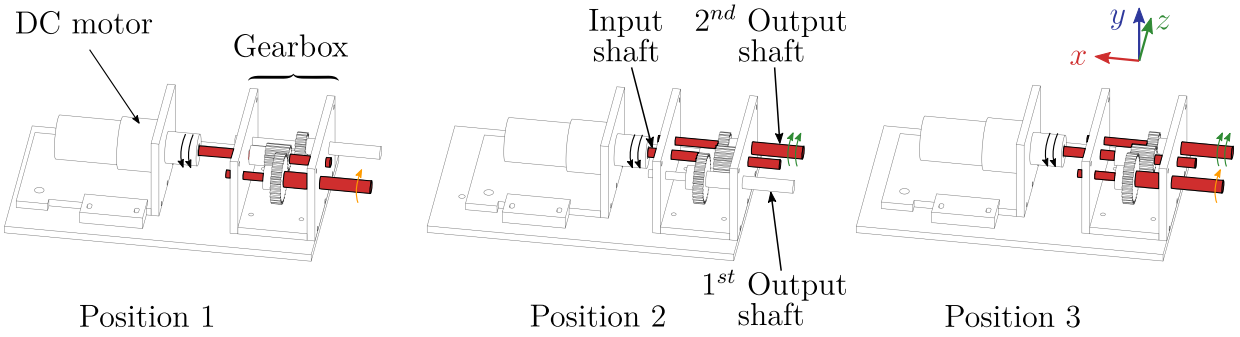

Figure 2.7: Schematic illustration of the gearbox transmitting the torque of a DC motor to the lead screws of the mechanism presented in Figure 2.6 (a). The gearbox reduction ratio is 1:0.5 and 1:1 for the first and second output shafts respectively. The activated shafts are colored in dark red.

The gearbox is equipped with a single motorized input shaft and two output shafts. As represented in Figure 2.7, the input shaft can be set in three predetermined positions. In position 1, the motorized gear engages only with the gear of the 1^{st} output shaft. In position 2, it activates only the 2^{nd} output shaft. In position 3, the motorized gear engages

with the gears of both output shafts simultaneously. Importantly, the gear attached to the 1^{st} output shaft has twice as many teeth as the motorized gear, while the gear on the 2^{nd} output shaft has the same number of teeth as the motorized gear. When integrated into the displacement mechanism shown in Figure 2.6 (a), the gearbox thus enables the activation of the 1^{st}, the 2^{nd}, or both lead screws with the same motor. The practical consequence is that when both screws are activated, the 2^{nd} one rotates twice as fast as the 1^{st} one. To mitigate the risk of damage caused by minor misalignments within the device, all couplings, including those between the motor and gearbox, as well as that between the gearbox and the lead screws, are flexible. Two manual brakes are also installed on the lead screws for stationary measurements.

The motor used is a 12 V DC motor commercialized by *Conrad* [126] specified to produce a nominal torque of 0.637 Nm. It is powered and controlled with a bespoke printed circuit board designed by P. Harmeling (Department of Electrical Engineering, Uliege). This board, which also acquires the signals from position sensors, is connected to a computer using a CAN interface. The interface allows the transmission of commands to the motor through a *LabVIEW* program.

Integration to the mapping system

The experimental system developed in the preceding section enables the fixation and controlled assembly of up to five magnetized samples arranged in a Halbach configuration. In order to assess the performance of the assembled configuration with magnetic field sensors, a support frame is designed to install the experimental system directly on the Hall probe mapping system presented in section 2.1. In doing so, the magnetic flux density distribution generated by the assembled Halbach array can be measured. A picture of the complete experimental system integrated into the mapping system is shown in Figure 2.8.

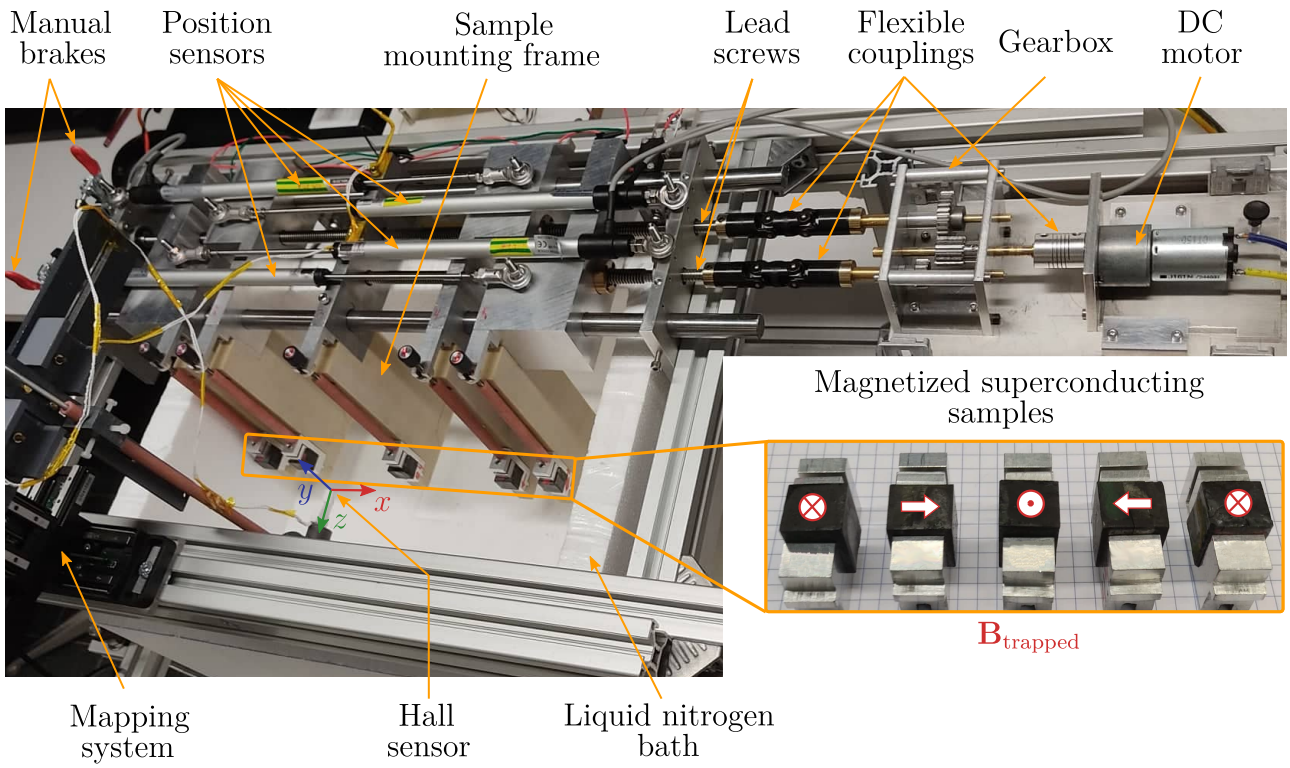

Figure 2.8: Photograph of the setup used to assemble and measure linear Halbach arrays.

Samples used

In chapters 3 and 4 of this thesis, multiple Halbach arrays, composed of diverse samples are experimentally assembled and measured using the system presented in this section. These samples have various shapes, sizes and magnetic properties, illustrating the versatility of the experimental setup. Figure 2.9 shows the set of samples that are involved in a Halbach array along this thesis. A description of these samples, as well as their corresponding points of investigation within the thesis, are provided below.

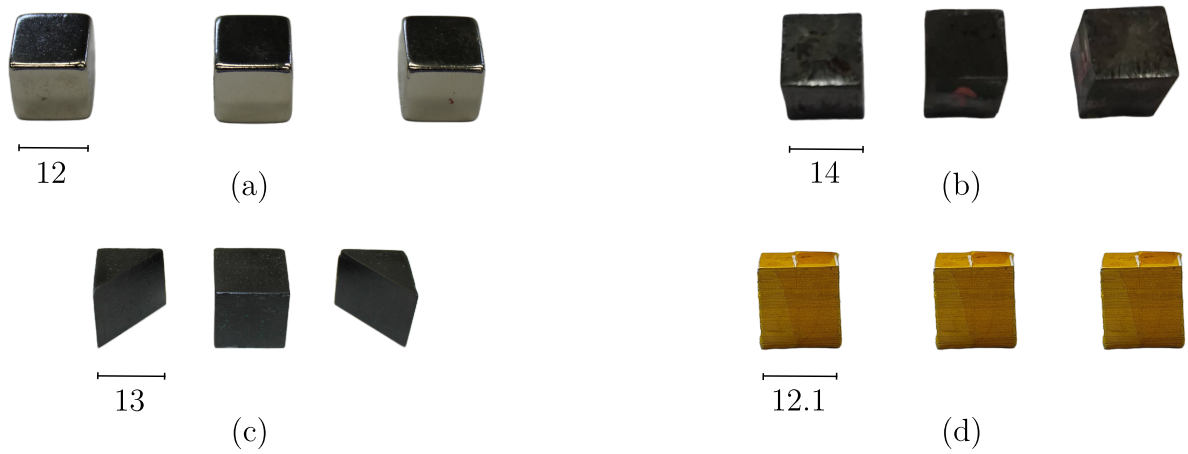

Figure 2.9: Picture of the various samples assembled in a Halbach array. (a) Nd-Fe-B permanent magnets. (b) $YBa_2Cu_3O_{7-x}$ samples from Cambridge University. (c) $YBa_2Cu_3O_{7-x}$ samples from *ATZ* company. (d) $YBa_2Cu_3O_{7-x}$ stacked tapes. All dimensions are in mm.

(a) **Nd-Fe-B permanent magnets**: Cubic permanent magnets of 12 mm side commercialized by *Supermagnete* [127]. They are used in chapter 3 and their assembly serves as a benchmark case for the assessment of the typical performance achievable when using permanent magnets of this size within a Halbach array.

(b) **$YBa_2Cu_3O_{7-x}$ samples from Cambridge university**: Bulk superconducting samples manufactured by the *Bulk Superconductivity Group* at Cambridge University by the top-seeded melt growth (TSMG) method [110, 128–130]. These samples exhibit a cuboidal shape with a side between 14 mm and 16 mm, they are used in chapter 3.

(c) **$YBa_2Cu_3O_{7-x}$ samples from *ATZ* company**: Cubic bulk superconducting samples with a side of 13 mm commercialized by *ATZ*. Two of these samples are cut along the diagonal of the cube to obtain samples in the shape of a triangular prism. The machining was also performed by *ATZ*. These samples are used in chapter 4 to investigate the impact of the geometrical shape of the peripheral samples in a Halbach array.

(d) **$YBa_2Cu_3O_{7-x}$ stacked tapes**: These samples are made of 120 second generation (2G) $YBa_2Cu_3O_{7-x}$ tapes from *Superpower* stacked on top of each other. Each tape within the stack originated from a single high-temperature superconducting tape of 12 mm in width. The insulation between the superconducting layers is ensured by the different buffer layers and the substrate within the tape, no additional insulation is added between individual tapes. The samples obtained are 12.6 mm in height and have a square section parallel to

the tape with a side of 12.1 mm. These samples are used in chapter 4 to investigate the impact of the anisotropy of the samples involved in a superconducting Halbach array.

Before combining them in a Halbach array, preliminary characterization measurements are carried out to assess the superconducting properties of each sample. More details related to these initial experiments and the corresponding superconducting properties can be found in chapters 3 and 4.

Experimental procedure

The equipment developed in this section can now be used to investigate the performance of a linear superconducting Halbach array made of up to five samples. Nevertheless, for reasons that will become more apparent after the conclusion of Chapter 3, the investigations conducted in the framework of this thesis are limited to configurations involving only three samples. Irrespective of the possible differences in geometric dimensions, shapes or superconducting properties from sample to sample, a standardized procedure is always employed to obtain the final configuration of the Halbach array. This procedure is shown schematically in Figure 2.10 and is presented in more detail below.

1. The samples are magnetized individually, one after the other at 77 K in field-cooling conditions in the air gap of the electromagnet described in section 2.1. The magnetization procedure starts from an applied field of 1.2 T and the field is removed at a constant rate of 1 mT s^{-1}. At the end of the magnetization of the third sample, a period of 45 min is allowed for magnetic relaxation.

2. While keeping them immersed in liquid nitrogen, the samples are transferred and secured in the experimental rig shown in Figure 2.8. At this point, the distance separating each sample ($\sim$80 mm) is sufficient to assume no interaction between them [101]. The array is then assembled by approaching the external samples towards the central one at a speed of 0.6 mm s^{-1} until the three samples are in contact. A second period of 45 min is allowed to allow further magnetic relaxation to occur.

3. A mapping of the magnetic flux density generated by the final configuration is performed in a plane parallel to the surface of the configuration (x-y plane).

A *LabVIEW* program has been developed to implement the following functions: (i) the acquisition of the signals from the sensors measuring the position of the carriages; (ii) the transmission of control commands to the DC motor; (iii) the acquisition of the signal of the Hall probe attached to the mapping system; (iv) the transmission of control commands to the 3D mapping system. This software application runs the experimental protocol shown in Figure 2.10 through a unified *LabVIEW* user interface.

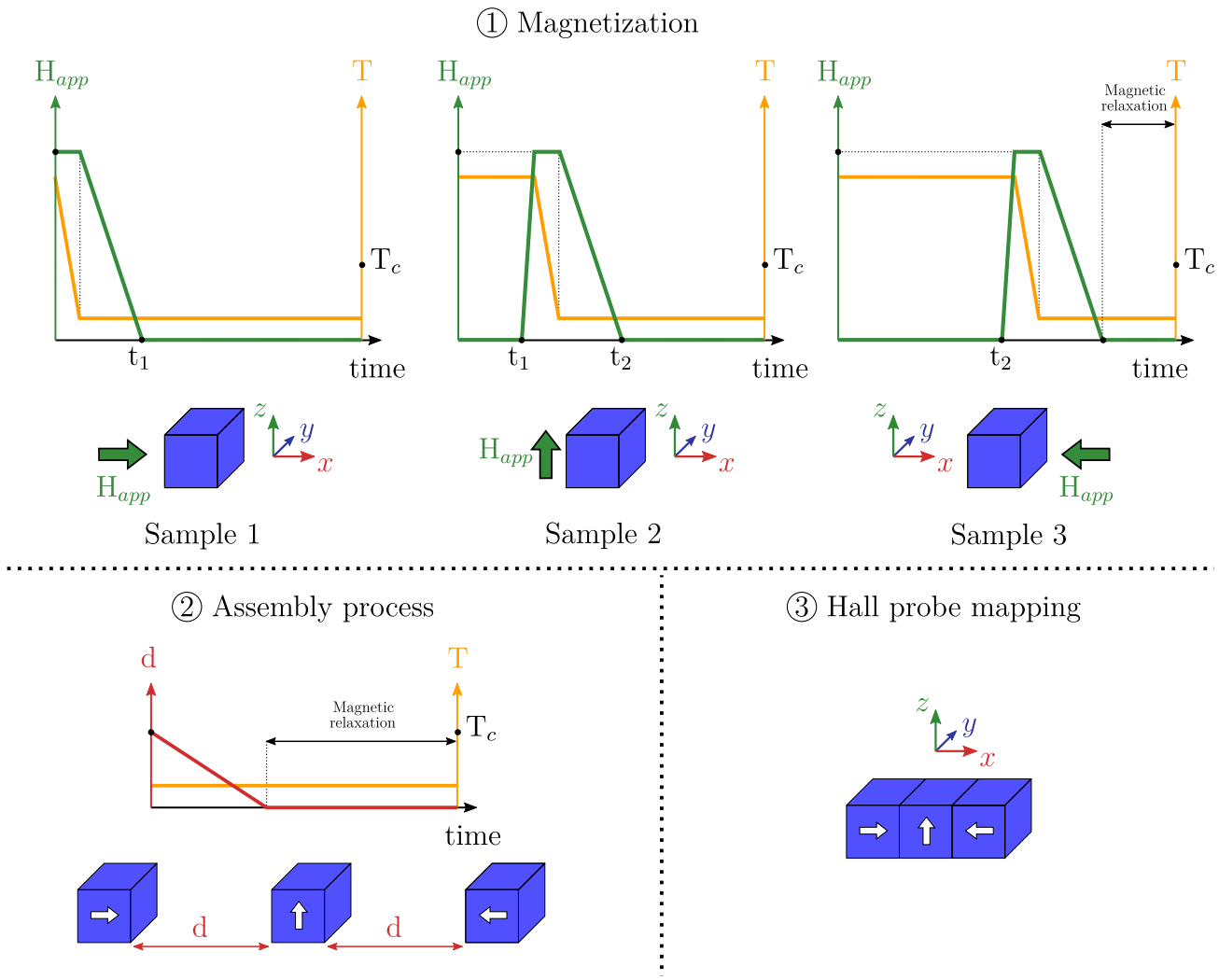

Figure 2.10: Schematic illustration of the systematic experimental process used to assemble and measure a linear Halbach array.

2.3 The Physical Property Measurement System

The *Physical Property Measurement System* (PPMS) is an experimental instrument commercialized by *Quantum Design* [131]. This experimental equipment can be used to measure several physical characteristics through a variety of insertion instruments which are also commercialized by *Quantum Design*. Furthermore, the versatility of the system offers the possibility to design bespoke insertion tools aimed at exploring configurations such as the dielectric properties of insulators [132] or the magnetic properties of bulk superconductors [112, 133–136].

More particularly, the PPMS includes a liquid helium cryostat enclosed in a liquid nitrogen cryostat, integrated into a thermal regulation system. This configuration allows for precise temperature control within a vacuum-sealed experimental chamber, spanning a temperature range from 1.9 K to 400 K. This experimental chamber consists of a cylindrical enclosure of 26 mm in diameter and 895 mm in height. Within this enclosure, samples can be inserted and subsequently cooled by a flow of helium gas. It should be noted however that the thermal uniformity is only guaranteed by the manufacturer in a region of 100 mm in height starting from the bottom of the experimental chamber. The experimental chamber is surrounded by a superconducting magnet cooled by liquid helium. This magnet can generate an axial magnetic field ranging from -9 T to 9 T. The thermal regulation system, the power supply of the superconducting magnet and various sensors are all connected to a control unit. This control unit is used to run various experimental procedures, including temperature and magnetic field sequences. For conventional experiments, a dedicated software called *MultiVu* can be employed. Alternatively, the PPMS also offers the possibility to be controlled via *GPIB* commands for more customized experimental setups.

A photograph of the PPMS cryostat together with the control unit is shown in Figure 2.11 and a schematic view of the experimental chamber is shown in Figure 2.12.

Figure 2.11: Overview of the PPMS cryostat and its control unit [137].

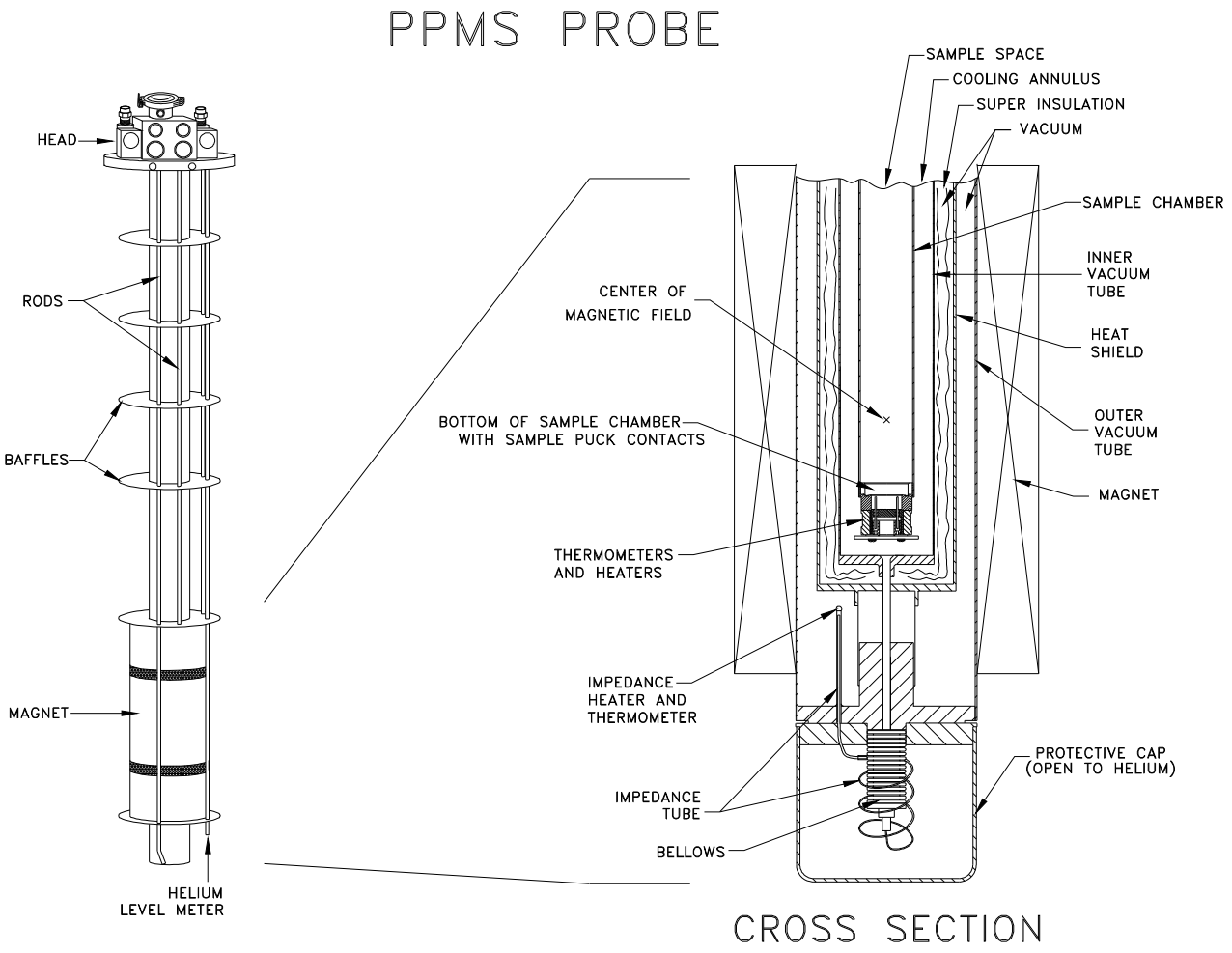

Figure 2.12: Major component of the PPMS probe [138].

2.3.1 Measurements with the AC measurement system

The AC measurement system (ACMS) is a module commercialized by *Quantum Design* that can be used both as a DC magnetometer or as an AC susceptometer [139]. The ACMS insert includes essential components such as coils, a thermometer, and electrical connections for conducting measurements of both types. The insert fits directly in the PPMS experimental chamber and is run by a dedicated software which facilitates the creation of customized field and temperature sequences. A sample can be attached to a rigid sample rod. The ACMS module includes a DC servo motor allowing the axial motion of this sample rod through the sensing (or detection) coils. The ACMS insert and coil set are shown in Figure 2.13.

The ACMS is used in the context of chapter 5 to carry out DC magnetization measurements. These measurements are used to extract the magnetization loop of a superconducting sample. The method is a flux extraction technique and includes the following experimental procedure. The sample is cooled initially to the temperature of interest in zero field. Then, the applied magnetic field is swept from zero to the maximum magnetic field strength B_{max}, followed by further sweeps from B_{max} to -B_{max}, and from -B_{max} to B_{max}, with discrete increments of 40 mT. At each step, the sample is translated through the detection coil set of the ACMS

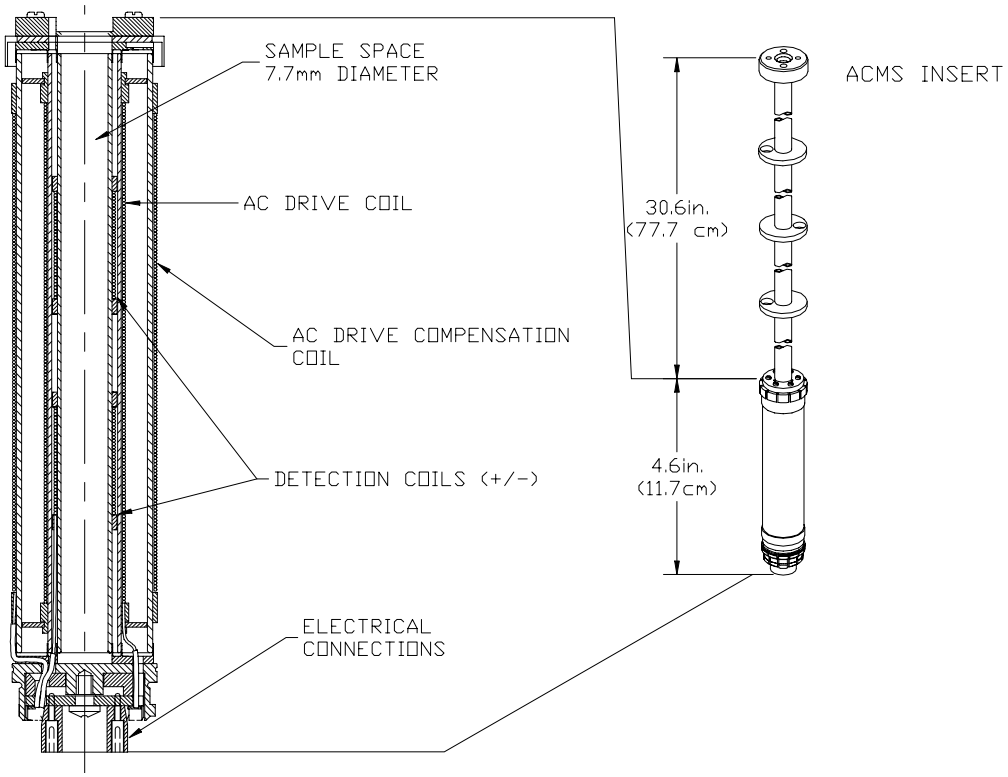

Figure 2.13: ACMS insert and coil set [139].

in approximately 0.05 seconds. The translation of the sample induces, across the detection coils, a voltage that is proportional to the rate of change of magnetic flux through them. The ACMS software performs a numerical integration of the voltage profile, followed by a fitting of the results with the known waveform for a dipole moving through the detection coils. This analysis enables the determination of the dipole magnetic moment of the sample at each applied magnetic field.

2.3.2 Development of a bespoke insertion tool

Chapter 5 of this thesis is devoted to the investigation of the magnetic behaviour of bulk superconductors rotated in a background field at different temperatures. The versatility of the PPMS makes it an ideal tool for investigating this. However, among the commercially available insertion instruments, none of them allows the rotation of large magnetized samples and the measurement of the magnetic field gradient in their vicinity. The design and development of a customized insertion tool were therefore carried out in the framework of this thesis.

This section is organized as follows. The specifications and requirements for the experimental system are outlined. Then, the design of both the sample holder and the rotational mechanism is described. This is followed by a detailed description of how mechanical motion is transferred into the vacuum-sealed experimental chamber. Finally, the motorization of the system is discussed.

Specifications and constraints

The design of the bespoke insertion tool requires the insertion and the clamping of two superconducting samples inside the experimental chamber of the PPMS. The samples are anticipated to have a cubic geometry with approximately 6 mm side. Within this setup, one of the samples has

to be clamped and held stationary, while the second sample should be rotated in a background magnetic field. The operation of the device is constrained by further requirements that are listed below:

- **Spatial constraints**: The instrument is intended to be inserted in the PPMS experimental chamber characterized by an internal diameter of approximately 26 mm and a height of 895 mm. Apart from the drive shaft and the motor, the whole system has to be located within the 100 mm at the base of the experimental chamber, i.e. in the zone where the temperature uniformity is guaranteed.
- **Environmental constraints**: The apparatus will be employed for magnetic measurements, requiring the selection of a material with minimal magnetic susceptibility to mitigate interference with the useful signals. Additionally, a high thermal conductivity is also desired to ensure uniform temperature distribution within the system once thermal equilibrium is reached. Taking into account these criteria, aluminium emerges as a promising candidate. Unless otherwise specified, all mechanical components in the section are fabricated from aluminium.
- **Mechanical constraints**: The mechanism has to be designed to enable an angular rotation of at least 180° for one of the sample holders with an axis of rotation perpendicular to the applied field. Taking into account potential alignment issues once the superconductors are placed in their sample holder, a further 10° angle is added to this minimal rotation requirement. Moreover, this rotating motion is intended to be applied to a magnetized superconductor in the presence of a background field. This process generates a magnetic torque that the motion mechanism has to overcome. The maximum torque achievable by the mechanism, while avoiding the risk of damage, is an important parameter that delimits the operational range and should be maximized during the design phase.

Sample holding system and rotational mechanism

The support structure is the mechanical part that serves as the anchor point for securing both the sample holders and the rotational axis. The dimensions of this structure define the physical space available for the mechanism and the holders, they are derived from a bespoke PPMS insertion tool previously developed within our laboratory [140] and are shown in Figure 2.14.

The structure, illustrated in Figure 2.14, consists of a cylindrical insert with dimensions of 26 mm in diameter and 100 mm in height. The available space within this structure for accommodating both the mechanism and the sample holders forms a rectangular window, measuring 66 mm in height and 20 mm in width. The central hole at the top of the structure is used to accommodate the driving shaft for motion transmission. Figure 2.14 also shows additional holes and grooves which serve either as fixation points or for cable management. Their precise dimensions and positioning are intentionally omitted in Figure 2.14 to ensure clarity. Comprehensive mechanical drawings for all designed components are available in Appendix C.2. Figure 2.14 also introduces the direction of axes employed throughout the design and the experimental investigations: the z-direction aligns with the direction of the applied field and the y-direction corresponds to the axis of rotation of the rotative sample holder.

The available space and support structure now being defined, the design of the mechanism is described. The main function of this mechanism involves the transmission of mechanical work

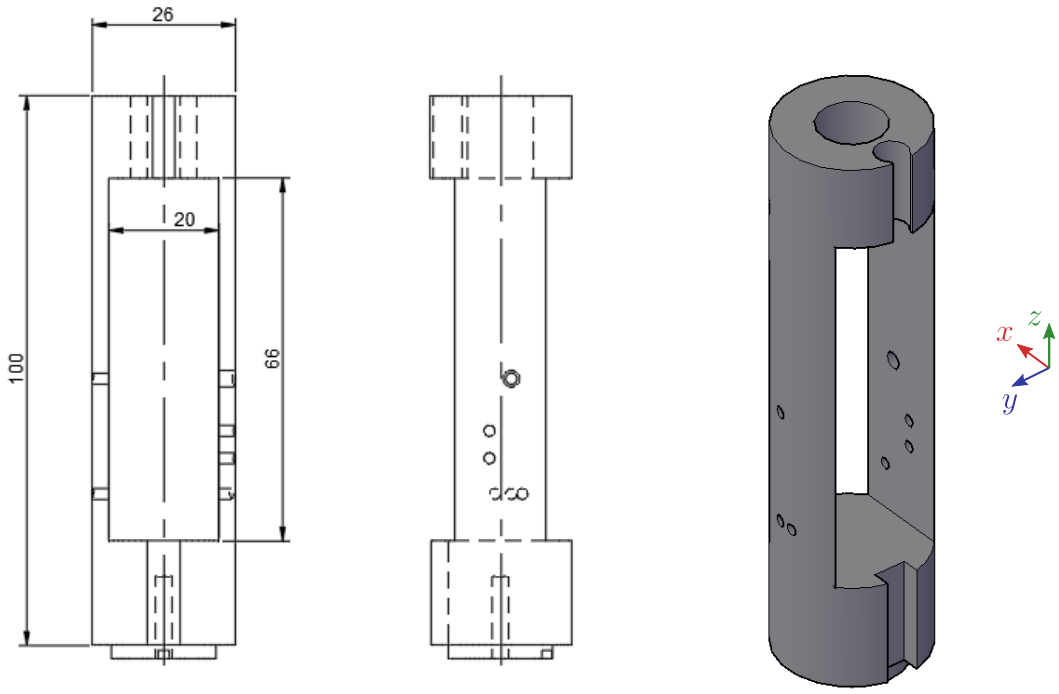

Figure 2.14: Schematic illustration of the support structure. All dimensions are in mm.

from a driving shaft centred within the experimental chamber, aligned with the z-direction, and its conversion into a rotational motion around the y-axis. The choice between a rotational or translational motion of the driving shaft opens up several potential options for generating the desired rotation. Each of these options presents advantages and drawbacks, considering factors such as complexity, size, and the torque that can be effectively transmitted. In the discussion below, two solutions that were initially considered are discussed succinctly and the reason why they were disregarded is exposed. The solution selected in this thesis is then presented in detail.

The first option is based on a rotating driving shaft, and a perpendicular gear mechanism to transfer mechanical torque from the z-axis to the y-axis. The operation of this mechanism is reasonably straightforward and is illustrated schematically in Figure 2.15 (a). In this configuration, two bevel gears would be installed on orthogonal axes, and when one of them rotates the other moves. Consequently, this system enables the transfer of rotational torque from one axis to another, which is perpendicular to it. One commercially available insertion tool for the PPMS, the horizontal rotator [141], is based on this working principle. However, an issue inherent to this mechanism is that any resistive torque exerted on the sample holder during its rotation is fully transmitted to the driving shaft. Given that the length of the driving shaft has to be approximately equivalent to the height of the experimental chamber, any torsional torque applied at one extremity of the shaft can lead to significant angular deformations along the shaft, rendering it unsuitable for the present application.

The second option for transmitting a rotational motion to the sample holder consists in employing a driving shaft operating in translation combined with a crank-slider mechanism converting this linear motion into a rotary motion. The working principle of this mechanism relies on three parts that are illustrated schematically in Figure 2.15 (b). The slider is a component

that moves in translation, its motion would be forced by the driving shaft in the present case. The connecting rod is a rigid bar that is attached to the crank at one end and to the slider at the other. As the slider undergoes linear displacement, the connecting rod transmits this motion to the crank. The crank is a rotating lever with an offset from the axis of rotation. The eccentricity causes the linear motion to be converted into rotational motion. This mechanism was previously employed within our laboratory [140] for the development of a bespoke PPMS insertion instrument capable of executing a 100° sample rotation while effectively counteracting a resistive torque of up to 0.48 N m. However, this mechanism cannot be used to rotate the sample beyond 180°. As a consequence, it is not suited to the experiments to be carried out.

The third possibility envisaged in this thesis consists in combining a driving shaft operating in translation with a rack and pinion system to convert the motion into a rotational one. The working principle is illustrated in Figure 2.15 (c). The system uses two primary components: a rack, which is essentially a linear toothed bar, and a pinion which is a gear equipped with teeth that mesh with the rack and whose rotation is given by the linear displacement of the rack. One of the main advantages of this mechanism is its flexibility in adjusting the maximum angle of rotation during the design phase. This can be achieved by modifying various parameters such as the radius of the gear, its module[1], or the stroke of the rack. Among the considered mechanisms, the rack and pinion system proves to be the most suitable for the experimental requirements, and it is decided to proceed with this working principle.

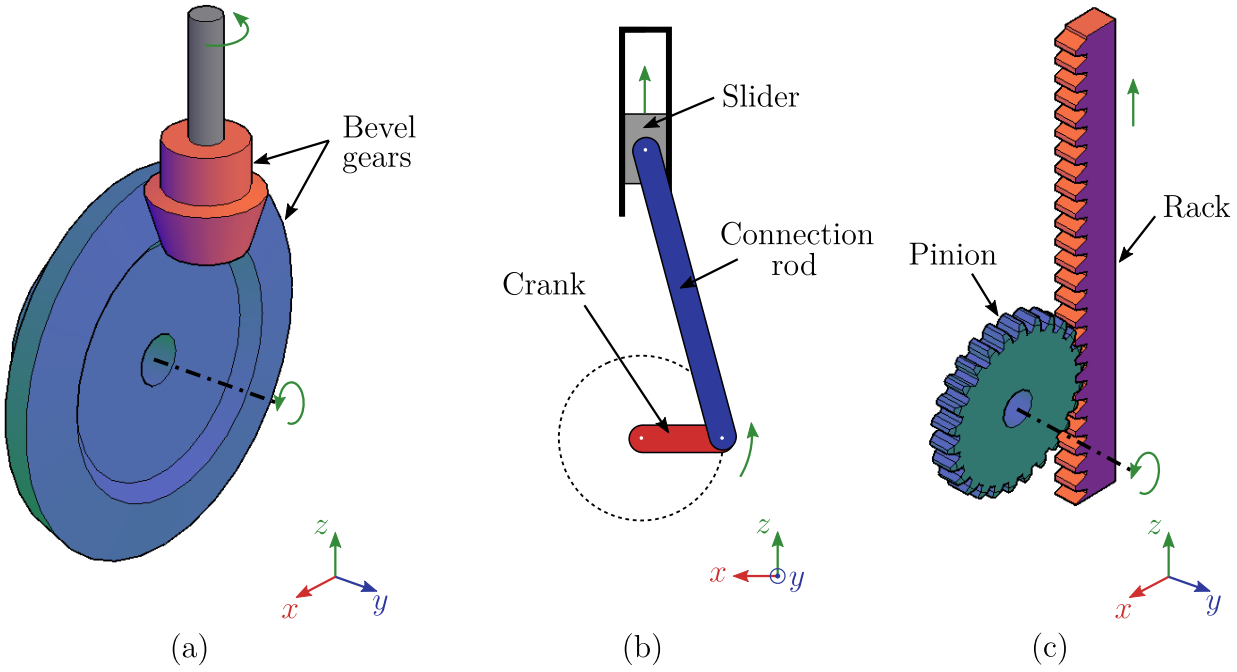

Figure 2.15: Schematic representation of the working principle of three rotational mechanisms. (a) Perpendicular gear mechanism. (b) Crank-slider mechanism. (c) Rack and pinion mechanism.

Based on the operating principle shown in Figure 2.15 (c), the careful selection of an appropriate rack/pinion pair is required. This selection process includes an iterative approach that aims at

[1]The module of a gear is defined as the ratio of the pitch diameter to the number of teeth in the gear.

maximizing the torque that can be achieved without damage, while simultaneously satisfying the constraints imposed by kinematic and spatial requirements. The final decision converged to a rack/pinion pair composed of brass with a module of 0.5 [142, 143]. The key dimensional parameters of this assembly are shown in Figures 2.16 (a) and (b).

As can be seen in Figure 2.16 two additional mechanical parts complete the mechanism:

- A piston is designed to make a structural connection between the rack and the drive shaft. The width (in the y-direction) of this component is 20 mm in order to ensure suitable guidance during its upward and downward motion within the support structure. A groove is also incorporated in this part for cable management.

- A rack guide, firmly attached to the supporting structure near the junction of the rack and the pinion, serves as an essential mechanical component for the sustained interlocking and engagement of the rack and pinion assembly during operation.

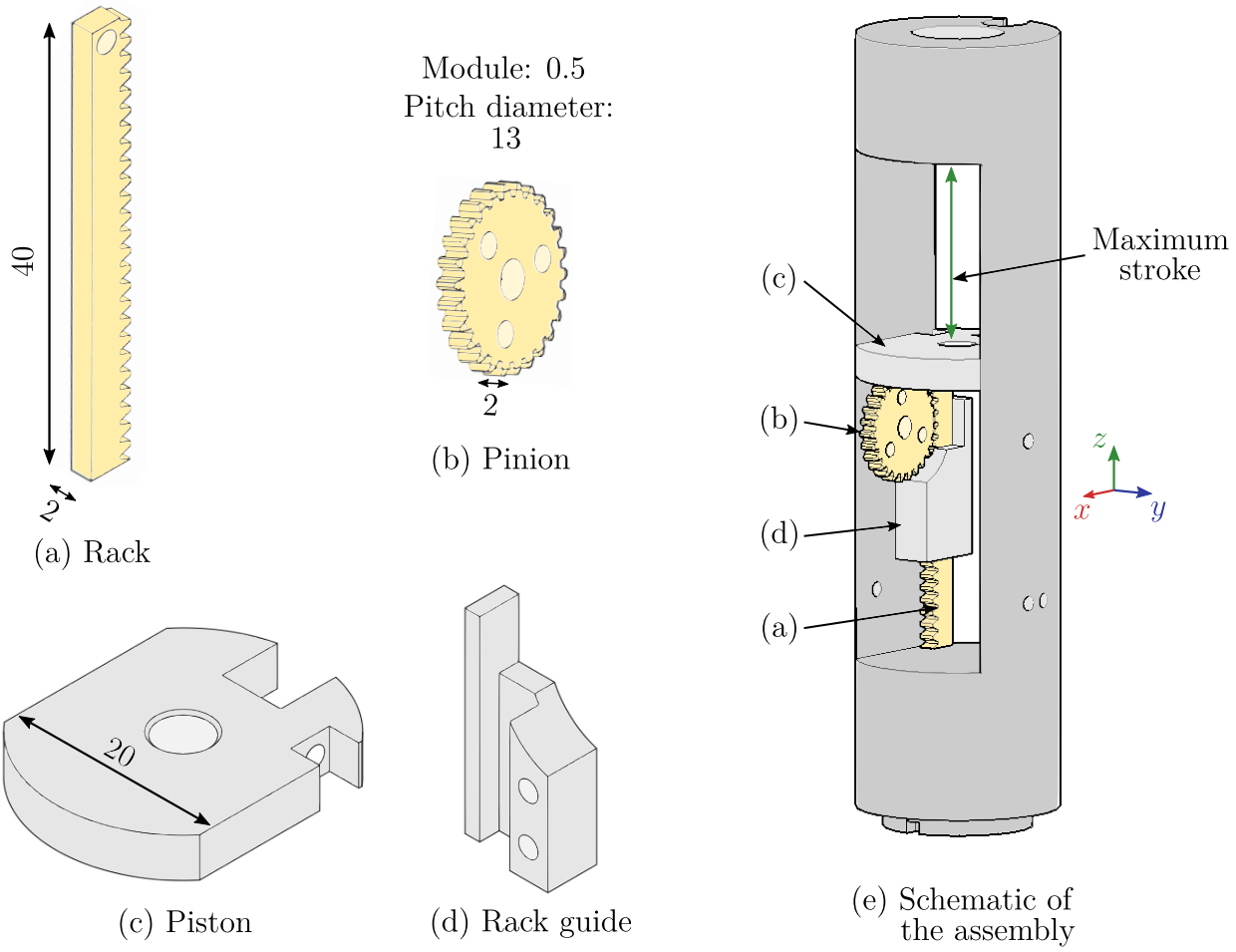

Figure 2.16: (a), (b), (c) and (d) Main mechanical parts of the rack and pinion mechanism together with their key dimensions. (e) Conceptual view of the mechanism assembled within the support structure with the rack positioned at its lowest point. All dimensions are in mm.

Based on the pitch diameter of the pinion, the resolution of the mechanism can be evaluated as follows: $\frac{13\pi}{360} \sim 0.12$ mm/°. In the final design, the maximum stroke of the rack, as highlighted in Figure 2.16 (b), is equal to 25 mm. Therefore, the mechanism allows for a rotation of maximum 208° which aligns perfectly with the specified requirements. Besides, the manufacturer certifies that the rack-pinion combination can withstand a maximum torque of 0.022 N m without deformation.

The placement and clamping of the superconducting samples in this insertion tool are now discussed. The design of the rotating sample holder is shown schematically in Figure 2.17 (a).

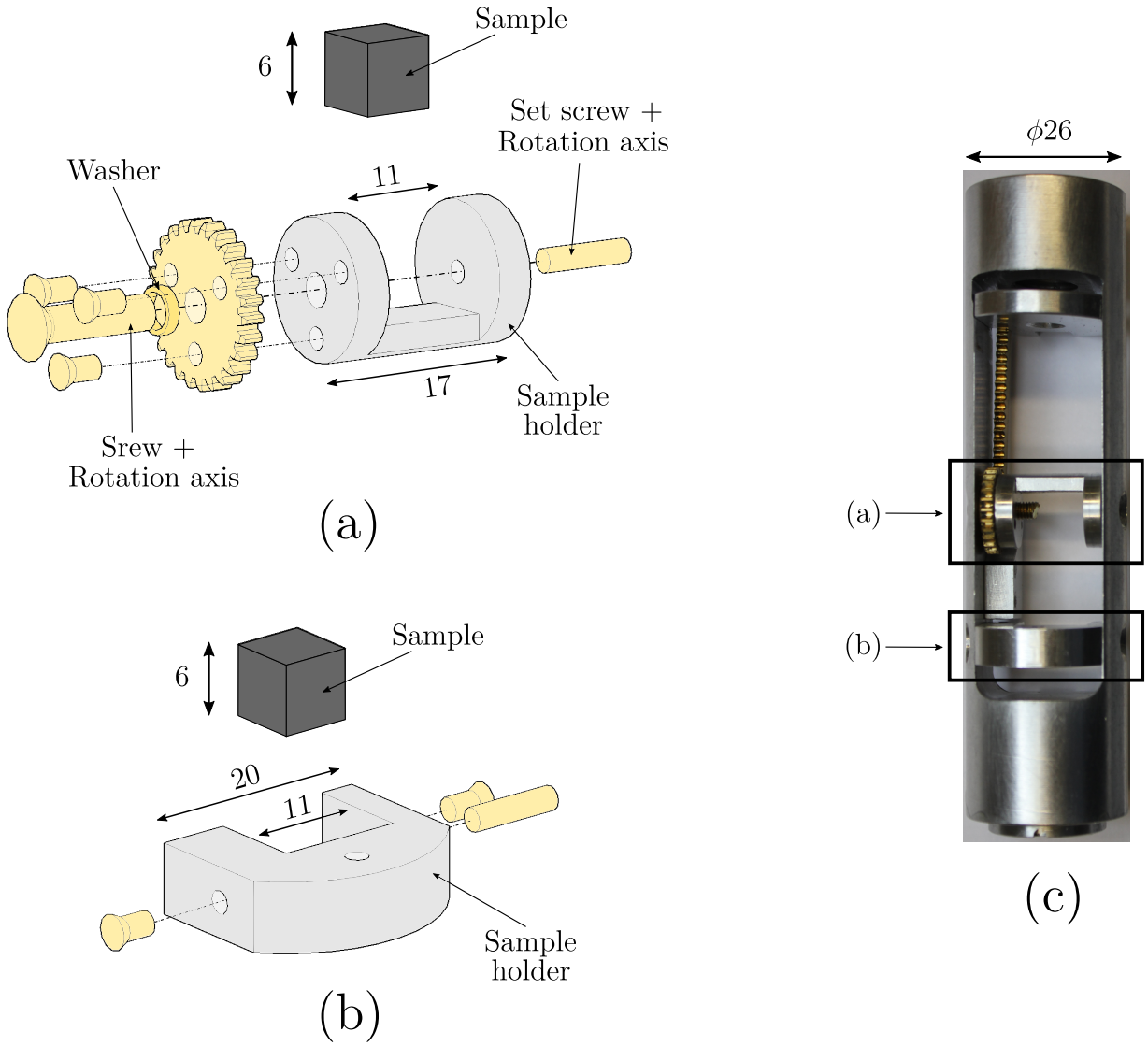

Figure 2.17: (a) Conceptual design of the rotative sample holder. (b) Conceptual design of the stationary sample holder. (c) Picture of the experimental system with the sample holders and the rack and pinion mechanism installed. All dimensions are in mm.

Considering the initial distance along the y-axis within the supporting framework, which is 20 mm, and removing the 2 mm width occupied by the rack and pinion mechanism (as shown

in Figure 2.16 (a)), it appears that the maximum dimension of the rotative sample holder along the y-axis is 18 mm. This size is reduced to 17 mm to accommodate the insertion of a washer between the support structure and the pinion. The washer helps reduce friction between these mechanical parts during the rotation. As shown in Figure 2.17 (a), the sample holder consists of a 12 mm diameter cylinder with a recess of 11 mm in width, specifically designed to accommodate the sample. The sample positioning is achieved through a set screw that aligns with the axis of the sample holder. In addition to clamping the sample, the screw serves also as the axis for rotation. On the opposite side of the sample holder, the pinion is attached using three screws, while a second axial screw serves as a linkage to the support structure along the rotation axis.

The sample holder for the stationary sample is shown schematically in Figure 2.17 (b). The width of this mechanical part is set to 20 mm to ensure a snug fit within the supporting structure. Attaching the sample holder to the support structure is achieved with two screws, purposefully positioned to restrict rotational movement along the y-axis. The same principle using a set screw is employed to clamp the sample inside the holder. The experimental system is designed so that the distance between the centres of the samples once installed in their respective holders should be 22 mm. However, placing precisely such small samples in the experimental system is challenging. The effective distance between the samples is therefore subjected to experimental calibration.

Transfer of a mechanical motion in the vacuum-sealed chamber

The previous section described how the linear motion of the driving shaft can be converted into a rotational motion. The controlled translation of the driving shaft, however, requires an actuator. Given the severe operational conditions within the experimental chamber, including spatial constraints, cryogenic temperatures, and possibly high magnetic fields, it is decided to locate this actuator outside the PPMS experimental chamber. The mechanism for transmitting the mechanical work generated by the external actuator to the driving shaft located within the vacuum-sealed chamber is described below.

The design of such a transmission mechanism is facilitated through the combination of three readily accessible commercial components added at the top of the experimental chamber as shown in Figure 2.18.

(a) **Rotary vacuum feedthrough (Figure 2.18 (a))**: This component enables the transmission of rotational motion across the wall of a vacuum chamber while preserving the integrity of the vacuum environment within the chamber. The rotating component incorporates bearings and seals, serving to establish a hermetic feedthrough. Additional mechanisms can be used to induce the rotation of the central shaft without compromising the vacuum inside the chamber. Note that linear vacuum feedthroughs also exist, but they are often designed to be operated manually by the user and more challenging to connect to a motor.

(b) **Adaptation flange (Figure 2.18 (b))**: This part serves as a transitional component connecting the rotary vacuum feedthrough and the T-connector that presents two different diameters while ensuring a hermetic seal.

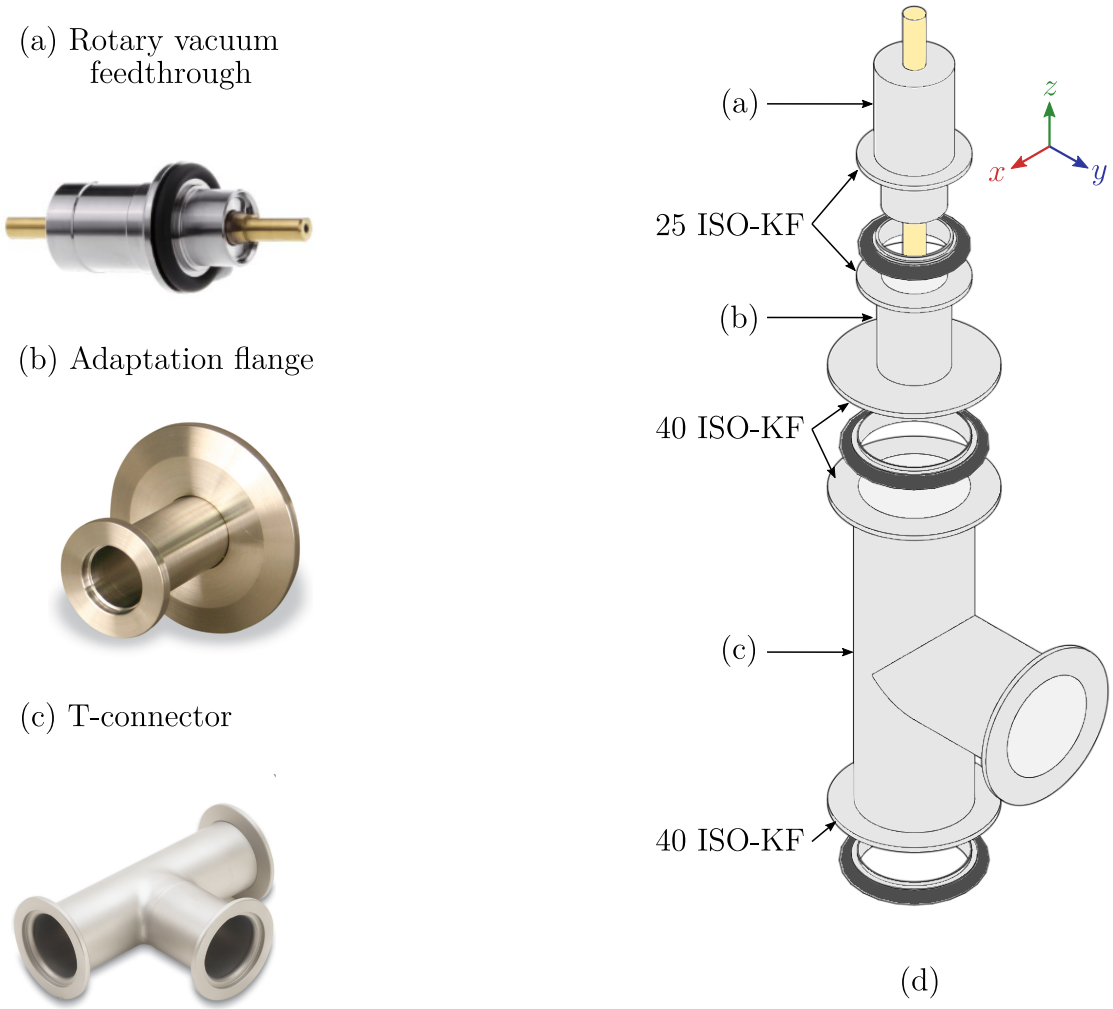

Figure 2.18: (a), (b) and (c) Picture of a rotary feedthrough [144], of an adaptation flange [145] and of a T-connector [145] respectively. (d) Conceptual design of the assembly allowing the transmission of rotational motion across the boundary of a vacuum chamber.

(c) **T-connector (Figure 2.18 (c))**: This component, placed between the top of the experimental chamber and the adaptation flange, introduces a lateral connection in the piping. In the present work, the T-connector has two goals. First, the lateral pipe (y-direction in Figure 2.18 (d)) facilitates the passage of electric leads across the boundary of the vacuum chamber, as discussed in section 2.3.3. Second, the T-connector also acts as a structural support for the mechanism that links the rotary vacuum feedthrough to the driving shaft, this point is clarified further in this section.

Based on the design presented in Figure 2.18 (d), it is now feasible to provide rotational motion within the experimental chamber. However, as discussed in the previous section, the operation of the experimental system relies on the linear motion of the driving shaft. Consequently, the engineering of an additional mechanism that converts the angular motion of the rotary feedthrough into a linear motion of the driving shaft is required. The transformation from circular to linear motion is accomplished through a screw and nut mechanism, the fundamental

operational concept of which has been presented in section 2.2. Here, the translational degree of freedom along the axis of the screw is locked for the nut and the rotational degree of freedom is blocked for the screw. The rotation of the nut is given by the rotary vacuum feedthrough, which in turn induces the linear displacements of the screw engaged within the nut.

The practical implementation of this mechanism within the experimental setup is shown schematically in Figure 2.19, in which the illustrations of the adaptation flange, the T-connector, and the O-rings have been deliberately omitted for clarity. As can be seen in Figure 2.19, several additional mechanical components are required for the mechanism to be complete. Their function is summarized below:

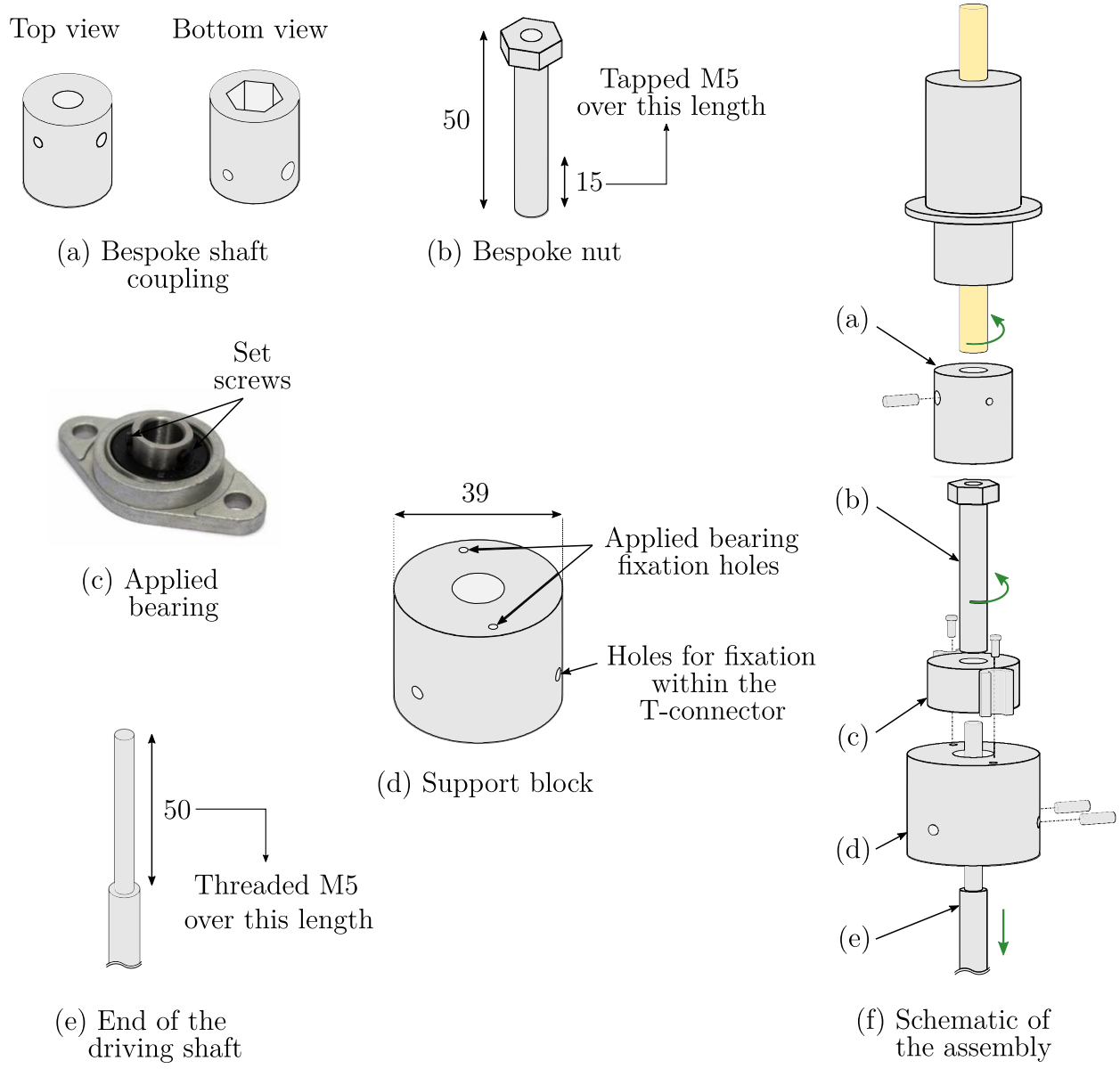

Figure 2.19: Conceptual design of the circular to linear motion transformation mechanism. (a) Bespoke shaft coupling. (b) Bespoke nut. (c) Applied bearing. (d) Support block. (e) End of the driving shaft. (f) Schematic of the assembly. All dimensions are in mm.

(a) **Bespoke shaft coupling (Figure 2.19 (a))**: This mechanical component serves as a connection between the rotary vacuum feedthrough and the nut. As schematically depicted in Figure 2.19 (f), the shaft coupling is attached to the shaft of the rotary vacuum feedthrough thanks to a set screw. On the opposing end of the coupling, there is a hexagonal recess into which the nut can be placed, thereby ensuring synchronized rotations without necessitating additional set screws. This particular coupling design facilitates straightforward installation and removal of motorization components.

(b) **Bespoke nut (Figure 2.19 (b))**: The designed nut exhibits two distinct characteristics. First, it is 50 mm long but it is tapped exclusively within the initial 15 mm of its length, which mitigates the friction between the screw and the nut. Second, the upper portion of the nut adopts a hexagonal shape, facilitating easy connection with the shaft coupling.

(c) **Applied bearing (Figure 2.19 (c))**: This commercially available component serves the purpose of constraining the translational movement of the nut while facilitating unimpeded rotational motion. The applied bearing is attached to the nut through set screws and is subsequently threaded into the support block.

(d) **Support block (Figure 2.19 (d))**: This mechanical component is used to secure the whole mechanism within the T-connector. This component consists of a tube with an external diameter of 39 mm, which allows a snug fit within the T-connector. The block is attached through the utilization of two set screws. Note that the position of the support block within the T-connector can be adjusted if needed.

(e) **End of the driving shaft (Figure 2.19 (e))**: The end of the driving shaft exhibits M5 threading spanning a distance of 50 mm, facilitating its engagement within the bespoke nut. Note that this threaded length is sufficient to adequately cover the entire displacement range calculated in the preceding section (25 mm).

Taking into account that the rack and pinion mechanism presents a resolution of 0.12 mm/° and that the pitch of a classic M5 screw is 0.8 mm/turn, the final resolution of the mechanism is calculated as follows $\frac{0.8}{0.12} \simeq 6.6$ °/turn.

Motorization

The last aspect under consideration to finalize the mechanical design of the bespoke insertion tool is related to the choice of a suitable actuator for the operation of the primary shaft of the rotary vacuum feedthrough. The criteria considered during this selection process include the preference for a relatively compact motor possessing a nominal torque exceeding 0.05 N m as well as an easy integration with a *LabVIEW* software program. Although several potential options would be appropriate for this purpose, the decision converged on a bipolar 12V - 1A stepper motor. Figure 2.20 shows the fully assembled motor block, and the two primary components involved are detailed below.

(a) **NEMA 14 stepper motor** [146]: This stepper motor exhibits a nominal torque of 0.1 N m and a step angle of 1.8°. The rear shaft is exposed facilitating the installation of an encoder.

(b) **Rotary encoder** [147, 148]: This commercial encoder is employed for the precise measurement of the angular position of the motor, featuring a resolution of 300 counts per

complete rotation. It is fitted over the rear shaft of the stepper motor and tightened with a set screw. It is accompanied by a printed board circuit (PCB) that can be directly connected to the USB port of a computer which allows straightforward interfacing of the encoder signal in a *LabVIEW* program.

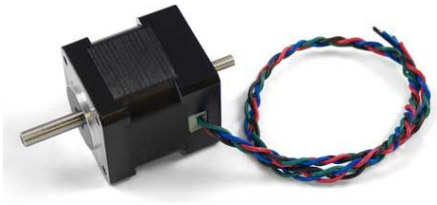

(a) NEMA 14 stepper motor

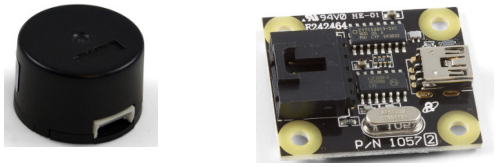

(b) Rotary encoder

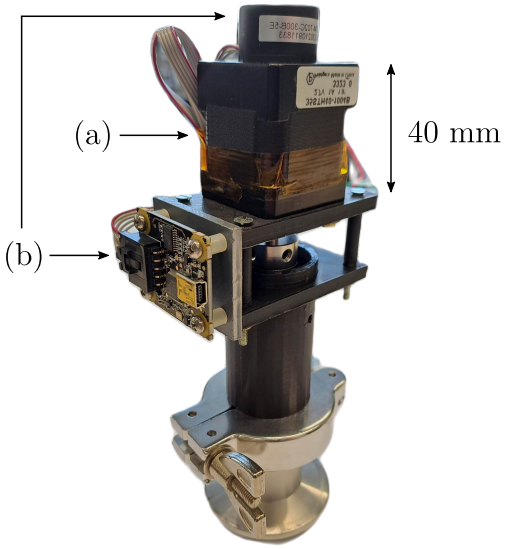

(c) Assembled motor block

Figure 2.20: Picture of the fully assembled motor block alongside pictures of its two primary components.

Considering the step angle of the selected motor (1.8°) and the resolution of the mechanism computed in the preceding section (6.6°/turn), the resolution of the complete insertion instrument can be derived: 0.033°/motor step.

The stepper motor is controlled thanks to a customized PCB that was developed previously in our laboratory [140]. This electronic board is connected to a computer using an RS-232 interface which allows the transmission of commands to the motor through a *LabVIEW* program.

2.3.3 Development of a gradient measuring probe

The insertion tool developed in the previous section allows the placement and the controlled rotation of superconducting samples within the experimental chamber of the PPMS. Nevertheless, in its current configuration, no sensor has been integrated yet. In this context, a probe enabling to measure the gradient of the magnetic flux density in the region between the superconducting samples is constructed.

In this section, the design of the probe and the cable management within the PPMS experimental chamber are first discussed. Second, the calibration process both at ambient and cryogenic temperatures is described.

Design and cable management

The determination of the gradient of magnetic flux density can be carried out by post-processing measurements of the magnetic flux density at various positions between the magnetized superconductors. Very often, this flux density distribution is measured using a single Hall probe, moved at various positions using a mapping system. In the present case, the limited available space makes the integration of a Hall sensor displacement mechanism impractical. The distribution of magnetic flux density is therefore chosen to be measured using several stationary Hall sensors. The home-made experimental system including the stationary Hall sensors will be called "multi-Hall probe" hereafter.

The multi-Hall probe consists of a stack of 7 PCBs of 0.4 mm in height as shown in Figure 2.21. In this configuration, each PCB in the stack, except for the base PCB, is equipped with two *Lakeshore* HGT-2101 Hall sensors [149], one is soldered on the top surface, the other on the bottom surface. Each stage is soldered to its neighbour which provides electrical contact from one stage to the next and facilitates to feed all the sensors placed electrically in series, cf. Figure 2.21 (a). The multi-Hall probe is designed to be tightened directly on the stationary sample holder. When the probe is installed, the centres of the Hall sensors are aligned in the z-direction.

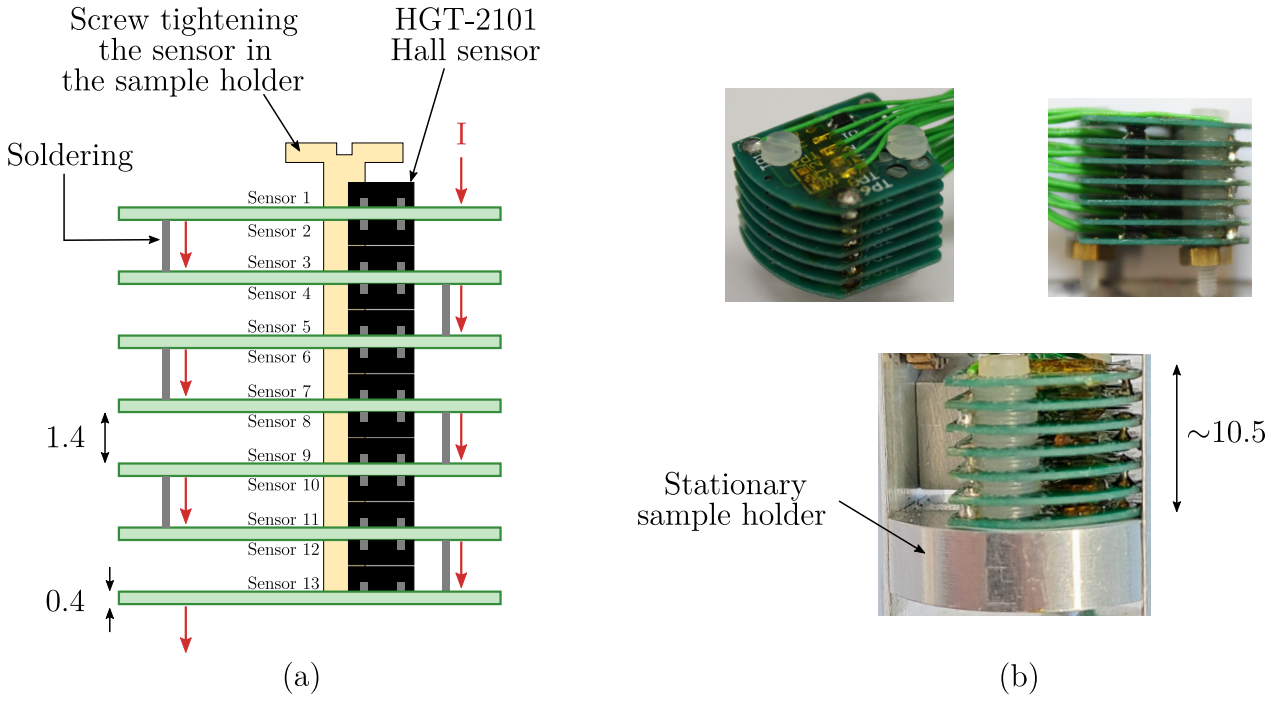

Figure 2.21: Bespoke multi-Hall probe used for the determination of the magnetic flux density gradient (a) Conceptual view. (b) Pictures of the probe. All dimensions are in mm.

Based on the design presented in Figure 2.21, a total of 13 Hall sensors have to be powered and monitored from the exterior of the PPMS experimental chamber. Since the Hall sensors are all connected in series, the whole probe requires 28 wires (2 current leads and 2×13 wires for the differential voltages) to be interfaced with the exterior of the PPMS while preserving the integrity of the vacuum environment. A 12-pin connector is already integrated at the bottom of

the PPMS experimental chamber. A commercially available specialized connecting puck [150] attached to the base of the bespoke insertion tool facilitates the convenient routing of 12 electrical leads towards the outside of the PPMS. The remaining 16 electrical leads are directed towards the top of the experimental chamber where they are routed to the outside through the horizontal branch of the T-connector connected to a commercially available instrumentation feedthrough [151]. The specific pin assignments for each electrical connection are summarized in Figure 2.22.

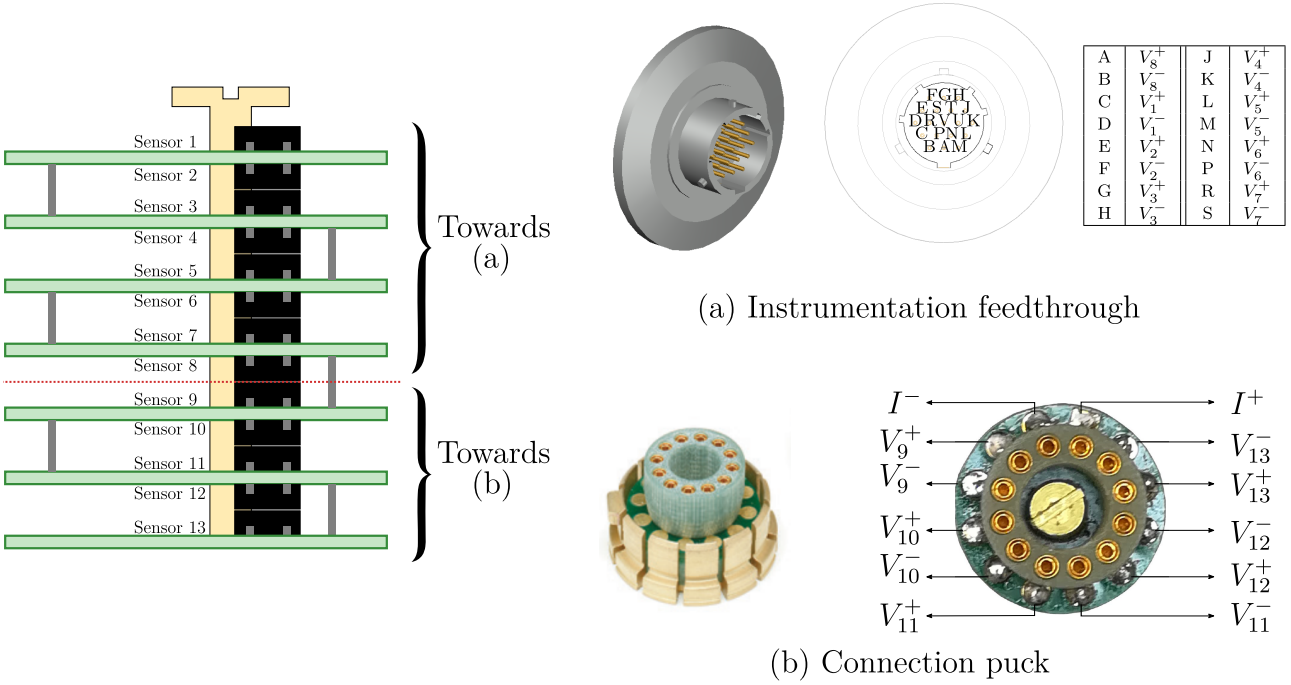

(a) Instrumentation feedthrough

(b) Connection puck

Figure 2.22: Wires routing and pin assignments of the gradient measuring sensor.

Calibration

The calibration of the sensitivity and offset of the Hall sensors of the multi-Hall probe is performed at five specific temperatures within the PPMS: 60 K, 65 K, 70 K, 75 K and 80 K. For experiments that will be conducted at other temperatures, a linear interpolation between the two closest measured values is performed to determine the calibration constants. At each temperature, the individual offset is evaluated by averaging the output signal of each Hall probe over a period of 300 s when no field is applied. When possible, the offset of each sensor is reassessed at the start of each experimental run; otherwise, the previously determined offset is used. Regarding calibration of the sensitivity, the applied field is increased from 0 to 2 T with steps of 50 mT while monitoring the output signal of each sensor. Subsequently, a linear regression is applied to derive the sensitivity values. In practice, the sensitivity is found to exhibit minimal variations with temperature within the explored temperature range. The sensitivity of all sensors is found to fall in the range [0.19-0.23] mV/mT. Although the sensors are operated outside the temperature range recommended by the manufacturer, it is remarkable to observe that the experimentally determined sensitivities remain well within the range specified in the data sheet [149]. The same calibration procedure is also conducted at ambient temperature, for which the sensitivity of the Hall probes is measured to lie in the range [0.15-0.18] mV/mT.

Following the determination of calibration constants for each Hall sensor, a preliminary experiment is conducted outside the PPMS to calibrate, at ambient temperature, the relative distance between the active surfaces of the Hall sensors. A schematic illustration of this experiment is shown in Figure 2.23 (a).

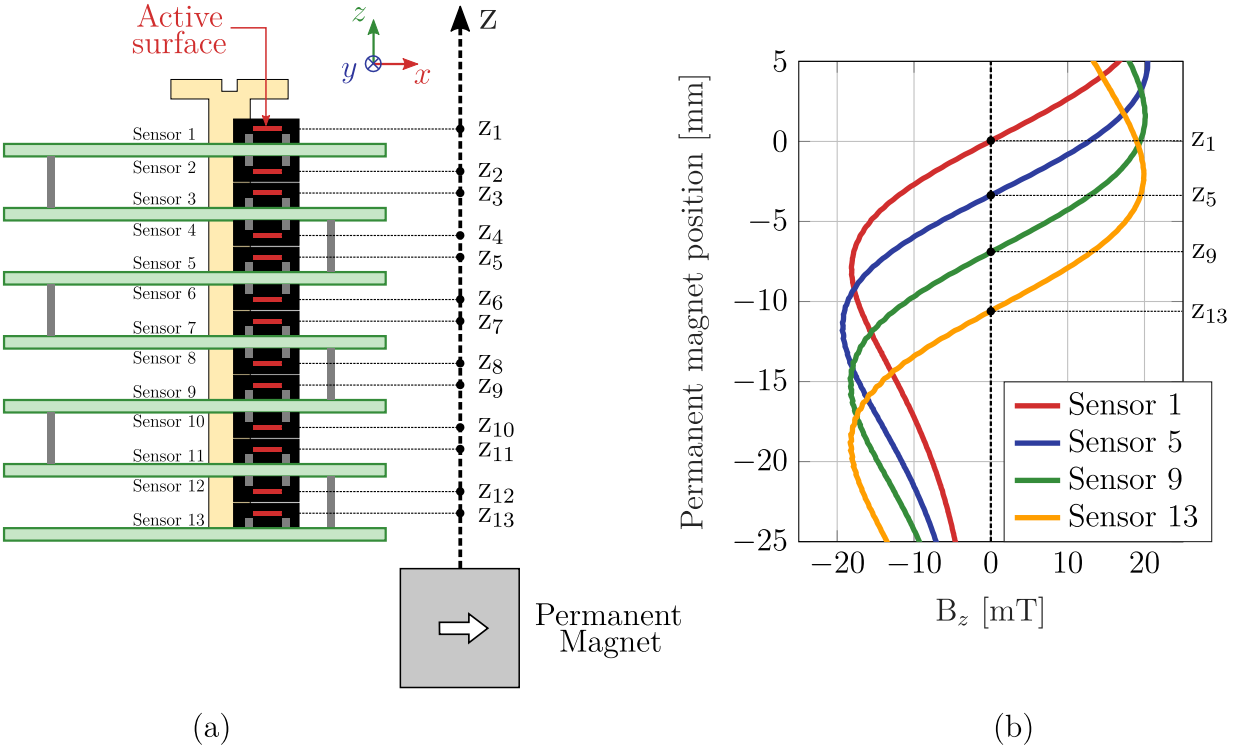

Figure 2.23: (a) Schematic illustration of the experiment to calibrate the relative distance between the active surfaces of the Hall probes within the gradient measuring sensor. (b) Evolution of the magnetic flux density measured by 4 Hall probes distributed in the multi-Hall probe as a function of the position of the permanent magnet moved along the z-direction.

A cubic Nd-Fe-B permanent magnet of 10 mm side and main magnetization direction along the x-direction is moved along a line parallel to the z-direction. The motion is achieved using the 3D mapping system described in section 2.1. The multi-Hall probe is positioned as close as possible to the path of the permanent magnet and is oriented such that the Hall sensors measure the z-component of the magnetic flux density generated by the permanent magnet. In such a configuration, the output signal of a specific Hall sensor vanishes when the geometric centre of the permanent magnet is aligned with the active surface of that particular sensor. Therefore, by monitoring the evolution of the output signal of each Hall probe as a function of the permanent magnet position and comparing the positions at which each individual signal disappears, the relative distance between the active surfaces can be derived. As an illustration, the evolution of the flux density measured by 4 Hall sensors distributed in the multi-Hall probe as a function of the permanent magnet position is shown in Figure 2.23 (b). The permanent magnet position at which the signal of the highest Hall sensor in the stack vanishes is used as a reference position. The positions of all the other Hall probes relative to the reference are summarized in Table 2.1.

Given possible mechanical deformations when operating the gradient measuring sensor at

cryogenic temperatures, a second experimental run with the setup immersed in a liquid nitrogen bath is carried out. In an effort to minimize the thermal shock experienced by the sensors, the experimental setup is enclosed within a sealed chamber as shown in Figure 2.24 before immersing it in liquid nitrogen. To route wires within the enclosure, the instrumentation feedthrough illustrated in Figure 2.22 is used. Notably, among the 19 available pins on this feedthrough, two are allocated for current leads. Additionally, another two pins are reserved for a Pt100 temperature sensor, which is integrated into the system to monitor the temperature within the enclosure and make sure that the experiment is carried out once the thermal equilibrium is reached. The signals given by only 7 Hall sensors can be acquired during the manipulation. The positions of all the acquired Hall sensors relative to the uppermost sensor in the stack are summarized in Table 2.1. Two photographs of the experimental configuration are shown in Figure 2.24.

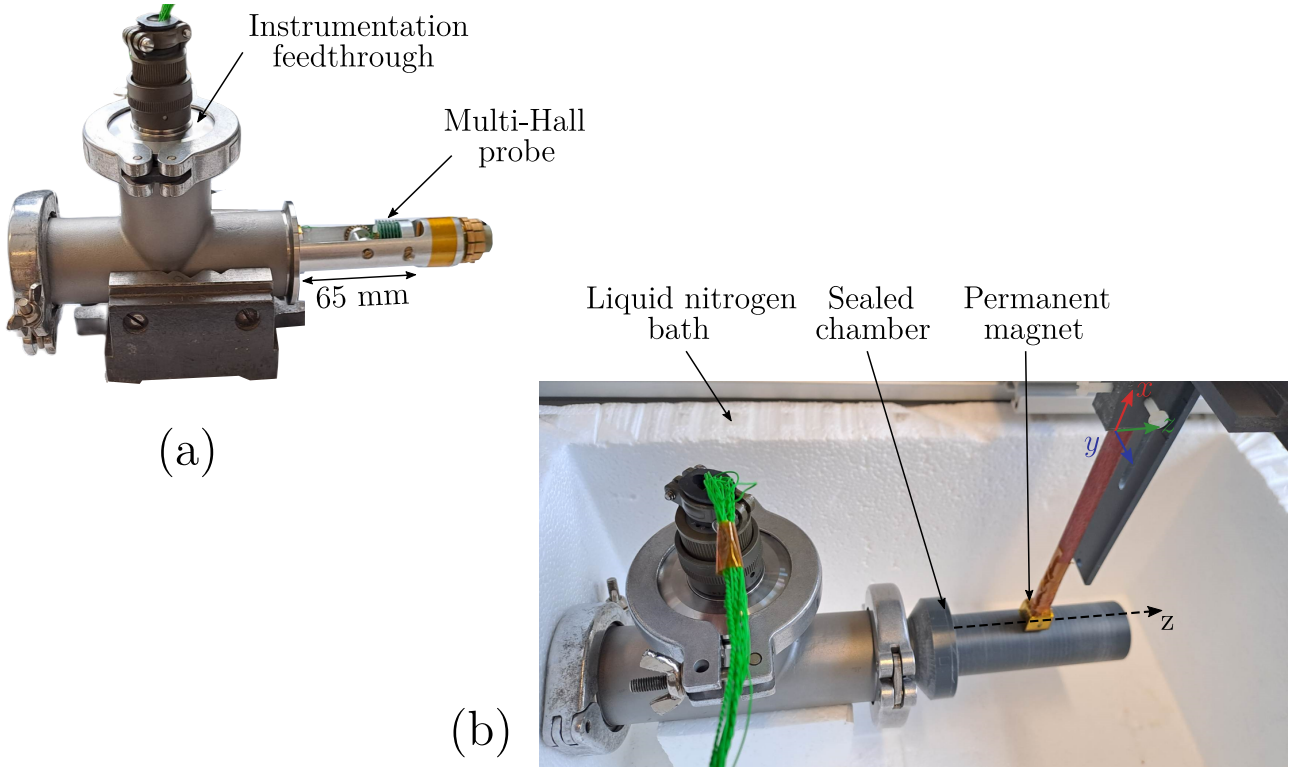

Figure 2.24: Photographs of the experimental setup used to calibrate the relative distance between the active surfaces of the Hall sensors within the multi-Hall probe at 77 K.

	$\lvert z_1 \rvert$ [mm]	$\lvert z_2 \rvert$ [mm]	$\lvert z_3 \rvert$ [mm]	$\lvert z_4 \rvert$ [mm]	$\lvert z_5 \rvert$ [mm]	$\lvert z_6 \rvert$ [mm]	$\lvert z_7 \rvert$ [mm]	$\lvert z_8 \rvert$ [mm]	$\lvert z_9 \rvert$ [mm]	$\lvert z_{10} \rvert$ [mm]	$\lvert z_{11} \rvert$ [mm]	$\lvert z_{12} \rvert$ [mm]	$\lvert z_{13} \rvert$ [mm]
300 K	0	1	1.8	2.8	3.4	4.3	5.3	6.1	6.9	7.9	8.8	9.7	10.6
77 K	0	1.1	1.9	2.8	3.3	4.2	5.2	/	/	/	/	/	/

Table 2.1: Relative distance between the active surfaces of the Hall sensors within the multi-Hall probe measured at 300 K and at 77 K. The position of the uppermost probe in the stack (sensor 1) is used as a reference.

Comparing the distance evaluated at ambient and cryogenic temperature as presented in Table 2.1, it can be noticed that the mechanical deformations due to the cryogenic environment do not induce significant modifications of the relative distance between the active surfaces of the Hall probes, at least for those monitored during the experiment performed at 77 K. In the following, it is assumed that the same holds true for the Hall sensors that could not be measured during the experiment conducted in the liquid nitrogen bath. The distances evaluated at ambient temperature are used for these probes.

2.3.4 Superconducting samples used

Preparation

The measurements conducted with the experimental setup described in section 2.3.2 rely on two cubic $YBa_2Cu_3O_{7-x}$ bulk superconductors. These cubic samples were not synthesized in a cubic shape but were extracted from two distinct larger cylindrical samples used in the experimental campaign carried out in [101]. These cylindrical samples were originally manufactured utilizing the TSMG method [110, 128–130] within the Bulk Superconductivity Group at Cambridge University. The selection of these samples is based on their highly similar superconducting properties [101].

To obtain the cubic specimens, a wire saw was employed to precisely cut the cylindrical samples. The extracted portions correspond to cubic regions positioned centrally within the cylinder, each of them including the seed of the initial sample. Additionally, a much smaller orthorhombic sample was also extracted from one of the cylindrical superconductors. This sample is intended for characterization measurements within the ACMS and is assumed to exhibit superconducting properties that are very close to those of the cubic samples. In this context, the orthorhombic samples are extracted as closely as possible to the original position of the cube within the initial bulk superconductor. A picture of each cubic sample placed inside their respective sample holders as well as a schematic illustration of their original positions within the cylindrical bulk is shown in Figure 2.25. Figure 2.25 also introduces the numbering of the samples used for all the measurements performed with the experimental setup described in section 2.3.2: the sample positioned in the fixed sample holder is labelled as "sample 1" while the sample in the rotating sample holder is denoted "sample 2".

Preliminary characterization

Before conducting any experiments within the setup outlined in section 2.3.2, trapped-field measurements are performed on the cubic $YBa_2Cu_3O_{7-x}$ superconductors at 77 K. In these preliminary manipulations, the sample is magnetized with a field-cooling procedure from 1.2 T and a field sweep rate of 1 mT s^{-1}. After the magnetization, a period of 45 min is allowed for magnetic relaxation and the trapped magnetic field is subsequently mapped at a distance of 5 mm above the surface of the sample using the Hall probe mapping system exposed in section 2.1. Based on the assumptions of a homogeneous and field-independent critical current density, the analytical model outlined in section 1.4.2 is adjusted to match the trapped-field measurements and obtain an approximation of the critical current density of the samples at 77 K: 2.3×10^8 A m^{-2}. The comparison of the adjusted analytical model and the trapped-field measurements performed on sample 1 is shown in Figure 2.26 for illustration.

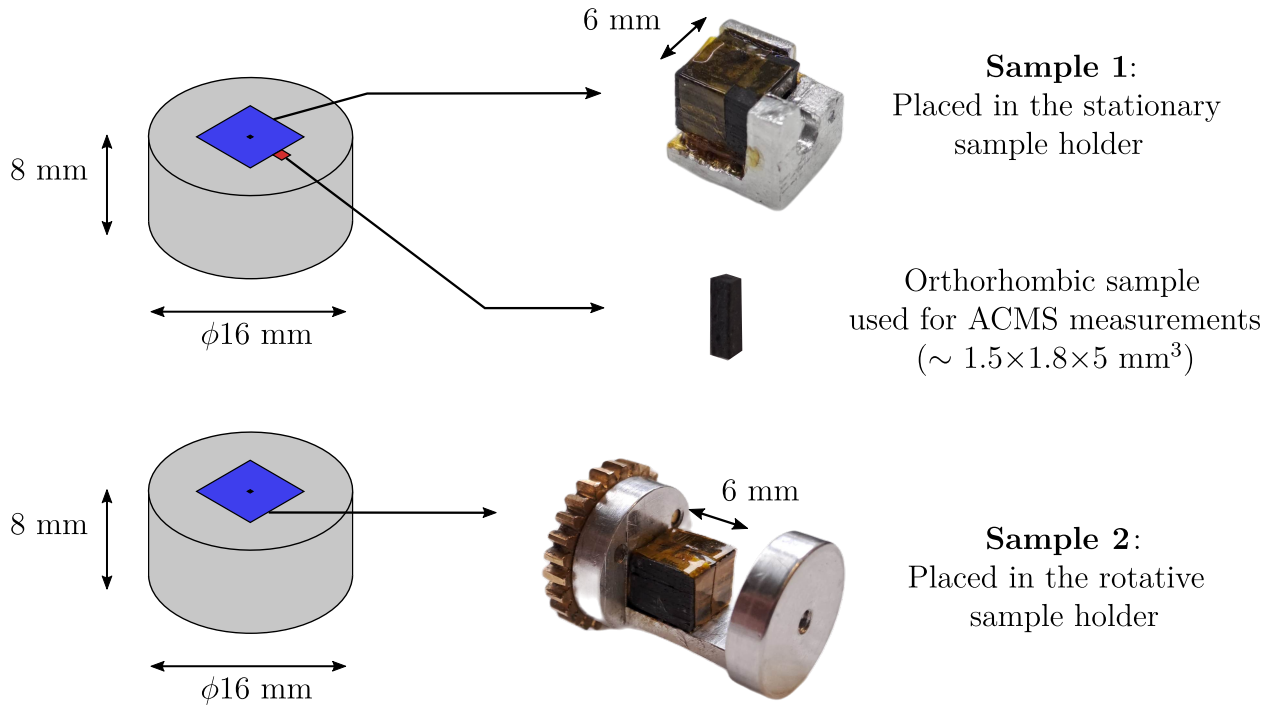

Figure 2.25: Picture of the cubic superconducting placed inside their sample holders. These samples were used for all the experiments carried out with the experimental setup described in section 2.3.2. A schematic representation of the orthorhombic sample used for characterization, as well as the position of the extracted portions within the initial cylindrical bulk superconductor, is also shown.

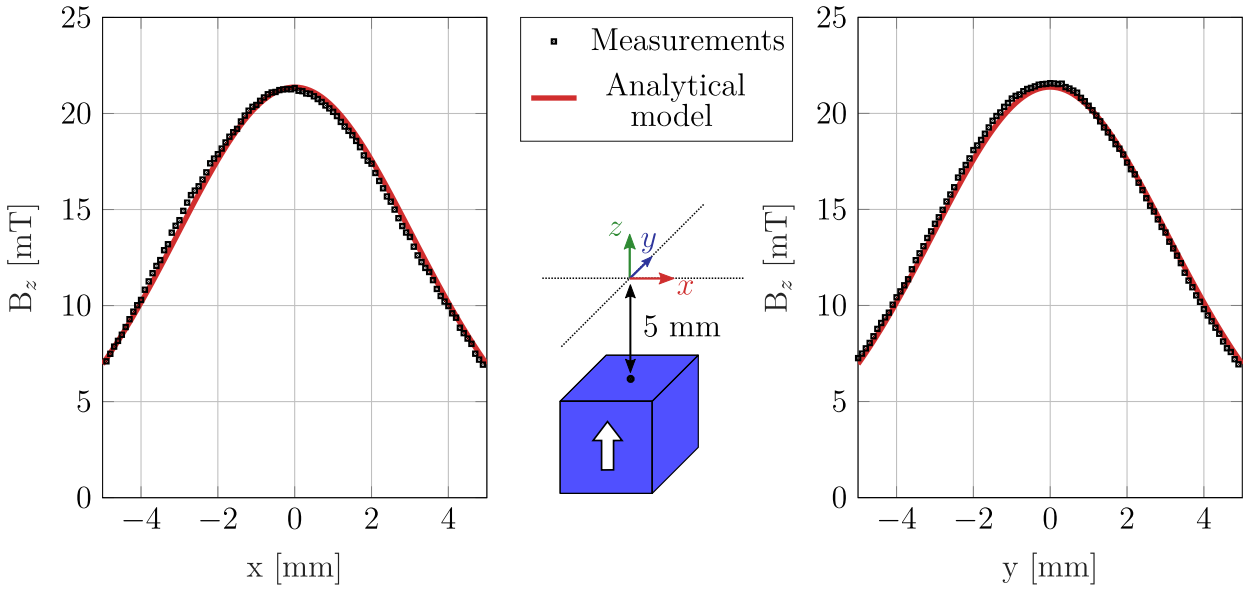

Figure 2.26: Comparison between the magnetic flux density measured at 77 K, 5 mm above the surface of a magnetized cubic superconductor of 6 mm side and the prediction of an analytical model. The model assumes a homogeneous and field-independent critical current density equal to 2.3×10^8 A m^{-2}.

As it will become clearer in chapter 5, the simplified analytical model is not well-suited for the detailed analysis of the experimental results obtained during the experiments conducted in the PPMS. Nevertheless, the approximation of a constant critical current density at 77 K is used in this section to derive the main experimental parameters. More particularly, the adjusted analytical model is used here to estimate two important characteristics of the samples for designing the experimental procedure. The first corresponds to the magnetic flux density trapped at the centre of the superconductor when it is in the critical state, denoted as B_{centre} [152]. To ensure full penetration of the sample, the field applied during a field-cooling magnetization should be at least equal to B_{centre}, and at least twice as high in a zero-field-cooling magnetization. The second is the magnetic moment of the magnetized sample, noted $\mathbf{m}$. Considering that the magnetic torque acting on the sample when it is placed in a DC uniform field $\mathbf{B}$ can be written $\boldsymbol{\tau} = \mathbf{m} \times \mathbf{B}$ and considering the maximum torque that the mechanical system can withstand without risking damage (0.022 N m), the maximum field within which the magnetized superconductor can be rotated by an angle of 180° thanks to the mechanical system designed in section 2.3.2 can be derived from the knowledge of the magnetic moment.

Based on the approximated critical current density at 77 K, this preliminary reasoning is also extended to two other temperatures (65 K and 59 K) thanks to the widely employed equation [153–155]:

$$J_c(T) = J_c(T_{ref}) \left(\frac{T_c - T}{T_c - T_{ref}} \right)^{\alpha}, \tag{2.1}$$

where $T_{ref} = 77$ K, $T_c = 92$ K and where the parameter α is a non-linear function of temperature [155]. In the context of this rough estimation, however, α is set to one which is equivalent to assume a linear dependence of the critical current density with temperature.

The physical parameters obtained through this methodology at each temperature experimentally investigated are succinctly presented in Table 2.2. Note that the estimated value of B_{centre} at 77 K retrospectively supports the assertion of a complete penetration state within the superconducting sample during this preliminary characterization.

	J_c [A m^{-2}]	B_{centre} [mT]	$\|\|\mathbf{m}\|\|$ [A m^2]	$B_{bg,max}$ [mT]
77 K	2.3×10^8	760	0.05	440
65 K	4.1×10^8	1368	0.09	245
59 K	5.1×10^8	1672	0.11	200

Table 2.2: Estimation of the experimental parameters that can be explored using the cubic superconductor of 6 mm side within the experimental setup described in section 2.3.2. The estimation is based on the trapped-field measurements performed at 77 K and is extrapolated to other temperatures thanks to equation (2.1). $B_{bg,max}$ denotes the maximum background field in which the sample can be rotated without damaging the mechanical system.

Placement in the experimental setup

$YBa_2Cu_3O_{7-x}$ bulk superconductors are inherently brittle materials, and the cutting process used in sample preparation may introduce cracks in the samples. When incorporating these samples into our custom-designed system within the PPMS, a significant concern arises regarding the possibility of breaking the sample which, if not properly managed, could result in debris contaminating the PPMS experimental chamber. To mitigate this risk, three precautionary measures are applied. First, the samples are glued within their respective sample holders using cryogenic adhesive before clamping them within the system. This step reduces the likelihood of fragments detaching. Second, the design of the sample holders incorporates a complete enclosure of the samples when the entire system is assembled, further minimizing the possibility of debris dispersion. Third, the experimental enclosure containing the samples is entirely enveloped in polyimide tape before insertion into the PPMS. The positioning of the superconducting samples in the assembled experimental setup is illustrated in Figure 2.27.

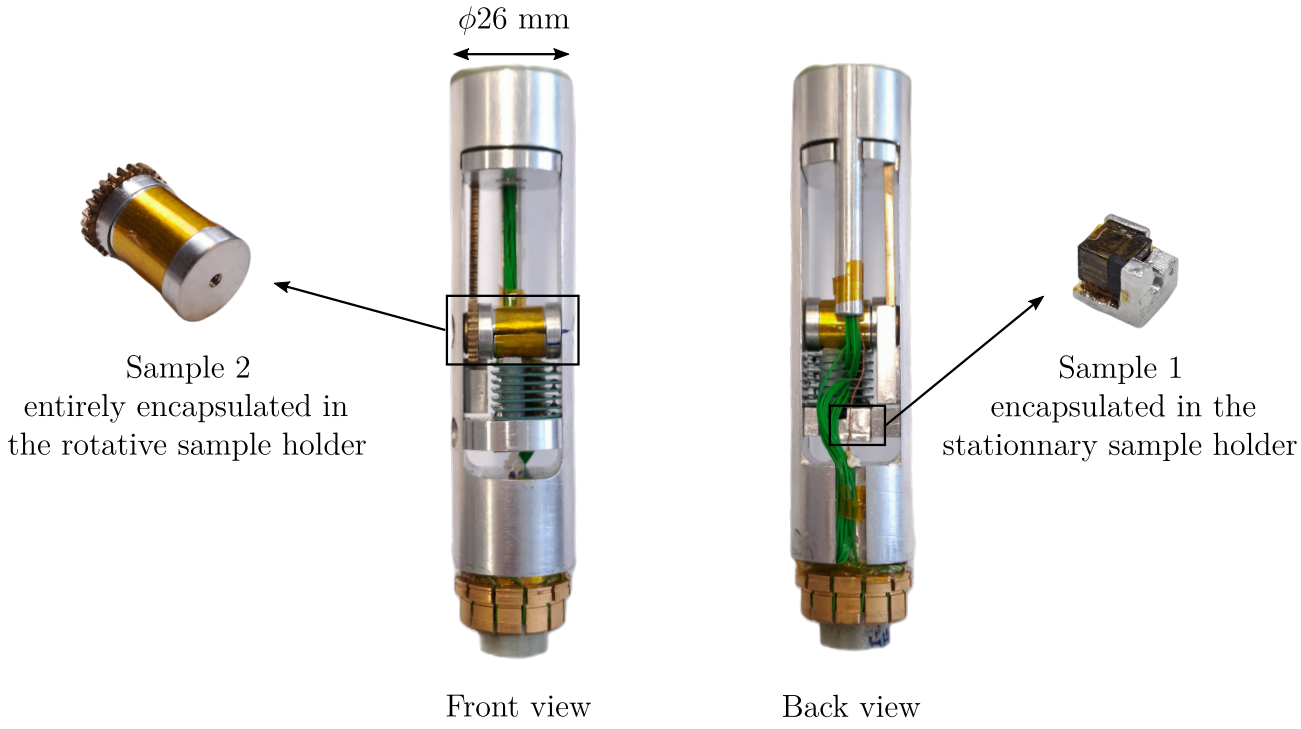

Figure 2.27: Photograph of the experimental setup completely assembled showing the positioning of the superconducting samples within the system.

2.3.5 Experimental procedure

A series of experiments are carried out using the experimental setup detailed in section 2.3.2. Various configurations, comprising both single and dual-sample scenarios at temperatures of either 77 K, 65 K and 59 K could be investigated. While specific experimental parameters for each configuration under investigation may differ, a common framework was consistently applied across all experiments. This standardized procedure is visually depicted in Figure 2.28 and is presented in more detail below.

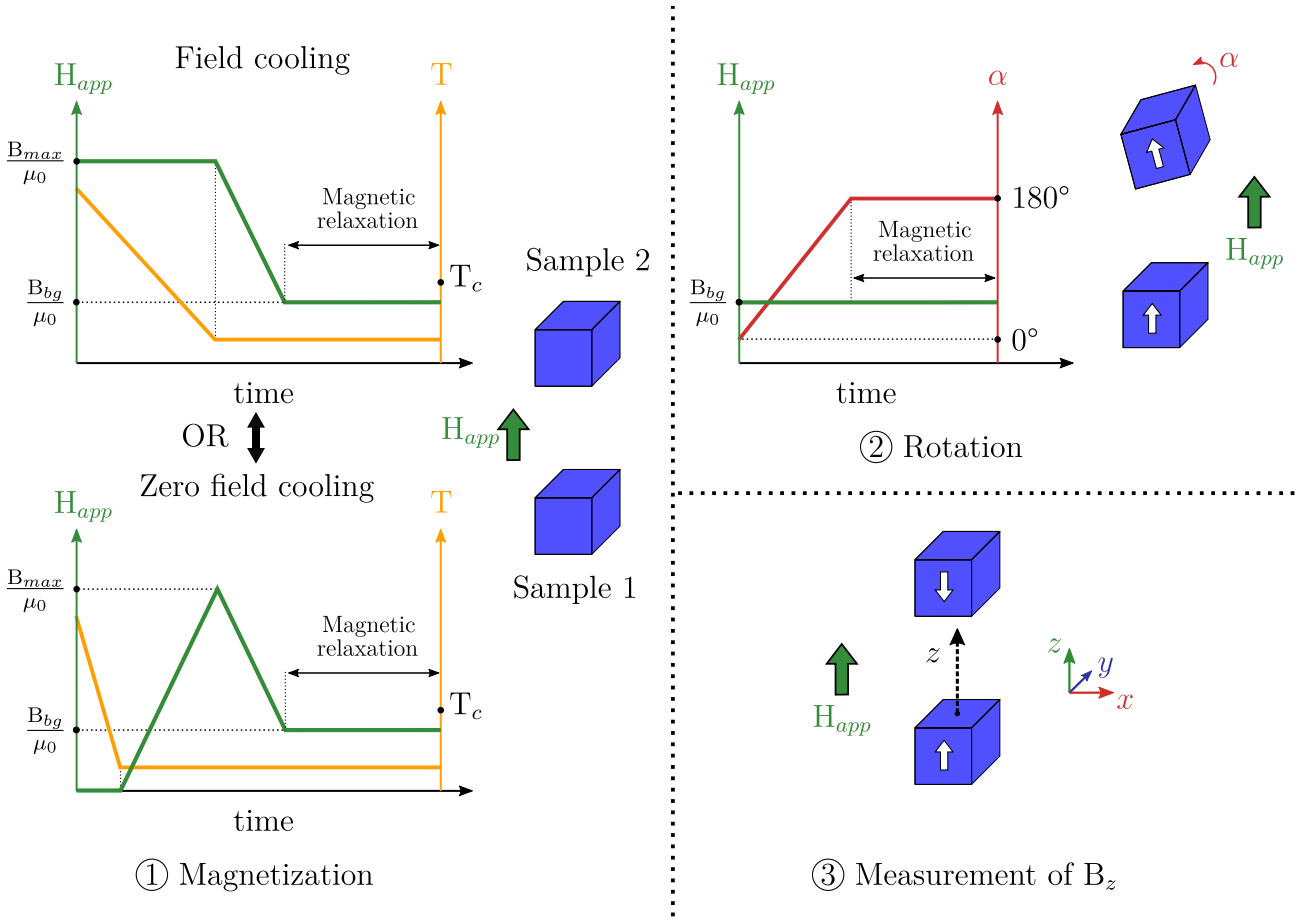

Figure 2.28: Schematic illustration of the systematic experimental process used during the experiments conducted within the PPMS.

The experimental process consists in following systematically three steps.

1. The samples are magnetized either in field-cooling or in zero-field-cooling conditions. For experiments performed at 77 K, the zero field-cooling process is preferred because it allows the precise measurement of the initial offset of the Hall sensors at the beginning of the magnetization process. When conducting experiments at 65 K, however, a field-cooling procedure is applied to prevent the application of a too-high magnetic field. For both magnetization processes, the applied magnetic field is oriented in the z-direction which coincides with the alignment of the c-axis of the samples. The maximum applied field is noted $\frac{B_{max}}{\mu_0}$ and the field sweep rate is 15 mT s^{-1}. A notable feature of this procedure is that the field-decreasing step is stopped when the applied field reaches the threshold $\frac{B_{bg}}{\mu_0}$, then it remains unchanged for the rest of the experiment. A period of 45 min starting at the end of the field-decreasing step is allowed for magnetic relaxation.

2. The rotating sample holder is rotated by an angle of 180° at a constant speed of 5° s^{-1}. After this rotation, a second period of 15 min is allowed for further magnetic relaxation. Note that this step is performed even if no sample is placed in the rotative holder so that the total magnetic relaxation period is the same for all experiments.

3. The magnetic flux density distribution component parallel to the applied field is measured

at 13 positions between the samples using the multi-Hall probe presented in section 2.3.3. Unless otherwise stated, the magnetic flux densities and gradients of magnetic flux density are taken at this specific instant. Since the applied field is aligned with the direction sensed by the Hall sensors, the exclusive contribution of superconducting samples can be derived by subtracting $B_{bg} \neq 0$ from the measurements.

A *LabVIEW* program was developed to implement the following functions: (i) the acquisition of data from the PPMS sensors; (ii) the transmission of control commands to the PPMS control unit; (iii) the acquisition of the rotary encoder signal; (iv) the transmission of control commands to the stepper motor and (v) the acquisition of the signals of the 13 Hall sensors involved in the gradient measuring sensor. This program enables the execution of the experimental procedure schematically represented in Figure 2.28 within a single *LabVIEW* interface.

A list of the experiments carried out within the PPMS and the experimental parameters are presented in Table 2.3. Except for experiments in which B_{max}=B_{bg}, the field B_{max} is significantly larger than the minimum required for full penetration according to the estimation in Table 2.2.

2.4 Summary

In this chapter, the design and the functioning of two bespoke cryogenic experimental setups were presented.

The first setup is composed of five aligned carriages each of which is designed to accommodate a superconducting sample with a parallelepiped shape and geometrical dimensions between 12 mm and 16 mm. Among these carriages, the central one remains stationary while the motion of the other four can be imparted in a controlled manner through the activation of lead screws. A readily available 3D $x\,y\,z$ micropositioning system equipped with a cryogenic Hall probe was integrated into the apparatus for measurement of the magnetic flux density. Therefore, the final setup allows for the clamping of up to 5 pre-magnetized superconducting magnets arranged linearly and facilitates their reproducible translational movement along the alignment axis and the measurement of the magnetic flux density distribution in their vicinity. A systematic procedure was also described for assembling experimentally a superconducting linear Halbach array with this equipment and evaluating its performance.

The second experimental system discussed in this chapter is a bespoke insertion instrument for the *Physical Property Measurement System*. This instrument incorporates a rotation mechanism, facilitating a 190° rotation of a sample holder within the experimental chamber. The methodology used to transfer mechanical work to this mechanism while preserving the hermeticity of the experimental chamber was elucidated. Additionally, a stationary sample holder is included, cubic superconducting samples of 6 mm side can be clamped in each holder. A bespoke "Multi-Hall probe" including 13 aligned Hall sensors was designed, assembled, calibrated and incorporated into the system for measuring the field distribution in the region between the samples over a length of approximately 10.6 mm. This insertion tool allows for the measurement of the field gradient produced with a combination of two trapped-field magnets in the presence of a non-vanishing background magnetic field. The systematic experimental procedure that can be followed to investigate this extensively was delineated.

T° [K]	Magnetization process	B_{max} [mT]	Sample	B_{bg} [mT]
77	ZFC	2400	1	0 100 200 300
			2	0 100 200 300
			1 + 2	0 100 200 300
	FC	100 200 300 400	2	100 200 300 400
65	FC	4000	1	0 50 100 150
			2	0 50 100 150
			1 + 2	0 50 100 150
	FC	50 100 150	2	50 100 150
59	FC	7000	1 + 2	0 50

Table 2.3: Comprehensive list of the experiments carried out within the PPMS.

3 Linear Halbach array

A method typically considered to generate a magnetic flux density gradient consists in combining several permanent magnets in a Halbach array. Permanent magnets exhibit non-parallel magnetization in this assembly which leads to an increase in the magnetic flux density on one side. Recent work has aimed to optimize an array of neighbouring Nd-Fe-B permanent magnets to increase the gradient while minimizing the repelling forces during the assembly process [14–16, 156]. With such technique, however, the saturation magnetization $\mu_0 M_{sat}$ of the magnetic material used (1.4 T for Nd-Fe-B permanent magnets [33, 34] and 2.4 T for soft ferromagnetic Fe-Co alloys [35]) limits the maximum achievable field gradient and its spatial extent.

In this context, the ability of bulk superconductors to trap large magnetic fields is of great interest as they can be employed as pseudo-permanent or "trapped-field" magnets. The trapped field of such magnets can be enhanced by increasing their dimensions [111, 157–159] and is not limited by any saturation magnetization. The maximum field trapped in a bulk superconductor to date is 17.6 T [52], almost one order of magnitude higher than the fundamental limit for iron. With such values, magnetized superconductors are an attractive alternative for permanent magnets in applications requiring a large magnetic flux density $\mathbf{B}$ or a large gradient of flux density $\nabla||\mathbf{B}||$ [2–5, 160–165]. In particular, magnetic drug delivery was demonstrated with bulk superconductors [166–170], or under a DC field, using a "zebra" architecture of alternated superconductors and ferromagnets to generate the required gradients [171].

In this chapter, the combination of several cuboid superconductors in a Halbach configuration is investigated experimentally and numerically. The assembly process is more critical than for a classic Halbach array given that the trapped current loops in each magnetized sample may be altered by the proximity of another sample. The magnetization of two neighbouring superconductors in the array being perpendicular, the situation is comparable to a "crossed-field" configuration, in which the trapped field of a superconductor is affected by an external magnetic field which is not parallel to its main axis of magnetization [133, 172–178].

In a few reports, the placement of several trapped field superconductors in close proximity was investigated [159, 179–181]. A DC field varying sinusoidally in space was generated through the use of two staggered rows of stationary samples with parallel magnetizations [182–187]. A magnetic concentration effect was successfully demonstrated by exploiting flux trapping together with flux exclusion with samples having different critical temperatures [188, 189]. A circular

Halbach array of superconductors for rotating machines was proposed and designed by Hull *et al* [190]. Experiments involving the combination of several superconducting magnets with perpendicular magnetizations however remain unexplored and are the focus of this chapter.

The chapter is organized as follows. First, the assembly of a classic Halbach array made of three cubic permanent magnets ($12 \times 12 \times 12$ mm^3) is investigated experimentally. The measurements conducted on this well-known configuration will allow us to point out its practical interest as well as to highlight the characteristics that are specific to superconducting trapped-field magnets later on. After that, a set of characterization measurements are carried out at 77 K on bulk $YBa_2Cu_3O_{7-x}$ superconductors and are employed to adjust the parameters of an analytical and a finite element model. Finally, the focus is directed towards the experimental and numerical results related to the combination of magnetized bulk superconductors in order to assess the feasibility and interest of assembling such a configuration.

3.1 Halbach array made of permanent magnets

Before assembling the three permanent magnets in a Halbach array, the magnetic flux density distribution 1 mm above their top surface is measured at room temperature with the Hall probe mapping system. The measured samples are the cubic Nd-Fe-B permanent magnets with 12 mm sides. Based on the assumption that the magnetic flux density produced by permanent magnets can be modelled by a surface current flowing at the periphery of the sample, the analytical model is applied to reproduce measurements. More specifically, the value of the parameter K_c is adjusted to obtain the best agreement between experimental data and analytical predictions. This leads to $K_c = 10^6$ A m^{-1} for the three permanent magnets. Considering this surface current, the permanent magnets are expected to exhibit a magnetic moment $||\mathbf{m}||$ equal to 1.77 A m^2. This value is confirmed experimentally through the direct measurement of the magnetic moment using the bespoke flux extraction magnetometer. The results of the mappings conducted and the comparison to the adjusted analytical model are shown in Appendix A.1.

Following this preliminary characterization, three permanent magnets are assembled in a Halbach array and the field generated is measured at ambient temperature. Figure 3.1 (b) shows the distribution of the z-component of the magnetic flux density measured 1 mm above the surface of the assembly. A centred line parallel to the x-direction is extracted from this mapping and compared to the predictions of the adjusted analytical model in Figure 3.1 (c), the contribution of the central permanent magnet is also highlighted in that figure. In this configuration, the model assumes a vector summation of the flux densities generated by each permanent magnet in the array and no alteration of the individual magnetization is considered.

As can be seen from the data represented in Figure 3.1 (c), the analytical model predicts very appropriately the magnetic flux density distribution measured experimentally. This observation gives evidence that the magnetic flux density produced by the Halbach configuration including three Nd-Fe-B permanent magnets can be seen as the addition of the individual and independent contributions of the flux density generated by each magnet. This result is expected since the applied field $\mu_0 H_{app}$ should typically exceed 1 T to observe irreversible demagnetization of Nd-Fe-B magnets [191], which is much larger than the stray fields ($\sim$ 500 mT) of the permanent magnets used.

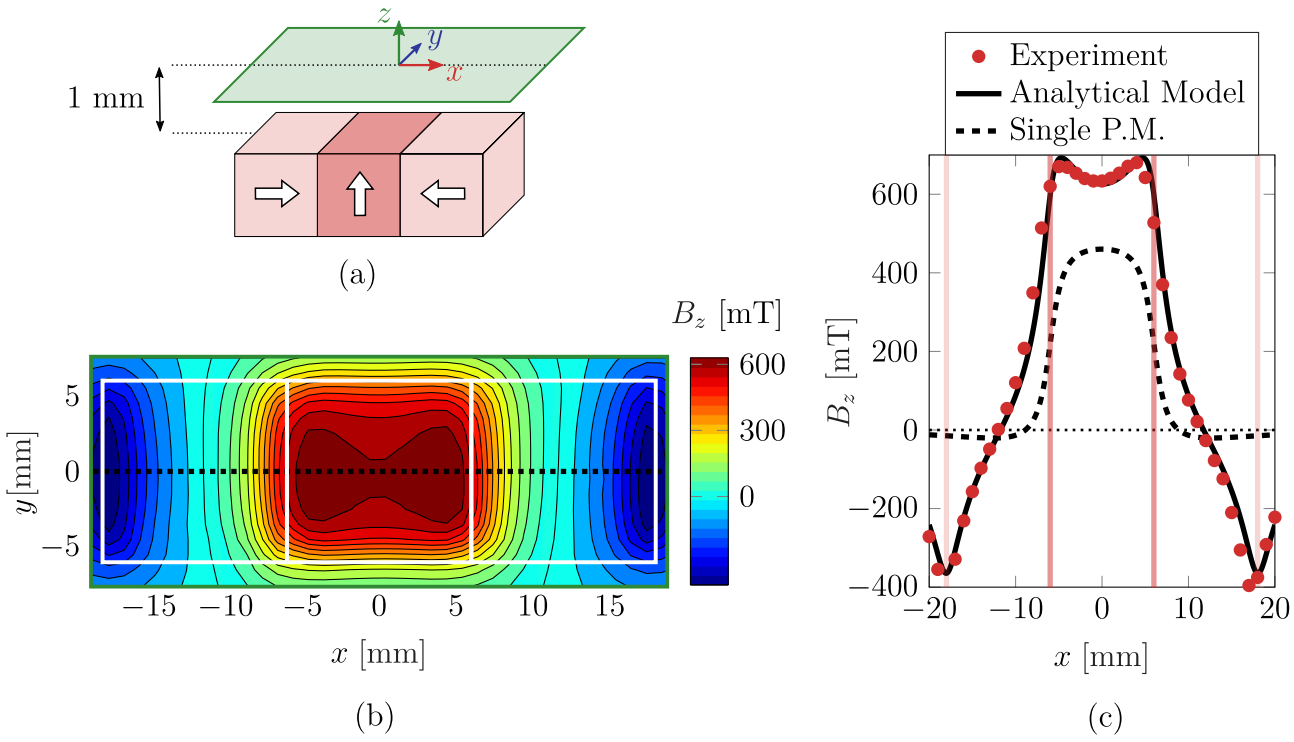

Figure 3.1: (a) Schematic representation of the position of the mapping plane with respect to the Halbach array. (b) Contour plot of the z-component of the magnetic flux density measured at ambient temperature 1 mm away from the surface of a Halbach array made up of three cubic Nd-Fe-B permanent magnets with 12 mm side. The white lines depict the border of the permanent magnets. (c) Mapping results along a centred line parallel to the x-direction. The red vertical lines are located at the border of the samples. The experimental data are compared to an analytical model assuming a simple vector summation of the flux densities generated by each permanent magnet in the array and no alteration of the individual magnetization.

The excellent agreement between measurements and analytic calculations observed in Figure 3.1 (c) gives great confidence in the ability of the analytic model to capture correctly the magnetic flux density produced by the Halbach array made of permanent magnets. In that context, the adjusted analytical model is further exploited to compute the magnetic flux density gradient generated within a x-z plane including the three centres of the samples. This specific computation serves as a benchmark for evaluating the typical performance achievable with permanent magnets of that particular size. The results of the calculation are presented in Figure 3.2 (a). For comparison purposes, the spatial region where the amplitude of the gradient generated by a single permanent magnet (the central one) is higher than 1 T m^{-1} is delimited by the yellow dashed line in the same figure. The computed gradient along a line parallel to the x-direction located at a distance of 20 mm from the top surface of the array (i.e. at $z = 32$ mm) is extracted from this plane and presented in Figure 3.2 (b).

The spatial region where the amplitude of the gradient generated by the Halbach array exceeds 1 T m^{-1} is coloured in dark red in Figure 3.2 (a). It can be noticed that the spatial extent of that region is bigger than that associated with the central permanent magnet only. This observation underlines a primary interest in assembling permanent magnets in Halbach array configurations:

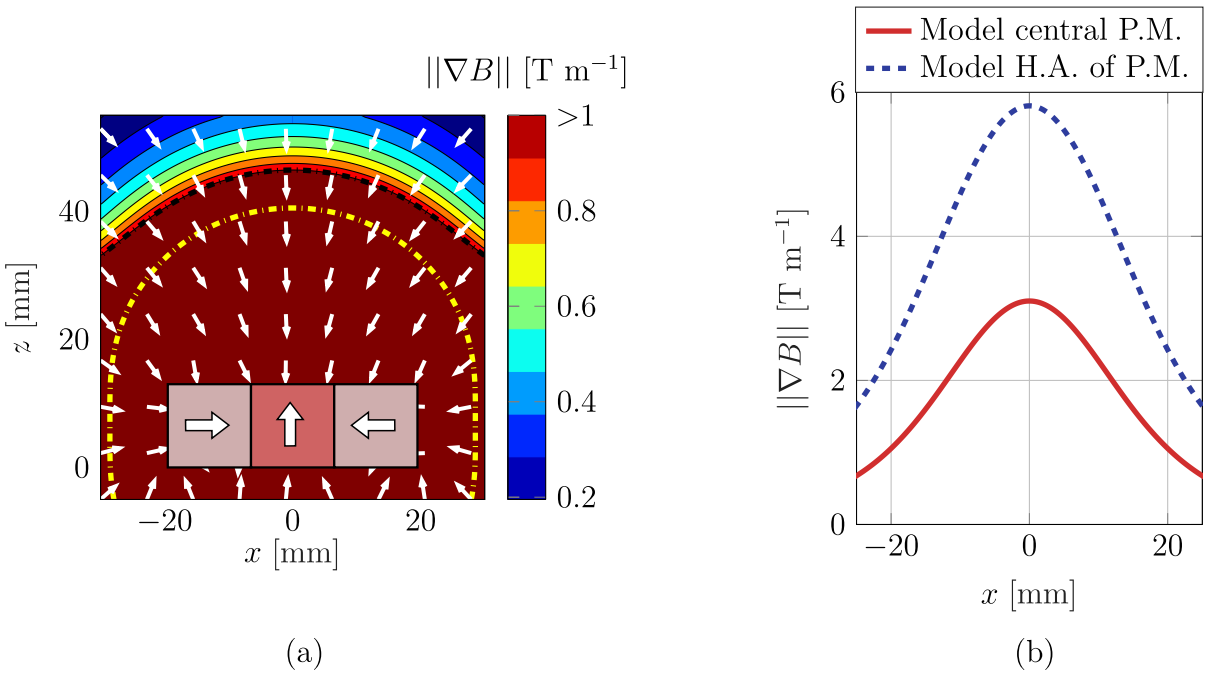

Figure 3.2: Results of the calculations performed with the adjusted analytical model assuming a simple vector summation of the flux densities generated by each permanent magnet in the array and no alteration of the individual magnetization. (a) Contour plot of the amplitude of the magnetic flux density gradient generated by the Halbach array within a x-z plane encompassing the centres of the samples. The small white arrows show the direction of the gradient, and the yellow dashed line delimits the spatial region where the amplitude of the gradient generated by a single permanent magnet (the central one) is higher than 1 T m^{-1}. (b) Comparison between the magnetic flux density gradient generated by a single permanent magnet and that produced by the Halbach array along a line parallel to the x-direction located at a distance of 20 mm from the top surface of the assembly.

it increases the range of the magnetic flux density gradient generated in comparison to isolated magnets. Then, Figure 3.2 (b) shows that at a distance of 20 mm, the maximum magnetic flux density gradient generated by the central permanent magnet alone is equal to 3.1 T m^{-1} while this value increases to 5.8 T m^{-1} when considering the Halbach array. Therefore, the assembly of three permanent magnets in such a configuration results in nearly doubling the gradient produced at a specified distance.

3.2 Characterization of individual superconductors

In the context of conducting experiments related to the assembly of a superconducting linear Halbach array, a set of 9 cuboids $YBa_2Cu_3O_{7-x}$ bulk superconductors were manufactured by the Bulk Superconductivity Group of Cambridge University. Before considering combining several of them, an initial phase of characterizing measurements is conducted on each sample. These preliminary measurements serve a dual purpose. First, among the 9 available samples, only 3 are selected for integration into a Halbach arrangement. This selection process is carried out to ensure that the selected samples exhibit superconducting properties as close as possible to one another. Second, the results of these characterizations are employed to adjust the numerical parameters employed both in analytical and finite element models.

3.2.1 Selection of the samples

The selection of the most appropriate samples is based on the results of two sets of experiments. The first consists of a Hall probe mapping of the trapped field at 77 K. In these experiments, each sample is magnetized in a direction parallel to its crystallographic c-axis through a field-cooling procedure starting from 1.2 T and a constant field removal rate of 1 mT s^{-1}. A period of 45 min is observed to allow for magnetic relaxation and subsequently, the magnetic flux density distribution is measured 1 mm above the top surface of the sample, i.e. the face containing the seed. In the second set of characterizing measurements, an identical magnetizing procedure is followed. However, the time evolution of the trapped field during the magnetic relaxation period is measured with a *Lakeshore* HGT-2101 Hall sensor [149] placed centrally against the top surface of the sample. It is then assumed that this time evolution follows equation (1.9) and the measurements are employed to adjust the parameters $B_{z,0}$, t_0 and the critical exponent n for each sample.

As an illustration, the results of these preliminary measurements associated with one of the selected samples are shown in Figure 3.3. The comprehensive dataset of individual trapped magnetic field mappings is available in Appendix A.2. Table 3.4 summarizes the value of the field measured 1 mm above the centre of the surface of the superconductor and the value of the critical exponent for the three selected samples. Note that a trapped field mapping measurement is also conducted above the bottom surface of the selected samples. A comprehensive table also presenting the results for the non-selected samples is provided in Appendix A.2.

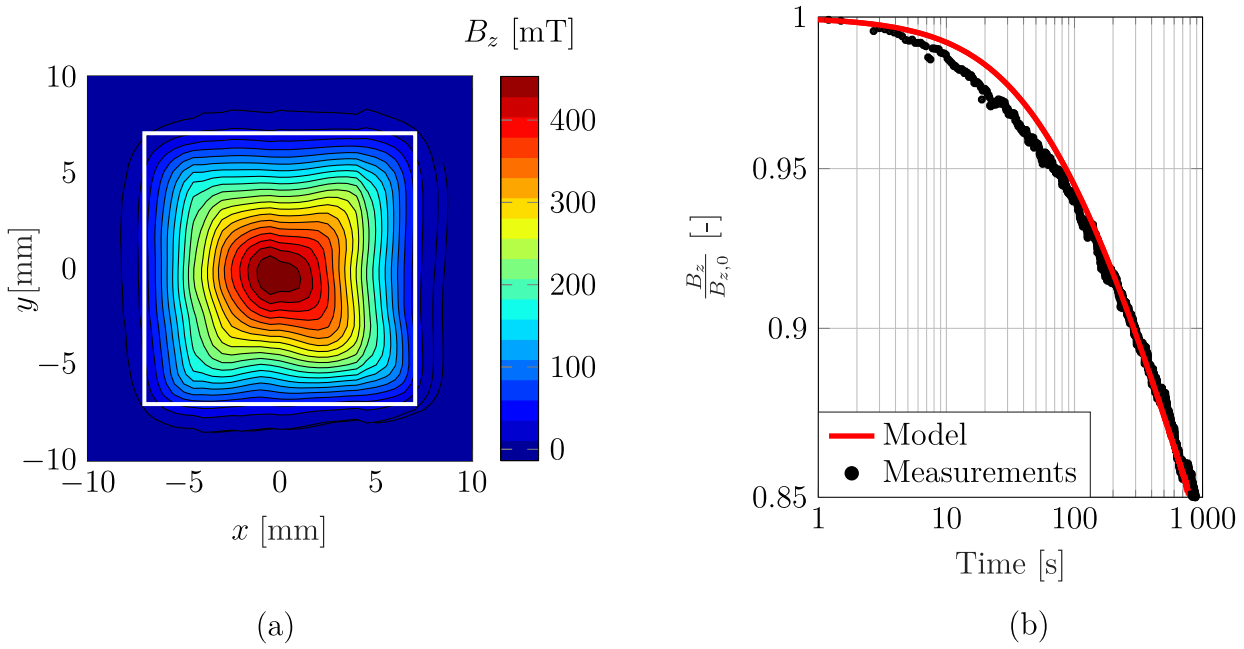

Figure 3.3: (a) Distribution of the z-component of the trapped magnetic flux density measured at 77 K, 1 mm above the top surface of sample 1218. The white line depicts the border of the superconductor. (b) Comparison between the measured relaxation of the trapped magnetic flux density of sample 1218 at 77 K and the Zeldov model. The parameters for the model are $B_{z,0} = 574$ mT, $t_0 = 70$ s and $n = 16.5$.

As it may be noticed in Table 3.4, a specific position within the array is attributed to each

Serial number	Sample position	Trapped field 1 mm above the top surface [mT]	Trapped field 1 mm above the bottom surface [mT]	Critical exponent [-]
1218	①	440	112	16.5
1219	②	466	145	19.1
1220	③	461	98	21.8

Table 3.4: Trapped field value and critical exponent at 77 K for the three selected samples. The top surface corresponds to the surface including the seed.

selected sample. The exact dimensions of the samples and the meaning of the position numbering within the array are presented in Table 3.5 and in Figure 3.4 respectively. It should be pointed out that in the assembled array, each bulk superconducting sample is magnetized parallel to its c-axis. Therefore, the c-axis of the sample ② is parallel to the z-direction while the c-axes of samples ① and ③ are respectively parallel and anti-parallel to the x-direction. Furthermore, the seed of sample ② is located on the side where the mapping is performed while the seeds of samples ① and ③ are located on the faces in contact with sample ②.

Serial number	Sample position	a_x [mm]	a_y [mm]	a_z [mm]
1218	①	15.2	14.1	14.1
1219	②	14.4	14.4	15.9
1220	③	14.3	14.3	14.5

Table 3.5: Dimensions of the superconductors involved in the superconducting Halbach array.

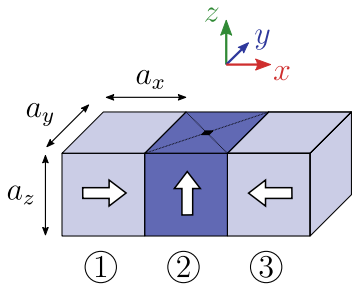

Figure 3.4: Position of the superconductors in the superconducting Halbach array.

3.2.2 Parameters of the analytical model

We now focus on the adjustment of the analytical model presented in section 1.4.2 with the characterization measurements conducted in the previous subsection. More specifically, the methodology employed for determining the value of J_c to be used in the model is discussed.

A striking observation that emerges for each sample when examining the trapped magnetic field measurements provided in Table 3.4 is the noticeable difference between the trapped magnetic fields measured above the two opposing surfaces of the superconductor. This observation can be explained by a progressively decreasing J_c away from the seed of the sample, as an inhomogeneous J_c is sometimes found for melt-textured (RE)BCO superconductors [192–194]. In the analytical model used in the context of the present chapter, a critical current varying along the c-axis is used together with equation (1.83) in order to reproduce the trapped flux density both above the top and bottom faces of the sample. More precisely, two different evolutions of the critical current density along the c-axis are investigated. The first corresponds to a linear variation of J_c between a value at the top surface and another value at the bottom surface. The second corresponds to a constant critical current density in the upper part of the superconductor followed by an abrupt drop to 0 at a given position along the c-axis. These two simplified (linear and step-like) $J_c(z)$ are considered for their simplicity. The parameters

of both models are adjusted for each sample to obtain the best agreement with experimental trapped-field data. As an illustration, the measured trapped field of sample ① is compared to both models in Figure 3.5.

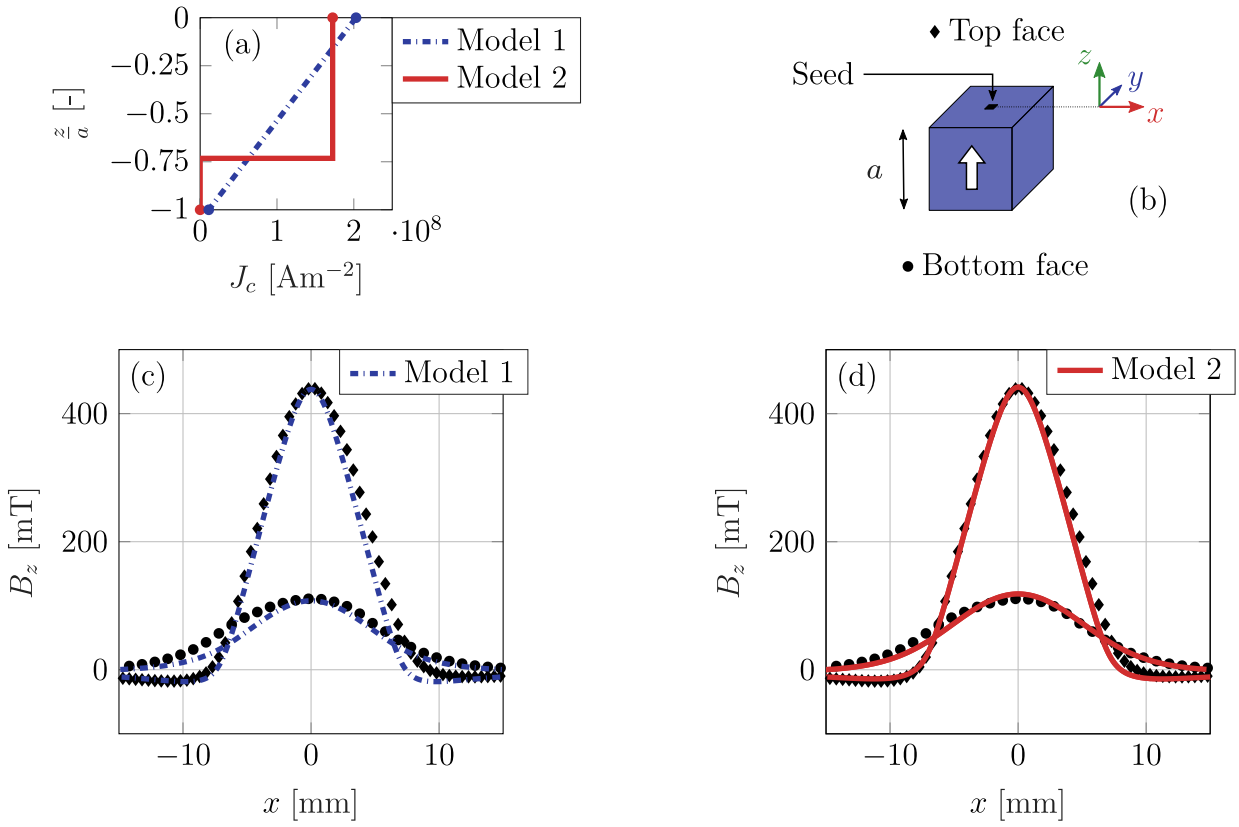

Figure 3.5: Comparison between the measured trapped field and the analytical model assuming the superconductor is in the critical state and exhibits a field-independent critical current density. Measurements are performed at 77 K, 1 mm away from the surface of sample 1218 both above the top and bottom surface. (a) Evolution of J_c along the c-axis considered in each analytical model. (b) Geometry and coordinate definition. (c) and (d) Comparison of the experimental data to an analytical model assuming a linear and a step-like $J_c(z)$ relation respectively.

Both simplified $J_c(z)$ dependences give results that are in excellent agreement with the measured trapped field distribution for a small computational effort. It should nevertheless be noted that trapped-field measurements are mainly sensitive to the current loops close to the surface above which the Hall probe mapping is performed. It is therefore impossible to determine which J_c distribution is the most appropriate using Hall probe mapping measurements only, since both $J_c(z)$ lead to very similar distributions.

In order to access an experimental parameter that can discriminate the particular J_c distributions shown in Figure 3.5 (a), the dipole magnetic moment of the sample is considered, which is proportional to the average value of J_c over the whole bulk superconductor. Using the bespoke flux extraction magnetometer, the volume dipole magnetic moment of each sample is measured 45 min after the end of the magnetization process. The measurements are presented in Table 3.6 together with the value computed analytically based on the two J_c distributions considered above.

Serial number	Sample position	Magnetic moment [A m^2]		
		Model 1	Model 2	Magnetometer measurements
1218	①	0.71	0.84	0.97
1219	②	0.85	1.02	1.19
1220	③	0.72	0.81	0.87

Table 3.6: Comparison between the measured magnetic moment of the cuboid bulk superconductors with the values computed analytically. Model 1 assumes a linear variation of J_c along the c-axis. Model 2 assumes a constant critical current density followed by an abrupt drop to 0 at a given position along the c-axis.

In Table 3.6 both models underestimate the magnetic moment of the sample in comparison to the measured value. This suggests that the J_c distributions represented in Figure 3.5 offer an oversimplified perspective of the actual situation and that a more elaborated distribution should be used. However, given the excellent agreement in terms of trapped flux distribution observed in Figure 3.5, it is decided to keep the analytical model as simple as possible and to use the model leading to the highest magnetic moment, i.e. Model 2. The value of the numerical parameters used for each superconductor is presented in Table 3.7 and schematically represented in Figure 3.6. Using these parameters, the maximum flux density trapped inside the superconductors is found to be equal to 1.2 T. This result supports that a field-cooling process under 1.2 T is enough to fully magnetize the bulk superconductors to be used in the Halbach array. Note that due to the non-homogeneous J_c distribution along the c-axis, the maximum magnetic flux density is not reached at the geometrical centre of the sample within this model.

Serial number	Sample position	J_c [A m^{-2}]	b [mm]
1218	①	1.7×10^8	4.5
1219	②	1.7×10^8	3.8
1220	③	1.8×10^8	5.4

Table 3.7: Numerical parameters used for modelling the individual trapped field with the analytical model.

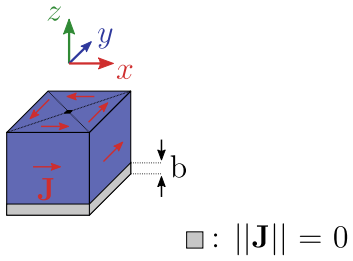

Figure 3.6: Schematic representation of the analytical model accounting for the critical current inhomogeneity along the c-axis.

3.2.3 Parameters of the finite element model

As it will become clearer in the next section, the primary objective of the finite element simulations carried out in this chapter is to achieve a qualitative comprehension of the phenomena occurring during the assembly process of the array rather than seeking a quantitative concordance with experimental results. In this context, further simplifying assumptions are introduced within this numerical model. First of all, it is assumed that all samples of the array are perfect cubes with a side of 14 mm and exhibit the same superconducting properties. Additionally, the critical

current is assumed to be isotropic, field-independent and homogeneous within the whole superconductor volume. The inhomogeneity of the critical current density along the c-axis pointed out in the previous section is thus completely ignored in the framework of the finite element simulations.

The critical exponent used in the simulation is fixed to $n = 20$ which is reasonably consistent with experimentally measured values, as detailed in Table 3.4. The value of the critical current density value is set to 2.3×10^8 A m^{-2}. This specific value is selected to ensure that the trapped field computed 1 mm above the superconductor surface, following a magnetic relaxation period of 45 min, aligns reasonably well with the values measured experimentally above the top surface of the sample as presented in Table 3.4.

Due to the 3-dimensional nature of the investigated problem and the requirement for re-meshing the entire domain at each time step during the modelling of the assembly process (as detailed in section 1.3.5), the process of mesh refinement increases dramatically the numerical cost of the simulations. In order to keep a reasonable computing time, the mesh size inside the superconducting region is around 1/24 the cube side ($\sim$ 0.5 mm).

3.3 Superconducting Halbach array

In this section, the three cuboid bulk superconductors characterized previously now combined in a linear Halbach array are investigated. Both numerical and experimental approaches are investigated and the main differences with Nd-Fe-B permanent magnets are highlighted.

3.3.1 Finite element modelling results

Using the numerical parameters derived in the previous section, the modelling procedure presented in section 1.3.6 is applied to compute the current density distribution within the three bulk superconductors during the assembly process of the Halbach array. Figure 3.7 compares the current density distributions before and after the assembly process of the array. This comparison is carried out in two different planes. Plane 1 (shown in red in Figure 3.7) includes the c-axis of the central sample and the centres of all the samples. Plane 2 (shown in green in Figure 3.7) is parallel to the contact surface between the samples and cuts the central sample at 0.1 mm from its edge.

As shown in Figure 3.7, the finite element simulation predicts a noteworthy alteration in the distribution of the current density within the samples during the assembly procedure. This reconfiguration is anticipated to occur exclusively within the vicinity of the interface between adjacent superconductors. In the simulation, this region is found to be only one finite-element thick, the actual thickness is therefore expected to be of the order of 0.5 mm. However, validating this thickness numerically would necessitate a more accurate matching of the individual superconducting and geometrical characteristics of each sample and a refinement of the mesh within the superconducting region. This would result in a drastic increase in the numerical cost of the simulation. An alternative approach for determining this thickness with the analytical model will thus be proposed in the next section.
From the results shown in Figure 3.7, a qualitative description of the current density distribution after the assembly process may be deduced. The results within the central sample are considered first. Before the assembly, the current distribution in this sample is close to the distribution expected for the critical state, i.e. a uniform current density for which Plane 1 is

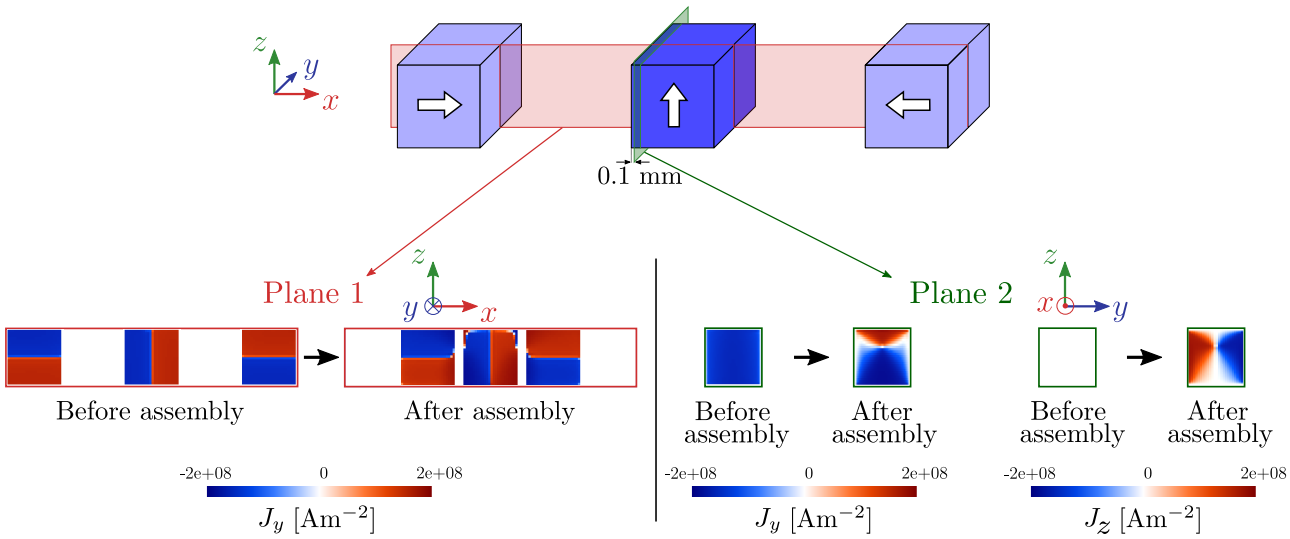

Figure 3.7: Comparison of the y and z-components of the current density distribution before and after the assembly of the superconducting Halbach array computed by the finite element model. The white arrows represent schematically the main direction of the trapped flux density in each sample. A field-independent critical current density of 2.3×10^8 A m^{-2} is considered in this simulation.

symmetrically shared with positive and negative values. Note that the magnitude of the current density ($\sim 2 \times 10^8$ A m^{-2}) is lower than the critical current density used in the simulations (2.3×10^8 A m^{-2}) because of the flux creep delay between the end of the magnetization and the beginning of the assembly procedure.

The situation changes significantly when the samples are brought into close proximity, particularly in regions adjacent to the neighbouring superconducting samples. As appears from the results in Plane 2, the supercurrents close to the sample borders flow in loops that are perpendicular to the x-axis after the assembly of the array, i.e. perpendicular to the direction of magnetization in the two adjacent samples. The z-component of the magnetic flux density generated by these regions above the centre of the array is thus smaller than before assembling the configuration. In addition, these modified current loops are found to oppose the field generated by the closest neighbouring sample. This redistribution has two consequences: (i) a reduction in the contribution of the central sample to the magnetic flux density above the centre of the array, and (ii) the emergence of a new negative contribution to the magnetic flux density produced at this specific location.

Figure 3.7 also shows that the current distribution in the peripheral samples is much less affected than the current in the central sample during the assembly process. The current loops in these samples are found to remain mostly perpendicular to the x-axis and are close to their initial distribution. This much smaller impact on the current distribution of the two peripheral samples may be understood considering that besides its own trapped field, the only significant field contribution experienced by a peripheral sample during the assembly process corresponds to the return field lines associated with the trapped field of the central sample. From the results obtained in equations (1.86) and (1.87), this contribution is expected to be approximately 6

times smaller than the trapped field of the central sample, regardless of the particular value of the critical current density. The situation is completely different for the central sample. This sample is aligned with the c-axis of the peripheral samples and is thus subjected, at the end of the assembly process, to a maximum field amplitude equal to the trapped field at the centre of their top surfaces.

3.3.2 Experimental results

A superconducting linear Halbach array is now experimentally assembled and measured with the samples characterized in the previous section. The distribution of the z-component of the magnetic flux density measured at 77 K, 1 mm above the top surface of the central sample is presented in Figure 3.8 (b). The initial model used for comparing measurements of the flux distribution above the array assumes that the behaviour of magnetized bulk superconductors is analogous to that of permanent magnets during the assembly of the array. This implies that the distribution of current density within each superconductor is presumed to remain unchanged even after the superconductors have been brought into close proximity. Figure 3.8 (c) presents a comparison between the measured magnetic flux density and the sum of the individual contribution of each sample computed with the analytical model. Note that the model incorporates the inhomogeneous distribution of J_c within each sample.

In the region above the peripheral samples ($x < -7$ mm and $x > 7$ mm in Figure 3.8 (c)), the analytical predictions match experimental data satisfactorily. However, the model assuming no alteration of the individual magnetization significantly overestimates the maximum flux density generated above the centre of the superconducting Halbach array. The maximum field strength measured experimentally is 471 mT, merely 5 mT higher than the trapped field of sample ② only. The contribution of samples ① and ③ to the magnetic flux density generated above the centre of the array thus appears to be rather small, unlike the Halbach array made of Nd-Fe-B permanent magnets. In contrast, the analytical model, which presumes no alteration in the current density within the central sample, predicts a field of 530 mT, i.e. 13% higher. This observed disagreement between measurements and analytical predictions suggests that the current density in the superconductors is altered during the assembly process, which is consistent with the results obtained with the finite element model.

In order to improve the agreement with the experimental magnetic flux distribution, the current density distribution presumed within the analytical model is modified. Based on the qualitative observations performed with the finite element model, it is assumed that the interactions between the samples result in a current redistribution occurring in two zones of equal thickness e on both sides of the superconductor located at the centre of the array. This is schematically represented in Figure 3.9 (a). Within these zones, the current is assumed to flow in loops perpendicular to the x-direction in such a way that it opposes the contribution of the closest neighbouring sample. The current density there is also assumed to be field-independent and anisotropic, i.e. the current density parallel to the z-direction (aligned with the c-axis of the central sample) is assumed to be three times smaller [195] than the value of the central superconductor (sample ②) given in Table 3.7. As explained in [196], accounting for the critical current anisotropy results in a more complex current distribution in these zones as depicted schematically by the yellow arrows in Figure 3.9 (a). In order to grasp the impact of this alteration on the magnetic flux density distribution generated above the Halbach array, the modified model is employed

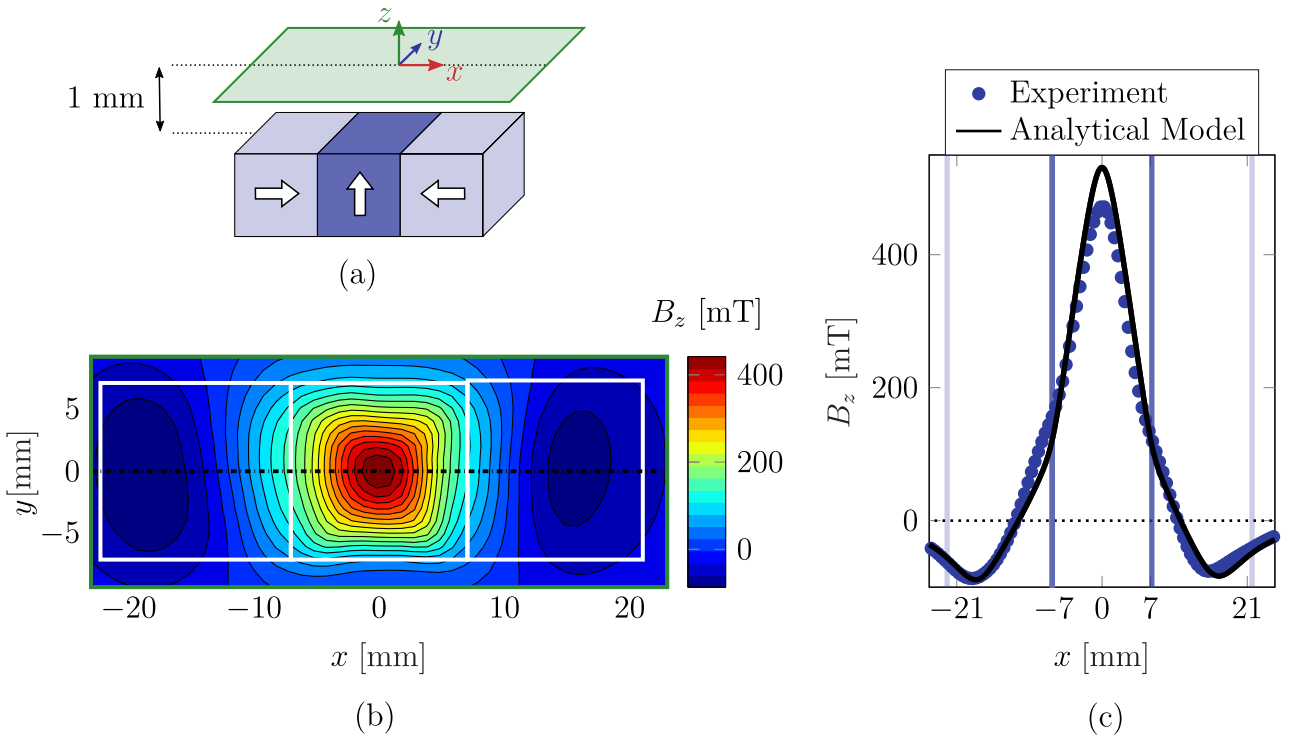

Figure 3.8: (a) Schematic representation of the position of the mapping plane with respect to the superconducting Halbach array made of three bulk superconductors. (b) Contour plot of the z-component of the magnetic flux density measured at 77 K, 1 mm above the top surface of the central sample. The white lines depict the border of the samples. (c) Mapping results along a centred line parallel to the x-direction. The blue vertical lines are located at the border of the samples. The experimental data are compared to an analytical model assuming a simple vector summation of the flux densities generated by each superconductor in the array and no alteration of the individual magnetization.

to compute the magnetic flux density profile along a line parallel to the x-direction for several values of the thickness e. The results of these calculations are presented in Figure 3.9 (b).

Based on the results obtained in Figure 3.9 (b) for the range $x <$ -7 mm and $x >$ 7 mm (i.e. above the peripheral samples), it can be observed that for values of e ranging from 0 to 2 mm, the magnetic flux density distribution over the peripheral superconductors is only weakly affected by the modification of the current distribution envisaged. However, focusing on the value of the field generated above the centre of the array, it can be noticed that increasing the thickness e of the zones where the current distribution is altered results in a reduction of the magnitude of this specific field. As a result, the value of the thickness parameter e can be adjusted so that the predictions of the modified analytical model above the central sample align with experimental data without altering the concordance above the peripheral samples already observed in Figure 3.8 (c). After adjusting this parameter, it is found that the value $e = 0.8$ mm leads to a satisfying agreement with experimental measurements. This concordance is illustrated in Figure 3.10 along three distinct lines parallel to the x-direction.

In practice, the current density distribution is likely to be more elaborated than the simplified

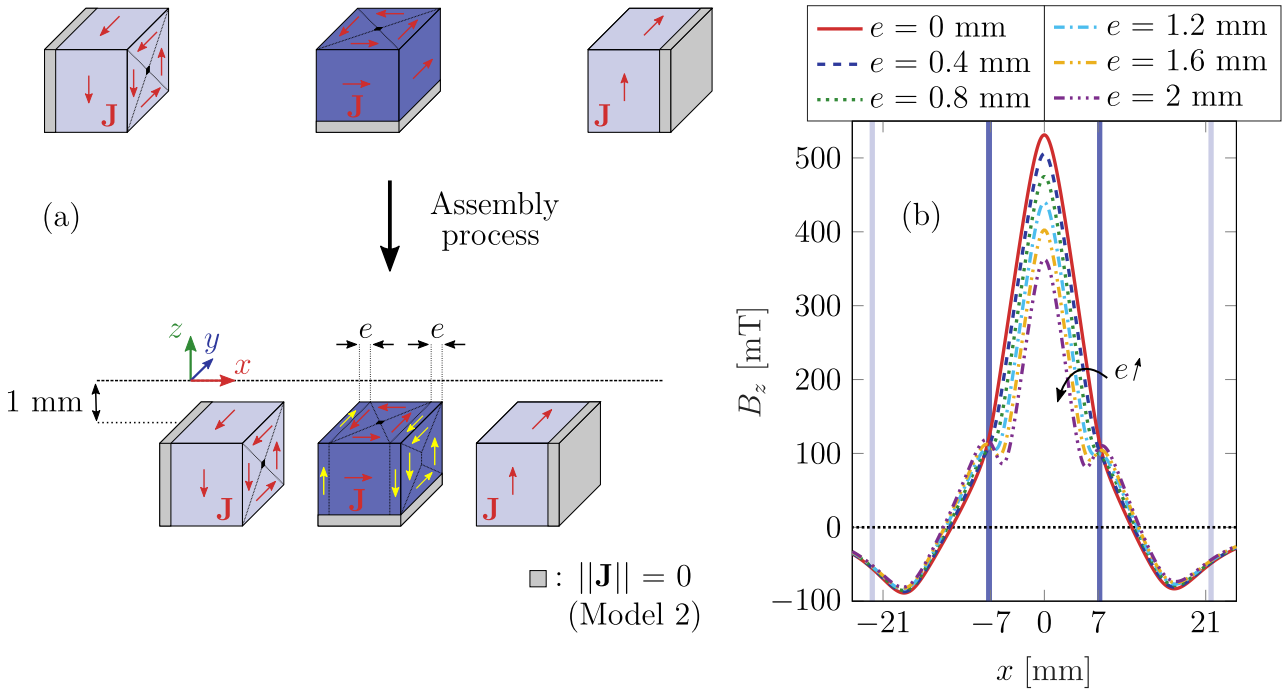

Figure 3.9: (a) Schematic representation of the analytical model of a superconducting Halbach array accounting for the interactions between the samples. The red arrows show the current distribution in the samples before assembling the array while the yellow arrows show the modifications induced by the interaction during the assembly process. (b) Distribution of the z-component of the magnetic flux density generated 1 mm above the top surface of the central sample of the superconducting Halbach array computed by the analytical model for several values of the thickness e along the line x. The model assumes that during the assembly of the configuration, the current distribution in the central sample is altered over two zones of equal thickness e.

picture shown in Figure 3.9 (a). Nevertheless, this simplified approach allows the determination of the thickness e effortlessly and is able to capture effectively the main features of the actual magnetic flux density generated by a superconducting Halbach array as pointed out in Figure 3.10. With such agreement with experimental measurements, the adjusted modified analytical model can be employed to evaluate the magnetic flux density gradient generated with the superconducting Halbach array within a x-z plane including the centres of the samples. The results are presented in Figure 3.11 (a). For comparison purposes, the yellow dashed line in that figure delimits the zone where the gradient produced by the sample ② only (before the current alteration) is higher than 1 T m^{-1}. The computed gradient along a line parallel to the x-direction located at a distance of 20 mm from the top surface of the sample ② (i.e. $z = 35.9$ mm) is extracted from this plane and presented in Figure 3.11 (b).
From the results plotted in Figure 3.11 (a), a similar observation to the one conducted for Halbach arrays composed of permanent magnets can be performed: the spatial region within which the gradient generated by a superconducting Halbach array surpasses 1 T m^{-1} extends beyond that associated with the central sample only. This observation is promising as it underscores that despite the current alteration occurring within the central sample, assembling magnetized superconductors in a Halbach array remains a convincing prospect for extending the range of the magnetic flux density gradient produced. Figure 3.11 (b) shows that, at a distance of

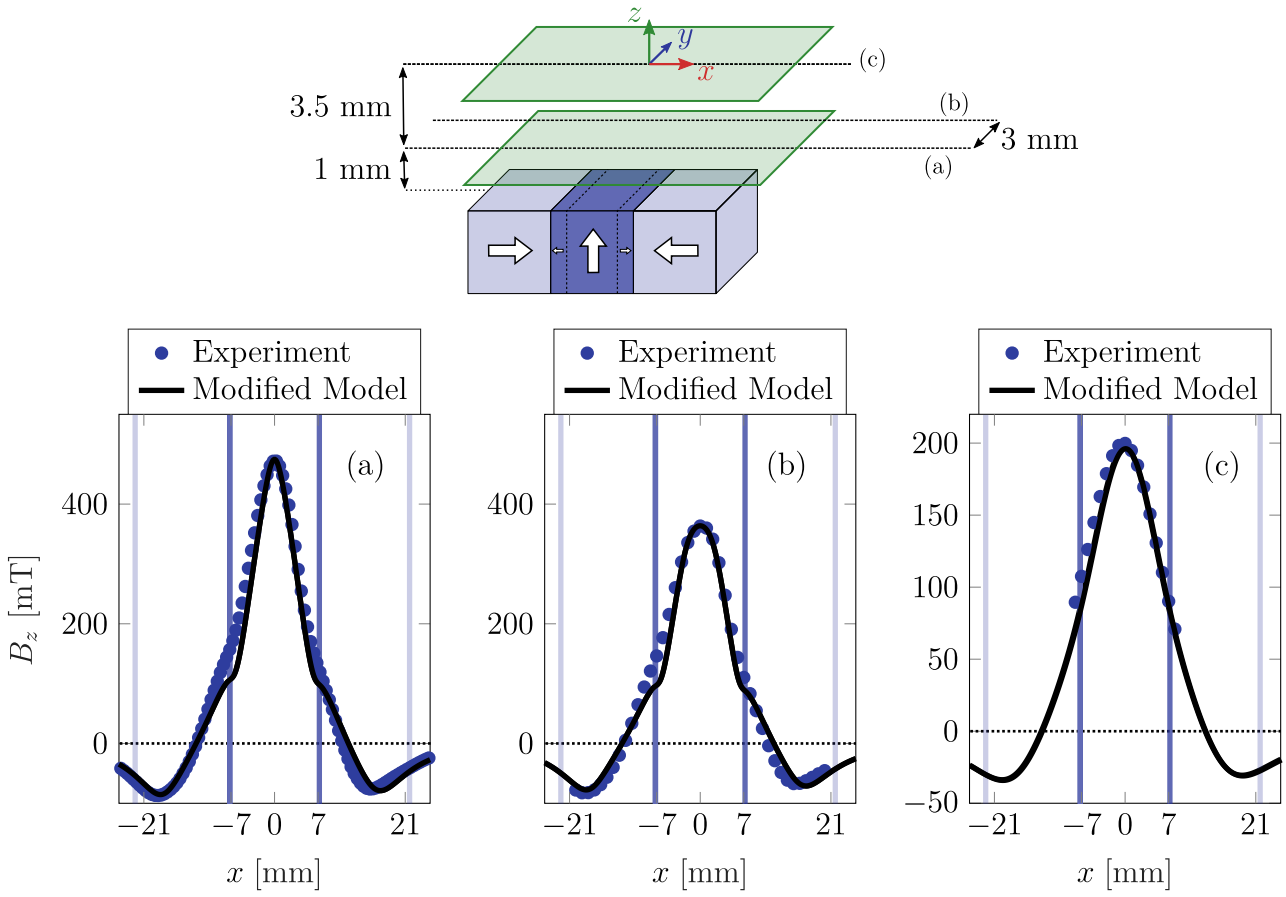

Figure 3.10: Measured distribution of the z-component of the magnetic flux density of a superconducting Halbach array along three distinct lines parallel to the x-direction at 77 K. The results are compared to the predictions of an analytical model computing the vector summation of the flux densities generated by each superconductor in the array. The model assumes that the current distribution in the central sample is altered over two zones of equal thickness $e = 0.8$ mm as represented schematically in Figure 3.9 (a).

20 mm, the maximum magnetic flux density gradient generated by sample ② only is equal to 1.4 T m^{-1} while this value increases to 1.8 T m^{-1} when considering a complete Halbach with a model accounting for the current density modification occurring during the assembly process. This 29 % increase also highlights the benefits of combining magnetized superconductors in such a configuration. However, when employing an analytical model that assumes no modification in current density during the assembly process, the maximum magnetic flux density gradient calculated 20 mm above the centre of the array reaches 2.1 T m^{-1}. Therefore, it can be deduced that the maximum potential of superconducting Halbach arrays made of three magnetized superconductors is not achieved since preventing the occurrence of the re-organization of current density would result in a further increase in the gradient generated at a distance of 20 mm from the assembly corresponding to 21% of the value obtained for a single superconductor.

Comparing the estimated performances of a Halbach array made of three Nd-Fe-B permanent magnets shown in Figure 3.2 (b) and made of three bulk superconductors presented in Figure 3.11 (b), it appears that the magnetic flux density gradient achieved with the supercon-

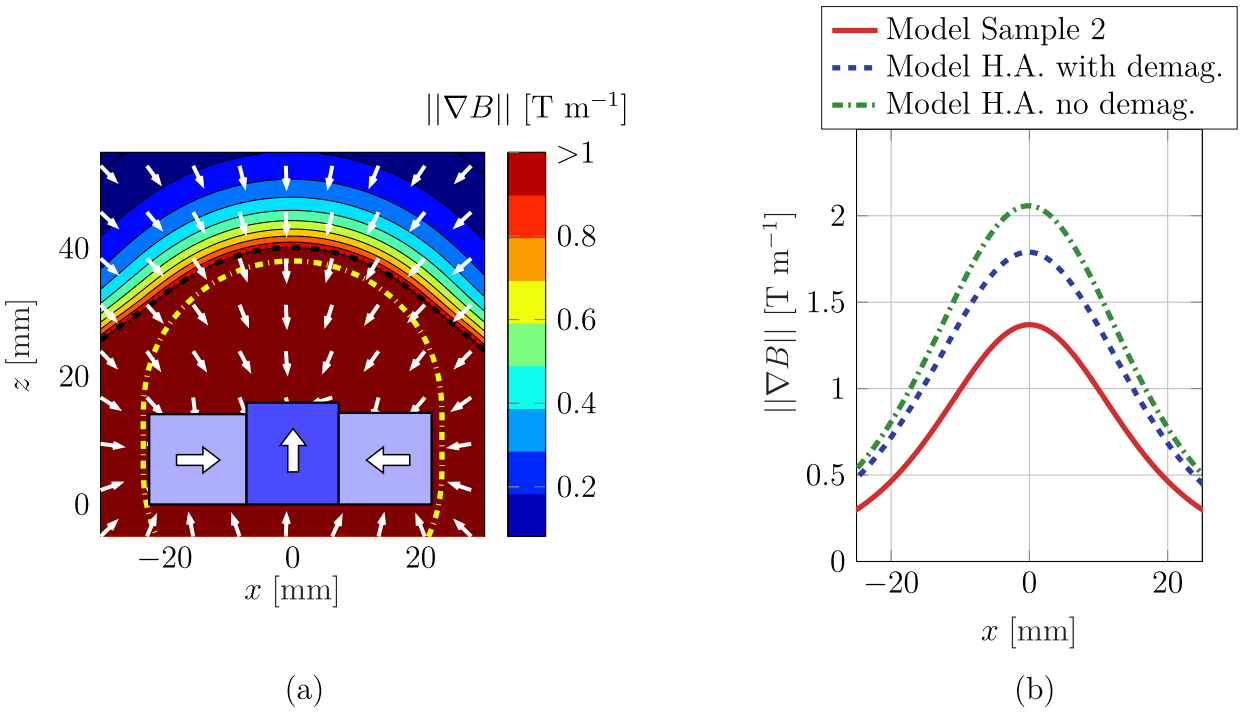

Figure 3.11: Results obtained with the modified analytical model computing the vector summation of the flux densities generated by each superconductor in the array. The model assumes that the current density distribution in the central sample is altered over two zones of equal thickness $e = 0.8$ mm as represented schematically in Figure 3.9 (a). (a) Contour plot of the amplitude of the magnetic flux density gradient generated by the superconducting Halbach array within a x-z plane encompassing the centres of the samples. The small white arrows show the direction of the gradient, and the yellow dashed line delimits the spatial region where the gradient produced by the central sample only (before the current alteration) is higher than 1 T m^{-1}. (b) Comparison of the magnetic flux density gradient along a line parallel to the x-direction at a distance of 20 mm from the top surface of the central sample computed for: (i) the central sample only; (ii) the complete array computed with the model accounting for the current density alteration; (iii) the complete array computed with the model ignoring the current density modification.

ducting Halbach array is approximately three times smaller. Nevertheless, the performances of the permanent magnets are constrained by the saturation magnetization of the material and consequently, the gradient achievable with them could not be increased further. The situation is completely different when considering magnetized superconductors since their individual trapped field can be enhanced either through a decrease in the operating temperature or by increasing their geometrical size. To illustrate this, two simplified approximations are conducted.
First the temperature below which it should become advantageous to employ the measured superconducting Halbach array instead of that made of permanent magnets is estimated. For simplicity, it is considered in this rough estimation that the critical current density of the superconductors depends linearly on temperature. Within the hypotheses of the analytical model employed throughout this chapter, the magnetic flux density gradient is directly proportional to J_c and is therefore assumed to vary linearly with temperature as well. As a result, considering that the critical temperature of $YBa_2Cu_3O_{7-x}$ bulk superconductors is approximately 92 K and that at 77 K the superconducting Halbach array produces a field gradient of 2.1 T m^{-1} at a

distance of 20 mm, the measured permanent magnet assembly is expected to be outperformed as soon as the operating temperature is decreased below 50 K.

Second, the required geometric dimensions of superconducting samples necessary to produce a magnetic gradient similar to that observed with the permanent magnet assembly when operating the superconducting Halbach array at 77 K is approximated. In order to do so, the same critical current density values as the one presented in Table 3.7 are used and all the geometrical dimensions presented in Table 3.5 are progressively increased while keeping the aspect ratio unchanged. The analytical model assuming no current density alteration during the assembly process is then applied to compute the maximum magnetic flux density gradient generated at a distance of 20 mm from the array. It is finally assumed that the actual gradient generated is 14% smaller than the computed value because of current density alteration occurring during the assembly process. Following this procedure, it can be computed that a 25% increase in the geometric dimensions of the superconducting samples is sufficient to equal the performances of permanent magnets. Having cubic samples of such dimensions (i.e. $\sim$19 mm in side) is perfectly realistic since the dimensions of bulk $YBa_2Cu_3O_{7-x}$ samples can routinely reach 25 mm to 35 mm [110].

The primary challenge that remains consists in managing the repulsive forces arising between the superconductors, which scale with the square of the trapped field strength of individual magnets. Since the repulsive forces develop in a direction perpendicular to the axis of the array, it is to be noted that the main task is not really to reduce the distance between the magnetized superconducting samples, but to do so in such a way they are kept aligned with each other. Provided that these repulsive forces can be effectively addressed, the approximate analysis conducted above highlights that the gradient of magnetic flux density generated with a linear superconducting Halbach array can rapidly surpass the capabilities offered by permanent magnets.

3.4 Summary

In this chapter, the magnetic flux density distribution and gradient generated by a Halbach array comprised of three Nd-Fe-B permanent magnets was first investigated experimentally. As expected for permanent magnets, it was shown that this field distribution can be seen as the sum of the individual contributions of each sample involved within the array and that these individual contributions can be determined through characterization measurements conducted before assembling the array. When compared to the performance of a single permanent magnet, it was also pointed out that assembling permanent magnets in a Halbach array results in (i) an increase in the spatial extent of the magnetic flux density gradient generated and (ii) an increase of almost 100% in the gradient generated at a distance of 20 mm from the configuration.

After that, a set of characterization measurements were carried out on 9 cuboids $YBa_2Cu_3O_{7-x}$ bulk superconductors with a side length between 14 mm and 16 mm. The measurements highlighted that these samples are characterized by an inhomogeneous distribution of the critical current density along the crystallographic c-axis. The numerical parameters of the analytical model outlined in section 1.4.2 were adjusted and successfully reproduced the measurements.

Then, the experimental system described in section 2.2 was used to successfully assemble and measure a linear superconducting Halbach array of three $YBa_2Cu_3O_{7-x}$ bulk superconductors. Both finite element simulations and analytical calculations were compared to the measurements of the magnetic flux density distribution above the array of trapped-field magnets. Similarly to the behaviour of permanent magnets, it was shown that in comparison to the performances of a single trapped-field magnet, this assembly of magnetized superconductors leads to (i) an increase in the spatial extent of the magnetic flux density gradient and (ii) an increase of 29% in the gradient generated at a distance of 20 mm from the configuration. Although this relative increase is smaller than that observed with permanent magnets, it was shown numerically that the superconducting assembly can rapidly outperform the permanent magnets through a decrease in the operating temperature or by increasing the geometrical size of the samples.

A detailed examination of the experimental and numerical results showed that the peripheral superconducting samples within the array can be assumed to remain in the critical state despite the close vicinity of the central superconductor. However, the approach of the peripheral samples towards the central sample during the assembly procedure disturbs the current density distribution in the central superconductor. This alteration of the current distribution results in a reduction of the maximum magnetic flux density generated above the centre of the array, ultimately limiting the performances. Preventing the occurrence of the re-organization of current density is expected to lead to a further increase in the gradient generated at a distance of 20 mm from the assembly corresponding to 21% of the value obtained for a single superconductor.

When considering the assembly process of a linear superconducting Halbach array made of five samples, as illustrated in Figure 2.4, a similar alteration of the current density distribution is anticipated to take place within the outermost samples as well. In that context, rather than including additional magnetized samples in the Halbach arrangement, it is decided to focus the research efforts in this thesis towards the development of methods allowing the reduction of the impact of such current reorganization. This specific aspect is the focus of the next chapter.

4 Overcome the demagnetization of superconducting Halbach array

As explained in the previous chapter, magnetized bulk superconductors are promising alternatives to replace permanent magnets within Halbach arrays. The targeted applications are those that require a substantial gradient in magnetic flux density across a range of several centimetres. It was shown that the assembly procedure of such a superconducting system plays a crucial role, re-organization of the current loops occurs in the magnetized samples during the assembly process. A similar re-organization of current loops has been reported in "crossed-field" experiments [133, 172–178]. In these "crossed-field" studies, a magnetized superconductor is subjected to a time-varying external magnetic field perpendicular to its main axis of magnetization, which is analogous to the conditions encountered when assembling a linear superconducting Halbach array. The reorganization of the current loops during the assembly was shown to result in a diminution of the gradient generated by the final assembly. In this context, the present chapter is devoted to the proposal and the investigation of three different approaches to mitigate the detrimental impact of these current alterations on the performances of superconducting Halbach arrays.

First, the substitution of bulk superconductors with stacks of superconducting coated conductors is considered. Such "quasi-bulks" made of stacked tapes exhibit trapped-field performance comparable to bulk superconductors [53, 197, 198] and are known to be less affected by crossed-field demagnetization [173, 199–202]. Similarly to bulk superconductors, these stacked-tape samples are not constrained by any saturation magnetization. The field generated by a Halbach array made of superconducting stacked tapes, therefore, is expected to increase through the reduction of the operating temperature or the use of larger samples. Unlike bulk superconductors, however, the induced supercurrents in stacked tapes cannot flow along a direction perpendicular to the stack. The primary objective of the initial approach is to take advantage of this anisotropy to hinder the development of current loops that arise when the two adjacent superconductors approach each other, as illustrated by the yellow arrows in Figure 3.9 (a).

Next, considering that the predominant current alteration occurs within the central superconductor and is initiated by the trapped field of the peripheral samples, the second approach aims at reducing the magnetic flux density produced by the peripheral samples on the side surface of the central superconductor. To this end, the impact of the geometrical shape and of the position of the peripheral samples along the z-direction are investigated.

In the third and last approach, an additional superconductor placed above the central one is used. This additional superconductor is magnetized simultaneously with the central one and removed after the assembly process. The removal of the additional superconductor generates a time-varying field applied on the central superconductor to re-magnetize it.

4.1 Superconducting Halbach array made of stacks of coated conductors

In this section, the combination of three superconducting stacked-tape samples in a Halbach array configuration is considered. The numbering of the samples as a function of their position within the array as well as the orientation of the tapes within each stack is schematically represented in Figure 4.1. When the central sample consists of superconducting tapes stacked along the z direction, current loops cannot form in the y-z plane.

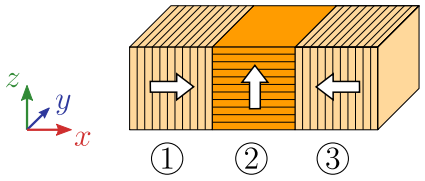

Figure 4.1: Schematic representation of a superconducting Halbach array made of three stacked-tape samples.

The methodology employed to assess the efficiency of this superconducting configuration closely mirrors the approach followed in the previous chapter. First, characterization measurements performed on individual stacked-tape samples are used to adjust numerical parameters. Next, the assembled configuration is investigated both numerically and experimentally. Finally, the spatial distribution of the generated magnetic flux density gradient is predicted and analyzed.

4.1.1 Characterization of individual superconductors

The trapped field of each sample is evaluated through a Hall probe mapping measurement conducted at 77 K, 1.5 mm above the top surface of the superconductor. For these experiments, the samples are magnetized in a direction perpendicular to the tapes with a field-cooling process starting from 1.2 T, a field removal rate of 1 mT s^{-1} and a 45 min period of magnetic relaxation. Since all the tapes within the sack initially originate from the same wire, the engineering critical current density is expected to be homogeneous within the whole sample. To verify this, an additional Hall probe mapping is carried out 1.5 mm above the bottom surface of one of the stacked-tape samples (sample ②). In all the performed mapping, the central trapped field is consistently found to be equal to 200 mT ± 2 mT. The time evolution of the trapped field during the magnetic relaxation period is also measured and confronted to equation (1.9) to derive the critical exponent value which is found to fall consistently between 21 and 24. A more comprehensive presentation of these characterization measurements can be found in Appendix A.3.

Parameters of the analytical model

The analytical model based on Biot-Savart's law is used to compute the magnetic flux density generated by a magnetized superconducting stack of tapes. In this context, the model assimilates the sample to a homogeneous material characterized by a constant and field-independent engineering critical current density J_e and ignores the layered structure of the stack. The value of the current density used within the model is adjusted to reproduce as closely as possible the trapped-field measurements, this procedure leads to $J_e = 1.3 \times 10^8$ A m^{-2}. For illustration, the

measured distribution of the magnetic flux density along a central line parallel to the x-direction, 1.5 mm above the sample surface is compared to analytical calculations in Figure 4.2 (c).

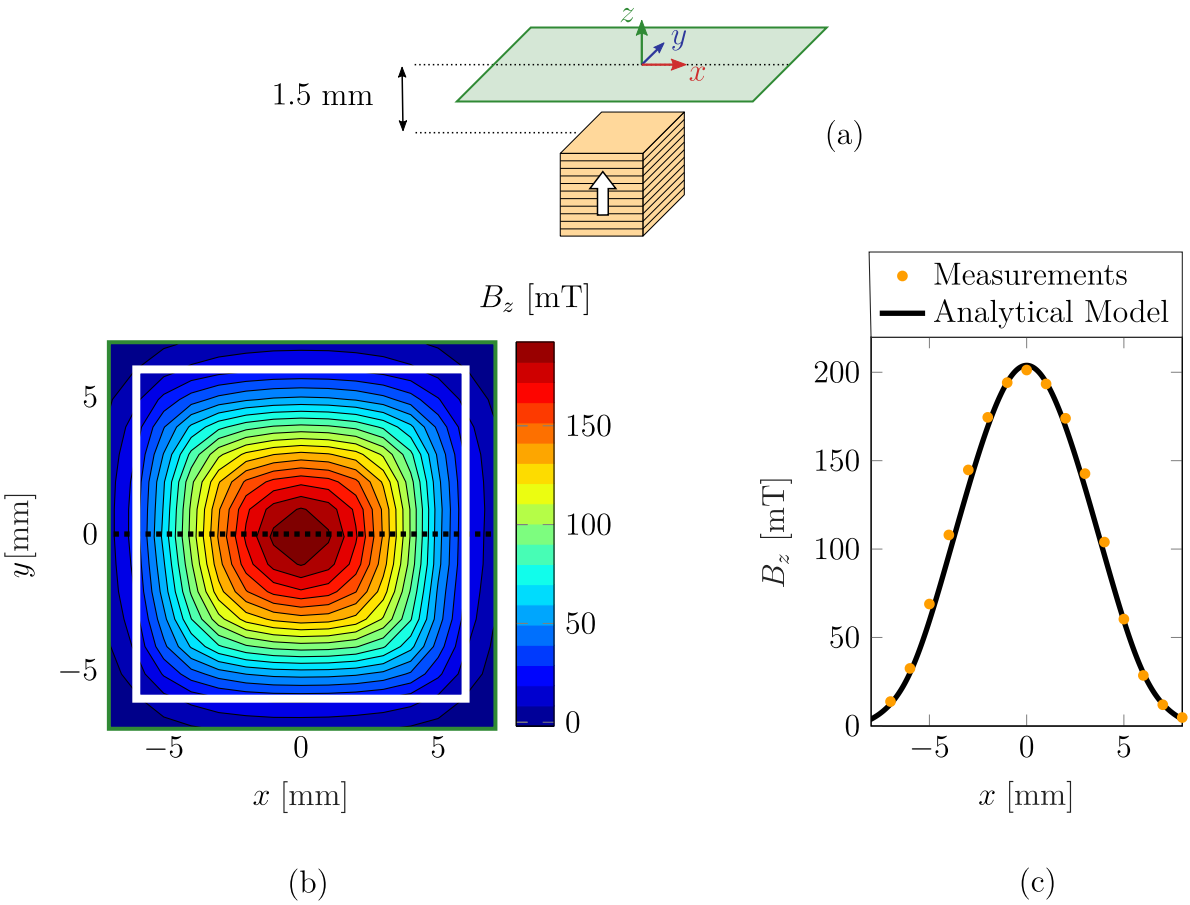

Figure 4.2: (a) Schematic representation of the Hall probe mapping performed. (b) Contour plot of the magnetic flux density measured at 77 K, 1.5 mm above the surface of the stacked tapes 1. The white line depicts the border of the sample. (c) Comparison of the measured distribution of the magnetic flux density to the analytical calculations along a central line parallel to the x-direction. The model considers a homogeneous superconducting sample in the critical state characterized by an engineering critical current density $J_e = 1.3 \times 10^8$ A m^{-2}.

Despite the simplifying assumptions of the model employed, the excellent agreement observed in Figure 4.2 (c) gives confidence in the ability of the model to predict effectively the field distribution produced by a magnetized stack of superconducting tapes.

Side note concerning the value of J_e: According to the manufacturer specifications, the tapes used should exhibit a critical current $I_c \sim 240$ A, measured in self-field. Based on this critical current, considering that there are 120 tapes within the stack and that the total height is 12.6 mm, one may expect an engineering critical current density of $\sim 1.9 \times 10^8$ A m^{-2}. The value deduced experimentally (1.3×10^8 A m^{-2}) appears notably lower than this estimate, which may be attributed to two primary factors. First, considering an $I_c(B)$ dependence one might indeed expect the engineering current of the fully magnetized stack to be smaller than the value deduced from individual tape samples [203–205]. Second, the J_e value deduced experimentally

refers to the amplitude of currents after a waiting time of approximately 45 min following the magnetization process. This results in a further decrease of the current density.

Finite element model parameters

In the context of the finite element simulations, the superconducting samples are assumed to be perfect cubes with a side of 12 mm. For consistency with the simulations performed in the previous chapter, the critical exponent is set to $n = 20$ which remains reasonably consistent with the value derived experimentally for stacked tapes. Concerning the value of the engineering critical current density, it is assumed to be field-independent and homogeneous within the whole stacked tapes. The value of J_e is fixed to 1.7×10^8 A m^{-2} so that the trapped field computed at the end of the 45 min magnetic relaxation period following the magnetization process matches the measurements. The strong anisotropic behaviour of the stacked-tape samples is taken into account in the model in a simplified manner: a linear resistive term is introduced in the power law employed. The electric constitutive law used for modelling stacked tapes writes:

$$\mathbf{E} = \left[\frac{E_c}{J_e} \left(\frac{||\mathbf{J}||}{J_e} \right)^{n-1} \mathbb{1} + \mathrm{diag}(\rho_1, \rho_2, \rho_3) \right] \mathbf{J}, \tag{4.1}$$

where ρ_i is set to 10^{-8} Ω m in the direction perpendicular to the tapes, and to 0 in the other directions. Note that with the parameters used in the simulations, $\frac{E_c}{J_e} \simeq 6 \times 10^{-11}$ Ω m, i.e. approximately three orders of magnitude smaller than the resistivity value added in the direction perpendicular to the tapes. The mesh size within the superconducting region is around 1/12 of the cube side ($\sim$1 mm).

4.1.2 Finite element modelling results

The assembly process of magnetized superconducting stacked tapes in a Halbach array is modelled using the finite element model and the anisotropic electric constitutive law presented in the previous section. The computed distribution of the current density in each stacked-tape sample predicted by the finite element model before and after the assembly process are presented in Figure 4.3. For conciseness, the comparison is only examined in two cut planes. The first one (shown in blue in Figure 4.3) is the Oxz plane, where the origin O corresponds to the centre of the central superconductor. The second (shown in green in Figure 4.3) is parallel to the y and z-directions and cuts the central superconductor at 0.1 mm from its edge.

Before the assembly process, the supercurrents J_y crossing the Oxz plane (Plane 1 in Figure 4.3) are almost uniform with positive and negative signs for each half of the cross-section, as can be expected for three fully magnetized superconductors. The magnitude of the current density ($\sim 1.3 \times 10^8$ A m^{-2}) is lower than the J_e of the stacked-tape samples ($\sim 1.7 \times 10^8$ A m^{-2}) because of the flux creep occurring during the 45 min delay between the end of the magnetization and the beginning of the assembly. Similarly, the supercurrents along the left face of the central superconductor (Plane 2 in Figure 4.3) are uniform as can be expected for square supercurrent loops. As can be noticed in Figure 4.3, however, a current density re-organization occurs in the central stack during the assembly process despite the strong anisotropy of the stacked tapes. Figure 4.4 (b) shows a simplified representation of the current loops induced in stacked superconducting tapes during the assembly procedure. This representation is compared to that observed in bulk superconductors (Figure 4.4 (a)). Two features characteristic of the stacked tapes appear:

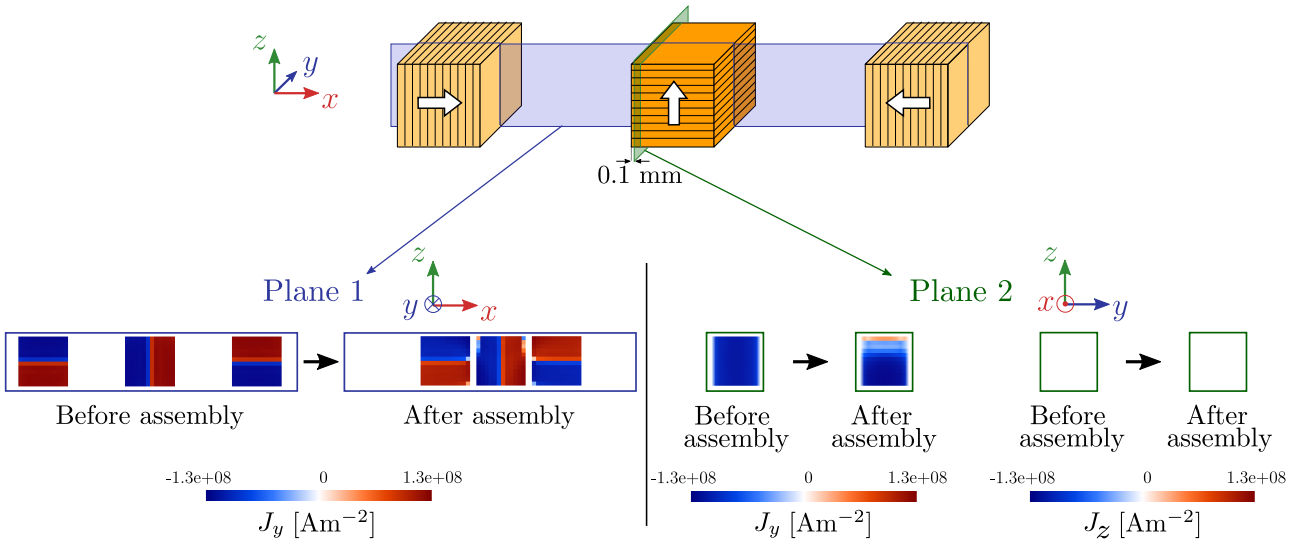

Figure 4.3: Comparison of the distribution of the y and z-components of the current density before and after the assembly of the Halbach array made of stacked tapes, as computed by the finite element model. The white arrows represent schematically the main direction of the trapped flux density in each sample. A field-independent critical current density of 1.7×10^8 A m^{-2} is considered in this simulation.

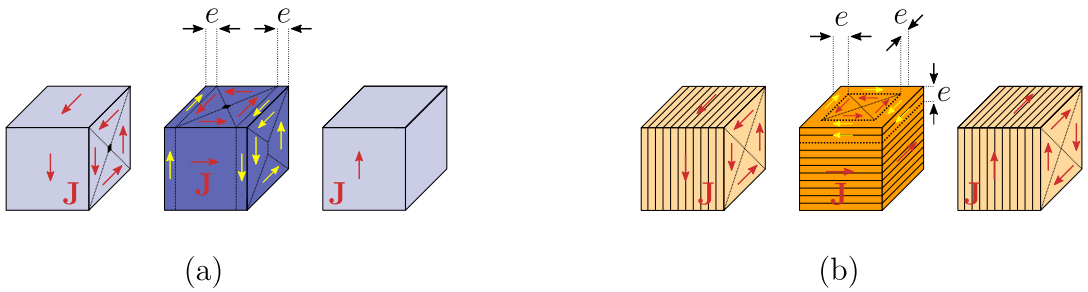

Figure 4.4: Schematic comparison of the modification of the current density after the assembly process for (a) bulk samples and (b) stacked tapes, as deduced from the finite element modelling results shown in Figure 4.3.

- Due to the layered structure, the supercurrents in the central sample continue to flow in loops perpendicular to the z-direction even after the assembly process. Although the main magnetization direction of the peripheral samples is parallel to the x-direction, the magnetic flux density produced by the peripheral samples on the lateral surface of the central sample exhibits a non-zero z-component, as shown with further details below. The current reorganization observed in the central sample (illustrated by the yellow arrows in Figure 4.4 (b)) is thus most likely induced by this particular field component of the peripheral stacks. The z-component increases as the peripheral samples are brought closer.
- The current density is mostly altered in a region close to the top face of the central sample. This result makes sense given that this region corresponds to the location where the z-component of the trapped field of the peripheral samples is positive and is the highest, as can be observed in Figure 4.5.

Given that the current alteration during the assembly process is initiated by the magnetic field produced by the peripheral samples on the side surface of the central superconductor, it is of interest to examine the distribution of the 3 components of this field as they are predicted by the analytical model. The field generated by the left superconductor only is computed within a plane corresponding to the contact surface between the left and central superconductors. The results of this calculation are shown in Figure 4.5.

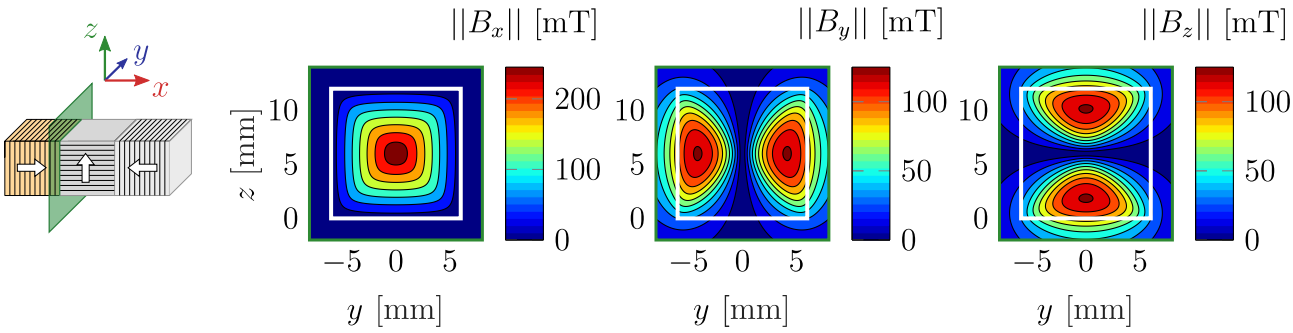

Figure 4.5: Distribution of the magnetic flux density generated by the left stacked-tape sample only, along the lateral face of the central superconductor. The distribution is computed with the analytical model assuming a homogeneous superconducting sample in the critical state characterized by an engineering critical current density $J_e = 1.3 \times 10^8$ A m^{-2}. The white lines show the border of the central sample.

Figure 4.5 shows that both the y and z-components of the calculated field are non-zero over the side surface of the central superconductor. More precisely, having a closer look at the distribution of $||B_z||$, it can be highlighted that the area exhibiting high values of B_z according to the analytical model corresponds to the region where a current alteration is predicted by the finite element simulation (cf. Figure 4.3). This suggests that the z-component of this field is indeed responsible for the current alteration occurring during the assembly process of a superconducting Halbach array made of stacked tapes.

The alteration of the current distribution shown in Figure 4.4 (b) is expected to cause a reduction in the magnetic flux density generated by the final assembly. To verify this statement, the configuration is experimentally assembled and measured in the next section.

4.1.3 Experimental results

A superconducting linear Halbach array made of superconducting stacked-tape samples is now assembled and measured experimentally. In Figure 4.6, the field measured at 77 K, 1.5 mm above the surface of the configuration is confronted to: (i) the predictions of the finite element model; (ii) the field profile computed with the analytical model assuming that the current distribution remains unchanged during the assembly process.

First, the flux density in the region above the peripheral samples of the array ($x <$ -6 mm or $x >$ 6 mm in Figure 4.6 (c)) is examined. In this region, both models are found to give very similar results that are also in agreement with experimental data. The coincidence of the finite element model and the analytical model assuming no demagnetization is expected given that no significant current re-distribution in the peripheral samples is predicted by the finite element

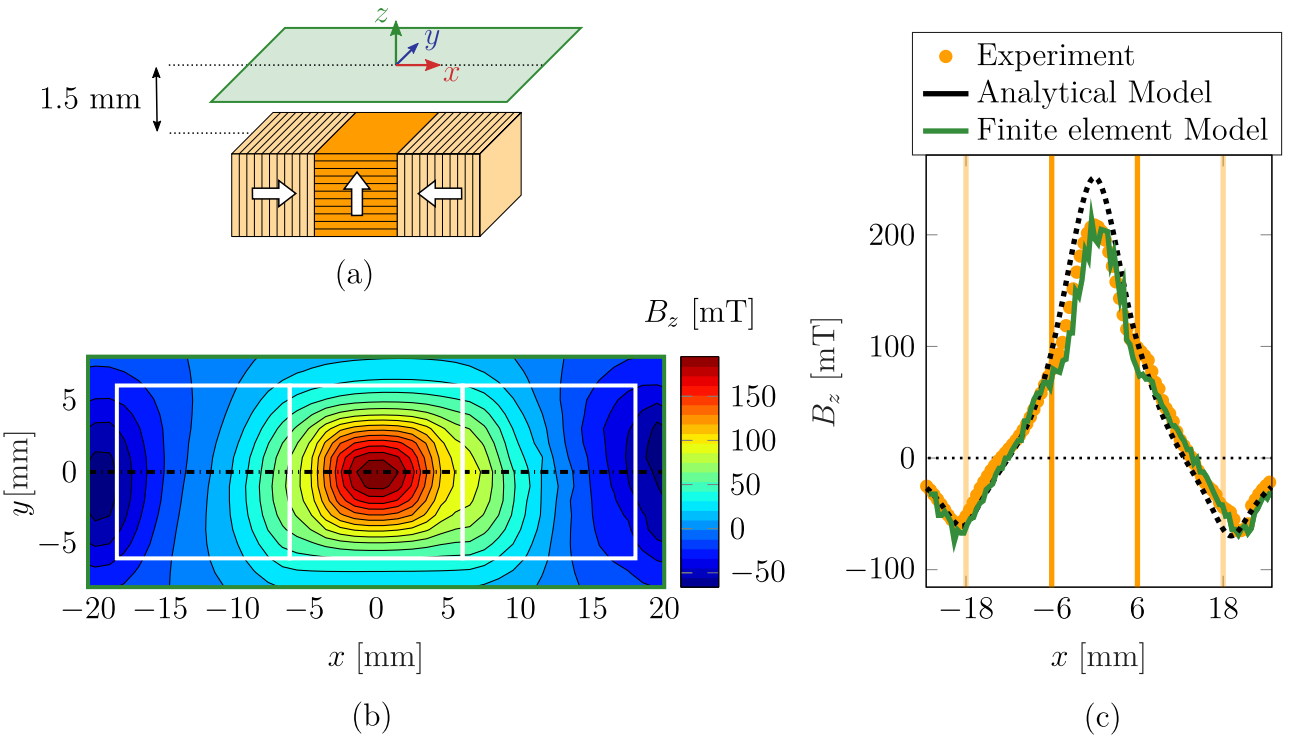

Figure 4.6: (a) Schematic representation of the position of the mapping plane with respect to the superconducting Halbach array made of three stacked-tape samples. (b) Contour plot of the z-component of the magnetic flux density measured at 77 K, 1.5 mm above the top surface of the assembly. The white lines represent the edges of the samples. (c) Mapping results along a centred line parallel to the x-direction. The orange vertical lines are located at the border of the samples. The experimental data are compared to (i) the finite element model predictions and (ii) an analytical model assuming a simple vector summation of the flux densities generated by each superconductor in the array and no alteration of the individual magnetization.

model (cf. Figure 4.3). In the region above the central superconductor (-6 mm $< x <$ 6 mm), the agreement between finite element predictions and experimental data remains satisfying, whereas the analytical model ignoring the current re-distribution significantly overestimates the field generated. This observation gives evidence that a current alteration indeed occurs in the central sample.

Figure 4.6 (c) shows that the maximum field measured experimentally is 205 mT. The ideal value predicted by the analytical model assuming no demagnetization is 22% higher, i.e. 250 mT. Given that the magnetic flux density measured above the central sample before assembly is 200 mT, the contribution of the peripheral samples over the centre of the array is thus almost completely erased by the supercurrent alteration occurring during the assembly procedure. The practical conclusion to be drawn is that, although the layered structure of the stacked tapes leads to a current distribution that differs from that in bulk superconductors (see Figure 4.4), the deleterious impact on the resulting magnetic flux distribution above the array is found to be similar in both cases.

Similarly to the reasoning followed for bulk superconductors, the analytical model is then modi-

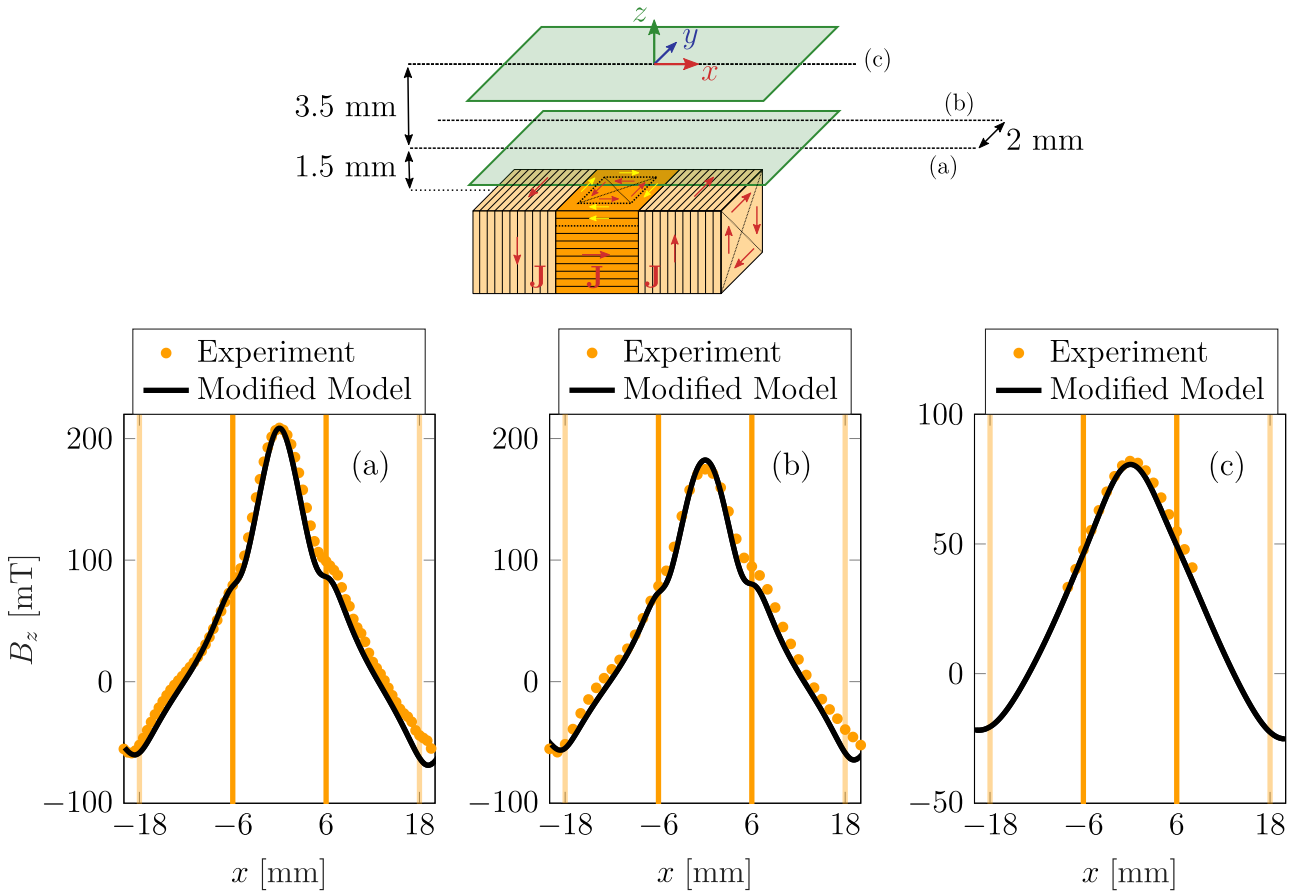

Figure 4.7: Measured distribution of the z-component of the magnetic flux density of a superconducting Halbach array made of stacked-tape samples along three distinct lines parallel to the x-direction at 77 K. The results are compared to the predictions of an analytical model computing the vector summation of the flux densities generated by each superconductor in the array. The model assumes that the current distribution in the central sample is altered in a square annulus region of equal height and thickness e = 0.9 mm as represented schematically in Figure 4.4 (b).

fied to improve the matching with experimental trapped-field measurements. More precisely, the current distribution used in the analytical model is changed following the qualitative observations performed with the finite element model. As represented graphically in Figure 4.4 (b), it is assumed that the current alteration occurs only within the central sample, in a square annulus region of equal height and thickness denoted e. In this region, the supercurrent is assumed to flow in loops anti-parallel to the z-direction and the value of the engineering critical current density is assumed to remain the same. After adjusting the parameter e, it is found that the value $e = 0.9$ mm leads to a very satisfactory agreement with trapped-field measurements. A comparison between the measurements and the predictions of the modified analytical model along three distinct lines parallel to the x-direction is shown in Figure 4.7.

The actual current density distribution within the stacked-tape samples after the assembly procedure is very likely to be more elaborated than the simplified description shown in Figure 4.4 (b). However, the satisfying agreement observed in Figure 4.7 suggests that the simplified model captures the main features of the magnetic flux density generated by the final assembly.

Therefore, this adjusted model is used to evaluate the magnetic flux density gradient within a x-z plane containing the centres of all samples. The results of this calculation are presented in Figure 4.8 (a). The spatial zone where the gradient produced by the central stacked tapes only (before the current alteration) exceeds 1 T m^{-1} is delimited by the yellow dashed line in that Figure. The results along a line parallel to the x-direction at a distance of 20 mm from the configuration (i.e. at z = 32 mm) are shown in Figure 4.8 (b).

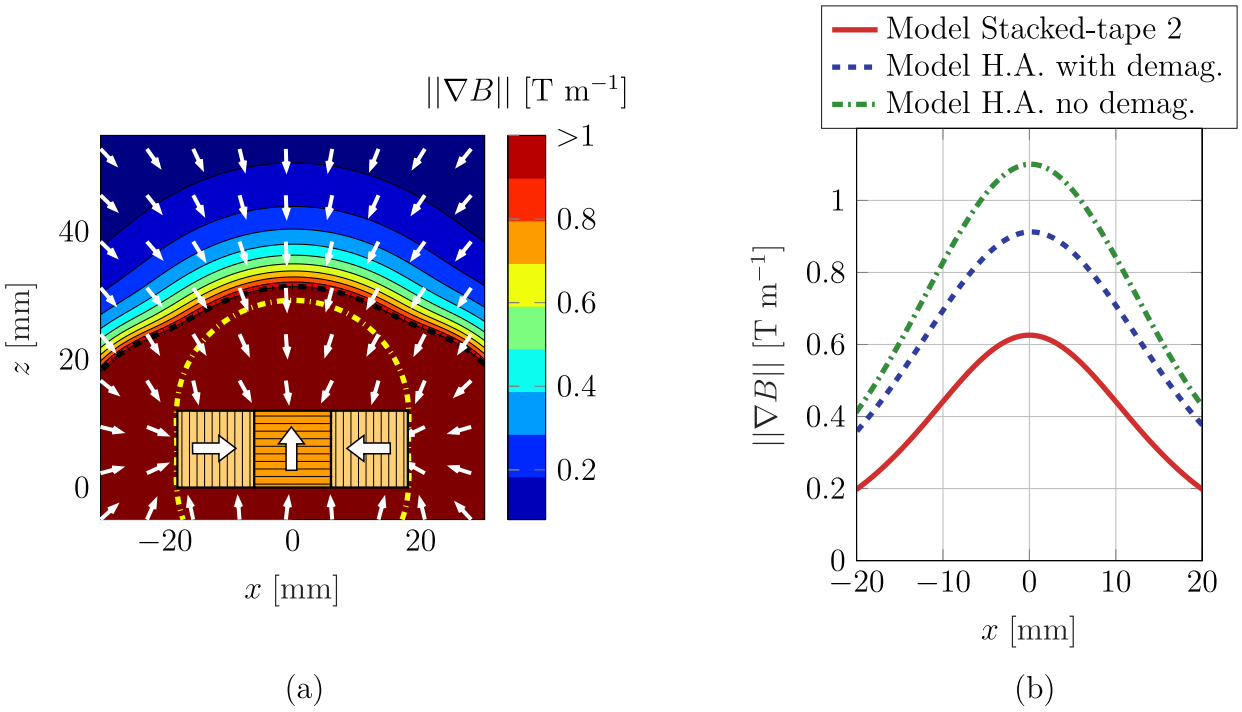

Figure 4.8: Results obtained with the modified analytical model computing the vector summation of the flux densities generated by each superconductor in the array. The model assumes that the current distribution in the central sample is altered in a square annulus region of equal height and thickness e = 0.9 mm as represented schematically in Figure 4.4 (b). (a) Contour plot of the amplitude of the magnetic flux density gradient generated by the superconducting Halbach array within a x-z plane including the centres of the samples. The small white arrows show the direction of the gradient, and the yellow dashed line delimits the spatial region where the gradient produced by the central sample only (before the current alteration) exceeds 1 T m^{-1}. (b) Comparison of the magnetic flux density gradient along a line parallel to the x-direction at a distance of 20 mm from the top surface of the central sample computed for: (i) the central stacked-tape sample only; (ii) the complete array computed with the model accounting for the current density alteration; (iii) the complete array computed with the model ignoring the current density modification.

Figure 4.8 (a) shows that the region where the gradient produced by the superconducting assembly exceeds 1 T m^{-1} is more extended for the array than for the central superconductor only. The maximum magnetic flux density gradient generated by the central stacked tapes 20 mm above the centre of its top surface is equal to 0.6 T m^{-1}. The gradient computed at this specific location for the complete assembly is equal to 0.9 T m^{-1} when accounting for the current density alteration and to 1.1 T m^{-1} when ignoring the reorganization of the current loops. Therefore, although the current distribution at the end of the assembly procedure of a

Halbach array made of stacked tapes differs from that found for bulk superconductors, similar practical conclusions can be drawn concerning the magnetic flux density gradient generated in both cases.

4.2 Geometrically modified superconducting Halbach array

Following the discussion in the previous section, it appears that introducing a strong anisotropy in the central superconductor of the Halbach array does not really mitigate the re-distribution of supercurrents and the associated alterations taking place during the assembly procedure. Furthermore, it was also confirmed that this modification of current loops is most likely initiated by the magnetic flux density produced by the peripheral samples on the sides of the central superconductor. With that knowledge in mind, the idea explored in this section is to reduce the field strength at this specific location. Three assemblies are considered and investigated to this end, they are schematically represented in Figure 4.9 and briefly described below.

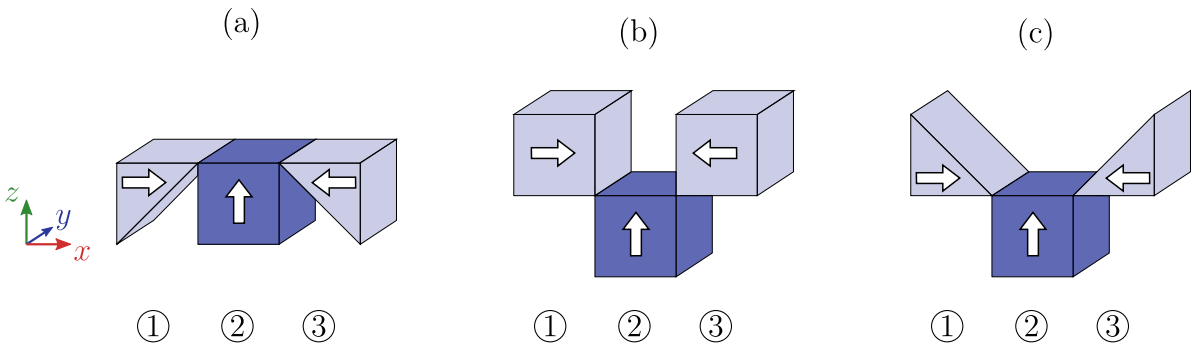

Figure 4.9: Schematic representation of the modified Halbach array aiming at reducing the field strength on the side of the central superconductor. The white arrows depict the main magnetization direction of each sample.

The first configuration (Figure 4.9 (a)) consists in modifying the geometrical shape of the peripheral sample. Here, peripheral samples in the shape of triangular prisms are used instead of cuboids. In the following, this first modified assembly is referred to as the "truncated Halbach array". In the second assembly (Figure 4.9 (b)), the vertical position of the peripheral samples is changed, and the bottom face of these superconductors is now aligned with the top surface of the central sample. For the third configuration (Figure 4.9 (c)), both the geometrical shape and the vertical position of the peripheral samples differ from the classic assembly. The truncated Halbach array is investigated both experimentally and numerically while the other two configurations are explored by numerical modelling only. It should be pointed out that for each considered configuration, the crystallographic c-axis of each sample is aligned with the main magnetization direction.

4.2.1 Superconducting truncated Halbach array

The experimental study of this section is entirely conducted with the $YBa_2Cu_3O_{7-x}$ bulk superconductors manufactured by the *ATZ* company. Using the axis definition shown in Figure 4.9 (a), the largest dimension of each sample in the x, y and z-direction is equal to 13 mm.

Furthermore, all the magnetic flux density measurements of the current section are carried out using the 3-axis cryogenic Hall sensor recently developed in our lab [119]. As previously stated, this sensor enables simultaneous acquisition of the three components of the magnetic flux density **B**, facilitating the experimental assessment of the distribution of the magnetic flux density gradient. Due to the dimension of the probe, however, the mapping plane cannot be positioned as closely to the measured configuration as achievable with the *Arepoc*® Hall sensor. As indicated in [119], the closest distance separating the external structure of the probe and the active surface of the Hall sensors is equal to 2.2 mm. Here below, the mapping measurements are performed at a further distance (ranging between 2.7 mm and 4.7 mm) to avoid any interference during the displacement of the probe.

Characterization of individual samples and analytical model adjustment

Two preliminary Hall probe mapping measurements are first conducted at 77 K, 4.7 mm above the top and bottom surface of the cubic superconductor (sample ②). For both measurements, the sample is magnetized in a direction parallel to its *c*-axis through a field-cooling process starting from 1.2 T with a field removal rate of 1 mT s^{-1} and a 45 min period of magnetic relaxation. The central trapped field measured in both mappings is found to be equal to 151 mT ±2 mT which gives confidence in the homogeneity of the critical current density within the sample. Following the same magnetization protocol, the experimental assessment of the dipole magnetic moment for this particular sample results in a value of $||\mathbf{m}|| = 0.97$ A m^2. The measurement is conducted using the extraction magnetometer. Based on this measurement and on the assumptions that the critical current density is field-independent and homogeneous, the value of J_c can be evaluated from the expression of the dipole magnetic moment of a cubic superconductor of side a in the critical state: $J_c = 6||\mathbf{m}||/a^4 = 2 \times 10^8$ A m^{-2}. The magnetic flux density distribution predicted with the analytical model using the above-mentioned value of J_c is compared to measurements in Figure 4.10 (c).

As can be observed, measurements and analytical predictions nicely agree with each other for all magnetic flux density components. This observation gives confidence both in the validity of the analytical model and in the methodology employed so far in this thesis, which consists in adjusting the analytical model based on measurements of the z-component of the magnetic flux density distribution exclusively, and extrapolating the remaining field components using the adjusted analytical model.

Following the characterization of the cubic superconductor, the superconducting triangular prisms are magnetized along a direction parallel to their *c*-axes using a procedure identical to that employed for the cubic sample. The trapped field distribution at 77 K, in a plane perpendicular to the *c*-axis direction and located at a distance of 2.7 mm from the superconductor is measured. As a first approach, it is assumed that these samples exhibit a critical current density identical to that used for the cubic sample, i.e. $J_c = 2 \times 10^8$ A m^{-2}. Based on this critical current density and on the analytical model for superconducting triangular prisms, the anticipated field distribution is calculated and compared to the experimental measurements in Figure 4.11.

Despite the simplicity of the approach, very satisfying agreement is obtained with experimental data. This agreement is confirmed by conducting further trapped-field measurements described in Appendix B.1. Given this agreement between measurements and calculated field distributions,

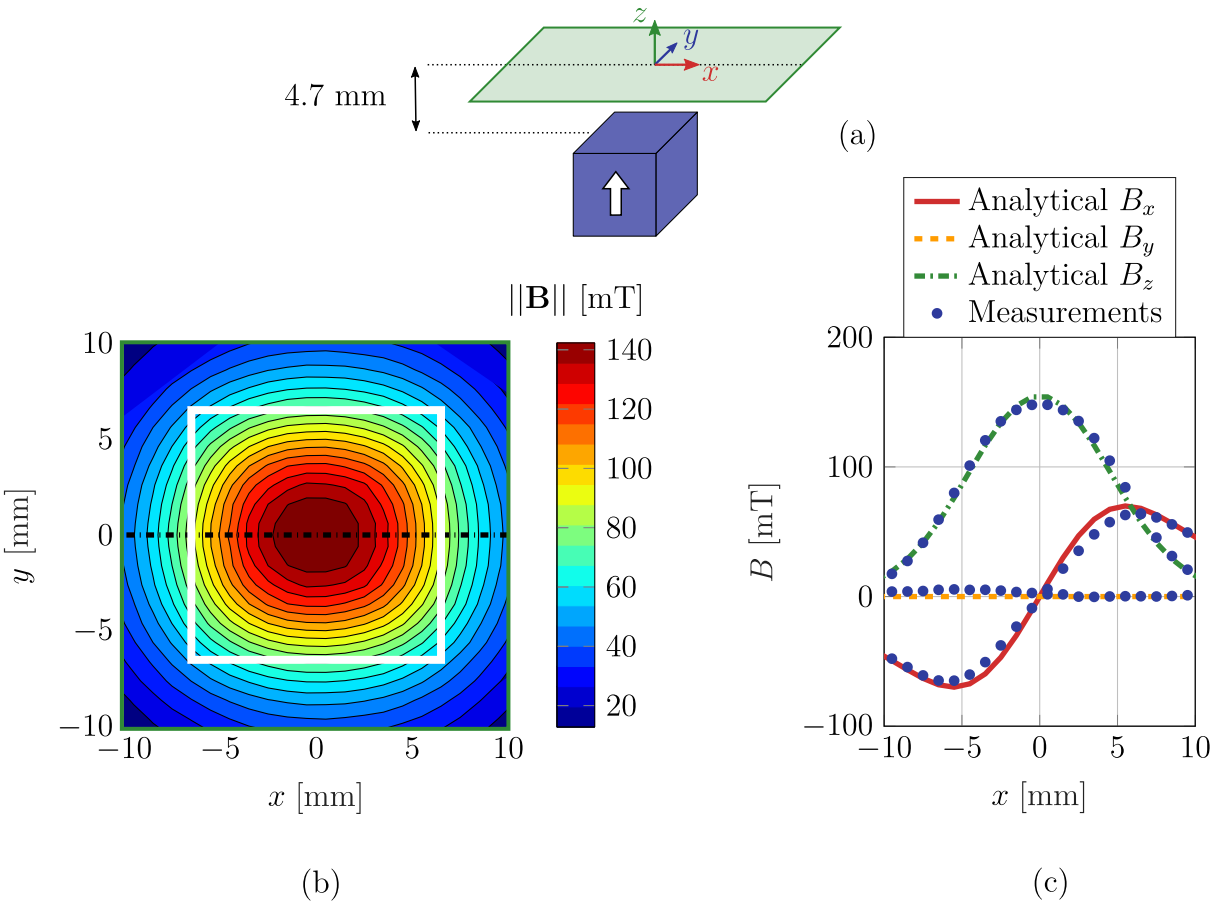

Figure 4.10: (a) Schematic representation of the Hall probe mapping performed. (b) Contour plot of the magnetic flux density measured at 77 K, 4.7 mm above the top surface of the cubic superconductor manufactured by the *ATZ* company. The white line depicts the border of the sample. (c) Comparison of the measured distribution of the 3 components of the magnetic flux density to the analytical calculations along a centred line parallel to the x-direction. The model considers a homogeneous superconducting sample in the critical state characterized by a critical current density $J_c = 2 \times 10^8$ A m^{-2}.

it is decided to keep the value $J_c = 2 \times 10^8$ A m^{-2} for all the samples manufactured by the *ATZ* company.

Now that the analytical model parameters are adjusted, the interest of investigating a truncated Halbach array structure can be highlighted. In this context, the magnetic flux density generated exclusively by the left peripheral superconductor on the lateral face of the central sample within a superconducting Halbach array is computed. This calculation is carried out under two distinct scenarios: (a) the samples within the array are perfect cubes with a side length of 13 mm and a critical current density of 2 $\times 10^8$ A m^{-2}; (b) the peripheral samples take the form of triangular prisms, each characterized by an identical critical current density. The resulting field distributions are presented in Figure 4.12. Comparing the calculated field in each depicted scenario in Figure 4.12 on a component-by-component basis reveals that the field strength produced on the lateral face of the central sample is approximately one order of magnitude smaller when considering peripheral samples in the form of triangular prisms. The deliberate decrease in field strength at this specific location is a targeted objective, as it is expected to

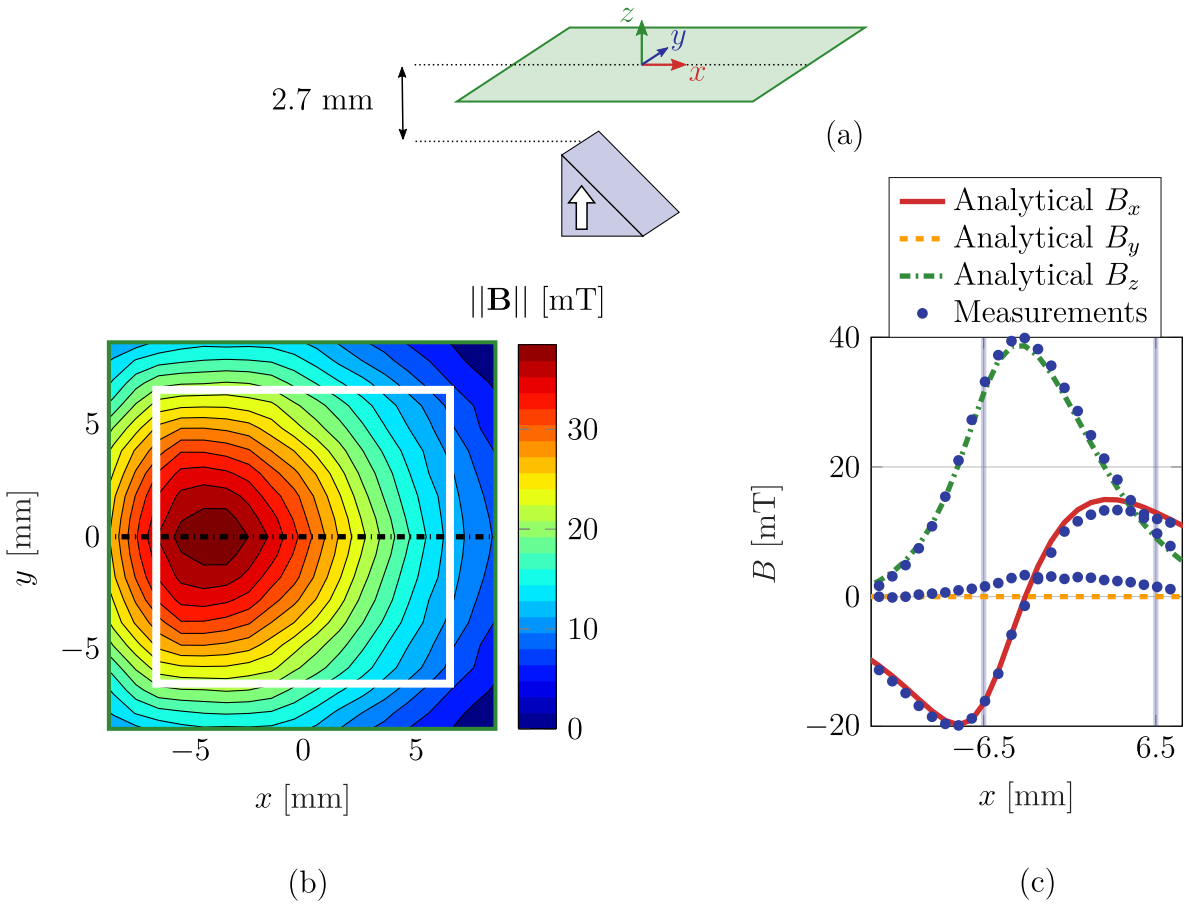

Figure 4.11: (a) Schematic representation of the Hall probe mapping performed. (b) Contour plot of the magnetic flux density measured at 77 K, 2.7 mm above a superconductor shaped as a triangular prism. The white line depicts the border of the sample. (c) Comparison of the measured distribution of the 3 components of the magnetic flux density to the analytical calculations along a centred line parallel to the x-direction. The model considers a homogeneous superconducting sample in the critical state characterized by a critical current density $J_c = 2 \times 10^8$ A m^{-2}.

yield a reduction in the alteration of current density inherent to the assembly procedure.

Finite element modelling

The assembly process of the superconducting truncated Halbach array is then modelled with finite element simulations. For all superconductors, the critical exponent is set to $n = 20$ and the critical current density is assumed to be homogeneous and equal to a field-independent value $J_c = 2.3 \times 10^8$ A m^{-2}. These parameters ensure that, after the magnetic relaxation period of 45 min, the remaining current density circulating within the superconductors closely approximates the value deduced experimentally. The mesh size within the superconducting region is around 1/12 of the cube side (∼1 mm). The computed distribution of the current density before and after assembling the configuration within two distinct cut planes is presented in Figure 4.13. The first corresponds to the Oxz plane and is shown in red in Figure 4.13. The second is parallel to the y and z-direction and cuts the central sample at 0.1 mm from its edge and is represented in green in Figure 4.13.

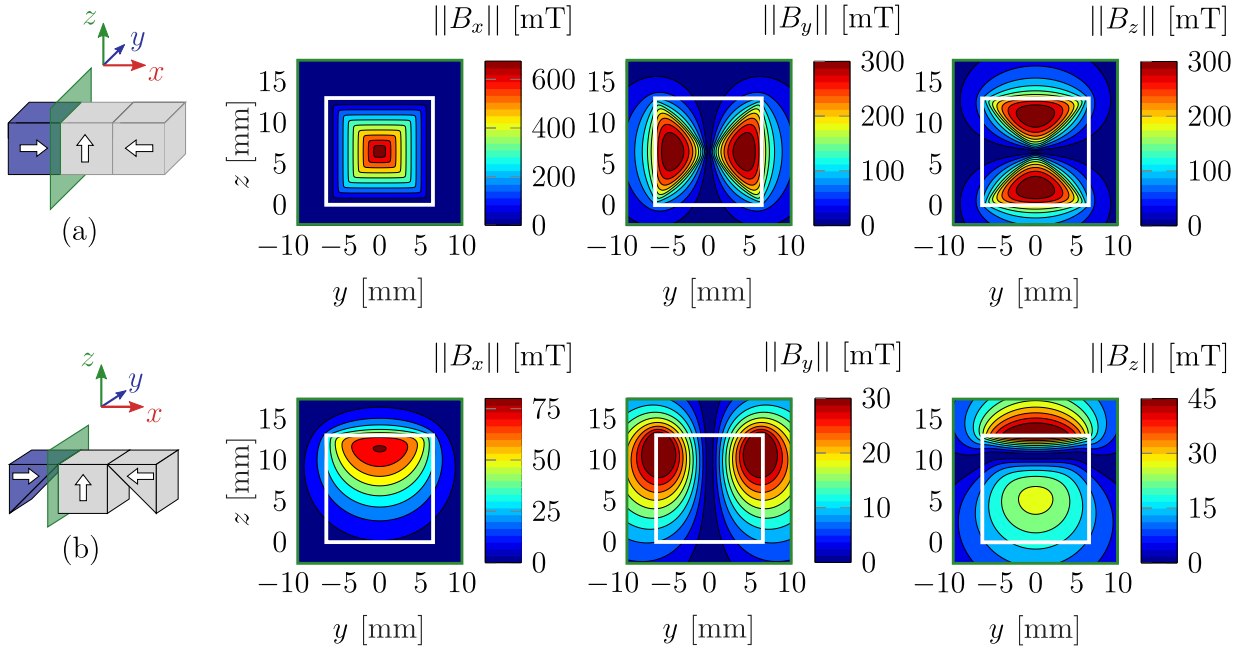

Figure 4.12: Magnetic flux density generated by the left superconductor on the lateral face of the central sample computed with the analytical model assuming a homogeneous superconducting sample in the critical state characterized by a critical current density $J_c = 2 \times 10^8$ A m^{-2}. (a) The peripheral sample is a cube with a side length of 13 mm. (b) The peripheral sample is a triangular prism with maximum dimension in the x, y and z-direction equal to 13 mm.

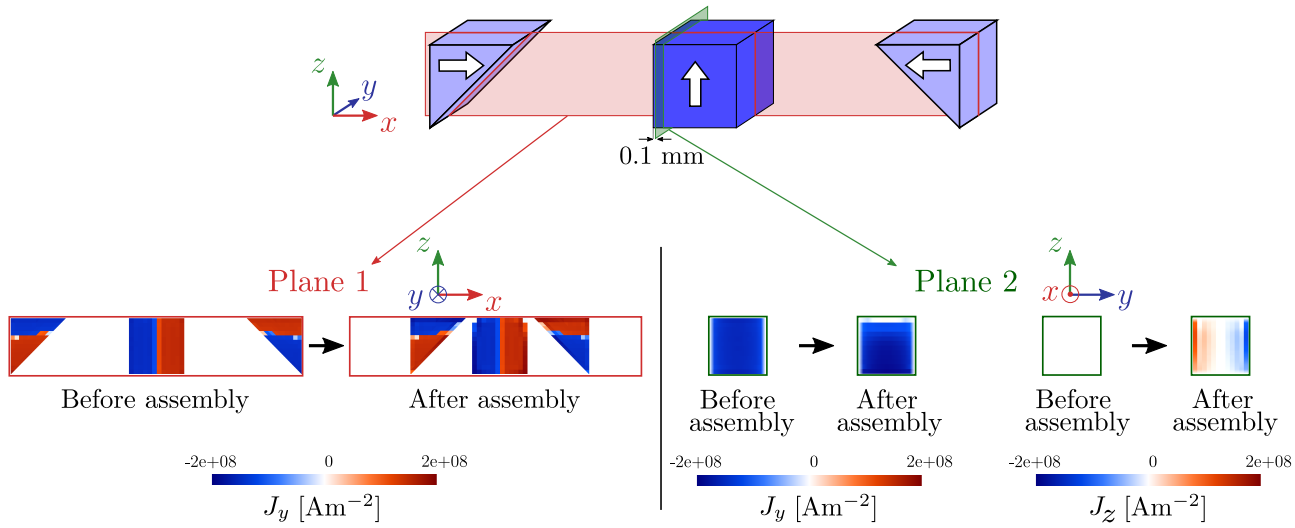

Figure 4.13: Distribution of the y and z-components of the current density before and after the assembly of the truncated superconducting Halbach array computed by the finite element model. The white arrows show the main direction of the trapped flux density in each sample. A field-independent critical current density of 2.3×10^8 A m^{-2} is considered in this simulation.

Figure 4.13 shows that before the assembly in Plane 1, each sample exhibits symmetrical

distribution with both positive and negative supercurrent flowing through the cut plane, aligning with expectations for fully magnetized superconductors in the critical state. The current distribution in Plane 2 before the assembly process is consistent with the expected square current loops within the central sample as well. After the assembly procedure, the current distribution deviates from the initial one in that the current density is no longer uniformly distributed. The alteration in current density, however, is considerably less pronounced than for cubic bulk superconductors (cf. Figure 3.7). The formation of current loops perpendicular to the x-direction is not anticipated within the central superconductor of a truncated superconducting Halbach array. In Figure 4.13, the alteration of the current distribution consists of (i) a reduction in the current density amplitude near the top surface; and (ii) a distortion of the current lines that are no longer perfectly aligned with the y-direction. The subsequent section experimentally investigates the impact of such minor alterations in current density on the field distribution generated by the final assembly.

Experimental assembly of the array

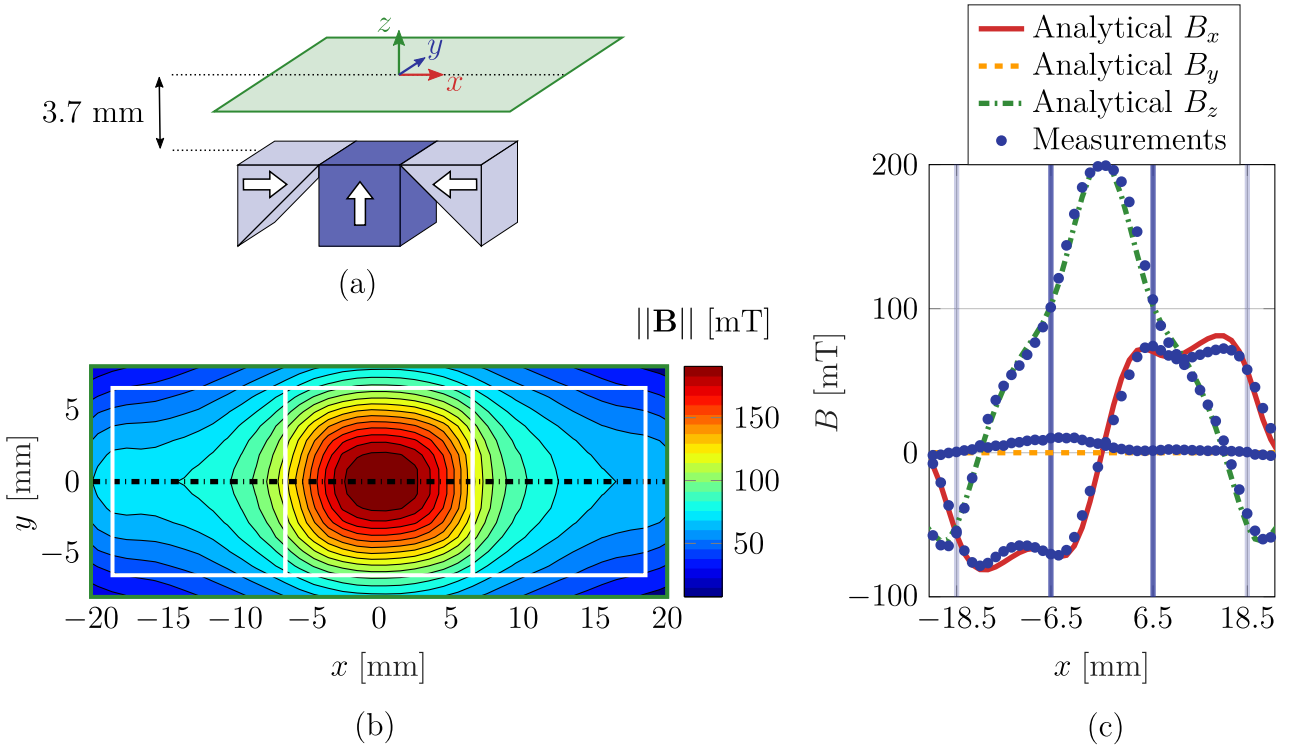

Figure 4.14: (a) Schematic representation of the position of the mapping plane with respect to the superconducting truncated Halbach array. (b) Contour plot of the magnetic flux density measured at 77 K, 3.7 mm above the top surface of the assembly. The white lines depict the borders of the samples. (c) Mapping results along a centred line parallel to the x-direction. The experimental data are compared to an analytical model assuming a simple vector summation of the flux densities generated by each superconductor of the array and no alteration of the individual magnetization.

The truncated superconducting Halbach array is now assembled and the magnetic flux density distribution is measured 3.7 mm above the surface of the final assembly. Figure 4.14 compares the measurements to the predictions of the analytical model assuming no current density modification during the assembly procedure.

As can be observed, a rather good matching is obtained between experimental data and the analytical model. This agreement is observed for all the field components, and a more detailed examination, described in Appendix B.2, shows that this agreement is kept at various distances from the configuration. This observation leads to the conclusion that, if any current density alteration exists, it does not manifest as a measurable change in the produced magnetic flux density. Consequently, using peripheral samples of triangular coss-section offers a very interesting alternative for mitigating the partial demagnetization of superconducting Halbach arrays.

The analytical model is now employed to assess the distribution of the magnetic flux density gradient generated by the superconducting truncated Halbach array within an x-z plane including the centres of the samples. The results of this calculation are presented in Figure 4.15 and are compared to the performance achievable with the central (cubic) superconductor only.

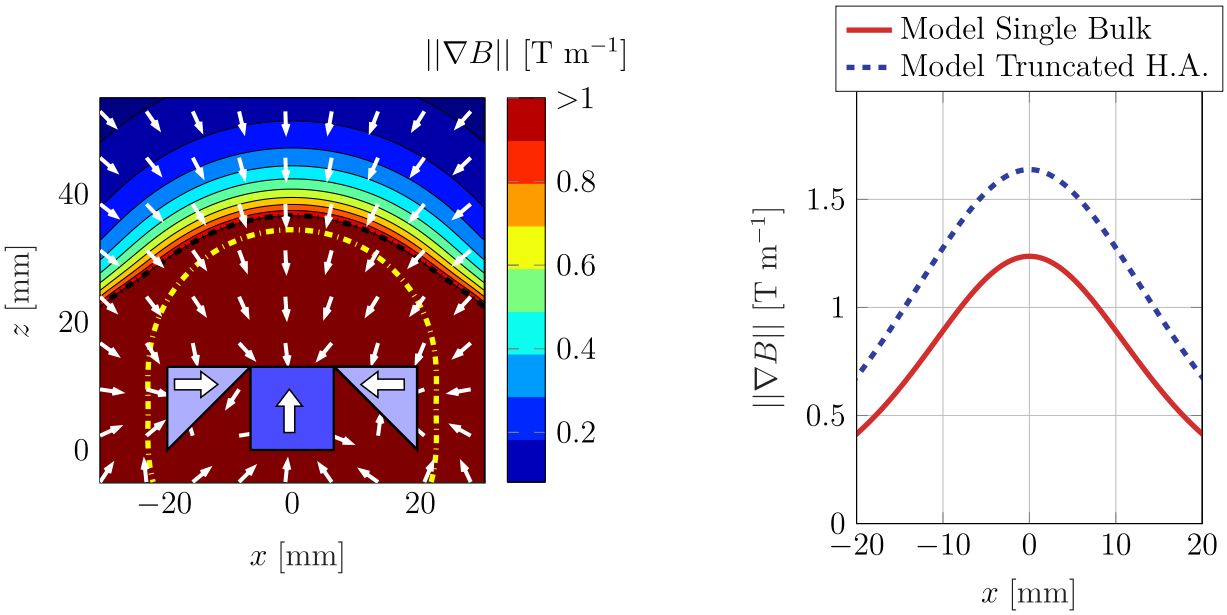

Figure 4.15: Results obtained with the analytical model computing the vector summation of the flux densities generated by each superconductor in the array. The model presumes no alteration of the individual magnetization. (a) Contour plot of the amplitude of the magnetic flux density gradient generated by the superconducting truncated Halbach array within a x-z plane including the centres of the samples. The small white arrows show the direction of the gradient, and the yellow dashed line delimits the spatial region where the gradient produced by the central sample only is higher than 1 T m^{-1}. (b) Comparison of the magnetic flux density gradient along a line parallel to the x-direction at a distance of 20 mm from the top surface of the central sample computed for: (i) the central sample only; (ii) the complete array.

As shown in Figure 4.15 (a), the advantage of the truncated Halbach array is to extend the spatial region where the generated gradient exceeds 1 T m^{-1}. Furthermore, Figure 4.15 (b) shows that the maximum field gradient produced at a distance of 20 mm reaches 1.6 T m^{-1} with the truncated Halbach array compared to 1.2 T m^{-1} with the central sample alone. Therefore,

it appears that a similar increase of the magnetic flux density gradient to the one observed with cubic peripheral samples is achieved, with the advantage of mitigating the demagnetization of the central sample.

The bespoke 3-axis cryogenic Hall probe is then used for evaluating the gradient of the magnetic flux density produced by the assembly within a x-z plane including the centres of the samples. Due to space constraints, the measurement of the gradient distribution was restricted to a limited area, the measurements are compared to analytical predictions in Figure 4.16.

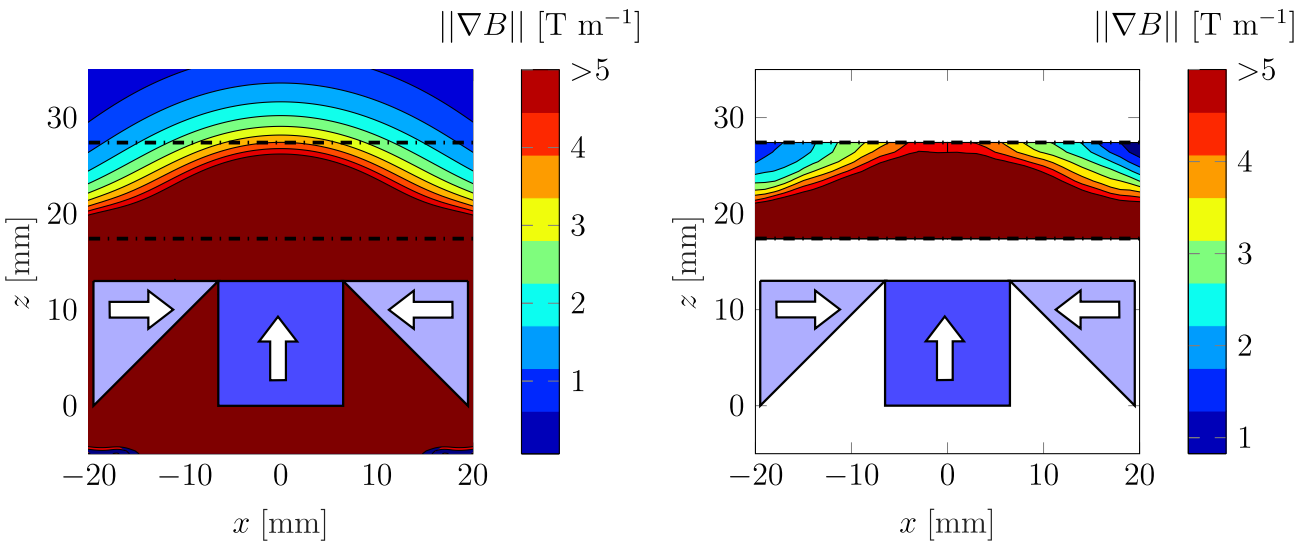

(a) Analytical model (b) Experiment

Figure 4.16: Amplitude of the gradient of the magnetic flux density generated by a superconducting truncated Halbach array in a x-z cutplane including the centres of all the samples. (a) Results obtained with the analytical model computing the vector summation of the flux densities generated by each superconductor in the array. The model presumes no alteration of the individual magnetization. (b) Results obtained by post-processing the experimental measurement carried out at 77 K with a bespoke 3-axis cryogenic Hall probe. The dashed black lines delimit the spatial zone where the experimental mapping is conducted.

As can be observed a satisfactory agreement is obtained between experimental and analytical data in the spatial region that could be measured. This comparison confirms the capability of the probe to derive experimentally the magnetic flux density gradient produced in a specific region and provides more confidence in the validity of the analytical model.

4.2.2 Vertical shift of the peripheral samples

The approach considered here consists in shifting the positions of the two peripheral superconductors in the array, as depicted in Figures 4.9 (b) and (c). This shift yields an increase in spatial constraints above the centre of the final structure. This is a potential disadvantage since the region above the central sample corresponds to the spatial zone where the exploitable field gradient is maximum. The interest of the present configuration, therefore, is mostly when the field gradients are exploited at a reasonable distance (roughly corresponding to the side length of the samples) of the structure. In the assembly shown in Figure 4.9 (c), triangular prism-shaped samples are employed to increase the available space above the arrangement in comparison to the configuration of Figure 4.9 (b).

Once assembled, the structures under consideration in this section generate a magnetic flux density gradient around them, the characteristics of which (direction, position of the maximum, etc.) differ from those of the gradients generated by the superconducting Halbach arrays considered so far. A detailed analysis of the field distribution generated by these specific structures is not the focus of this section. The objective is to illustrate two points: (i) it is possible to conceive arrangements of magnetized superconductors leading to minimal demagnetization, and (ii) the combined use of the finite element model and the analytical model allows verification that the current distribution remains unchanged during assembly and facilitates the assessment of the performance of the final configuration.

The assembly process of the two above-mentioned configurations is investigated with the finite element model using a common critical exponent and field-independent critical current density for all the samples equal to 20 and 2.3×10^8 A m^{-2} respectively. The largest geometrical dimension of each sample in the x, y and z-direction is equal to 13 mm. The modelled current distribution before and after the assembly procedure within a x-z plane containing the centres of the superconductors is presented in Figure 4.17.

As can be observed in Figure 4.17, for both configurations considered, the current density distribution computed at the end of the assembly procedure is extremely close to that obtained before initiating the approach of the magnetized samples. This minimal magnetization alteration results from the smaller strength of the magnetic flux density generated by the peripheral samples at the location of the central one, as compared to the linear superconducting Halbach array. This aspect is shown in more detail in Appendix B.3.

Figure 4.18 shows the amplitude of the gradient calculated with the analytical model assuming no demagnetization. As in previous sections, the gradient is computed within a x-z plane including the centres of the superconductors.

In Figures 4.18 (a) and (b), the magnetic flux density gradient range achieved with each final assembly surpasses significantly the performance of a single magnetized cubic superconductor. This observation, coupled with the findings from the finite element simulation, is highly promising. It suggests that with careful consideration of the field strength generated by each sample in close proximity to their nearest neighbours, it is possible to combine magnetized superconductors while avoiding their individual demagnetizations. Such combinations can be effectively employed to shape the distribution of the magnetic flux density at a reasonable distance from the assembly.

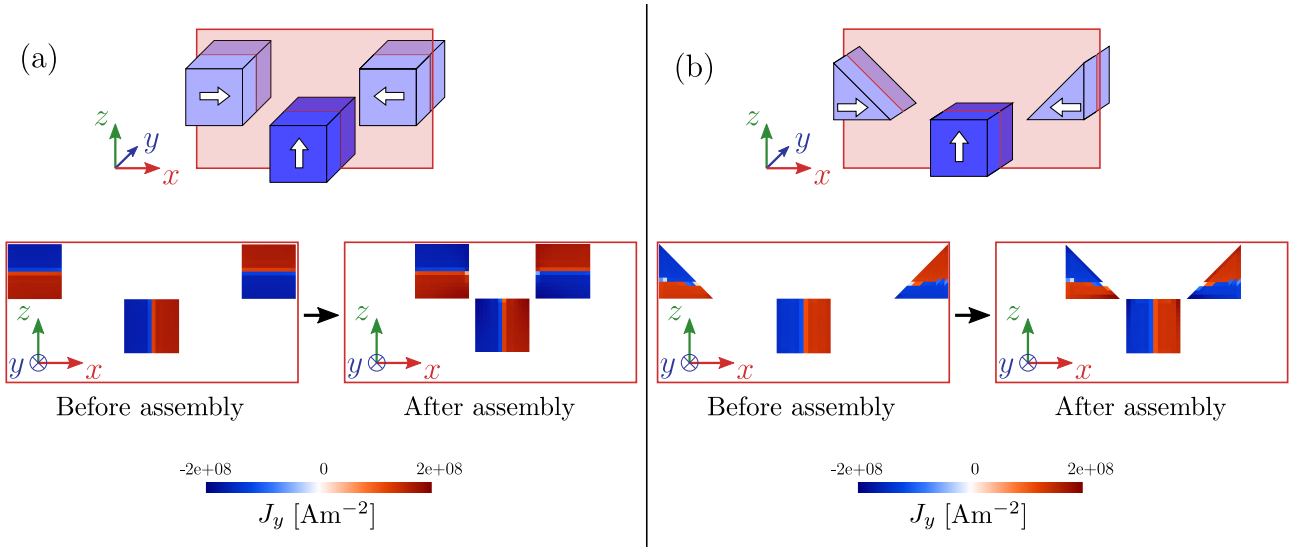

Figure 4.17: Comparison of the distribution of the y-component of the current density before and after the assembly process of the superconducting configurations depicted in Figures 4.9 (b) and (c) as computed by the finite element model. The white arrows represent schematically the main direction of the trapped flux density in each sample. A field-independent critical current density of 2.3×10^8 A m^{-2} is considered in this simulation.

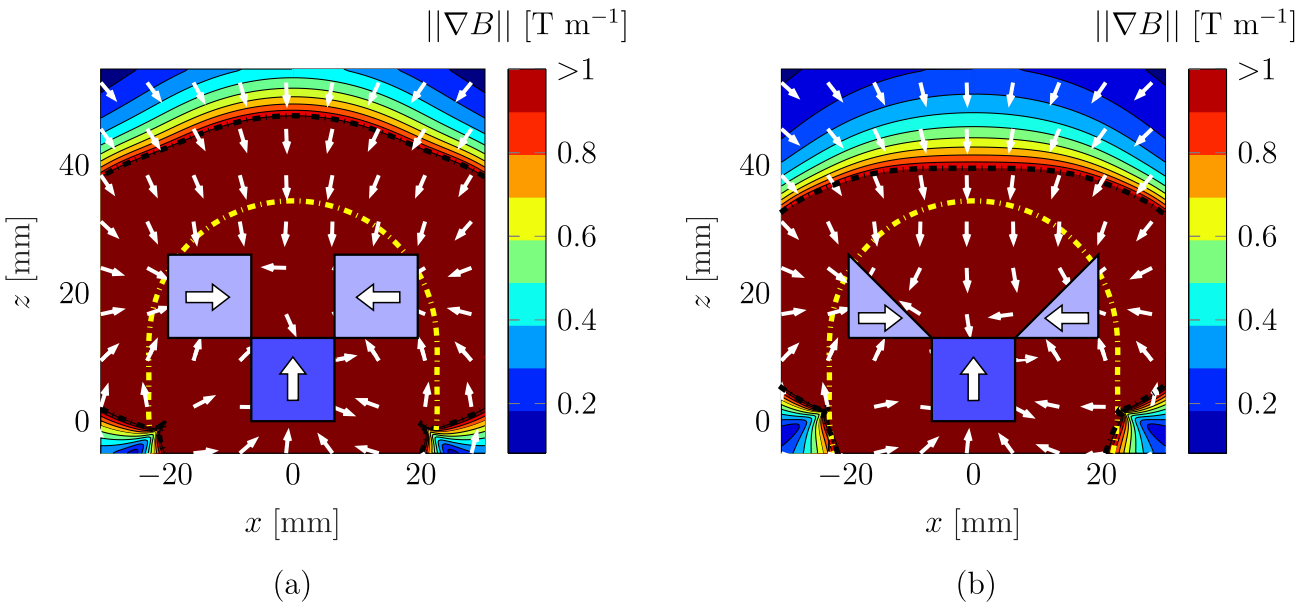

Figure 4.18: Contour plot of the amplitude of the magnetic flux density gradient generated by the superconducting configurations depicted in Figures 4.9 (b) and (c) within a x-z plane including the centres of the samples. The distributions are computed with an analytical model computing the vector summation of the flux densities generated by each superconductor in the configuration and assuming no current alteration during the assembly process. The small white arrows show the direction of the gradient, and the yellow dashed line delimits the spatial region where the gradient produced by the central sample only is higher than 1 T m^{-1}.

4.3 Modified assembly process

In the present section, an alternative procedure for assembling superconducting Halbach arrays is proposed and investigated. The idea of the method is to apply a time-varying field primarily directed along the z-direction on the central sample after the assembly process. Provided that the applied field amplitude is sufficient, a reconfiguration of the supercurrents flowing within the central sample is anticipated, leading to a partial remagnetization of the central sample. In order to achieve this, the suggested approach takes advantage of the trapped magnetic field of an additional magnetized superconductor as a source for the remagnetization field. The procedure is described step by step below and illustrated in Figure 4.19.

a) The magnetization process of the peripheral samples remains unchanged and is described in section 2.2. The central sample, however, is magnetized simultaneously with an additional superconductor placed just above it[1]. The additional sample and the central sample are maintained in contact and their c-axes are kept aligned during the whole magnetization process, as shown in Figure 4.20 (a). The same field sequence as the one described in section 2.2 is used for the simultaneous magnetization of the central and the additional samples.

b) The central and the additional samples are maintained stationary while the peripheral superconductors are approached from left and right.

c) The additional sample is removed from the array. The force required to extract the additional sample is numerically evaluated not to exceed 15 N for the samples used. This allows this second step to be performed manually by the experimenter. The retracting motion is expected to decrease progressively the z-component of the magnetic flux density experienced by the central superconductor and thus induce the desired re-magnetization.

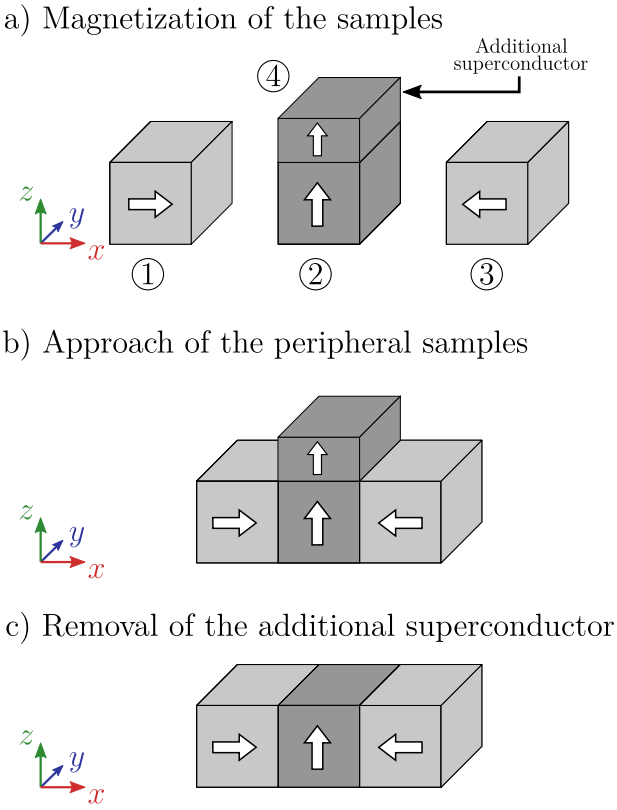

Figure 4.19: Schematic representation of the alternative method proposed for assembling a superconducting Halbach array and numbering of the samples.

This method is investigated both with bulk superconducting $YBa_2Cu_3O_{7-x}$ samples and with superconducting stacked-tape samples. Photographs of the central and the additional samples as well as their relative positions during the magnetizing process are shown in Figure 4.20 (a).

[1]Consequently, the total height of the "central + additional" samples stacked together is constrained by the space available in the cryostat used for magnetization shown in Figure 2.1 (b).

A schematic of the superconductors placed within the experimental rig is presented in Figure 4.20 (b).

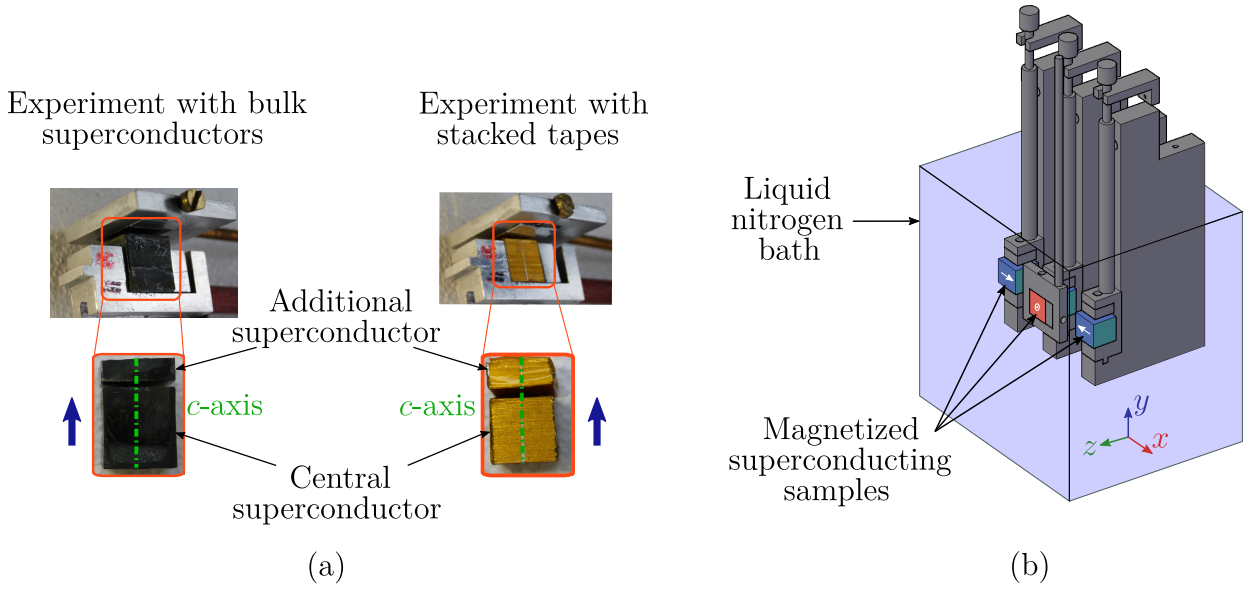

Figure 4.20: (a) Photograph of the central and additional samples during the magnetization process. The blue arrows represent schematically the main direction of the trapped flux density in both the central and additional superconductors after the magnetization process. (b) Schematic representation of the superconducting samples installed within the experimental system.

4.3.1 Samples used

The time-varying field experienced by the peripheral samples during the re-magnetization step should be limited as much as possible in order to avoid partially demagnetizing them. The dimensions along x and y of the additional sample are therefore made as close as possible to those of the central superconductor. The height of the additional sample (along the z-direction) has to be large enough so that its trapped field is sufficient to re-magnetize the central superconductor.

When the experiment is carried out with bulk superconductors, the samples ① to ③ correspond to the superconductors used in chapter 3, the trapped field at 77 K and the dimensions of these samples are presented in Tables 3.4 and 3.5 respectively. The sample ④ is extracted from one of the samples manufactured by the Bulk Superconductivity Group of Cambridge University (Sample 1222 presented in Appendix A.2). To do so, the initial superconductor is cut with a wire saw perpendicularly to its c-axis at 4.8 mm from its top surface[2]. The resulting sample is a rectangular prism of dimensions $14.2 \times 14.3 \times 4.8$ mm^3. The trapped field measured at 77 K, 1 mm above the centre of the top surface of this sample is equal to 430 mT.

When the experiment is carried out with stacked-tape samples, the samples ① to ③ correspond to the stacked tapes introduced in section 2.2, thus presenting an individual trapped field at

[2]It is decided to conserve the top part because it has been observed in the previous chapter that these samples are rather inhomogeneous and that the superconducting properties are better in the region closer to the seed.

77 K, 1.5 mm above their top surfaces equal to 200 mT ±2 mT. Regarding the additional stacked-tape sample, i.e. sample ④, it is made of 50 second generation (2G) $YBa_2Cu_3O_{7-x}$ tapes from *Superpower* stacked on top of each other. The resulting sample exhibits a squared cross-section parallel to the tape planes of dimensions 12.1×12.1 mm^2 and a height of 5.3 mm. The trapped field measured at 77 K, 1.5 mm above the top surface of the sample ④ is 173 mT.

4.3.2 Finite element modelling results

The alternative assembly process is modelled through the implementation of a two-step procedure. First, the distance between the central and the additional samples is set to 1.5 mm and the phases a) and b) shown schematically in Figure 4.19 are modelled following the same procedure as in the previous sections. The **A**-field and **H**-field distributions at the final time step of the approach of the peripheral samples serve as initial conditions for the second step. In this subsequent step, the distance between the central and the additional superconducting samples is incrementally increased at a rate of 1 mm s^{-1} until it reaches a value of 40 mm. When modelling the behaviour of bulk superconductors, the critical exponent of all samples is set to $n = 20$ and the critical current density is assumed to be homogeneous and equal to a field-independent value $J_c = 2.3 \times 10^8$ A m^{-2}, aligning with the parameters used in chapter 3. The modelled samples are perfect cubes with a 14 mm side, except for the additional sample which is a rectangular prism of dimensions $14 \times 14 \times h$ mm^3, where h is a parameter varying from 3 to 14 mm. Regarding the modelling of stacked-tape samples, the anisotropic behaviour of the superconductors is incorporated using equation (4.1). The critical exponent and the critical current density input in that relation are respectively set to $n = 20$ and $J_c = 1.7 \times 10^8$ A m^{-2}, which is consistent with the parameters used in section 4.1. The modelled samples are perfect cubes with a 12 mm side, except for the additional sample which is a rectangular prism of dimensions $12 \times 12 \times h$ mm^3, where h is a parameter varying from 3 to 12 mm.

The y and z-components of the current density distribution computed for bulk superconductors after the removal of the additional sample as well as the central field computed 1 mm away from the array are presented in Figure 4.21.

When no additional sample is considered ($h = 0$ mm), the current density distribution within the green plane in Figure 4.21 (a) after the assembly differs significantly from the initial one. The situation is exactly the same as that shown in Figure 3.7. Then, examining only the y-component of the current density, it appears that the final supercurrent distribution varies when an additional sample is employed during the assembly procedure. It can be observed that, as the height of the additional sample increases, the final current distribution approaches the initial one. Besides, it can also be noticed that irrespective of the height of the additional sample, the final current distribution exhibits a non-zero z-component that was not present before the assembly process.

In Figure 4.21 (b), the quantity $B_{\mathrm{c,ND}}$ denotes the field amplitude 1 mm above the centre (C) of the top surface of the central superconductor, as calculated using an analytical model that assumes no alteration in current distribution during the assembly process. Since this model ignores the demagnetization of the central sample induced by the peripheral samples (ND = "no demagnetization"), $B_{\mathrm{c,ND}}$ is independent of the height of the additional sample and can be interpreted as an ideal case, i.e. the upper limit of the attainable field strength

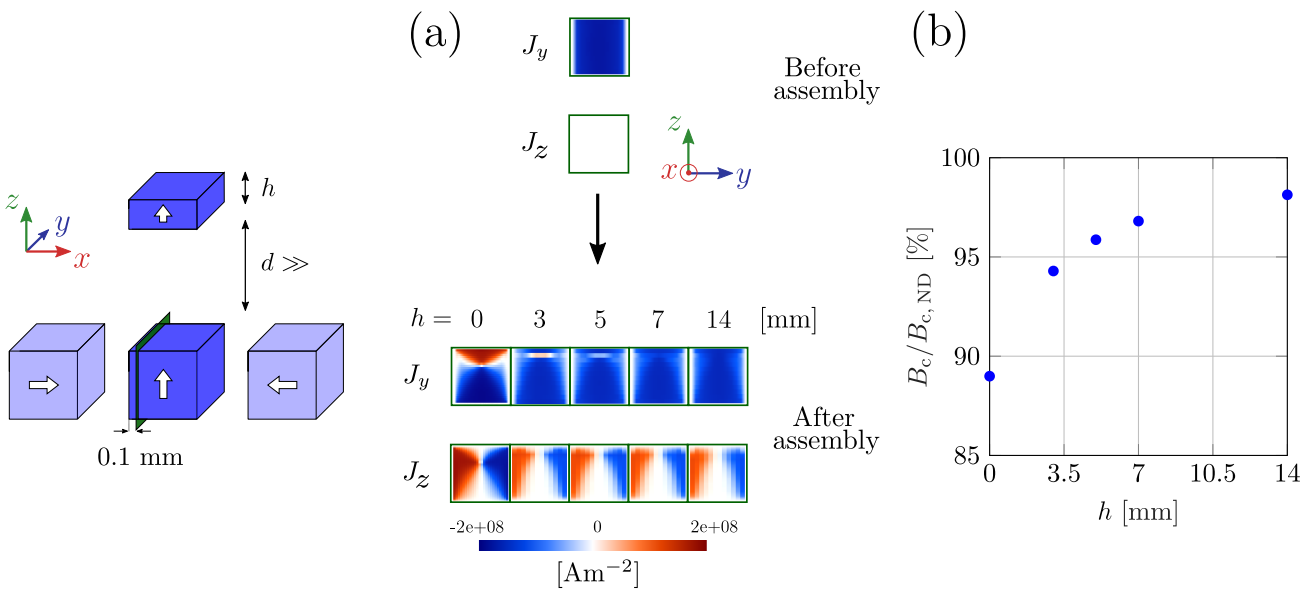

Figure 4.21: (a) Comparison of the y and z-components of the current density distribution before and after the alternative assembly of a Halbach array made of bulk superconductors computed by the finite element model for several heights of the additional superconductor. The results are presented in a y-z cut plane located at 0.1 mm from the lateral face of the central superconductor. (b) Ratio between the magnetic flux density computed with the finite element model (B_c) and with the analytical model assuming no demagnetization ($B_{c,ND}$), 1 mm above the centre of the top surface of the central superconductor and after the alternative assembly procedure for several heights of the additional superconductor. The white arrows represent schematically the main direction of the trapped flux density in each sample. A field-independent critical current density of 2.3×10^8 A m^{-2} is considered in these simulations.

using the array. As the height of the additional sample is increased, the field computed with the finite element model is found to become closer to the maximum field reachable with the array.

From these observations, it can be concluded that the retracting motion of the additional sample induces a re-configuration of the current loops within the central superconductor. While the initial current density distribution is not fully restored, this modification in the current pattern results in an increase in the magnetic flux density above the centre of the array. The simulations further demonstrate that the efficiency of the proposed method increases when taller additional samples are employed, as taller samples exhibit higher trapped fields.

The behaviour of magnetized superconducting stacked-tape samples is also examined through similar simulations. The y-component of the current density distribution computed within two distinct cut planes after the removal of the additional sample as well as the central field computed 1.5 mm above the array are presented in Figure 4.22.

Although the precise final current distribution in the central sample is different from that computed for bulk materials (as shown in Figure 4.21 (a)), similar qualitative observations can still be performed when examining the behaviour of stacked tapes. Indeed, it appears in Figure 4.22 (a) that the use of an additional sample leads to an evident modification of the supercurrent pattern within the central stacked tapes. Additionally, it can be observed that as the height of the

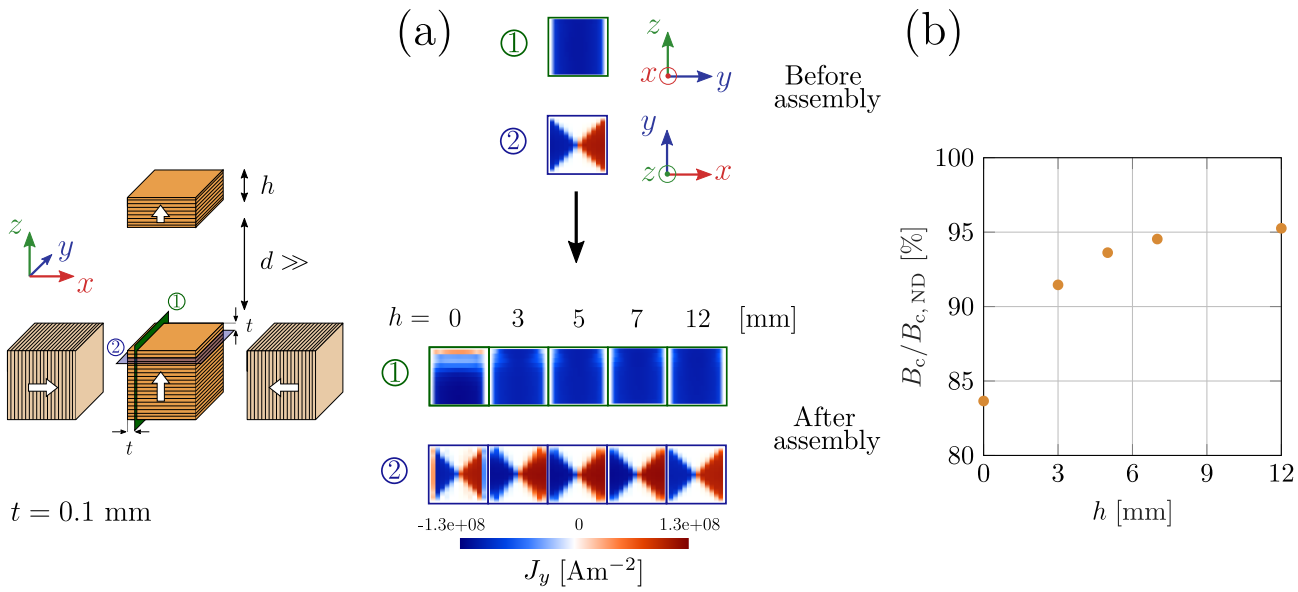

Figure 4.22: (a) Comparison of the y-component of the current density distribution before and after the alternative assembly of a Halbach array made of superconducting stacked tapes computed by the finite element model for several heights of the additional superconductor. The results are presented in a y-z cut plane located at 0.1 mm from the lateral surface of the central superconductor (Plane 1) and in a x-y cut plane located at 0.1 mm from the top surface of the central superconductor (Plane 2). (b) Ratio between the magnetic flux density computed with the finite element model (B_c) and with the analytical model assuming no demagnetization ($B_{c,ND}$), 1 mm above the centre of the top surface of the central superconductor and after the alternative assembly procedure for several heights of the additional superconductor. The white arrows represent schematically the main direction of the trapped flux density in each sample. A field-independent critical current density of 1.7×10^8 A m^{-2} is considered in these simulations.

additional sample is increased, the final distribution of the current becomes qualitatively closer to the initial one. As shown in Figure 4.22 (b), the field generated above the centre of the structure becomes closer to $B_{c,ND}$ as the height of the additional sample increases, which suggests that the modification of the supercurrent pattern positively impacts the performance of the array.

It should be noted that the simulations presented in this section were repeated with an extraction speed of the additional sample of 10 mm s^{-1} instead of 1 mm s^{-1}. After allowing a period of 45 min of magnetic relaxation after the retract motion, the central field evaluated in these simulations was found to differ at most by 3 mT from the results presented above. This observation gives confidence that the exact value of the retracting speed of the additional sample has actually little impact on the field generated by the final configuration after magnetic relaxation.

4.3.3 Experimental results

In this section, the alternative assembly process is tested experimentally both on a Halbach array made of bulk superconductors and on a Halbach array made of stacked-tape samples. Considering a potential lack of reproducibility arising from the unknown speed during the manual extraction of the additional sample (step c) in Figure 4.19, each experiment is conducted twice. The difference between the central field measured for the two runs of measurements is found

experimentally to be smaller than 2 mT, both for the experiments with bulk superconductors and with stacked tapes. The magnetic flux density distributions measured at 77 K above the final assembly in the first run of each experiment are presented in Figure 4.23. The experimental data are also compared (i) to the measurements obtained on a classic assembly of the Halbach array and (ii) to the predictions of the analytical model assuming no alteration of the individual magnetization, which can be viewed as the maximum potential of the assembly.

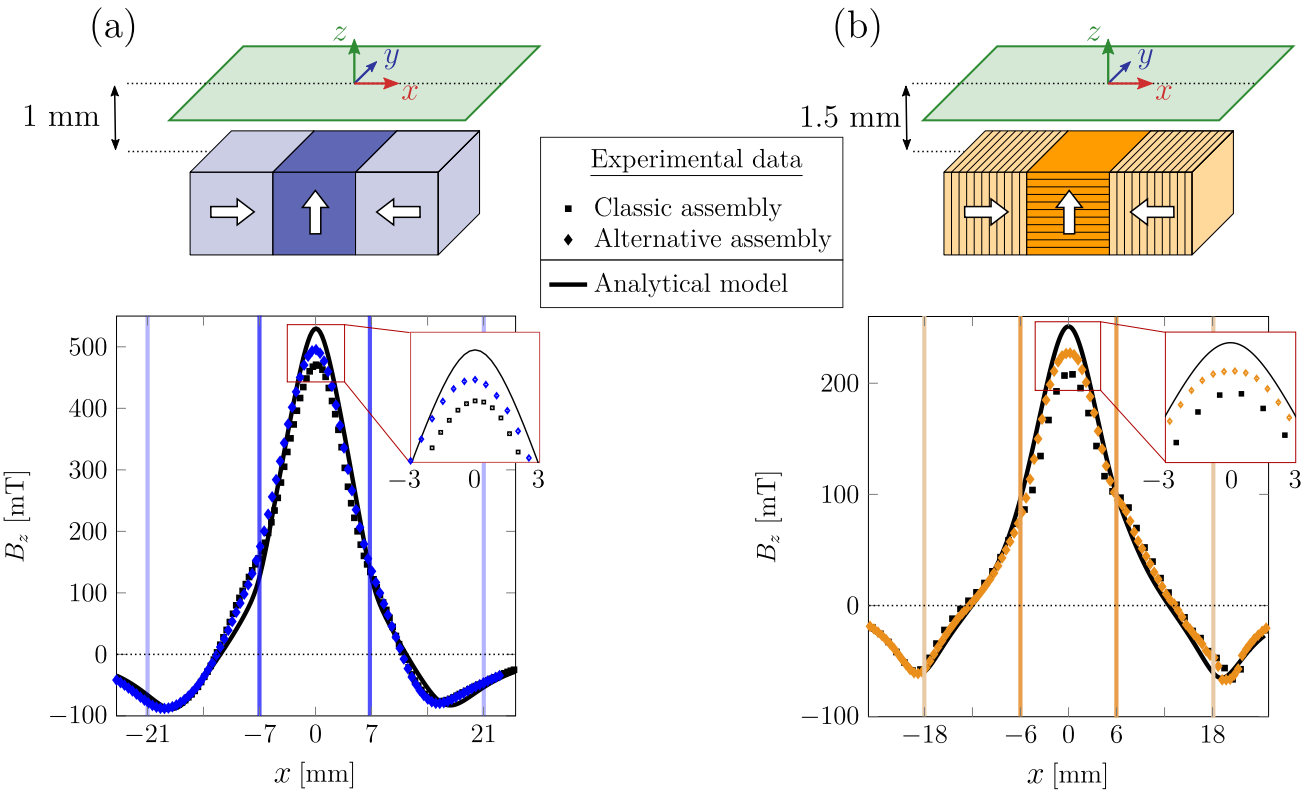

Figure 4.23: Evolution of the z-component of the magnetic flux density generated above the surface of a Halbach array made up of three superconductors and assembled with the alternative method along a line parallel to the x-direction. The vertical lines delimitate the borders of the superconducting samples, the white arrows represent schematically the main direction of the trapped flux density in each sample. The experimental data are compared both to the results obtained with a classic assembly process and to an analytical model assuming a simple vector summation of the flux densities generated by each superconductor in the array and no alteration of the individual magnetization. (a) Assembly of three bulk $YBa_2Cu_3O_{7-x}$ superconductors. (b) Assembly of three stacked tapes.

In the regions above the peripheral samples in Figures 4.23 (a) and (b), one can notice that the magnetic flux density distribution remains unchanged when the alternative assembly process is used. This result confirms that no significant modification is induced in the peripheral samples during the retract motion of the additional superconductor. The result differs when considering the experimental magnetic flux density distribution above the central sample, i.e. $|x| < 7$ mm for the bulk superconductors and $|x| < 6$ mm for the stacked tapes. The maximum field generated above the centre of the array is increased when using the alternative assembly process, which gives evidence that a re-magnetization of the central sample occurs.

For the bulk superconductors, the maximum field reached with a classic assembly was equal to 471 mT whereas it reaches 495 mT with the alternative assembly, i.e. a 5% increase is measured. For the assembly of stacked tapes, a classic assembly leads to a maximum field of 205 mT against 227 mT for the alternative assembly, i.e. an 11% increase is observed. The alternative assembly method is therefore more efficient for stacked tapes than for bulk superconductors. This fact can be understood when considering the location where the re-organization of the current loops occurs during the approach of the peripheral samples (cf. Figure 4.4). For bulk superconductors, the supercurrents are altered in a region close to the contact surface between the central and the peripheral superconductors. The behaviour of stacked-tape samples differs significantly as the alteration of the supercurrents occurs in a region close to the top surface of the central superconductor. The additional sample is therefore closer to the regions that need to be re-magnetized in the latter case and it makes sense to obtain a more efficient re-magnetization.

Finally, Figure 4.23 shows that the maximum central field predicted by the analytical model ignoring the current redistribution reaches 530 mT and 250 mT for a Halbach array made of bulk superconductors and of stacked tapes respectively, meaning that a further increase of the central field is still possible. This result is fully consistent with the finite element simulations: using an additional superconductor taller than 5 mm is expected to induce a more efficient re-magnetization. Note that the force required to extract the additional sample from the configuration increases with the height of the additional sample. This force is evaluated numerically to 15 N with the finite element model for an additional bulk sample of height 14 mm, such a force strength remains relatively easy to handle. Given that this force scales with the square of the trapped field of individual magnets, it may however become a true challenge when considering superconducting Halbach arrays of larger scale or when exploring the behaviour of superconducting Halbach arrays at lower temperatures. The removal force of the additional superconductor should therefore be considered from the design phase of the experimental system used for the assembly.

4.4 Summary

In this chapter, three methodologies for mitigating the partial demagnetization during the assembly process of superconducting Halbach arrays were proposed and investigated.

First, the potential substitution of bulk $YBa_2Cu_3O_{7-x}$ superconductors with quasi-bulks made of stacked coated conductor tapes was explored. An experimental investigation of the magnetic flux density generated by three permanently magnetized superconducting stacked-tape samples in a linear Halbach array was conducted at 77 K. A finite element model based on the mixed **H**-ϕ-**A** formulation successfully reproduced the flux density distribution measured experimentally. The model emphasized that the field generated by the array is limited by the re-organization of current loops induced in the central stacked-tape sample during the assembly process. Although the occurrence of such current alterations was already observed in chapter 3 when using bulk superconductors, it was shown that the regions of the stacked-tape sample affected by the assembly process differ significantly from their bulk counterparts: the loops generated by the assembly process are confined within the plane of the tapes, flow at the periphery of the central stack, mostly on the high-field side of the array. Replacing bulks with stacked tapes was found to have little effect on the demagnetization of the Halbach array.

Next, the second methodology consisted in modifying geometric parameters of the array: side superconductors (i) of triangular cross-section, (ii) with a vertical offset or (iii) both. Adjustments to both the shape and vertical positioning of the peripheral samples could effectively minimize the induced current re-organization in individual samples within the configuration. Furthermore, the superconducting assemblies maintain notable advantages in terms of the spatial extension of the magnetic flux density gradient in comparison to the performance of a single superconductor.

A modified combination procedure designed to re-magnetize the central superconductor following the approach of the peripheral samples was used as a third procedure. The method consists in maintaining two closely spaced magnetized superconductors stationary while approaching trapped-field magnets from left and right with their magnetization axes perpendicular to their neighbours. Then, the top central sample is removed from the array. It was shown experimentally that a re-magnetization occurs during the retracting motion of the additional top sample, even when the height of the additional sample is only one-third of the height of the main superconductors of the array. Despite not being complete, this re-magnetization allowed to increase the maximum field generated with Halbach arrays made of three bulk superconductors or three stacked tapes by 5% and 11% respectively. Although these enhancements might seem modest as relative quantities, it should be highlighted that the absolute gain can actually be significant, especially when one considers that the present maximum trapped field in a superconductor is 17.6 T [52]. Furthermore, in the context of using a superconducting Halbach array for exerting force on a magnetized particle, the particle experiences a force directly proportional to both its magnetization and the gradient of the magnetic flux density (cf. section 1.5). When the particle is not saturated, re-magnetizing the samples within the Halbach array yields a dual positive effect on the applied force: it increases both the generated magnetic flux density gradient and the magnetization of the particle. Finite element modelling finally showed that a more efficient re-magnetization is possible with this method by using a taller additional superconductor. Provided that the attraction force between the central and the additional superconductor can be handled, the proposed method can be applied with an additional sample presenting a higher trapped field. In that latter case, one could expect a Halbach array made of bulk superconductors or stacked tapes respectively to recover almost their full potential.

5 Gradient generation in background field

As shown in section 1.5, the force acting on a magnetic material results both from the magnitude and the gradient of the magnetic flux density **B**. Therefore, the combinations of magnetized superconductors examined in the previous two chapters serve a dual purpose: (i) generate the necessary gradient in magnetic flux density and (ii) provide the field strength necessary for magnetizing the material on which the force is exerted. The range of the magnetic force obtained with permanently magnetized superconductors suffers both from the decay of the magnetic field strength and the gradient with distance from the configuration.

Considering this limitation, an interesting alternative method has emerged, known as "dipole field navigation" [29–32]. In this method, the magnetic flux density gradient results from the insertion of a soft ferromagnetic core in a large uniform DC field. The presence of the DC field ensures a full magnetization saturation of the material on which the force is acting, while the soft ferromagnetic core introduces a localized distortion of the magnetic field. This distortion of the flux lines generates the required gradient. In such an approach, however, the saturation magnetization of the soft ferromagnetic core employed limits the maximum achievable field gradient.

Given that superconductors are not limited by magnetic saturation, they are attractive candidates for replacing the ferromagnetic cores in dipole field navigation. Nevertheless, the use of superconductors in this context raises several questions since their insertion and mechanical motion in the background DC magnetic field can alter their magnetization. In this chapter, the magnetic flux density gradient generated by two magnetized superconductors in the presence of a background DC field is investigated both experimentally and numerically. The studied configuration consists of two cubic $YBa_2Cu_3O_{7-x}$ superconductors of 6 mm side facing each other. The superconductors are separated by a distance approximately equal to 16 mm and have anti-parallel magnetization directions. This configuration is obtained after a simultaneous magnetization of the samples in the background DC field followed by a rotation of 180° of the top superconductor (as described in more detail in section 2.3.5). The targeted zone of large magnetic flux density gradient corresponds to the region between the superconducting cubes. Although the spatial extent of this area under investigation is rather limited, the comprehensive examination of a system of reduced dimensions offers the opportunity to understand the underlying physical phenomena while keeping the experimental constraints within a manageable limit. The measurements of the magnetic flux gradient will be used to validate the predictions of the

finite element model which can then be exploited to explore a broader range of parameters than those explored experimentally.

The chapter is structured as follows. First, experimental characterizations are carried out on individual samples to refine the critical exponent and the $J_c(B)$ dependence to be used in the finite element model. Next, the trapped-field ability of a cubic superconductor rotated in a DC uniform magnetic field is investigated. The field profiles and field gradients produced using two samples are then investigated and compared to numerical simulations. Finally, the efficiency of a single superconductor, initially field cooled and then subjected to rotation in a constant uniform field, is analyzed.

5.1 Single Sample characterization

5.1.1 Flux creep analysis

The magnetic relaxation of the 6 mm side cubic $YBa_2Cu_3O_{7-x}$ samples is first examined. For all experiments in this chapter, a 45 min waiting time follows the magnetization process. In this section, each sample is considered separately and the flux density is measured at different distances above the surface of the superconductors during the 45 min waiting time. It is then assumed that the flux density vs. time can be described using equation (1.9), and the experimental data are used to adjust the parameters $B_{z,0}$, t_0 and n. Two examples of such fits are shown in Figure 5.1. These fits correspond to the magnetic relaxation of the stationary sample measured in zero background field at 77 K and at 65 K.

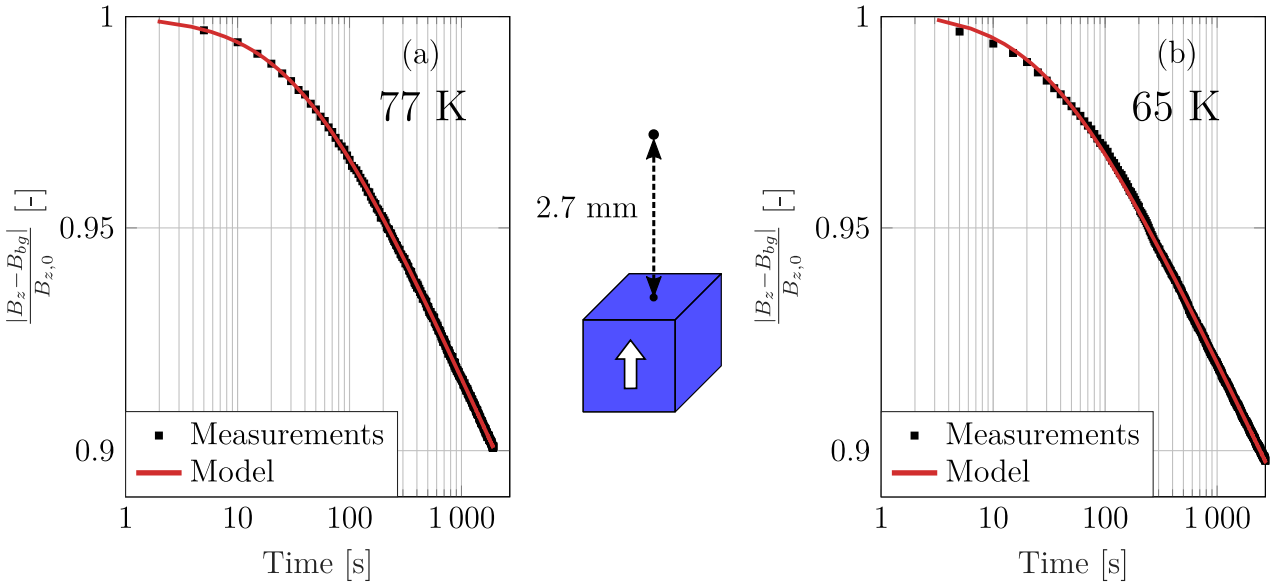

Figure 5.1: Comparison between the relaxation of the magnetic flux density measured 2.7 mm above the surface of the stationary sample and the adjusted Zeldov model. (a) Measurements at 77 K, for the model $B_{z,0}$=82 mT, t_0 = 35 s and n = 39. (b) Measurements at 65 K, for the model $B_{z,0}$=225 mT, t_0 = 31 s and n = 42.

The results of Figure 5.1 show an excellent agreement between the measured magnetic relaxation and the Zeldov model at both temperatures (77 K and 65 K). The values of the critical exponent,

n, extracted from the fits carried out at several distances from the sample, consistently fall within the range of 37 to 42. These critical exponent values align remarkably well with those derived for the cylindrical superconductors from which the cubic samples were extracted [101]. Based on these results, in the finite element simulations conducted in the framework of this chapter, the value n =40 is selected whatever the temperature regime considered. Interestingly, it is also observed experimentally that the critical exponent is almost unchanged with respect to the DC magnetic field strength in which the magnetic relaxation occurs.

5.1.2 Trapped field vs. background DC field

Single stationary superconductor in a background field

Here, the trapped field of a magnetized superconductor when the applied magnetic field does not return to zero during the magnetization process is examined. To investigate this, the cubic $YBa_2Cu_3O_{7-x}$ superconductor of 6 mm side and placed within the stationary sample holder (sample 1) is subjected to the controlled magnetization procedure outlined in section 2.3.5. The magnetic flux density profiles measured at 77 K and at 65 K for several background field strengths are shown in Figure 5.2.

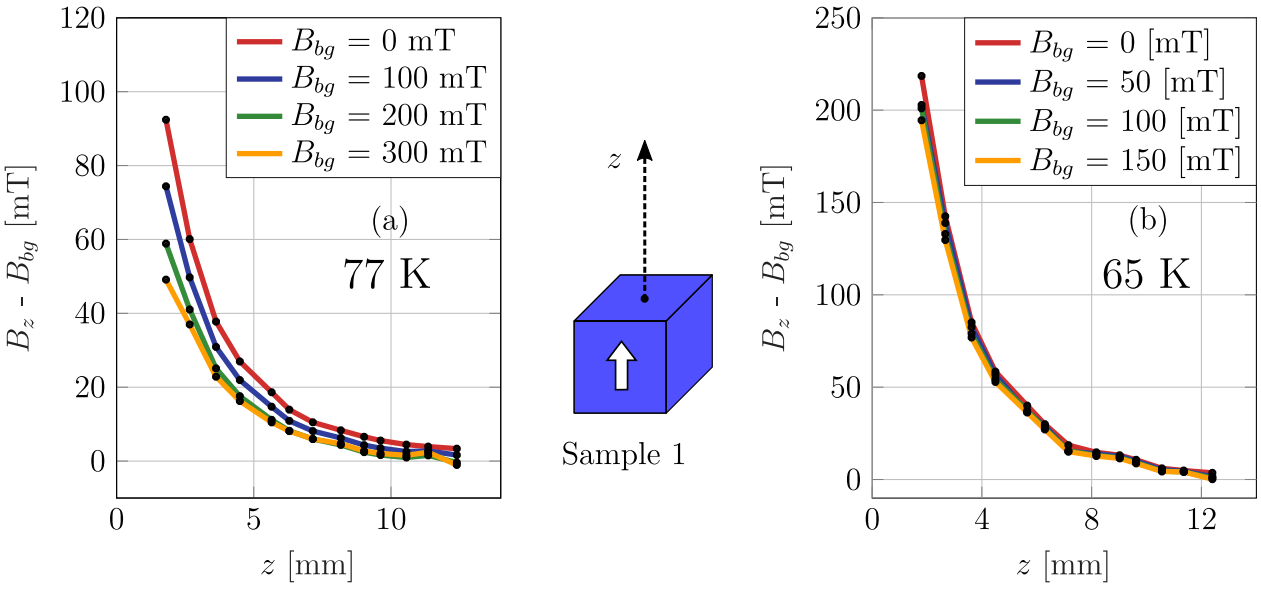

Figure 5.2: Magnetic flux density profile trapped by the stationary cubic superconductor in the presence of a background field along a line perpendicular to the top surface. (a) Measurements performed at 77 K. (b) Measurements performed at 65 K.

At 77 K (Figure 5.2 (a)), the flux density profiles are found to depend on the background DC field strength: when the DC field increases, the trapped magnetic field decreases. This suggests that, at 77 K, the critical current density of the superconductor is dependent on the magnetic field. At 65 K (Figure 5.2 (b)), the trapped-field profiles are much less affected by the DC field. The preliminary conclusion to be drawn is that the trapped field at both temperatures remains significant, even though it decreases with the DC field at 77 K. If higher fields are considered, a full $J_c(B)$ determination using $M(H)$ loops is needed. This is the subject of the next section.

Magnetization loops characterization

The magnetization loop of the orthorhombic $YBa_2Cu_3O_{7-x}$ superconducting sample is measured experimentally within the PPMS using the AC Measurement System option. The applied field is parallel to the c-axis of the superconductor and the measurements are carried out at four temperatures: 77 K, 70 K, 65 K and 59 K. Since the field dependence of J_c is usually less pronounced on lowering temperature, higher field strengths are used at lower temperatures. The measured dipole magnetic moment as a function of the applied field is shown in Figure 5.3.

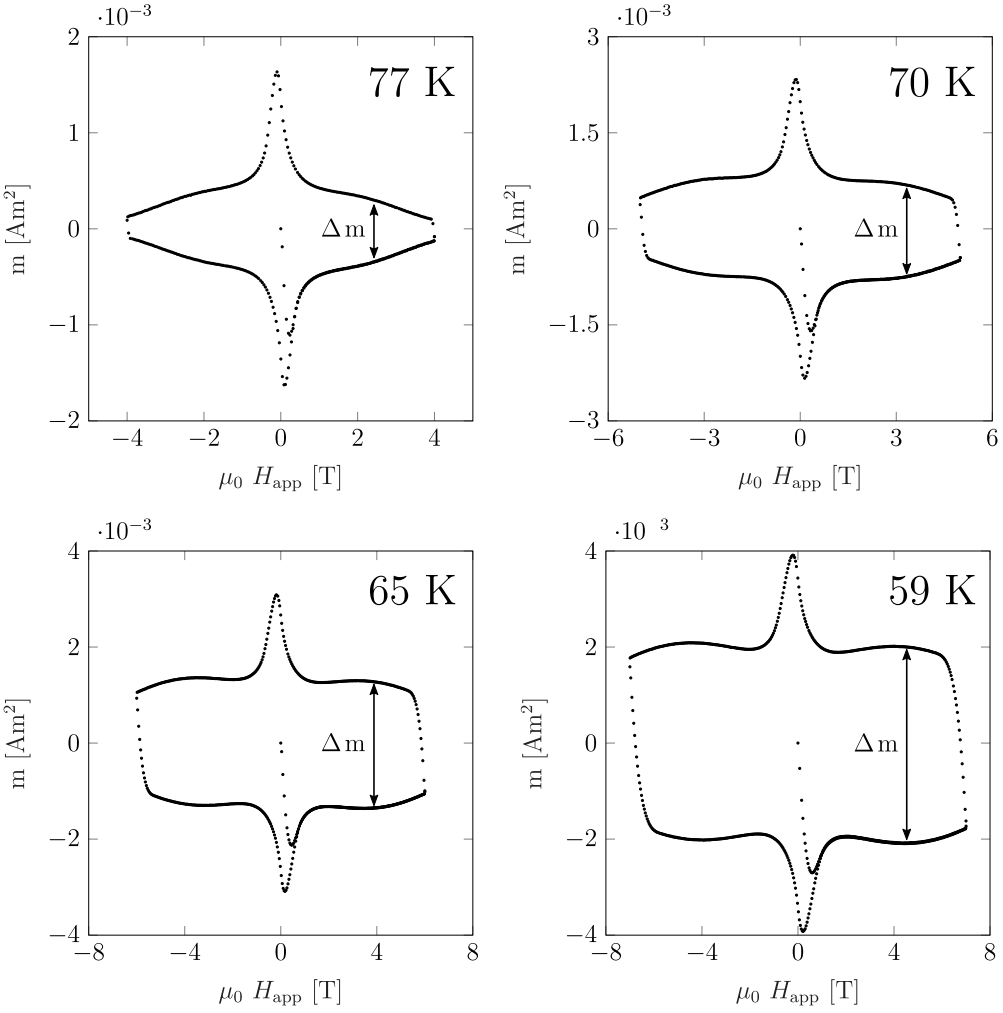

Figure 5.3: Magnetization loops $m(\mu_0 H_{app})$ of an orthorombic $YBa_2Cu_3O_{7-x}$ sample of dimensions $1.54 \times 1.75 \times 5.03$ mm^3 measured at 77 K, 70 K, 65 K and 59 K.

It is assumed that the sample is in the critical state, fully magnetized, with a uniform critical current density, noted J_c, throughout the sample and that the supercurrents flow in square loops strictly perpendicular to the crystallographic c-axis. For an orthorhombic sample of dimensions $2a \times 2b$ parallel to the crystallographic ab-planes and of dimension c parallel to the c-axis, one has [206]:

$$\begin{aligned} m &= \frac{1}{2}\int_V \boldsymbol{r} \times \mathbf{J}\ dV, \\ &= J_c\, 2a^2bc\left(1-\frac{a}{3b}\right). \end{aligned} \tag{5.1}$$

The magnetic moment m at each applied field is computed as the arithmetic mean of the values obtained during both ascending and descending sweeps of the applied field, i.e. $m(\mu_0 H_{app}) = \frac{\Delta m(\mu_0 H_{app})}{2}$. The critical current density deduced from the measurements thus writes:

$$J_c(\mu_0 H_{app}) = \frac{\Delta m(\mu_0 H_{app})}{4a^2bc\left(1-\frac{a}{3b}\right)}\ . \tag{5.2}$$

Strictly speaking, the condition of full penetration for equation (5.2) to remain valid requires that the magnetic field H_{app} is between the full penetration field H_p (i.e. the currents induced on increasing the field flow across the entire cross-section) and $H_{max} - 2H_p$ (i.e. the direction of induced currents when decreasing the field is the same across the entire cross-section).

Furthermore, equation (5.2) also assumes that the critical current density is homogeneous over the whole sample. When considering superconducting materials exhibiting field-dependent critical current densities, this assumption is not strictly verified. Nevertheless, the impact of the non-uniform J_c can be considered negligible provided that $J_c(\mu_0 H_i) \simeq J_c(\mu_0 H_{app})$, where H_i denotes the magnetic field at the centre of the sample [206].

In order to verify wether the $J_c(B)$ determined through the equation (5.2) makes sense even outside the $[H_p,\ H_{max} - 2H_p]$ interval, the following approach is used. An analytical $J_c(\mu_0 H_{app})$ dependence is assumed [207–209], and the parameters are adjusted to ensure the best possible match with J_c measurements determined from equation (5.2). The analytical law is then introduced in a finite element simulation computing numerically the magnetization curve. The validity of the functional dependence $J_c(\mu_0 H_{app})$ is assessed through the comparison of the magnetization curve obtained from measurements and that computed numerically.

As an example, one can use a first $J_c(\mu_0 H_{app})$ dependence corresponding to the widespread Kim's model [206] i.e.:

$$J_c(\mu_0 H_{app}) = \frac{J_{c,0}}{1+\frac{\mu_0 H_{app}}{B_0}}\ . \tag{5.3}$$

The magnetization curves computed with the finite element model using a Kim dependence are shown in Figure 5.4.

The agreement is poor since Kim's model assumes a monotonously decreasing $J_c(B)$. The experimental magnetic moment of the sample, however, exhibits a peak at high fields. This feature has already been observed for bulk superconductors in the literature [210–214] and is commonly referred to as the fishtail effect. To model this non-monotonous field dependence of J_c, the Kim's model needs to be extended by adding a Lorentzian term in the $J_c(\mu_0 H_{app})$ relationship [209]:

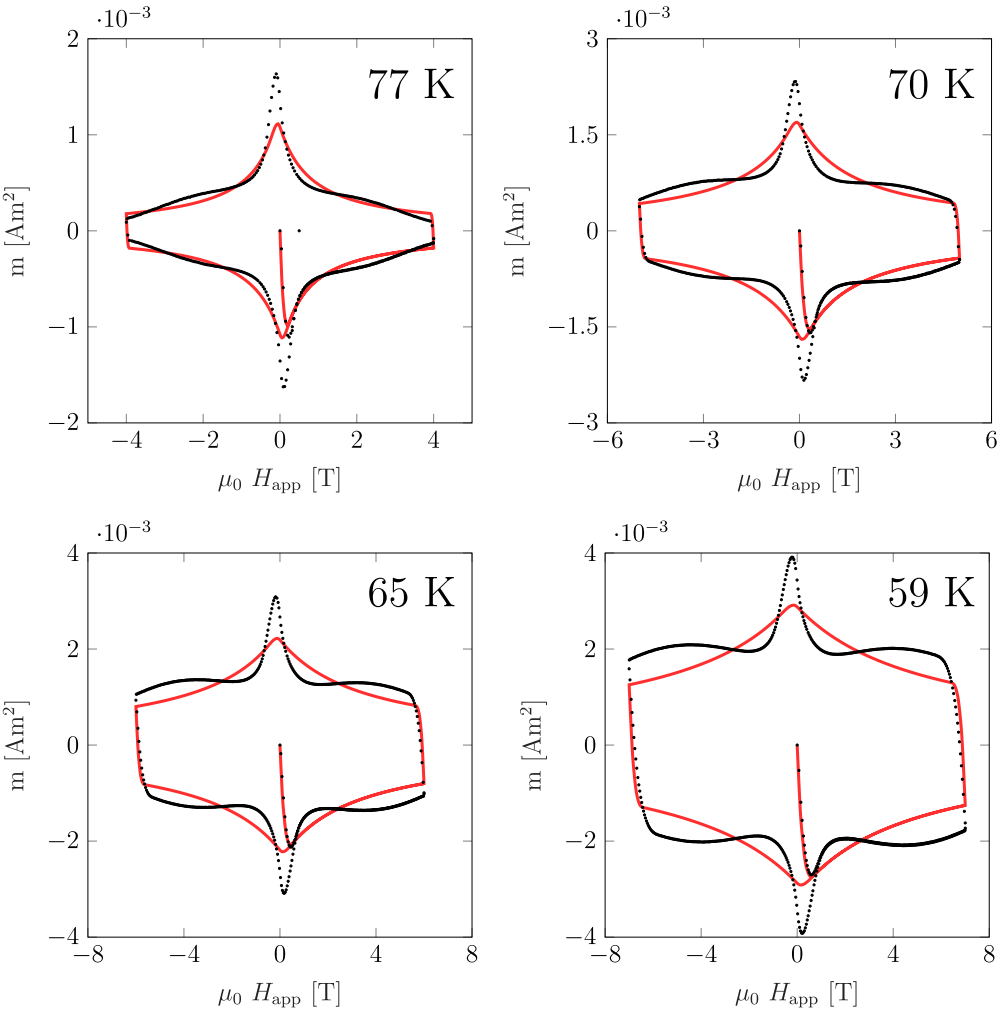

Figure 5.4: Comparison between the measured magnetization curves (black dots) and the one computed with the finite element model using a Kim dependence of the critical current density within the power law (red curve) at 77 K, 70 K, 65 K and 59 K.

$$J_c(\mu_0 H_{app}) = J_{c,0}\left[\frac{1}{1+\frac{\mu_0 H_{app}}{B_0}} + \frac{a}{(\frac{\mu_0 H_{app}}{B_0} - b_1)^2 + (b_2)^2}\right]. \tag{5.4}$$

In equation (5.4), $J_{c,0}$ and B_0 are the original parameters of Kim's model. The Lorentzian term reaches its maximum value when $\frac{\mu_0 H_{app}}{B_0} = b_1$ and the magnitude of this maximum is $\frac{a}{b_2^2}$. The parameter b_2 is defined such that the Lorentzian reaches half of its maximum value when $\frac{\mu_0 H_{app}}{B_0} = b_1 \pm b_2$, this parameter is often referred to as the scale parameter of the Lorentzian.

It has been shown that equation (5.4) is sufficiently general to parametrize a variety of fishtail effects and can be used to approximate a wide range of magnetization loop shapes. The magnetization curves computed with the finite element model using equation (5.4) are shown in Figure 5.5.

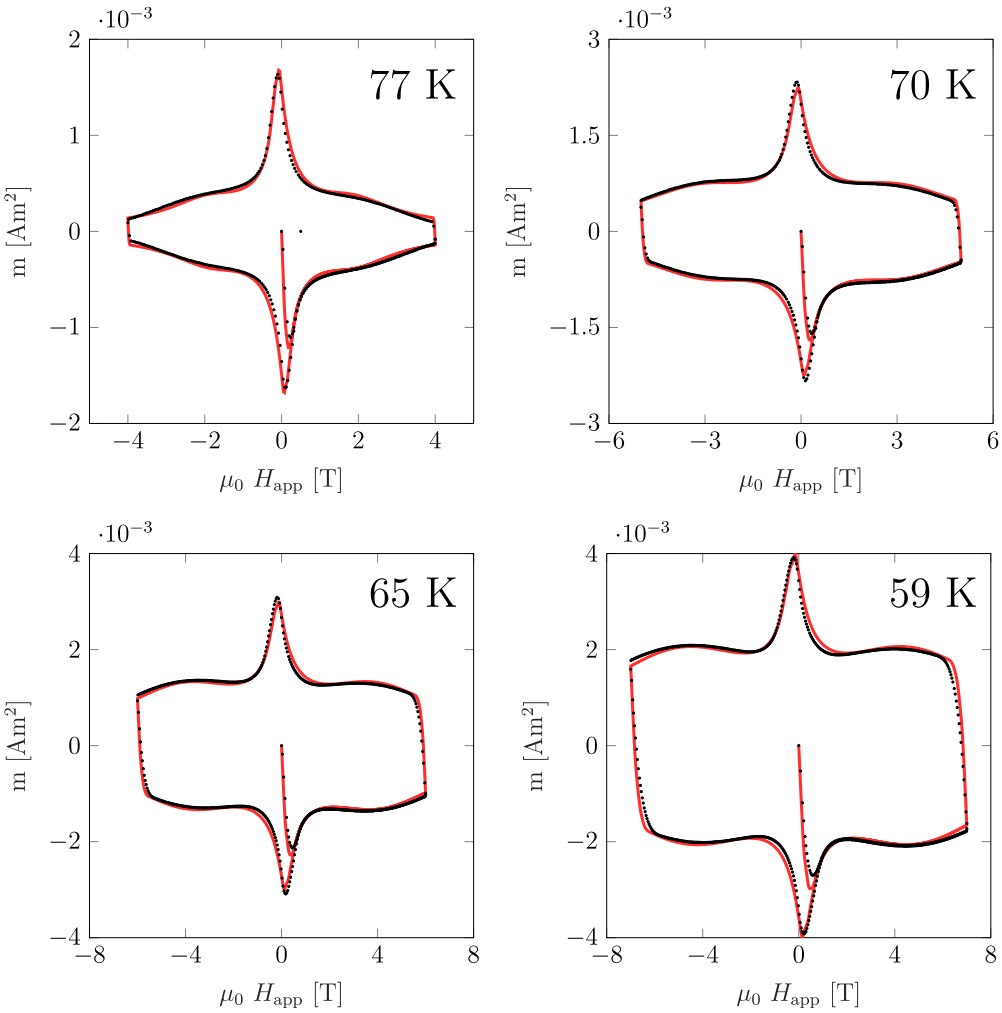

Figure 5.5: Comparison between the measured magnetization curves (black dots) and the one computed with the finite element model using an extended Kim dependence of the critical current density within the power law (red curve) at 77 K, 70 K, 65 K and 59 K.

At each investigated temperature, the measured magnetization curve is very satisfyingly approximated with the finite element model. This gives confidence in the adjustment method of the parameters of equation (5.4). The values of the parameters of equation (5.4) at each temperature are shown in Table 5.8, together with the critical current density value at zero field as predicted by equation (5.4).

Validation of the model

From now on, it is considered that the cubic $YBa_2Cu_3O_{7-x}$ superconducting samples exhibit a field dependence of the critical current density equal to that determined above for the orthorhombic sample. Using this $J_c(\mu_0 H_{app})$ law, the trapped-field measurements of a single cubic superconductor are compared to the predictions of the finite element model. This comparison is first performed for samples 1 and 2 at 65 K with no background DC field. The purpose is to determine, as precisely as possible, the true distance between each sample and each Hall probe once the samples are installed within the measurement system operated at cryogenic temperature. This distance could be evaluated theoretically based on the mechanical

	$J_{c,0}$ [A m^{-2}]	B_0 [mT]	a [-]	b_1 [-]	b_2 [-]	$J_c(0)$ [A m^{-2}]
77 K	9.9×10^8	125.8	8	15.1	10	10.1×10^8
70 K	10.8×10^8	249.3	17.7	12.5	9.9	11.6×10^8
65 K	13.7×10^8	306.9	35.1	13	11.1	15.3×10^8
59 K	19.3×10^8	274	94.3	17.4	16.7	22.4×10^8

Table 5.8: Values of the numerical parameters involved in the extended Kim's model (equation (5.4)) after adjustment to the magnetization curves measured at 77 K, 70 K, 65 K and 59 K.

drawings or measured at ambient temperature with a calliper. However, given the potential for mechanical deformations when the setup is operated at cryogenic temperatures, it is decided to adjust the distance between each sample and the closest Hall sensor to obtain the best agreement possible between the measured and the simulated flux density profile. These distances are then assumed to remain unchanged for all the other experiments (i.e. the distances are assumed to be temperature-independent in the range 59 K – 77 K). The resulting comparison and a schematic representation of the meaning of the different distances are presented in Figure 5.6.

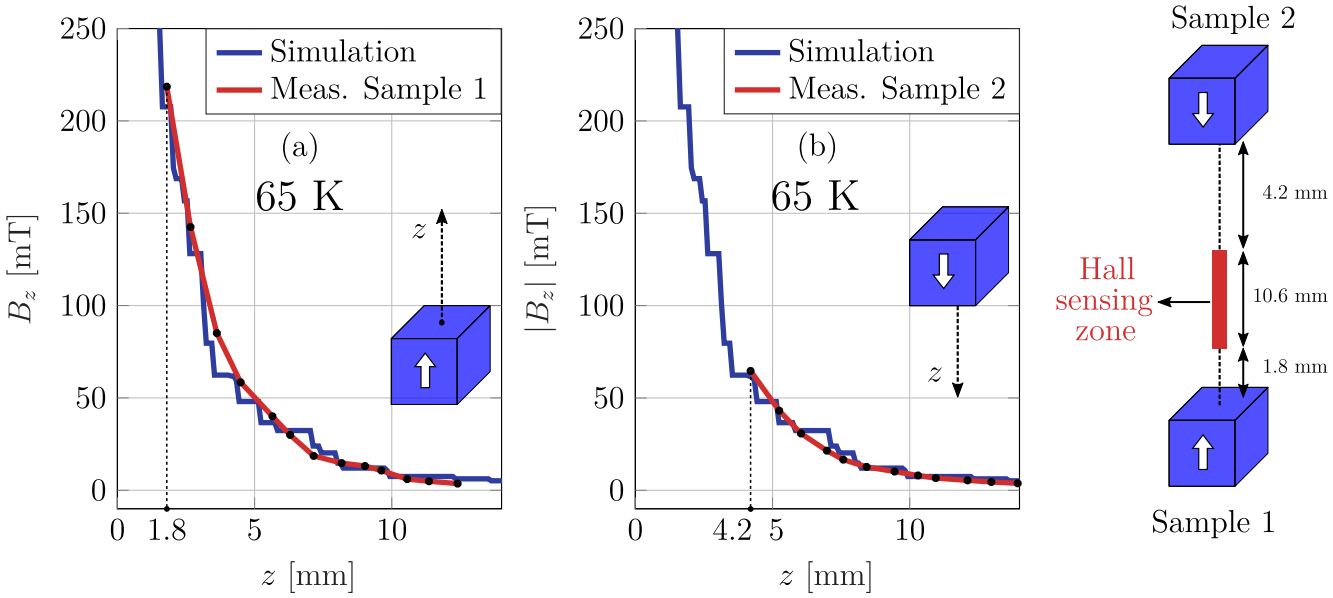

Figure 5.6: Comparison between the magnetic flux density profile measured experimentally at 65 K with no background field and the predictions of the finite element model. (a) Stationary sample. (b) Rotative sample.

From Figure 5.6 (a), the agreement between the flux density profile of the stationary sample measured at 65 K and the prediction of the finite element model is very satisfying provided that the distance between the top surface of that sample and the nearest Hall sensor in the probe is set to 1.8 mm. In Figure 5.6 (b), a good agreement is also achieved when the distance to the closest Hall sensor is equal to 4.2 mm for the rotative sample. A comparison between the magnetic flux density profiles obtained for samples 1 and 2 measured individually at 77 K with no background magnetic field and the finite element model predictions are shown in Figure 5.7.

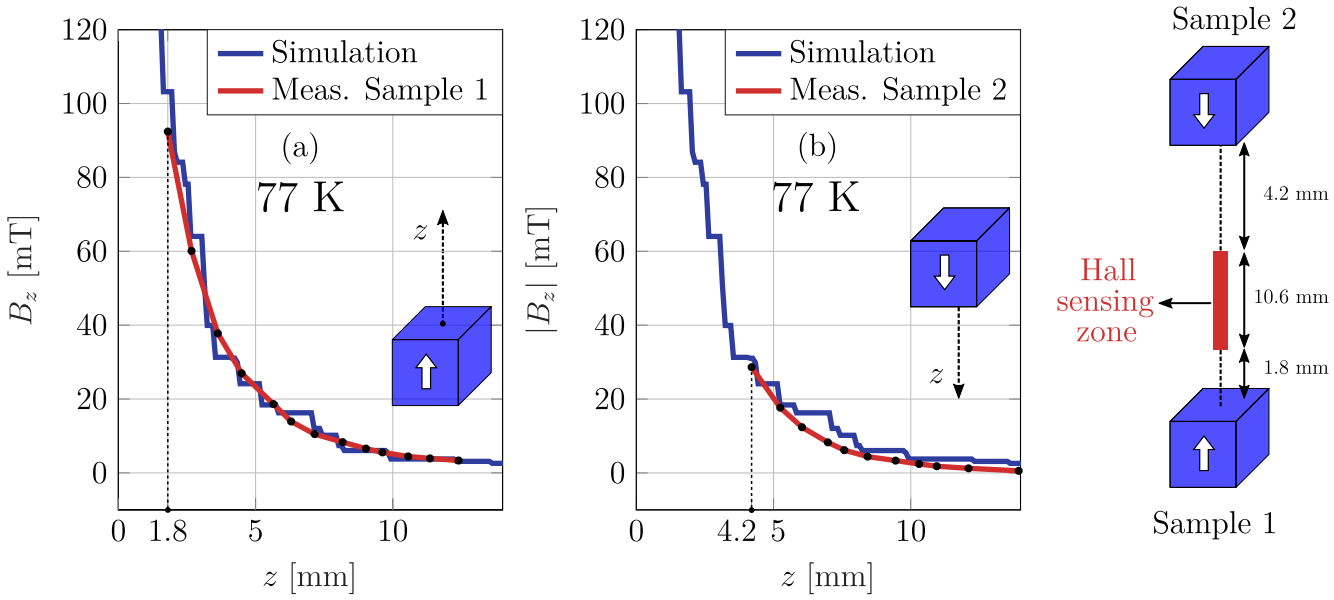

Figure 5.7: Comparison between the magnetic flux density profile measured experimentally at 77 K with no background field and the predictions of the finite element model. (a) Stationary sample. (b) Rotative sample.

A very satisfying agreement is also obtained at this temperature with the same distances. These results give confidence both in the distances determined above and in the results given by the finite element model. Knowing the distance between each sample and the Hall sensing zone as well as the height of the Hall sensing zone (∼10.6 mm, derived in section 2.3.2), the experimentally determined distance between the two superconductors in the experimental system at cryogenic temperature can be deduced. This distance is equal to 16.6 mm and compares satisfactorily to the distance expected from the mechanical drawings (∼16 mm).

Now that the distances between the Hall sensors and the superconducting samples in the system are known, the measured magnetic flux density trapped by a superconducting sample at a given distance from its surface as a function of the background field can be compared to the predictions of the finite element model. These comparisons at both 77 K and 65 K, are presented in Figure 5.8.

Figure 5.8 (a) deals with results obtained at 77 K. At zero background DC field, the predicted value exceeds the measured one by 3 mT. This discrepancy is considered very satisfactory considering that the critical current density was determined from measurements carried out on a different sample. When increasing the background magnetic field at the end of the magnetization process, the agreement between simulation and measurement remains. Similar observations can be made at 65 K (Figure 5.8 (b)), for which the decrease is much smaller than at 77 K. This suggests that the diminution of the trapped field due to the non-zero background field, already observed in Figure 5.2, can be reproduced using the $J_c(B)$ dependence introduced in the finite element model at 77 K and at 65 K.

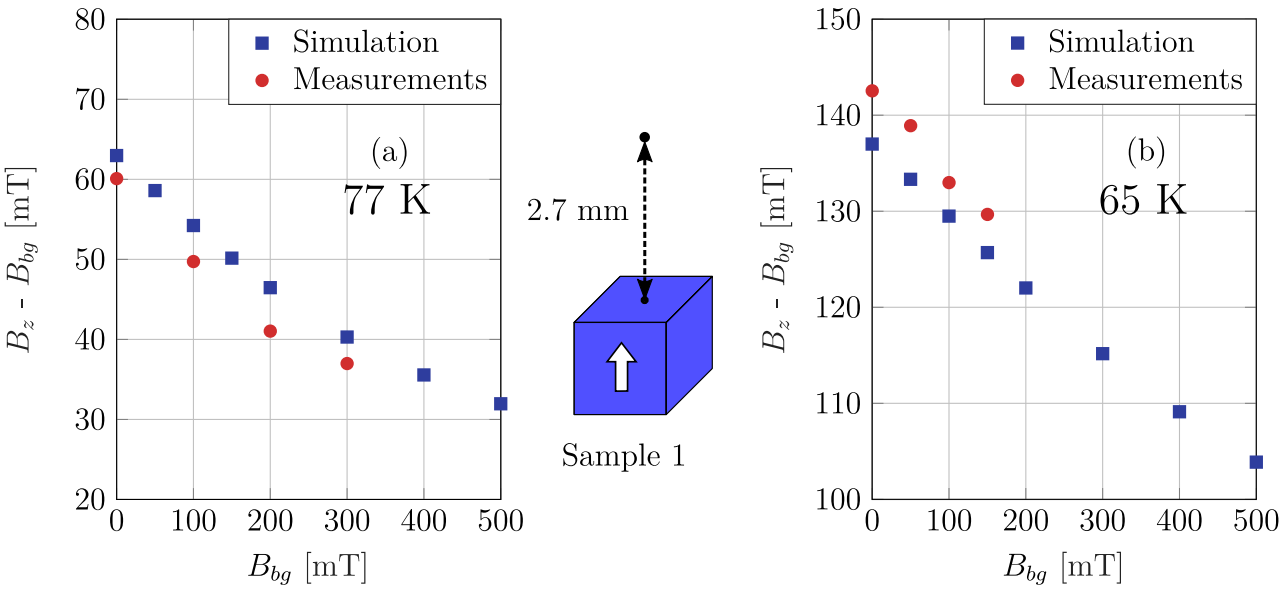

Figure 5.8: Comparison between the simulated and the experimental trapped field evaluated 2.7 mm above the surface of the stationary superconducting sample for different value of the background field. (a) 77 K. (b) 65 K.

5.2 Single superconductor rotated in a background field

Before considering configurations involving multiple superconductors, the field trapped by a magnetized superconductor after a rotation of 180° in a background field is investigated in the present section. The goal of these sets of experiments is to investigate the possible demagnetization caused by the rotation process. Figure 5.9 shows the magnetic flux density measured 4.2 mm above the surface of sample 2 at the end of the experimental procedure recalled briefly here. The samples are magnetized either in field-cooled or in zero-field-cooled conditions with a maximum applied field denoted B_{max} and a field sweep rate of 15 mT s^{-1}. The field-decreasing step of the magnetization procedure stops when the applied field reaches the threshold B_{Bg}, then it remains unchanged for the rest of the experiment. Following the magnetization, the rotative sample holder is rotated by an angle of 180° at a constant speed of 5° s^{-1} and the magnetic flux density distribution is then measured.

The measurements are compared to the predictions of the finite element model. The current distributions within the x-z cut plane including the centre of the superconductor, computed before and after the rotation, are presented in Figures 5.9 (b), (c), (e) and (f) for two specific background fields.

Measurements results at 77 K (red dots in Figure 5.9 (a)) are first considered. Comparing the two first data points: one observes that a 180° rotation performed within a background magnetic field of 100 mT has minimal influence on the trapped magnetic field measured above the surface of the superconductor. This gives evidence that the superconducting material retains nearly its entire trapped-field ability provided that the background magnetic field during the rotation remains below the 100 mT threshold. Above this threshold, the magnitude of the trapped magnetic field exhibits a decreasing trend as the background DC magnetic field is increased.

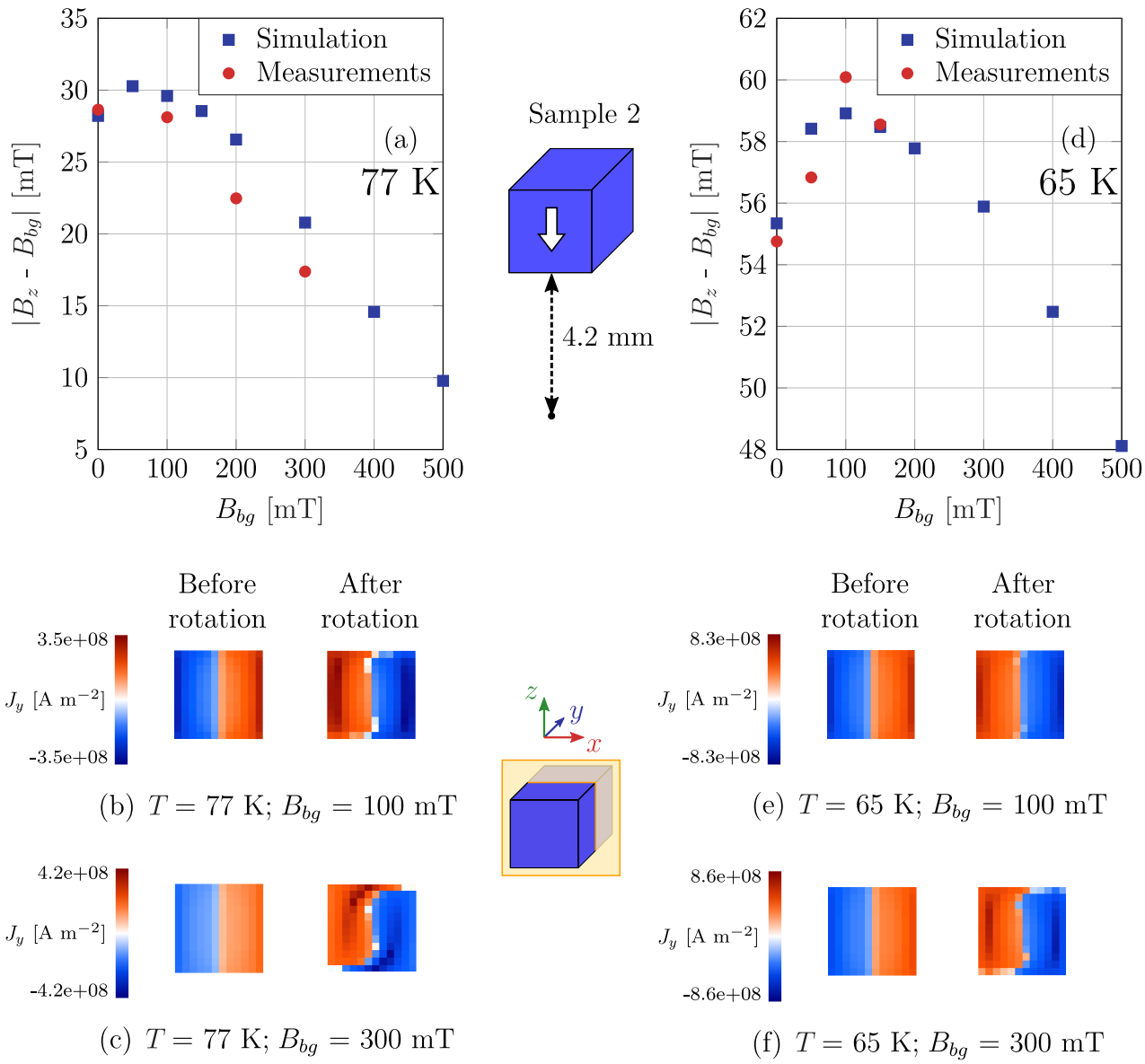

Figure 5.9: (a) and (d) Comparison between the simulated and the experimental trapped field evaluated 4.2 mm above the surface of the rotative superconducting sample at the end of the experimental procedure ($B_{max} \neq B_{bg}$) for various values of the background field at 77 K and 65 K respectively. (b), (c), (e) and (f) Current density distribution within the x-z cut plane including the centre of the superconductor computed with the finite element model before and after the rotation for specific values of the temperature and background field.

Remarkably, a similar behaviour is observed for the numerical simulations (blue squares in Figure 5.9 (a)): 180° rotations within background magnetic fields smaller than 100 mT are even expected to increase slightly the final trapped magnetic field. Although the finite element model captures correctly the general trend observed in the trapped magnetic field as the background field strength is increased, there is a 16 % difference between the measured data and simulations for $B_{bg} = 200$ mT and $B_{bg} = 300$ mT. Since supercurrent components parallel to the c-axis may be induced during the rotation, incorporating an anisotropic critical current density within the

finite element model could potentially enhance the accuracy of the numerical predictions.

It is of interest to investigate the current density distribution computed numerically before and after the rotation. Figure 5.9 (b) shows the results for a 100 mT background field. Before the rotation, the x-z cut plane is divided into two halves where the supercurrents J_y display opposite signs, as can be expected for a cubic superconductor in the critical state. After the rotation, it can be noticed that the amplitude of the current density is altered, however, the qualitative distribution remains approximately identical. Considering the results at 300 mT (Figure 5.9 (c)) instead of 100 mT, the supercurrents J_y changes signs (i) in the bottom region of the left half of the cross-section of the sample and (ii) in the top region of the right half of the cross-section of the sample. The current density alteration is thus more pronounced than at 100 mT. This re-organization of the current loops is consistent with the reduction of the measured trapped field. Similar current re-distributions have already been encountered in the literature in the context of crossed-field experiments [215]. Such a similarity is not surprising since during the rotation, the superconducting sample experiences a time-varying field component perpendicular to its main magnetization. This field component can be written $B_{bg}\sin(\alpha)$, where α denotes the angle formed by the c-axis of the superconductor with the z-direction.

A similar approach is employed for analyzing the results obtained at 65 K. The experimental data are shown in Figure 5.9 (d). Starting from a zero background field, the trapped field measured after the 180° rotation is found to increase with increasing background field strength, reaches a maximum for $B_{bg} = 100$ mT and then starts decreasing. Remarkably, the same trend is found in the numerically computed values, which suggests that the finite element model captures correctly the overall behaviour measured at this temperature regime as well. Interestingly, it can be noticed that for all the non-zero background field strengths investigated experimentally at 65 K ([50-150] mT), the trapped field measured after the rotation exceeds the one measured in zero background field. Numerical simulations support this observation and predict that this holds true as long as $B_{bg} \leq 300$ mT. Comparing this threshold background field to the limit of 100 mT found at 77 K, decreasing the temperature is not only beneficial in increasing the field and field gradient achievable but also in extending the range of background field in which the superconductor can be rotated without demagnetization. Finally, Figures 5.9 (e) and (f) show that supercurrents J_y do not change sign in the top right and bottom left region of the cut plane for background field smaller than or equal to 300 mT.

Additional finite element simulations are conducted on superconducting cubes of various side lengths to explore the impact of the geometrical size on the threshold background field. In these simulations, the field dependence of the critical current density is the same as the one used above to model experiments carried out at 77 K. Figure 5.10 shows the magnetic flux density computed 4.2 mm above the surface of the sample as a function of the background field in which the rotation is performed. Since the trapped field of the modelled superconducting cube increases with its side length, the results are normalized relative to B_c which corresponds to the trapped field evaluated 4.2 mm above the surface of the sample in zero background field.

From Figure 5.10, for a superconducting cube with dimensions of 6 mm, the complete preservation of trapped-field ability during rotation (i.e. $(B_z\text{-}B_{bg})/B_c \geq 100\%$) is anticipated as long as the background magnetic field (B_{bg}) remains below 100 mT. For larger samples, it appears that

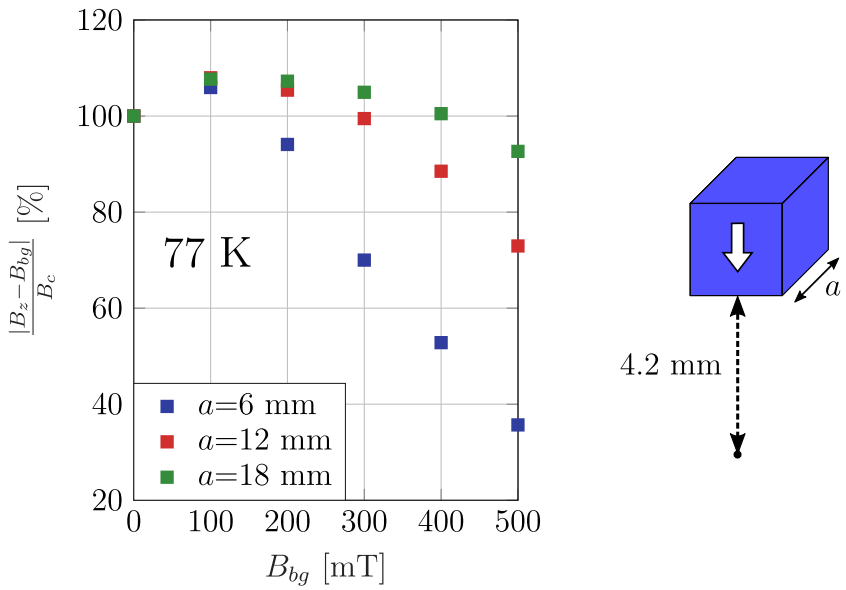

Figure 5.10: Numerical evaluation of the trapped field 4.2 mm above the surface of a superconducting cube of side length a at the end of the experimental procedure ($B_{max} \neq B_{bg}$) for various values of the background field. The results are normalized with respect to B_c which corresponds to the trapped field evaluated 4.2 mm above the surface of the sample in no background field.

this threshold field increases to 300 mT and 400 mT for cubes with side lengths of 12 mm and 18 mm, respectively. Consequently, it can be inferred that the use of larger samples extends the range of background magnetic fields within which the superconductor can undergo rotation without demagnetization.

5.3 Configurations using two samples

5.3.1 Zero background field

In the previous section, the demagnetization phenomenon of a rotating superconducting sample arising from its interaction with a constant background field was investigated. However, in experiments involving two superconducting samples, the background magnetic field is not the only potential source of current density alteration during rotational motion. The rather short distance between the magnetized superconductors during the rotation may result in a mutual demagnetization effect, similar to observations performed in chapters 3 and 4 within the framework of translational motions. In the following, configurations using two superconductors are first investigated in the absence of any background field. The goal is to determine whether a demagnetization effect arises due to the interaction between the two cubic samples positioned at a separating distance of 16.6 mm.

The simultaneous magnetization of the superconductors followed by the 180° rotation of the top sample is simulated using the finite element model both at 77 K and 65 K. The current density distribution in the x-z cut plane including the centres of both superconductors computed before and after the rotation is shown in Figure 5.11.

Figure 5.11 (a) shows that within each sample, the current density distribution remains un-

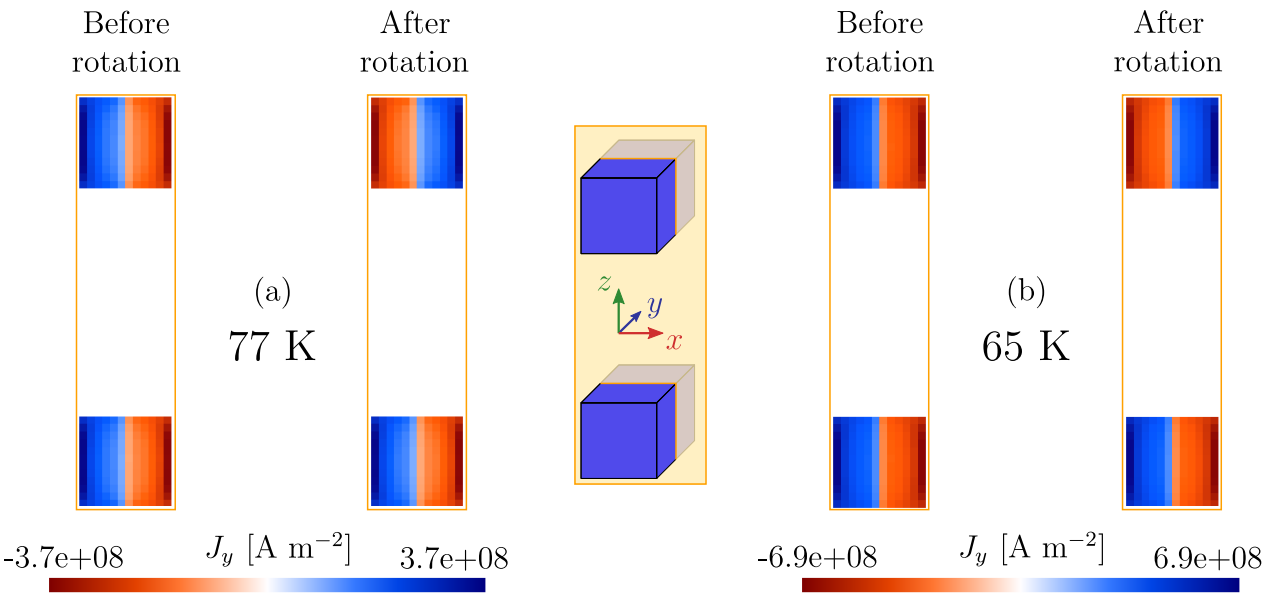

Figure 5.11: Current density distribution in the x-z cut plane including the centres of both superconductors computed with the finite element model before and after the rotation and in the absence of any background field. (a) 77K. (b) 65 K.

changed after the rotational process when compared to the distribution computed prior to any motion. This observation implies that, for such a separating distance, there is no discernible magnetic interaction between the samples. The same conclusion can be drawn at 65 K (Figure 5.11 (b)).

The configuration with two samples and no background field is then investigated experimentally. In Figures 5.12 (a) and (b), the measured magnetic flux density profile is compared to the one measured when only one sample, either sample 1 or sample 2, is placed in the experimental setup. Based on the measured profile, a cubic smoothing spline is performed and the derivative of this smoothed curve is computed to approximate the magnetic flux density gradient in each experiment, the results are shown in Figures 5.12 (c) and (d).

At 77 K (Figure 5.12 (a)), and more particularly the region close to the stationary sample ($z < 5$ mm), the profile measured for two samples is close to the measurements obtained for sample 1 only. Similarly, in the region close to the rotating sample ($z > 10$ mm), the profile in the configuration involving both samples is almost superimposed with the one measured in the presence of sample 2 only. These observations confirm experimentally that the distance between the superconducting samples is large enough to avoid any demagnetization due to the interaction between them during the rotation. In the intermediate region (5 mm $< z <$ 10 mm), each sample provides a non-negligible contribution to the total magnetic flux density. In this region, the profile measured in the configuration with two superconductors can be viewed as the sum of each individual contribution, which results in a different profile. A comparison between the magnetic flux density profile measured for the configuration with two superconductors and the sum of the contribution of sample 1 and sample 2 measured individually is presented in Appendix B.4. The magnetic flux density gradient computed for each case in that specific

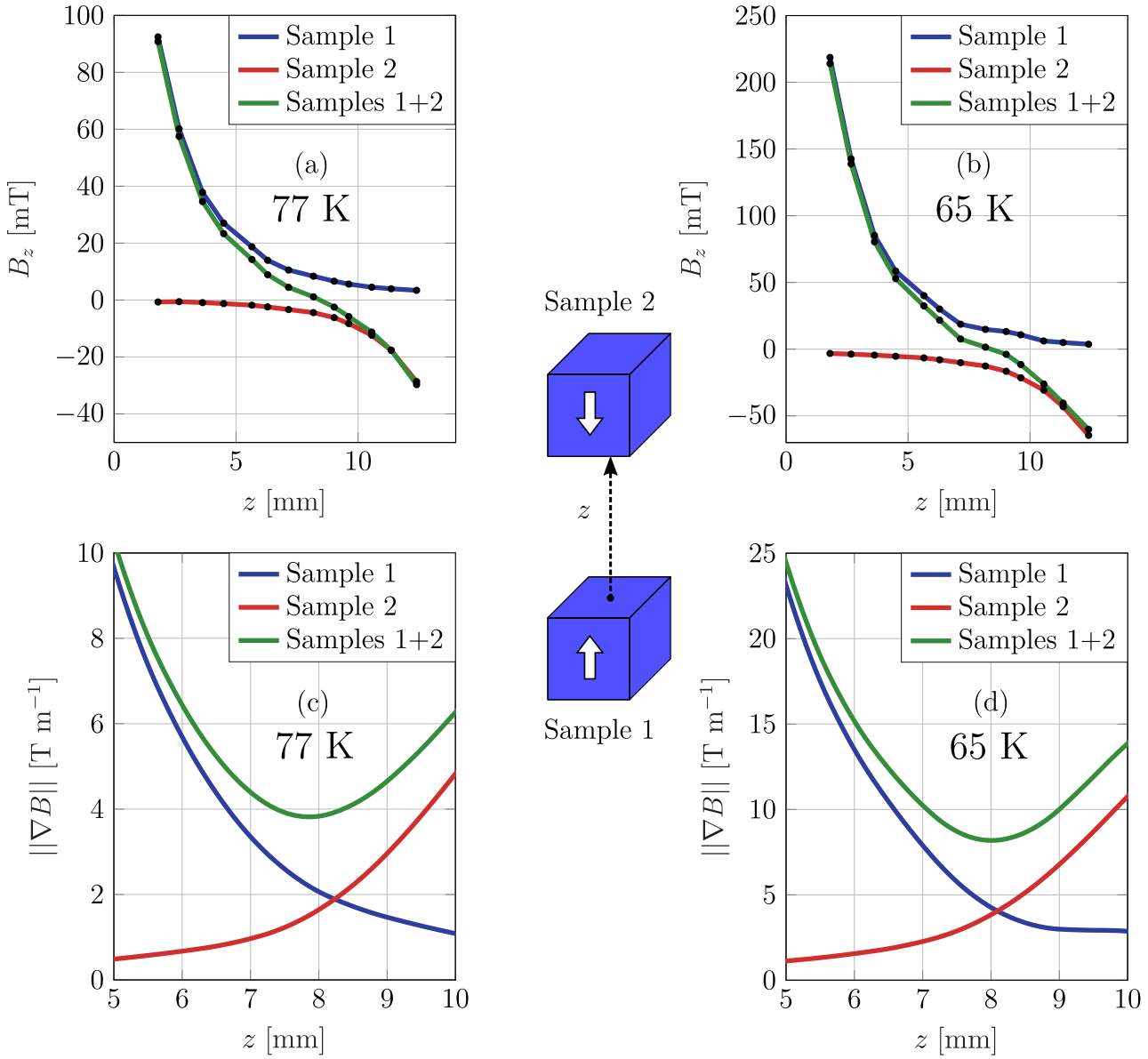

Figure 5.12: (a) and (b) Magnetic flux density profile measured at the end of the experimental procedure ($B_{max} \neq B_{bg}$) for configurations with either one or two superconductors with no background field at 77 K and 65 K respectively. (c) and (d) Gradient of the magnetic flux density profile for configurations with either one or two superconductors with no background field at 77 K and 65 K respectively.

region is plotted in Figure 5.12 (c): a higher field gradient is obtained in the intermediate region with the configuration with two samples. The gradient exceeds 3.8 T m^{-1} across the whole intermediate region, which is not the case for single sample configurations. The samples are therefore placed close enough to shape the magnetic flux density profile and generate, in between them, a higher field gradient than when they are employed alone.
As can be observed in Figures 5.12 (b) and (d), the behaviour measured at 65 K is qualitatively the same. The major difference is that higher fields and field gradients are reached, the magnetic flux density gradient generated at 65 K exceeds 8.4 T m^{-1} across the whole intermediate region.

The question that naturally arises is whether these increased values of magnetic flux density gradients remain unchanged when considering the existence of a non-vanishing background field; this topic is addressed in the next section.

5.3.2 Non-zero background field

Here the fields and field gradients achievable with two superconductors in the presence of a background field are investigated. This configuration combines the challenges discussed previously: the preservation of a non-zero background magnetic field at the end of the magnetization process and the 180° rotation of a superconductor within this background field while being in proximity to another magnetized sample. The magnetic flux density profiles and gradients are shown in Figure 5.13.

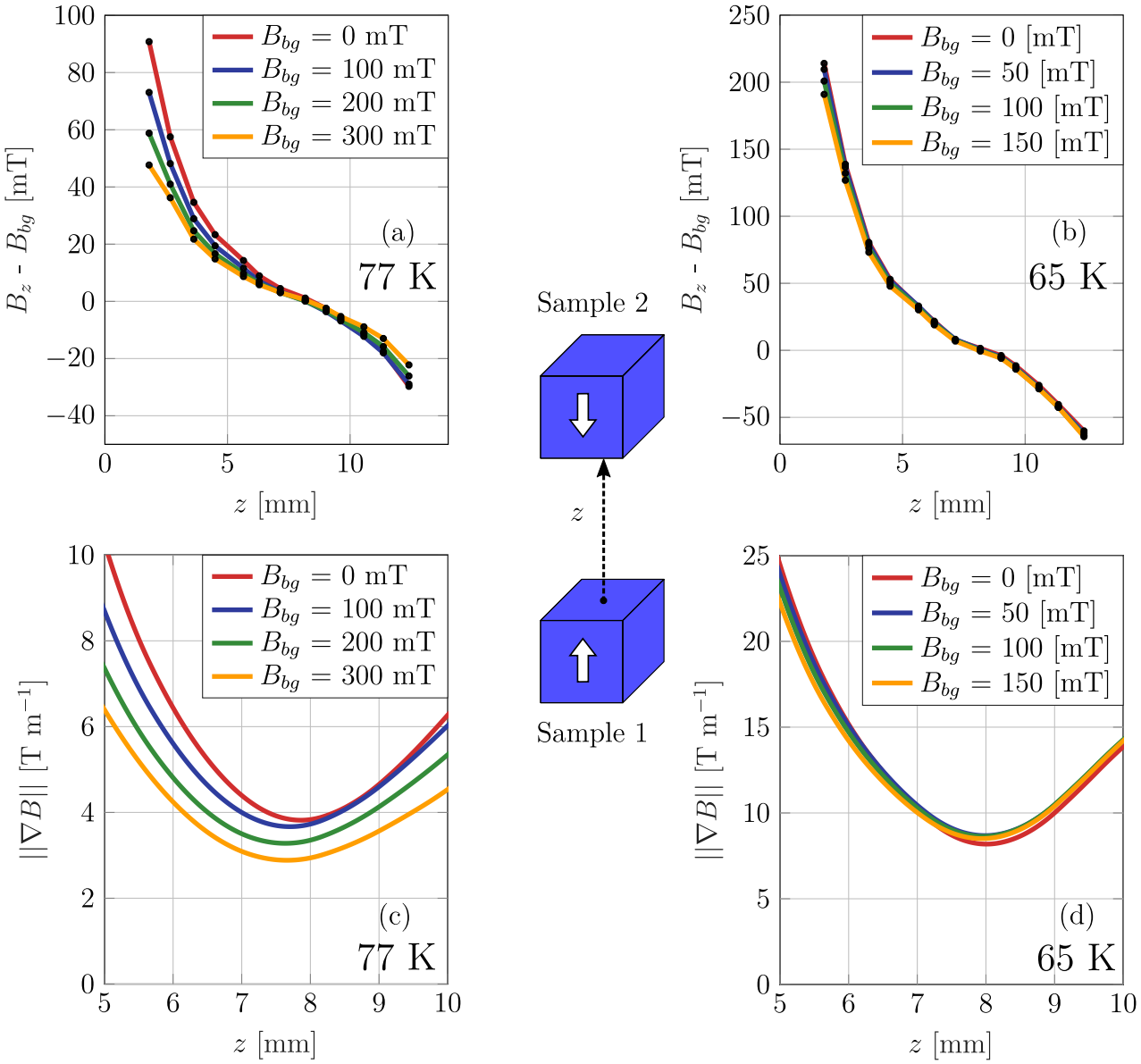

Figure 5.13: (a) and (b) Magnetic flux density profile measured at the end of the experimental procedure ($B_{max} \neq B_{bg}$) for a configuration with two superconductors for various values of the background field at 77 K and 65 K respectively. (c) and (d) Gradient of the magnetic flux density profile for configurations with either one or two superconductors for various values of the background field at 77 K and 65 K respectively.

At 77 K, in the region close to the stationary sample ($z < 5$ mm in Figure 5.13 (a)), the total magnetic flux density is found to decrease with increasing background DC field, which can be attributed to the $J_c(B)$ dependence. In the region close to the rotating sample ($z > 10$ mm), a decrease in the trapped field measured is only apparent when $B_{bg} \geq 200$ mT, which is a consequence of the current re-organization induced by the rotation of sample 2 in the background field. The magnetic flux density gradient generated in the intermediate region (Figure 5.13 (c)) decreases with increasing background DC field. Nevertheless, it should be pointed out that in a background of 300 mT at 77 K, the measured gradient throughout the intermediate region exceeds 2.9 T m^{-1}. This is not achievable when using only one of the samples even in a zero background DC field (cf. Figure 5.12 (c)).

Figures 5.13 (b) and (d) respectively show that, at 65 K, the different magnetic flux density profiles measured can hardly be distinguished from one another and that the magnetic flux density gradient exceeds 8.4 T m^{-1} across the entire intermediate region whatever the background field strength in the range [0-150] mT.

Two duplicate experiments are conducted at 59 K to illustrate the potential of the configuration at even lower temperatures. The flux density profiles and gradients measured are presented in Figure 5.14.

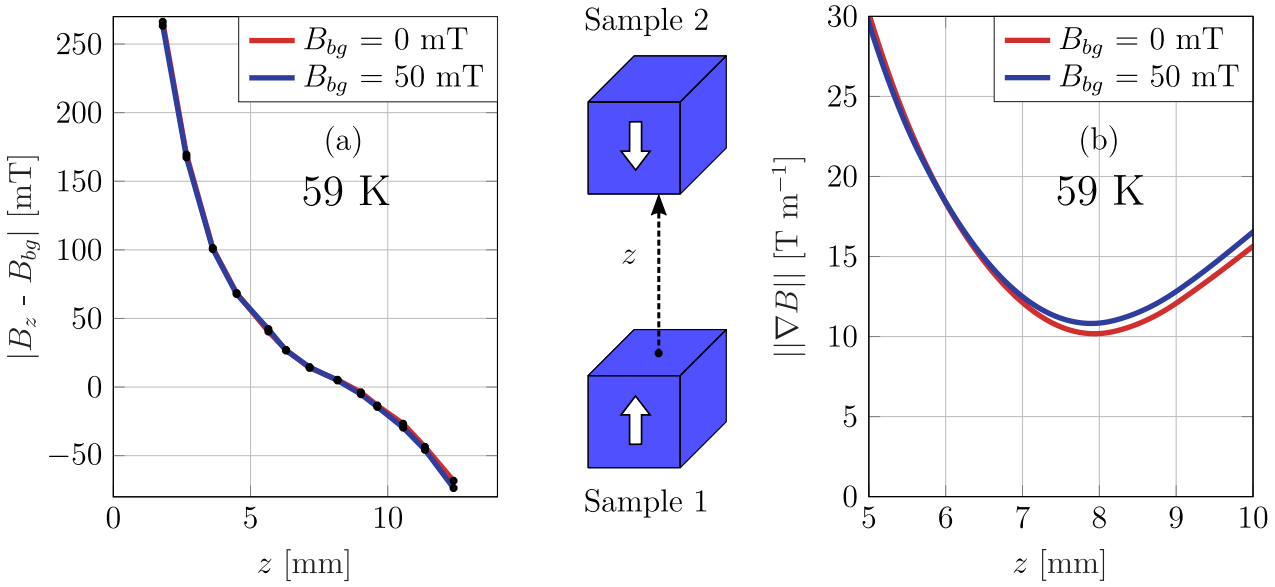

Figure 5.14: (a) Magnetic flux density profile measured at the end of the experimental procedure ($B_{max} \neq B_{bg}$) for a configuration with two superconductors for various values of the background field at 59 K. (b) Gradient of the magnetic flux density profile for the configuration with two superconductors for various values of the background field at 59 K.

In Figure 5.14 (b), it appears that at 59 K, the minimal magnetic flux density gradient generated by the assembly in the intermediate region surpasses 10 T m^{-1} when the background field is equal to 0 mT while it exceeds 10.8 T m^{-1} when $B_{bg} = 50$ mT.

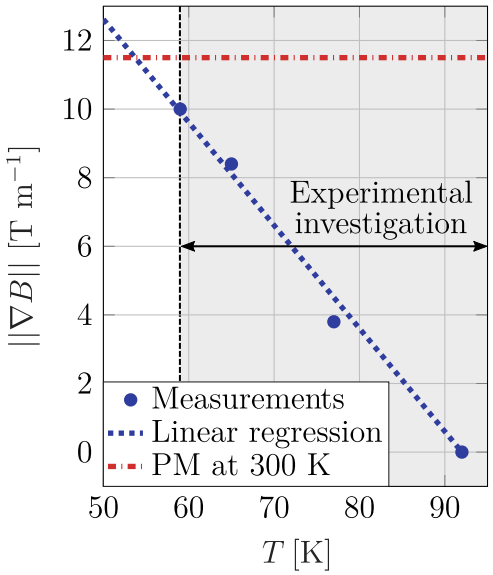

Figure 5.15: Minimal magnetic flux density gradient measured in the intermediate region with the configuration with two superconductors at various temperatures in zero background field.

To put such performances into perspective, instead of superconducting samples, two Nd-Fe-B cubic permanent magnets with 6 mm sides were placed in the experimental system. The minimal field gradient generated with such samples at ambient temperature in zero background field was measured to be 11.5 T m^{-1} in the intermediate region. This value is used as a benchmark to which the gradients measured in zero background field with the configuration with two superconductors at various temperatures are compared in Figure 5.15. In the temperature range investigated experimentally, permanent magnets outperform bulk superconducting $YBa_2Cu_3O_{7-x}$ samples. Nevertheless, contrary to permanent magnets, the gradient generated with superconductors is measured to increase almost linearly with decreasing temperatures. Operating the superconducting assembly at ∼50 K and below is therefore expected to surpass the performances of permanent magnets.

5.4 Field cooling and rotation in a constant background field

In this section, a situation in which the applied magnetic field cannot be controlled or swept as required to magnetize the superconducting samples is considered. This is the case when considering the use of an MRI scanner to generate the background field [216–222].

Here, the field gradient achievable with a superconducting sample initially field cooled in a constant field and subsequently rotated by an angle of 180° in the same background DC field ($B_{max} = B_{bg}$) are investigated. The magnetic flux density profiles and gradients measured at the end of this process are shown in Figure 5.16.

At 77 K (Figure 5.16 (a)), the final measured trapped flux density is increased when increasing the background field from 100 mT to 200 mT. Nevertheless, increasing B_{bg} to values higher than 200 mT results in a reduction of the final trapped flux density. This non-monotonic behaviour can also be observed in the magnetic flux density gradient in Figure 5.16 (c): among the value investigated experimentally, B_{bg}=200 mT is the background field leading to the highest generated gradient. The behaviour measured at 65 K (Figures 5.16 (b) and (d)) differs significantly from the one at 77 K in that both the trapped magnetic flux density and the magnetic flux density gradient increase with increasing background magnetic field within the whole range of background fields that were experimentally investigated. Moreover, it is highly promising to observe that, under a background magnetic field strength of 200 mT at 77 K or 150 mT at 65 K, the measured field gradients generated here are comparable with those attained in the previous section when performing a complete sample magnetization prior to the rotation.

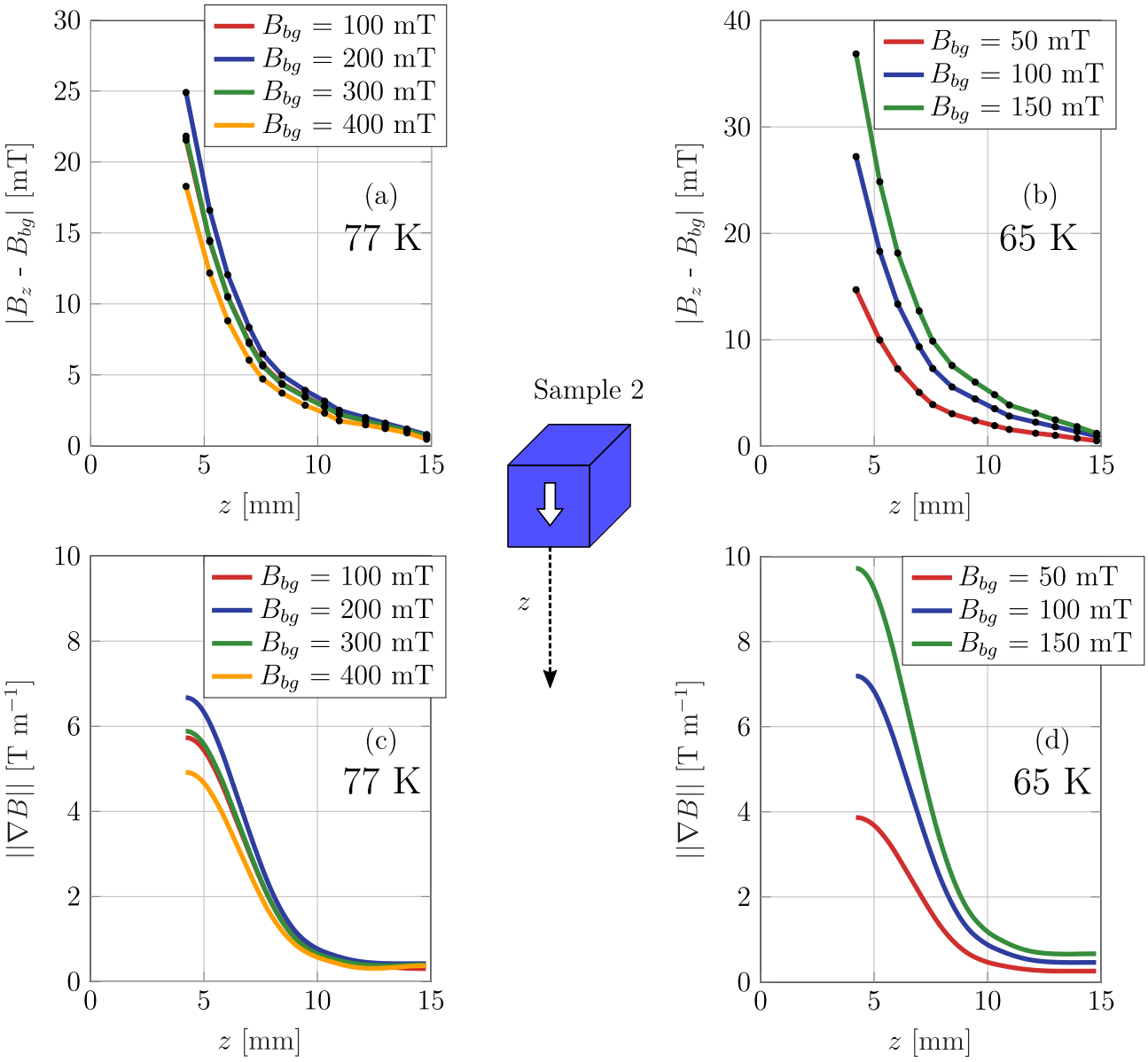

Figure 5.16: (a) and (b) Magnetic flux density profile measured after a field-cooling procedure followed by a 180° rotation in various background DC field at 77 K and at 65 K respectively. (c) and (d) Gradient of the magnetic flux density profile for a single sample configuration and various values of the background field at 77 K and 65 K respectively.

These results can be compared to finite element simulations. The trapped field computed at a specific distance above the superconductor surface is compared to the measurements and the associated current density distribution is shown in Figure 5.17.

Figure 5.17 (a) shows a very satisfying agreement between modelling and experiment: the finite element model reproduces the non-monotonic trend of the trapped field with increasing background field strength observed experimentally. Furthermore, it accurately anticipates that, within the range of background field strengths investigated experimentally, 200 mT emerges

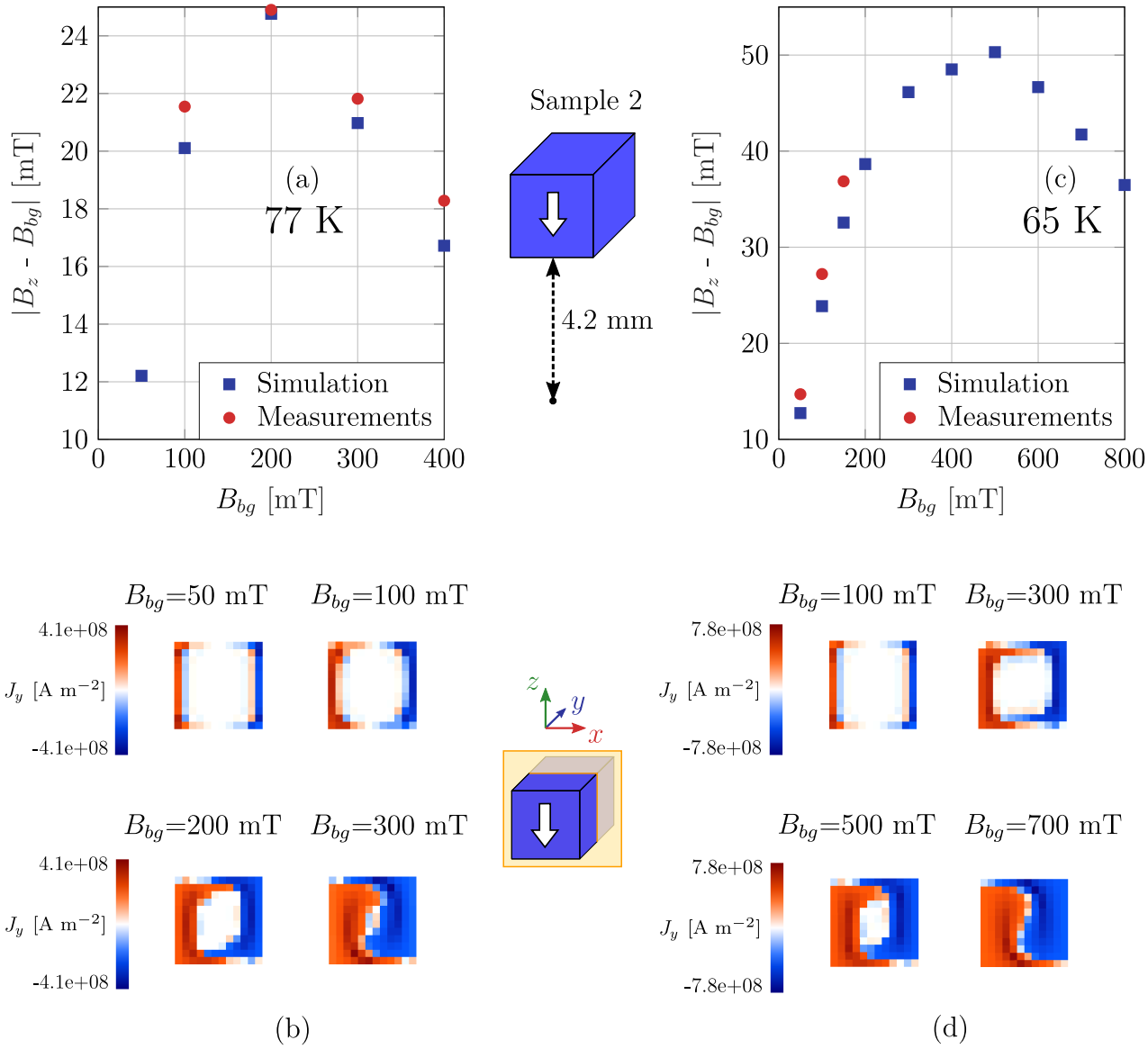

Figure 5.17: (a) and (c) Comparison between the simulated and the experimental trapped field evaluated 4.2 mm above the surface of the rotative superconducting sample after a field-cooling procedure followed by a 180° rotation in various background DC field at 77 K and 65 K respectively. (b) and (d) Current density distribution within the x-z cut plane including the centre of the superconductor computed with the finite element model after the 180° rotation of the sample for specific values of the background field at 77 K and 65 K respectively.

as the optimum level, yielding the highest trapped field magnitude. This agreement increases our confidence in the current density distribution computed and presented in Figure 5.17 (b). In this Figure, the extent of supercurrent penetration within the superconducting sample deepens as the background magnetic field strength is increased. Interestingly, the analysis also reveals that after a 180° rotation in a background field of 200 mT, the sample is not yet fully penetrated with supercurrents despite this configuration yields the highest trapped magnetic field. Figure 5.17 (c) shows that at 65 K as well the finite element model captures correctly

the general measured trend of the trapped magnetic field as the background field strength is increased. The simulations indicate that the maximum trapped-field ability of the sample is achieved when it is subjected to a 500 mT background field during rotation. For mechanical reasons, the experimental investigations at this temperature exclusively explored background field strengths below this threshold value. This is why the non-monotonic trend of the trapped field is not observed experimentally.

5.5 Summary

In this chapter, the magnetic flux density gradient exploiting the trapped field of either one or two cubic $YBa_2Cu_3O_{7-x}$ bulk superconductors was investigated experimentally and numerically. This investigation was conducted in the presence of a uniform DC magnetic field at 3 temperatures: 77 K, 65 K and 59 K.

First, measurements carried out on a single, stationary sample revealed a noteworthy reduction in the fields and field gradients generated at 77 K in the presence of a non-zero applied field at the end of the magnetization process. While still discernible, this phenomenon was measured to be significantly mitigated at 65 K and at 59 K. Using a finite element model based on the mixed **H**-ϕ-**A** formulation, the parameters of a field-dependent relationship for the critical current density were adjusted to successfully reproduce magnetization loop characterization measurements conducted at 77 K, 65 K, 70 K and 59 K. The comparison of the finite element model with the measurements highlighted that the decreased trapped field in the presence of a background field can be reproduced by considering the field dependence of the critical current density.

Next, the potential deleterious effect of a 180° rotation within a uniform magnetic field on the trapped field of an individual superconductor was investigated. Experimental and numerical results showed that, at 77 K, the full trapped-field ability of the superconducting sample is preserved, provided that the rotation occurs within a background magnetic field not exceeding 100 mT. This limit on the background field was found to increase to 200 mT when the temperature is decreased to 65 K. Further numerical simulations showed that enlarging the geometrical dimensions of the sample also increases this limit.

Then the magnetic flux density gradient generated by a pair of superconductors with anti-parallel magnetizations was measured at various temperatures. At 77 K, despite the alteration of the current distribution anticipated during the rotation in a finite background field, a gradient higher than 2.9 T m^{-1} was measured across the whole targeted region in the presence of a 300 mT background field. Enhanced performance was achieved at lower temperatures where magnetic flux density gradient exceeding 8.4 T m^{-1} (150 mT background field, 65 K) and exceeding 10.8 T m^{-1} (50 mT background field, 59 K) were demonstrated.

Finally, the field gradient produced by a single cubic superconductor subjected to a field-cooling process followed by rotation within a constant and uniform magnetic field was explored. A non-monotonic evolution of the generated gradient with increasing background field level was observed both experimentally and numerically. It was observed that, under the condition of a judiciously selected background field level, the measured field gradient obtained after this experimental procedure is comparable to those achievable through full sample magnetization before rotation.

Conclusions

This thesis was dedicated to the study of compact systems capable of producing remotely a magnetic force. This force is proportional to the magnetic flux density gradient produced by the system. Although numerous applications benefit from the generation of a substantial magnetic force, the main focus of the study is the magnetic drug delivery for which the necessary gradient must be generated at a distance of a few centimetres. In this context, the distribution and the gradient of magnetic flux density generated by various assemblies of superconducting trapped-field magnets were investigated. The first configurations considered were inspired by conventional arrays of permanent magnets. These combinations, when assembled with magnetized superconductors, were shown to outperform isolated superconducting trapped-field magnets in terms of magnetic flux density gradient and to offer the prospect of surpassing the performance of arrays made of permanent magnets. The assembly process of superconductors, however, was found to play a crucial role during which interactions between the magnetized samples may result in partial demagnetization. The principal objective of this study was therefore to determine how several trapped-field magnets with non-parallel magnetization directions can be combined efficiently, potentially in the presence of a uniform DC background field, to generate large magnetic field gradients in the centimetre range. The study was carried out using numerical modelling, analytical modelling and cryogenic experiments.

Starting from conventional finite element formulations, a methodology for modelling in 3D the behaviour of conducting regions in motion at distinct velocities was established. The method consists in expressing the governing equations within a specific conductor using a coordinate system that moves with that conductor. When applied to the **A**-formulation, careful consideration has to be given to the gauge condition employed for the magnetic vector potential in coordinate systems moving at different velocities. It was then shown that neither the **A**-formulation nor the **H**-ϕ-formulation is optimal for modelling mobile superconductors. This motivated the use of a surface-coupled **H**-ϕ-**A**-formulation to benefit from the advantages of each formulation. Throughout this thesis, the coupled formulation was used with a 3D finite element solver, providing precious insights into the distribution of current density within magnetized superconductors combined in various configurations. Additionally, a semi-analytical model based on the Biot-Savart law was developed to calculate the distribution of the three components of **B** generated by a cubic trapped-field magnet. This model assumes a predetermined current density distribution. The combined use of this semi-analytical model with the finite element model allowed for the evaluation of the magnetic flux density gradient generated by several superconducting assemblies.

Regarding the experimental side of the thesis, two cryogenic experimental setups were designed, assembled, calibrated and used. The first experimental setup aims at assembling magnetized superconductors by translation, at liquid nitrogen temperature. This experimental rig was used to combine three $YBa_2Cu_3O_{7-x}$ superconductors in a Halbach array and to measure the field distribution produced at 77 K. Both bulk, large grain samples and stacked-tape samples were investigated. A detailed comparison between experimental data and numerical simulations showed that a current distribution alteration is induced within the central trapped-field magnet when assembling such a superconducting configuration. This alteration causes a reduction of the magnetic flux density gradient generated. Considering bulk superconductors, the approach of the peripheral samples induces the formation of current loops parallel to the *c*-axis of the central sample. Although the apparition of such current loops is prevented when using stacked-tape samples, a current density alteration on the high-field side of the array still occurs. Despite this demagnetization effect, the assembled superconducting Halbach arrays were demonstrated to produce, at a distance of 20 mm, a magnetic flux density gradient approximately 30% higher than a stand-alone superconductor.

Various approaches were proposed and explored to mitigate the effects of the current density re-organization. Two ideas emerged as effective methods. The first consists in reducing the magnetic flux density amplitude generated by the peripheral samples on the lateral face of the central superconductor. To this aim, superconductors with a triangular cross-section were used as peripheral samples which led to the formation of a "truncated Halbach array". This superconducting assembly was shown to outperform the magnetic flux density gradient produced by isolated superconductors and to exhibit minimal demagnetization of the central sample. Numerical simulations were also performed to point out that the introduction of a vertical shift in the position of the peripheral samples allows the reduction of the current density alteration. The second idea consists in implementing a re-magnetization step following the assembly procedure. In this thesis, the trapped field of an additional sample, placed above the central superconductor of the array, was used as a re-magnetizing field. Using this method with a sufficiently tall additional sample, it was shown that one could expect superconducting Halbach arrays to recover almost their full potential.

The second experimental setup consists of an insertion tool compatible with the sample chamber of a *Physical Property Measurement System* (PPMS). The two advantages are that the experiments can benefit from the cryogenic controlled temperature environment of the PPMS and from the large DC field generated by the PPMS magnet. The insert developed in this thesis allows for the secure placement of two superconducting samples of rectangular shape with a side of $\sim$6 mm inside the experimental chamber of the PPMS. The insert includes a rotation mechanism that enables the controlled rotation of one sample by an angle of up to 190° while counteracting a resistive torque of up to 0.022 N m. In so doing the samples can be magnetized in-situ and the rotation mechanism can be used to generate any “non-parallel magnetization” configuration. The separating distance between the samples is approximately 16.6 mm and was shown to be sufficient to avoid any mutual demagnetization effect during the rotational motion. A bespoke "Mutli-Hall probe" is also integrated in the insert to measure precisely the magnetic flux density gradient in the close vicinity of the superconductor location. This instrument was used to measure successfully, at 59 K, 65 K and 77 K, the magnetic

flux density gradient generated between two facing cubic $YBa_2Cu_3O_{7-x}$ bulk superconductors with anti-parallel magnetization directions, potentially under a homogeneous background DC magnetic field. When this background field is zero, the combined contribution of each sample was measured to generate a higher magnetic flux density gradient in comparison to the one produced with a stand-alone superconductor. This observation remained valid in a non-zero background field provided that the background level does not exceed a threshold. Experiments showed that this threshold increases as the temperature decreases and numerical modelling also suggests that the threshold increases as the geometrical dimensions of the samples are enlarged. Unlike the behaviour of permanent magnets, the magnetic flux density gradient generated with facing superconductors was found to increase linearly with decreasing temperatures. At 59 K, a magnetic flux density gradient exceeding 10 T m^{-1} was achieved across the whole measured region.

Perspectives

The results presented in this thesis show that combining several magnetized superconductors is a promising avenue for generating compactly a substantial magnetic flux density gradient. Manipulations involving either larger samples or an operating temperature lower than 59 K could be carried out to surpass experimentally the performance offered by conventional permanent magnets. To motivate such an investigation and illustrate the expected results, the semi-analytical model developed in this thesis is used to evaluate the gradient produced 20 mm above the surface of a cubic sample (either a permanent magnet or a trapped-field magnet) of various side lengths. The results are presented in Figure 5.18 and confirm that larger superconductors are expected to outperform permanent magnets. The size corresponding to the cross-over is found to be around $\sim$ 24 mm when a J_c of 2×10^8 A m^{-2} is assumed, i.e. the experimental J_c at 77 K of the $YBa_2Cu_3O_{7-x}$ samples used in this thesis. Assuming a linear $J_c(T)$ dependence, one can expect a J_c of $\sim 4 \times 10^8$ A m^{-2} at 62 K, which reduces the coss-over size down to $\sim$ 14 mm.

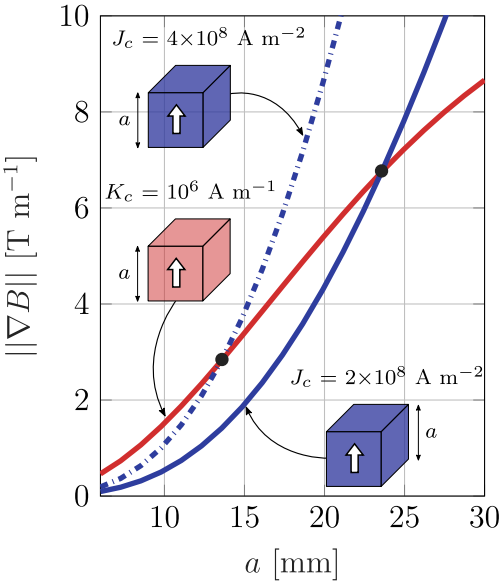

Figure 5.18: Magnetic flux density gradient generated at a distance of 20 mm from the surface of a cubic permanent magnet (in red) or trapped-field magnet (in blue).

Then, investigating further the magnetic flux density distribution generated by various superconducting assemblies is required to complete the present experimental study and to design an optimal structure depending on the specific application aimed for. Four investigative paths are illustrated schematically in Figure 5.19, briefly described below, and are considered to be stimulating starting points to further the research conducted in this work.

(a) **Halbach array made of 5 trapped-field magnets:** In this thesis, only superconducting Halbach arrays made of three samples were considered. The natural progression from this point consists of implementing the modified assembly procedure proposed in Chapter 4 to the case of a 5-sample superconducting Halbach array. In that case, a re-magnetization procedure would also be required for the outermost superconductors of the assembly.

(b) **Vertically shifted configurations:** In Chapter 4, numerical simulations were carried out to illustrate that vertically shifting the peripheral superconductors in a superconducting Halbach array including three samples results in a reduction of magnetization alteration during the assembly procedure. Implementation of a minor modification to the sample holder design would enable the introduction of this vertical shift, allowing for the experimental exploration of these assemblies using the setup devised in this research.

(c) **Influence of the aspect ratio:** The superconducting Halbach arrays assembled in this thesis involve exclusively cubic samples, another avenue of improvement thus corresponds to the examination of the influence of the aspect ratio of the trapped-field magnets on the magnetic flux density distribution.

(d) **2D Halbach structures:** Building on the understanding acquired when assembling linear superconducting Halbach array, the study can also be extended to the exploration of 2D superconducting Halbach structures.

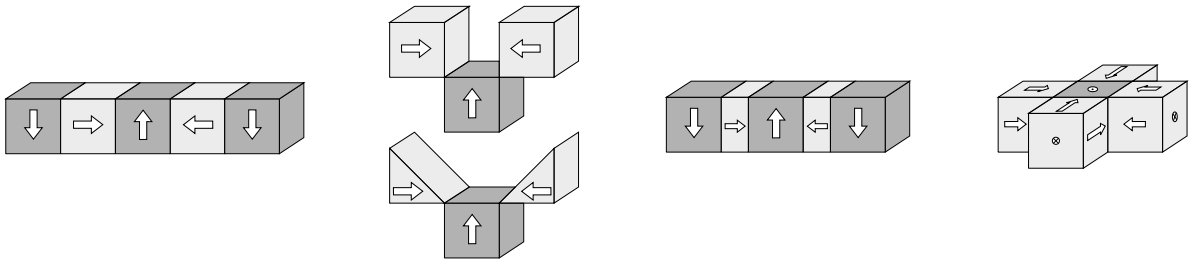

Figure 5.19: Schematic illustration of several superconducting assemblies to be investigated in future work.

Finally, in the presence of a non-zero background field, the results of this study focused on the gradient arising from a configuration with two superconductors. A relevant extension consists in the evaluation of the field gradient that can be achieved through the combination of more trapped-field magnets. Such an investigation would typically include the exploration of the performances of all the superconducting Halbach structures envisaged in this thesis in the presence of a uniform background DC field.

In summary, the results of this thesis deepened the understanding of the magnetic coupling physical phenomena arising when magnetized superconductors are combined. This offers stimulating outlooks for the future developments of superconducting assemblies generating significant magnetic flux density gradients.

A Additional characterizations

A.1 Cubic permanent magnet

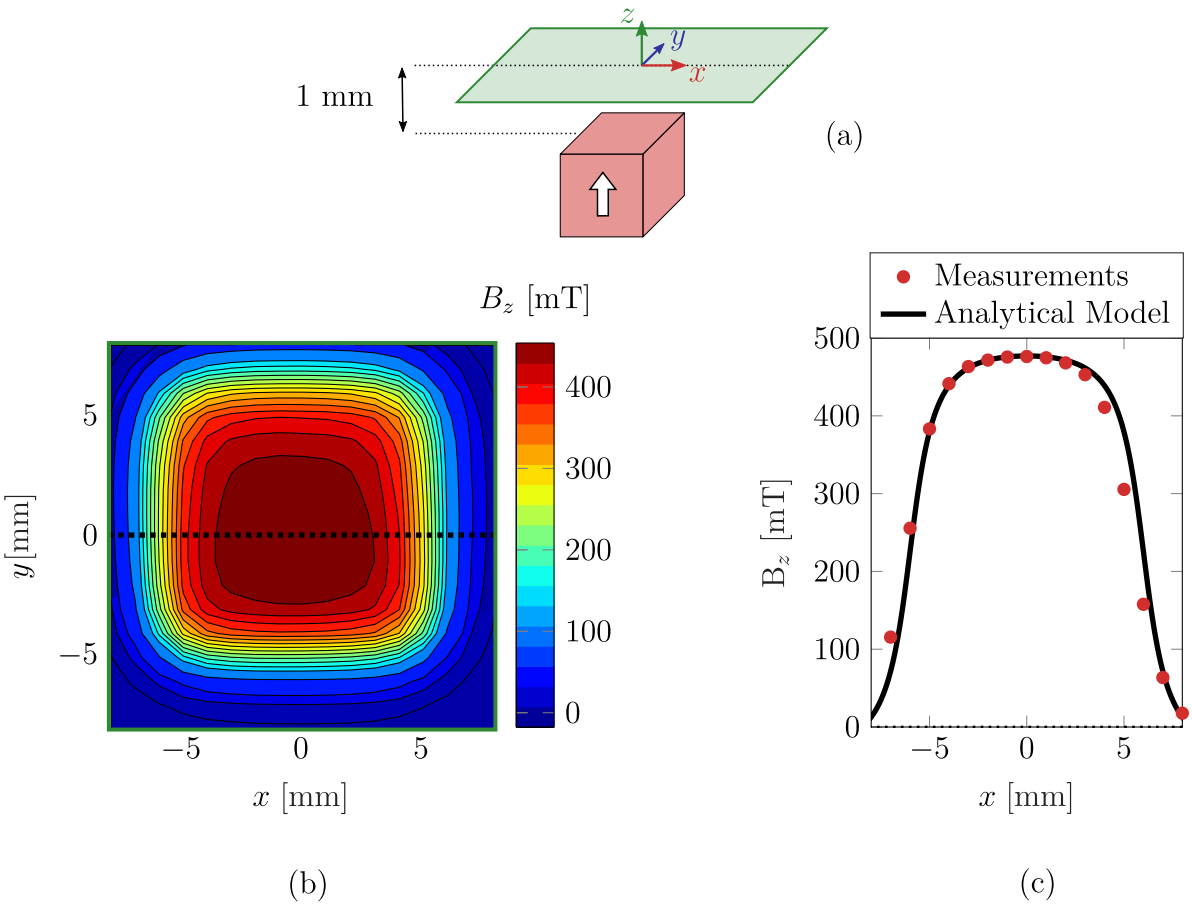

Figure A.1: Contour plot of the magnetic flux density measured at ambient temperature, 1 mm above the surface of a cubic Nd-Fe-B permanent magnet with a side of 12 mm. The analytical model assumes that the magnetic flux density distribution can be reproduced with a surface current density flowing at the periphery of the sample $K_c = 10^6$ A m^{-1}.

A.2 Bulk $YBa_2Cu_3O_{7-x}$ superconductors manufactured by the Bulk Superconductivity Group

For each mapping presented in this appendix, the bulk superconductors are magnetized in a direction parallel to the *c*-axis following a field-cooling procedure starting from 1.2 T and with a field removal rate of -1 mT s^{-1}. A magnetic relaxation period of 45 min is allowed before evaluating the field distribution. Samples 1218, 1219 and 1220 are selected to be assembled in a superconducting Halbach array. The sample 1222 is cut perpendicularly to its *c*-axis as described in section 4.3 to obtain the bulk additional sample required in the modified assembly process.

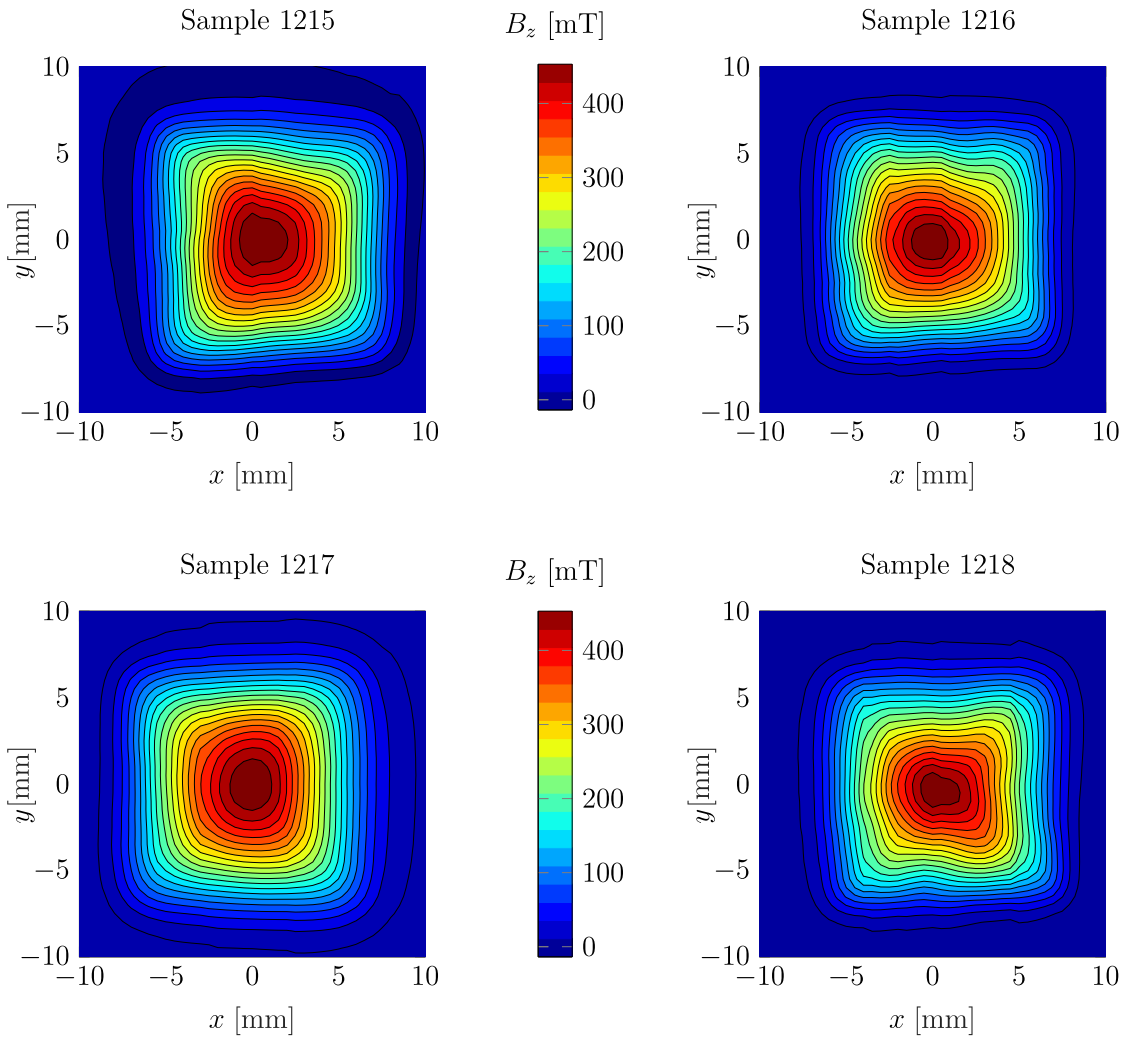

Figure A.2: Contour plot of the trapped field measured at 77 K measured 1 mm above the surface of the samples 1215 to 1218.

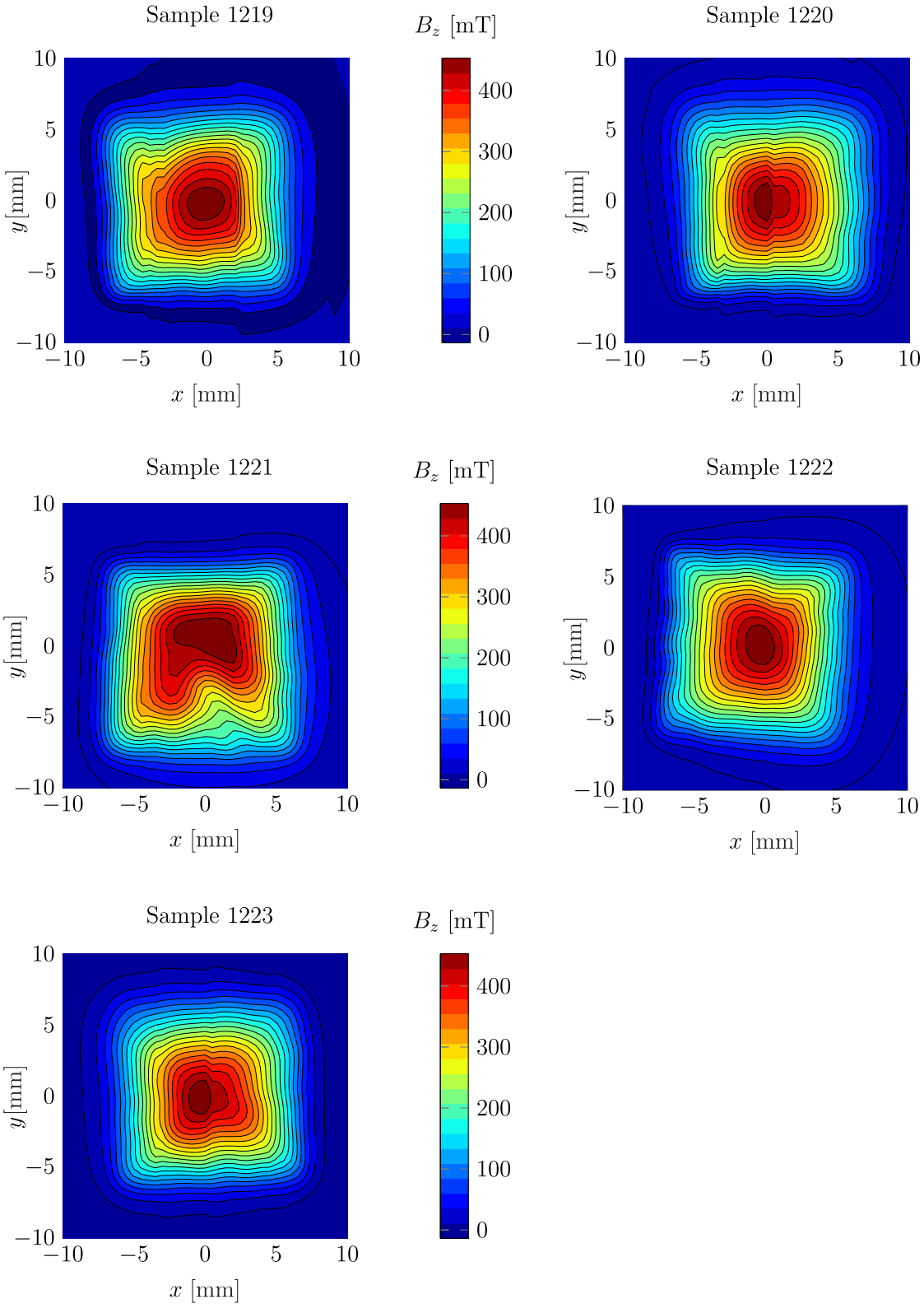

Figure A.3: Contour plot of the trapped field measured at 77 K measured 1 mm above the surface of the samples 1219 to 1223.

Serial number	Trapped field 1 mm above the top surface [mT]	Trapped field 1 mm above the bottom surface [mT]	Critical exponent [-]
1215	410	/	18.7
1216	505	/	26.6
1217	398	/	21.6
1218	440	112	18.5
1219	466	145	19.1
1220	461	98	21.8
1221	394	/	13.6
1222	509	/	18.9
1223	496	/	34.5

Table A.9: Summary of the trapped field measured at 77 K, 1 mm above the centre of the bulk superconducting samples and of the critical exponent of each individual sample.

A.3 Superconducting stacked-tape samples

For each mapping presented in this appendix, the superconducting stacked-tape samples are magnetized following a field cooling procedure starting from 1.2 T and with a field removal rate of -1 mT s^{-1}. A magnetic relaxation period of 45 min is allowed before evaluating the field distribution.

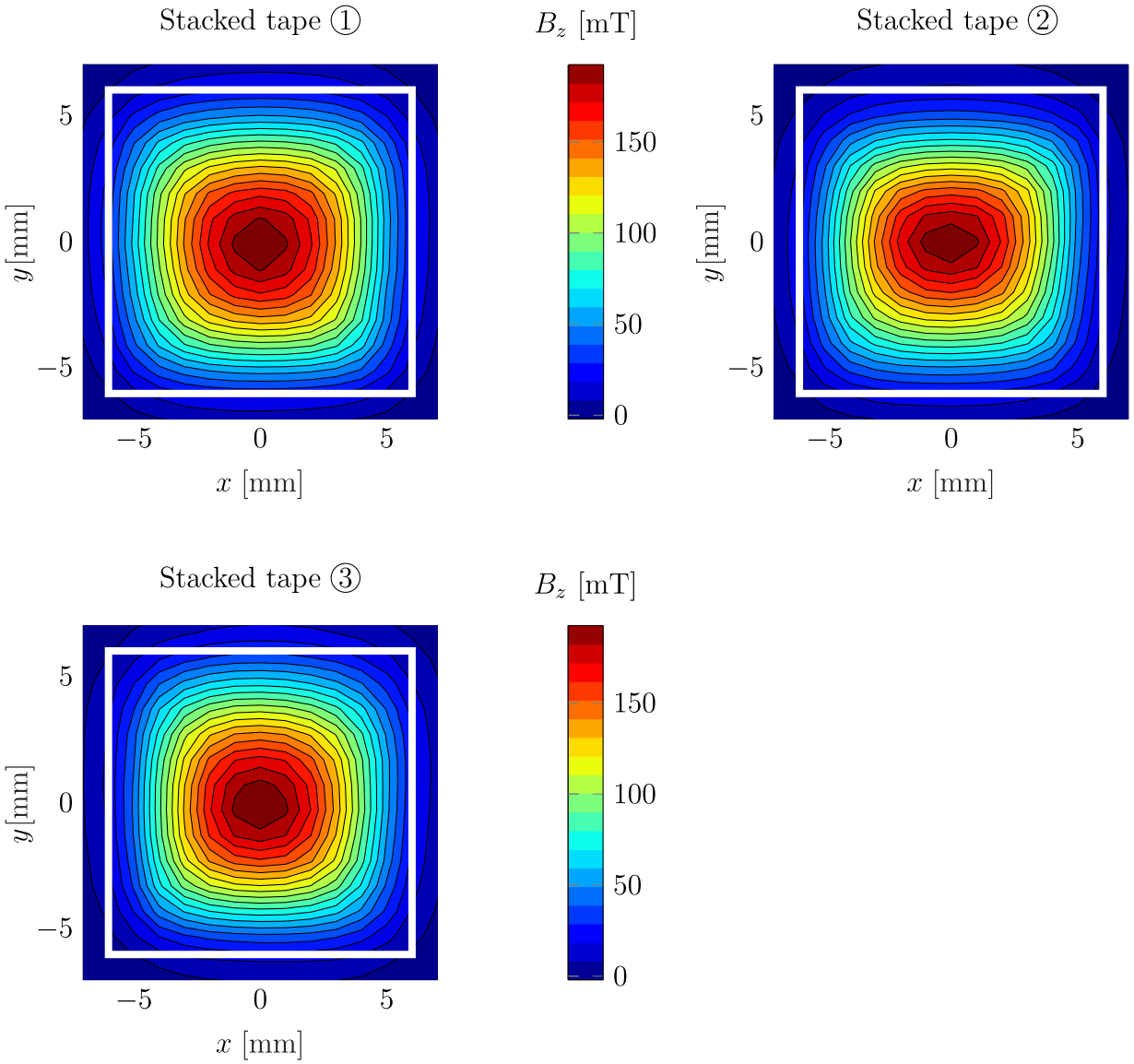

Figure A.4: Contour plot of the trapped field measured at 77 K, 1.5 mm above the surface of the 3 superconducting stacked-tape samples.

Sample number	Trapped field 1.5 mm above the top surface [mT]	Trapped field 1.5 mm above the bottom surface [mT]	Critical exponent [-]
①	198	/	23.8
②	202	201	21.3
③	201	/	23.5

Table A.10: Summary of the trapped field measured at 77 K, 1.5 mm above the centre of the superconducting stacked tapes samples and of the critical exponent of each individual sample.

B Additional results

B.1 Trapped-field measurements on a magnetized superconducting triangular prism

An additional trapped-field mapping experiment is conducted on a superconducting triangular prism to confirm the reliability of the magnetic flux density distribution anticipated by the analytical model. In this experiment, the sample is magnetized in a direction parallel to the c-axis following a field cooling procedure starting from 1.2 T and with a field removal rate of -1 mT s^{-1}. A magnetic relaxation period of 45 min is allowed before evaluating the field distribution. The c-axis of the sample is aligned with the x-direction and two x-y mappings are conducted at 3.7 mm and 4.7 mm above the top surface of the sample respectively.

B.2 Truncated superconducting Halbach array: further comparison to the analytical model predictions

The alignment between experimental trapped-field measurements obtained on the truncated superconducting Halbach array and the predictions of the analytical model presuming no current density modification during the assembly procedure is further illustrated through a comparison along 3 distinct lines parallel to the x-direction. As can be observed in Figure B.2, the fair concordance is conserved for all the considered lines. This gives confidence in the field distribution computed with the analytical model.

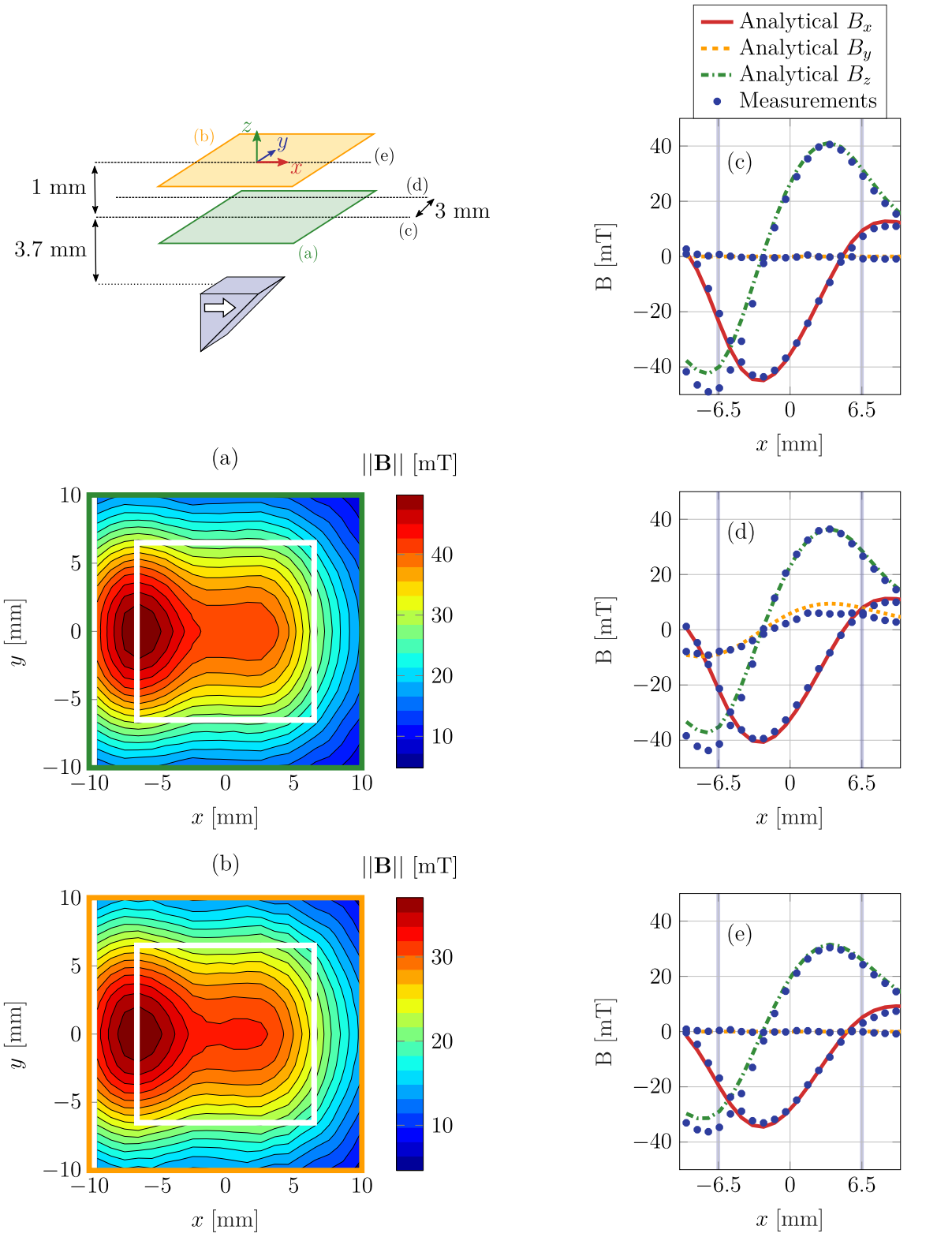

Figure B.1: (a) and (b) Measured distribution of the magnetic flux density generated by a superconducting triangular prism. The white lines delimit the borders of the sample. (c), (d) and (e) Comparison between the experimental data and the predictions of an analytical model assuming a homogenous superconducting sample in the critical state characterized by a field-independent critical current density $J_c = 2 \times 10^8$ A m^{-2}.

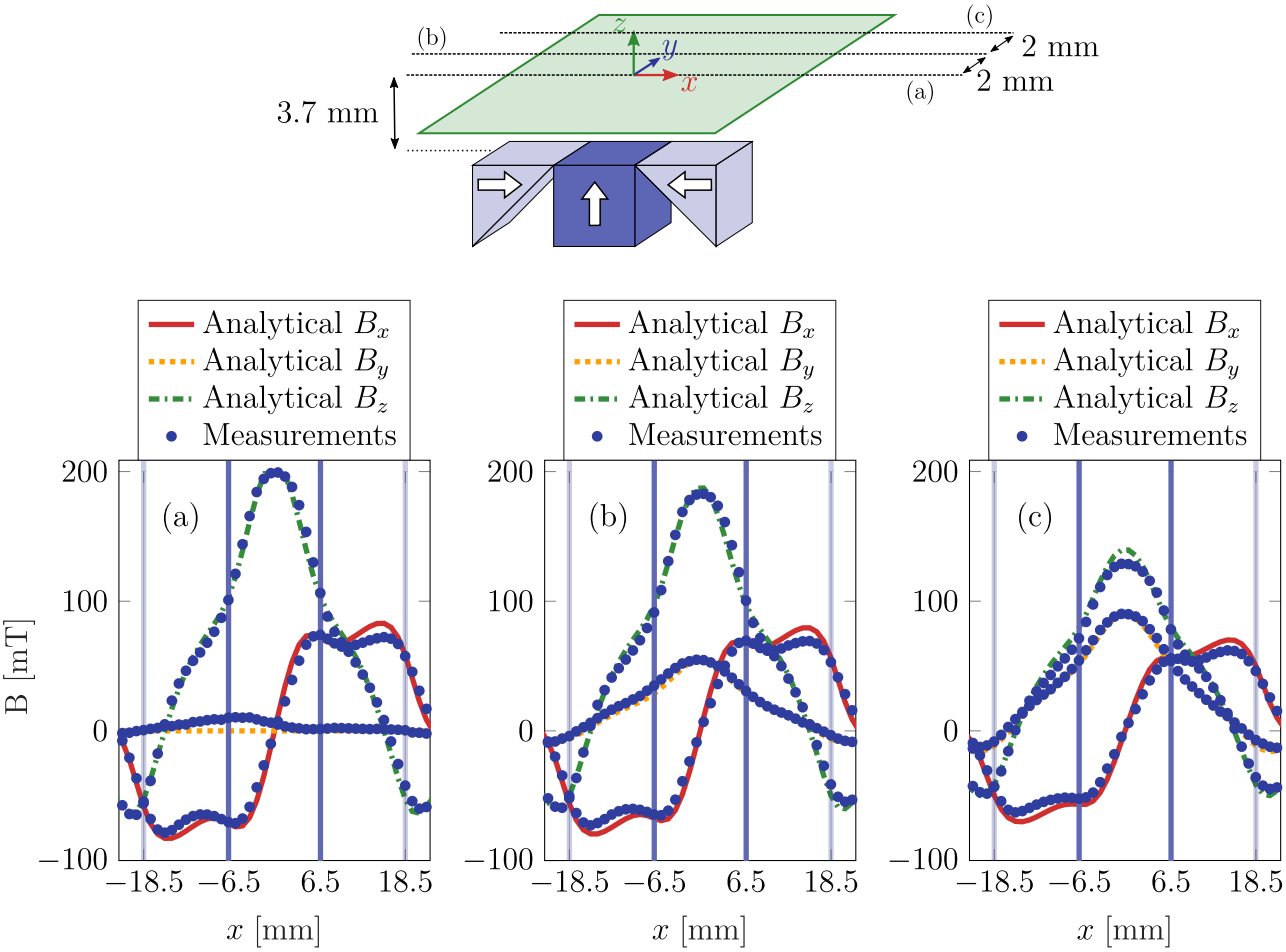

Figure B.2: Measured distribution of the 3 components of the magnetic flux density produced by a superconducting truncated Halbach array along three distinct lines parallel to the x-direction at 77 K. The experimental data are compared to an analytical model assuming a simple vector summation of the flux densities generated by each superconductor in the array and no alteration of the individual magnetization.

B.3 Assembly of 3 superconductors with a vertical shift of the peripheral sample: further discussion

In this section, further investigations are conducted to achieve a deeper understanding of the minimal modifications in current density anticipated for the superconducting assemblies depicted in Figures 4.9 (b) and (c). Given that the alteration of the current density distribution is initiated by the magnetic field produced by the peripheral samples close to the central sample, the distribution of the 3 components of this field is computed with the analytical model. The field generated exclusively by the peripheral superconductors within two planes is shown for each assembly in Figure B.3.

In Figure B.3 (a), on the upper surface of the central superconductor (plane ①), two noteworthy observations can be made. First, the amplitude of the magnetic flux density generated by the peripheral samples remains below 50 mT across the entire surface. This field amplitude is comparable to that computed on the lateral face of the central superconductor of a truncated Halbach array (cf. Figure 4.12 (b)) and is therefore expected to cause minimal alteration of the current distribution. Second, the magnetic flux density in this region is mainly anti-parallel to the z-direction. Consequently, the induced supercurrents are expected to flow anti-clockwise in loops perpendicular to the z-direction, thus aligning with the current distribution before assembling the configuration. On the lateral face of the central superconductor (plane ②) in Figure B.3 (a), the field generated by the peripheral samples is mainly anti-parallel to the z-direction as well. The assembly process of such a configuration is thus expected to strengthen the existing current density distribution within the central superconductor. Apart from a smaller field amplitude, the field distributions depicted in Figure B.3 (b) are similar to that presented in Figure B.3 (a). A reinforcement of the existing current loops in the central superconductor is therefore also expected for this superconducting arrangement.

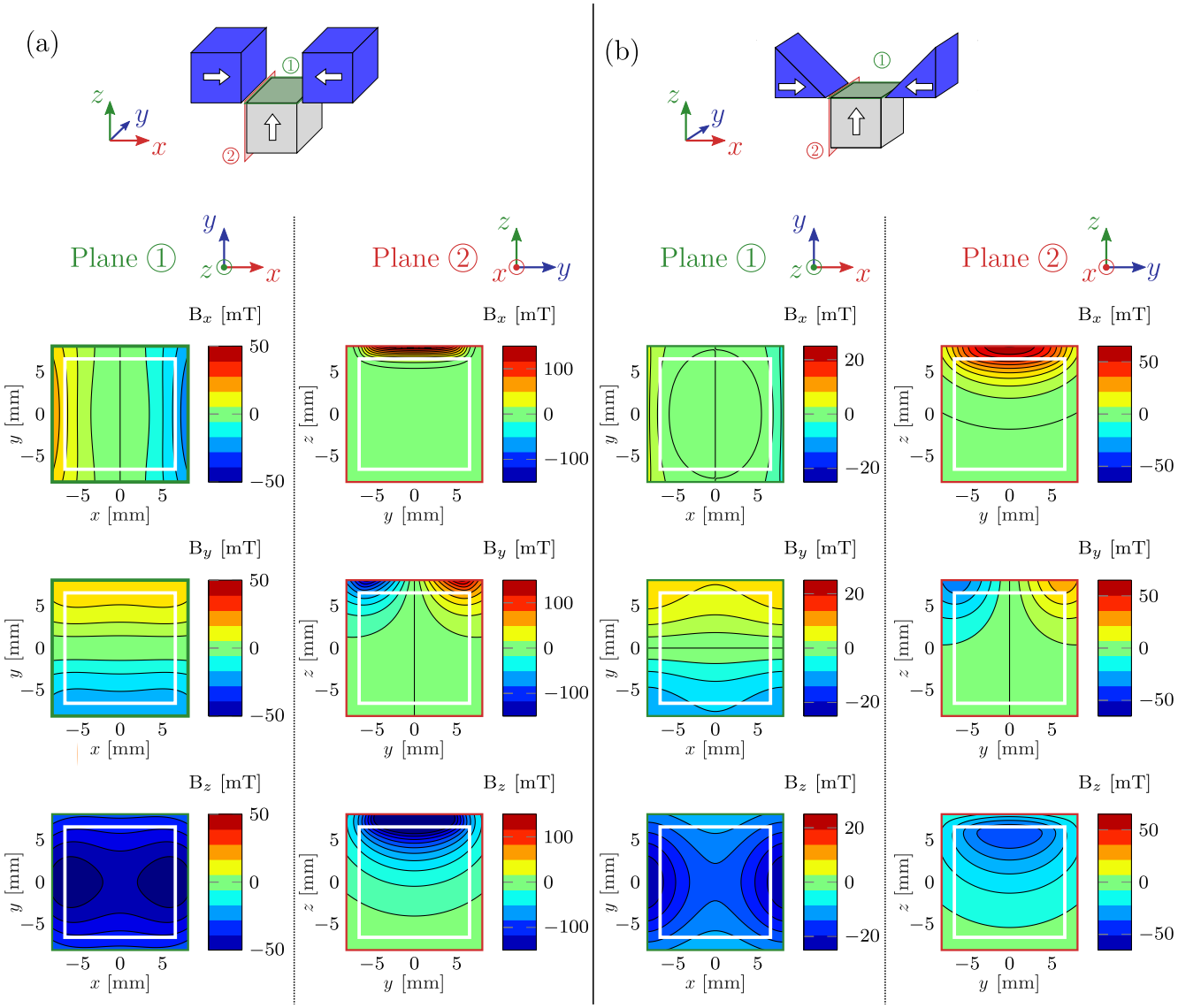

Figure B.3: Distribution of the magnetic flux density generated exclusively by the peripheral superconductors on the top and lateral face of the central superconductor as computed by the analytical model assuming homogeneous superconducting samples in the critical state characterized by a critical current density $J_c = 2 \times 10^8$ A m^{-2}. (a) The peripheral samples are cubes with a side length of 13 mm. (b) Peripheral samples are triangular prisms with maximum dimension in the x, y and z-direction equal to 13 mm.

B.4 Gradient generation in background field: Further investigation of the configuration with two superconductors

The magnetic flux density profile measured in zero background field for the configuration with two superconductors at 77 K and at 65 K is compared to the sum of the contributions of sample 1 and sample 2 measured individually.

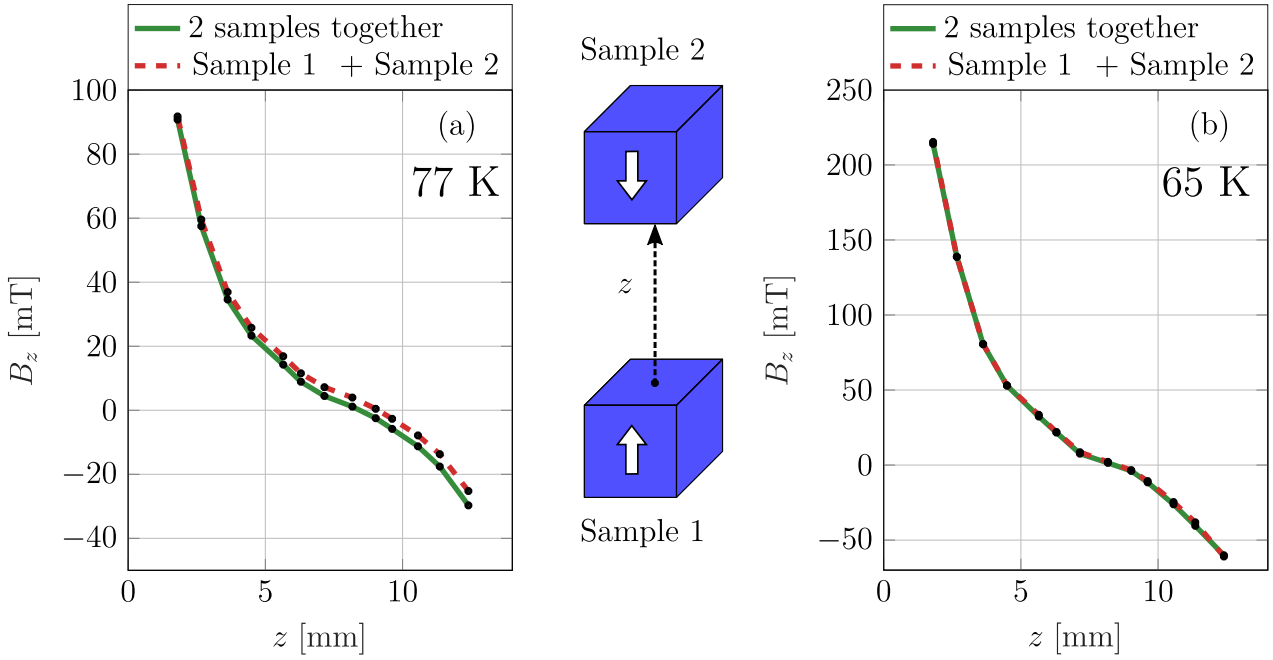

Figure B.4: Comparison between the magnetic flux density profile measured for the configuration with two superconductors (plain line) and the sum of the contributions of sample 1 and sample 2 measured individually (dashed line). (a) 77 K; (b) 65 K.

At 77 K (Figure B.4 (a)), in the region close to the stationary sample (z $<$ 5 mm), the measurements on the configuration with two superconductors are almost superimposed with the sum of each contribution. This observation confirms that no demagnetization is induced due to the interaction between the samples during the rotation. In the region close to the rotative sample (z $>$ 10 mm), a maximum difference of 3 mT is observed between both plots. Considering that the precise placement of the samples in the experimental system is challenging and that a misplacement of sample 2 in the z-direction as small as 0.3 mm could explain this 3 mT difference, the agreement is still considered satisfactory. The same conclusion can be drawn at 65 K (Figure B.4 (b)) since both plots can hardly be distinguished from one another.

C Mechanical drawings

C.1 Setup designed to assemble Halbach arrays

C.1.1 Mechanical parts manufactured in aluminum

These parts were manufactured at the mechanical workshop of the physics department at the University of Liege. The numbering used is presented in Figures C.1 and C.2. The drawings of all the mechanical parts manufactured in aluminium are presented in Figures C.3 to C.11.

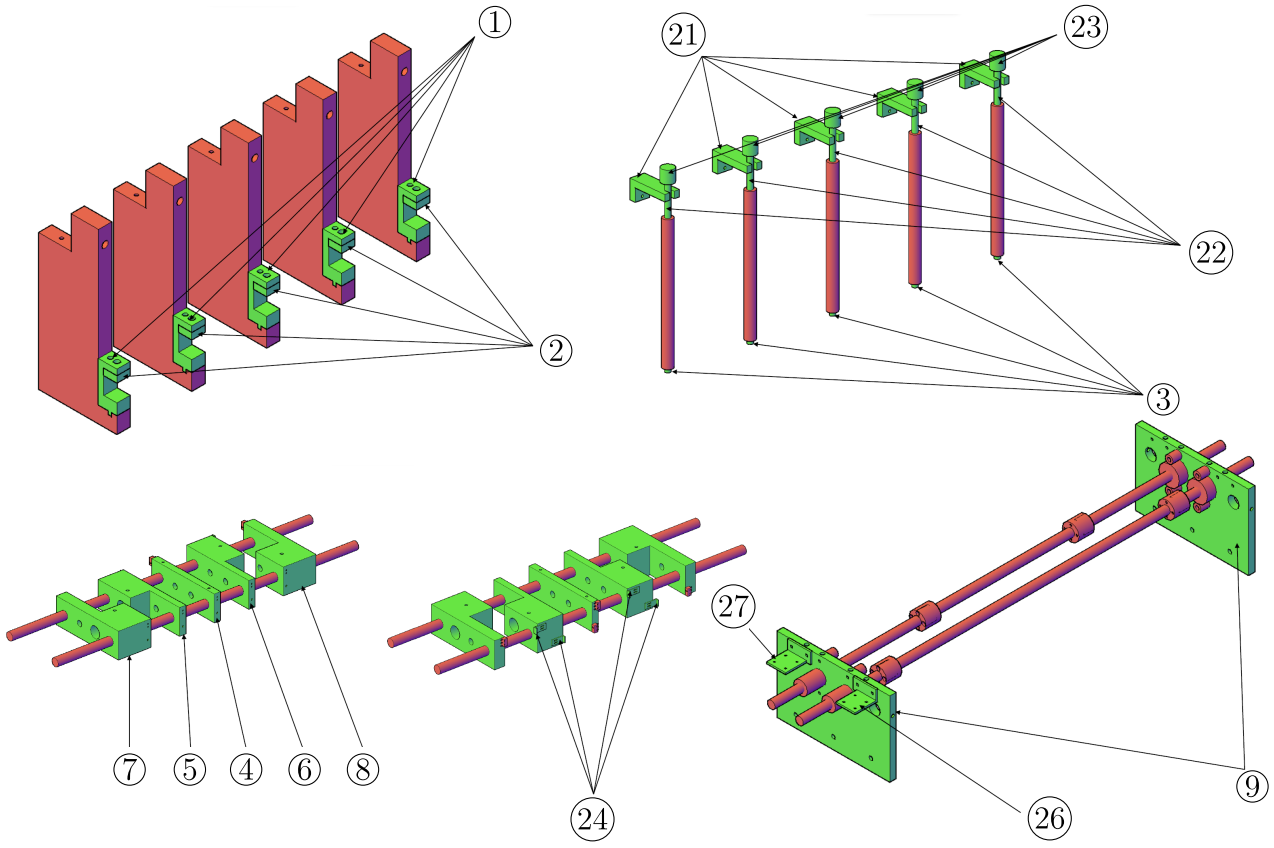

Figure C.1: Numbering of the mechanical parts manufactured in aluminum.

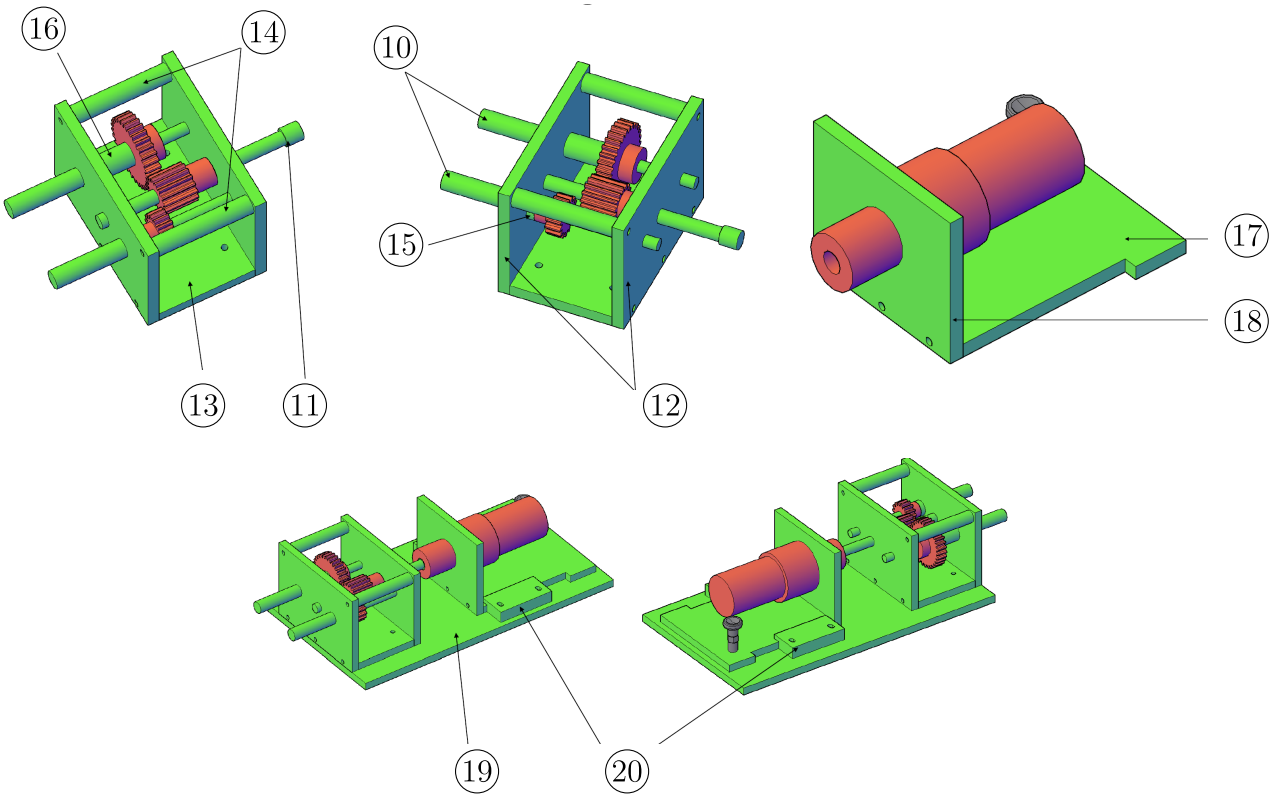

Figure C.2: Numbering of the mechanical parts manufactured in aluminum.

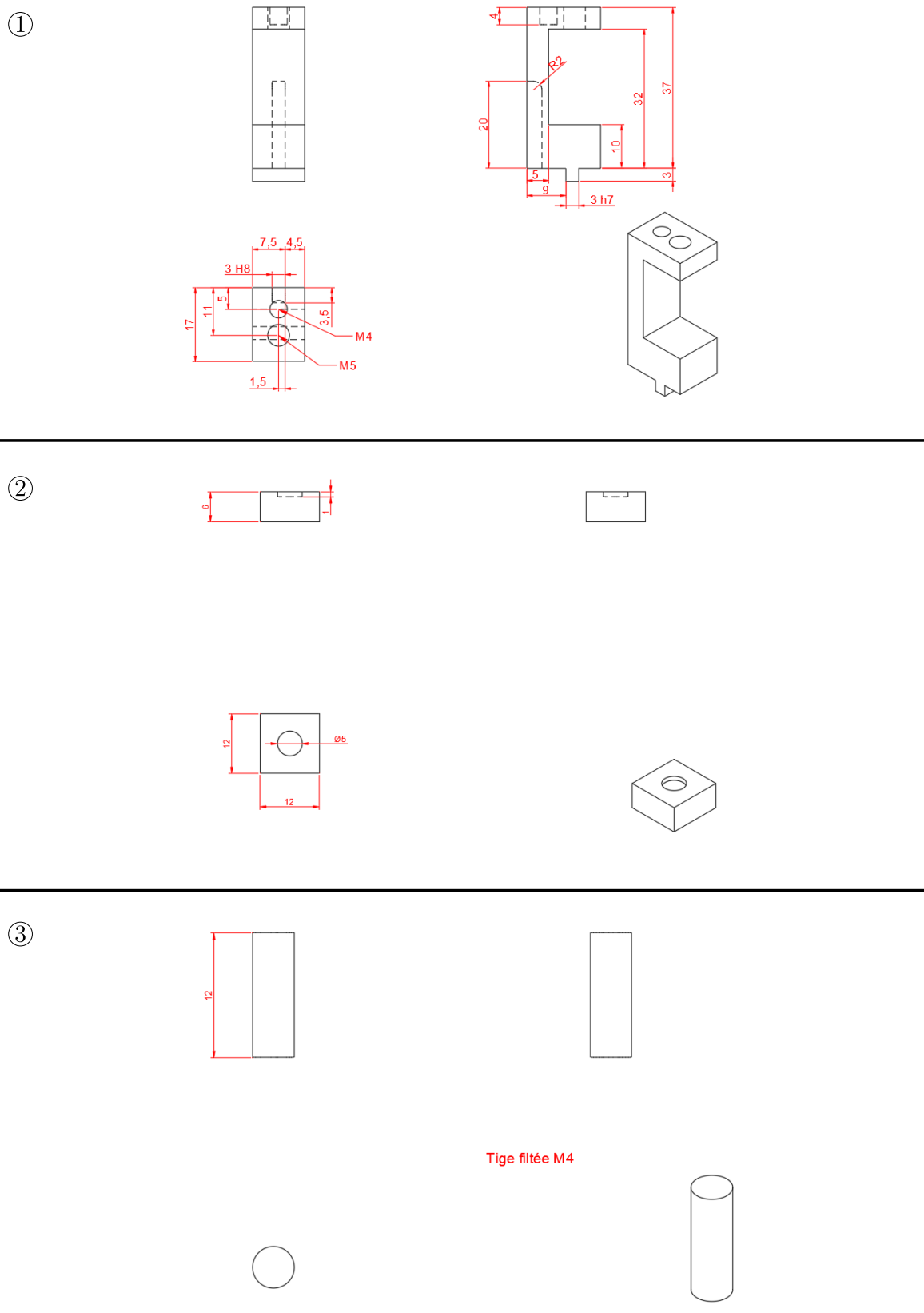

Figure C.3: Mechanical drawings of the of the components 1, 2 and 3.

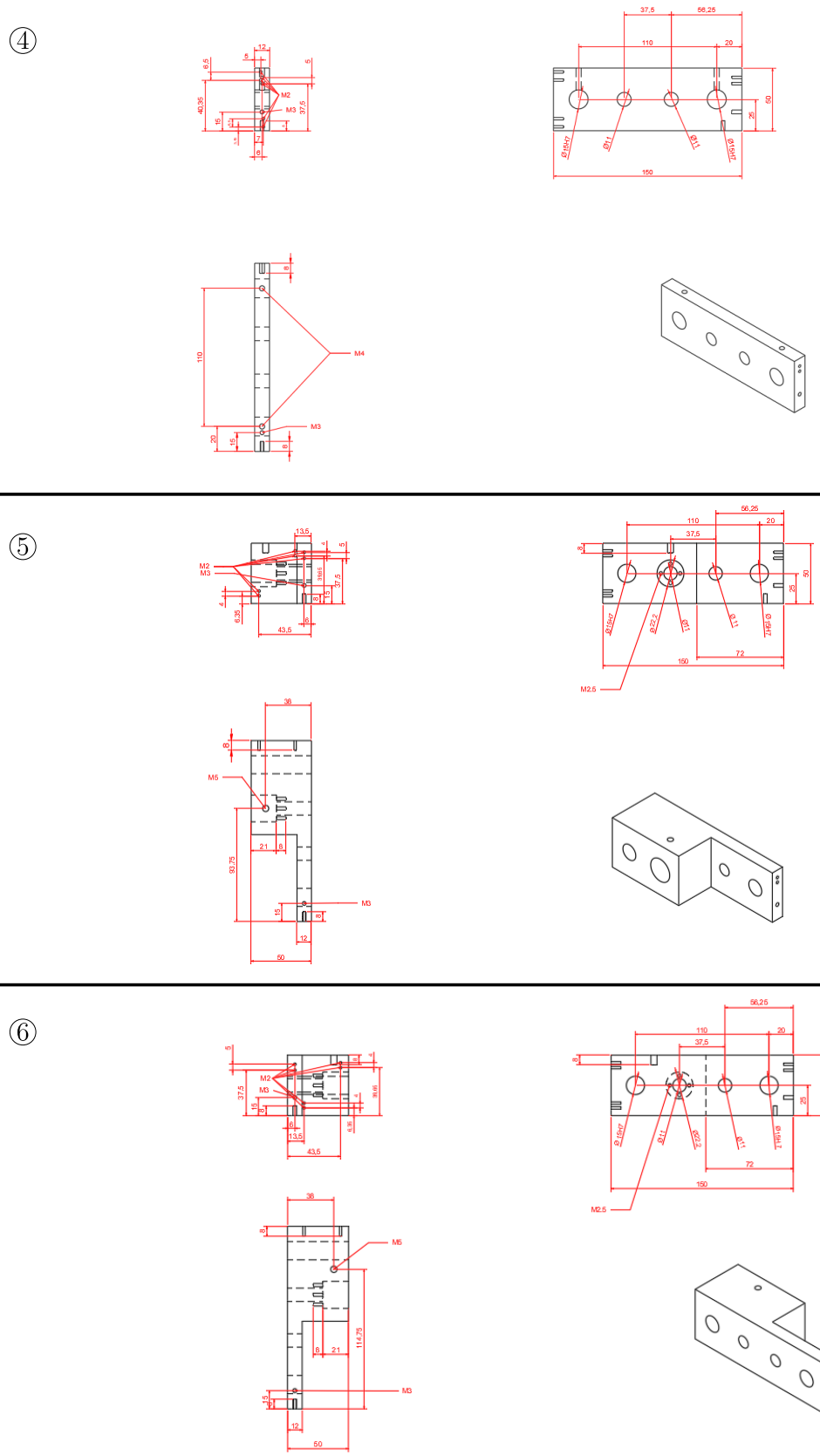

Figure C.4: Mechanical drawings of the of the components 4, 5 and 6.

⑦

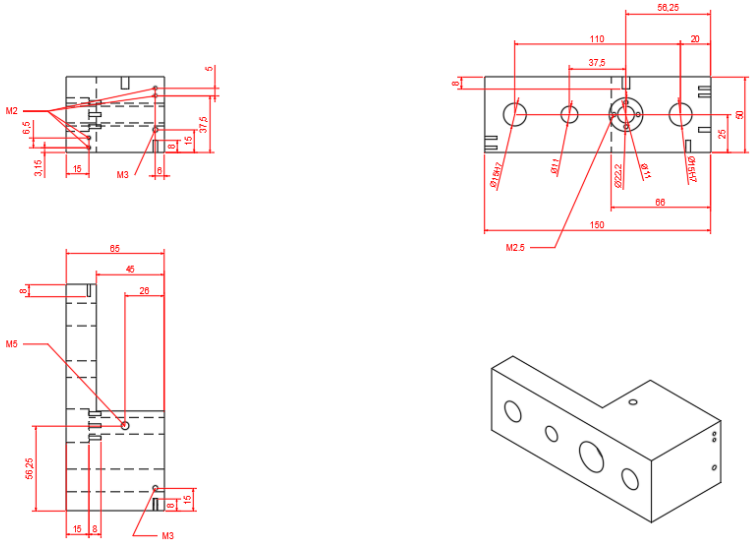

⑧

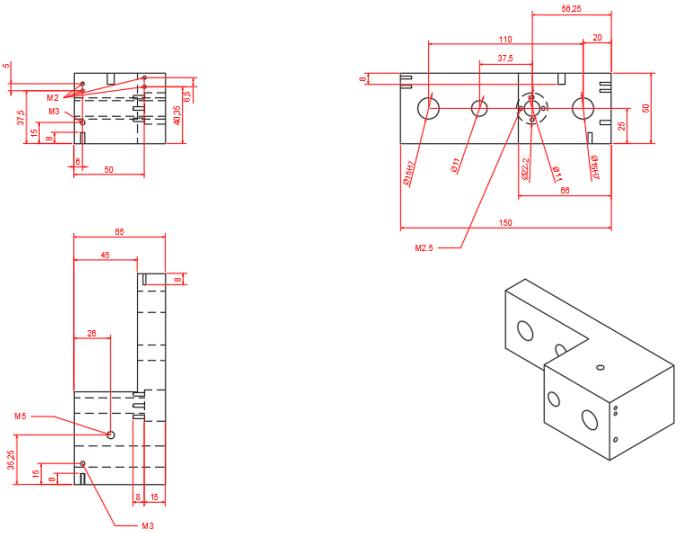

⑨

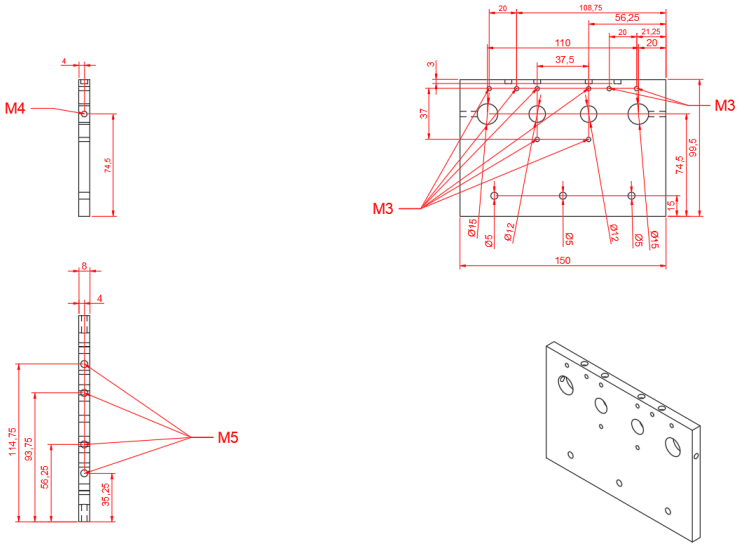

Figure C.5: Mechanical drawings of the of the components 7, 8 and 9.

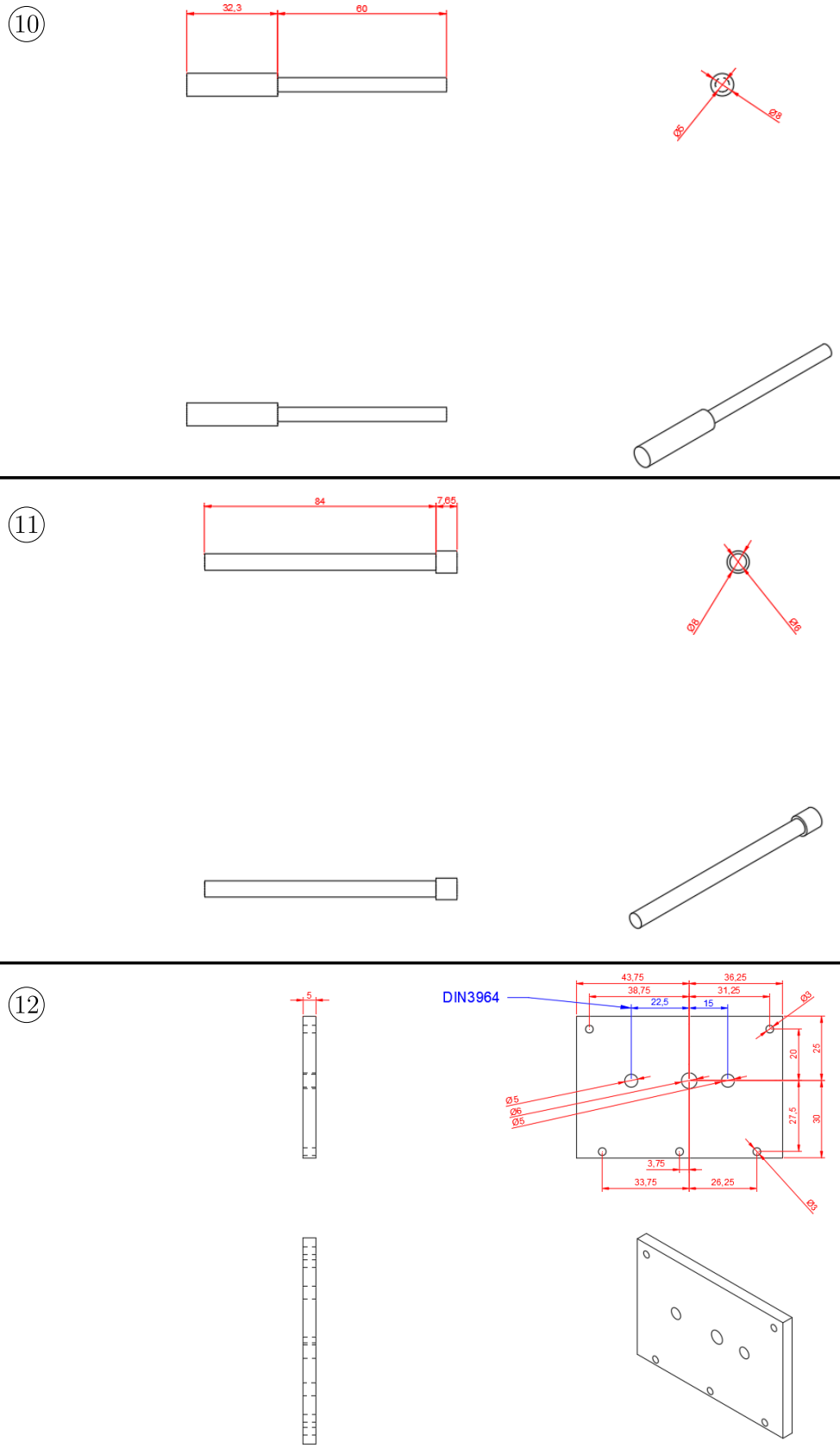

Figure C.6: Mechanical drawings of the of the components 10, 11 and 12.

13

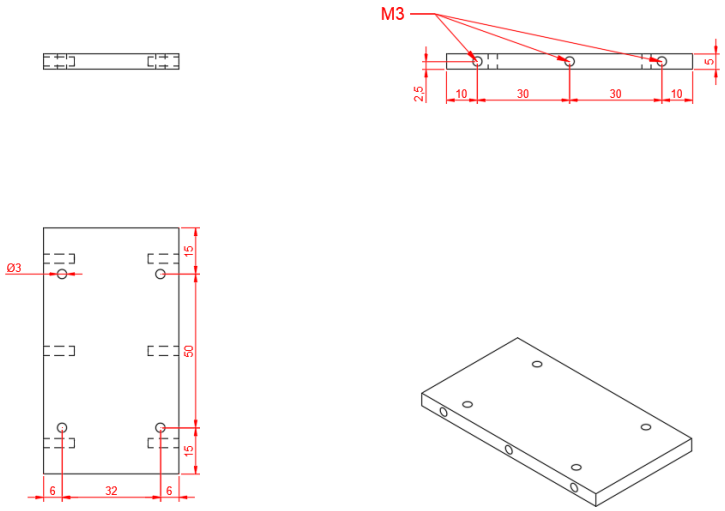

14

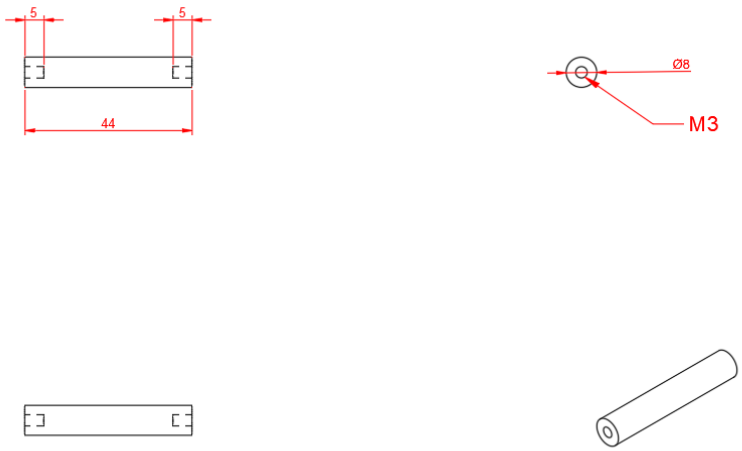

15

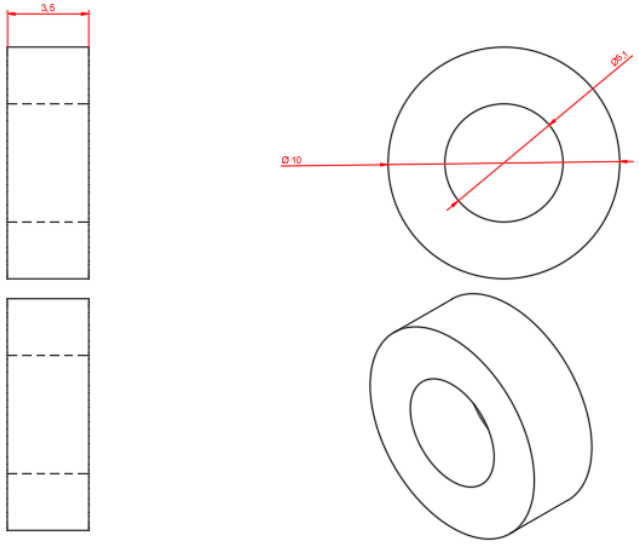

Figure C.7: Mechanical drawings of the of the components 13, 14 and 15.

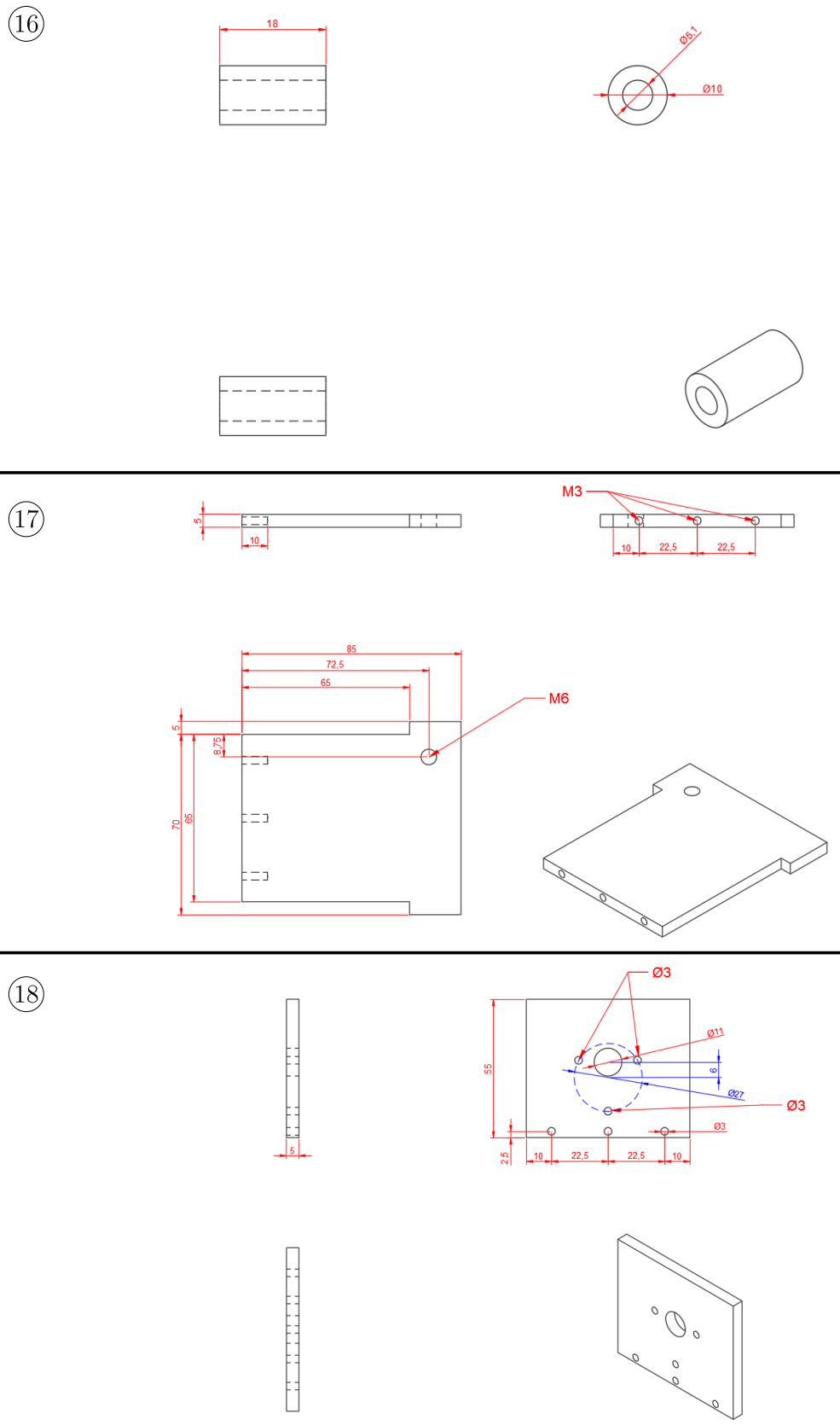

Figure C.8: Mechanical drawings of the of the components 16, 17 and 18.

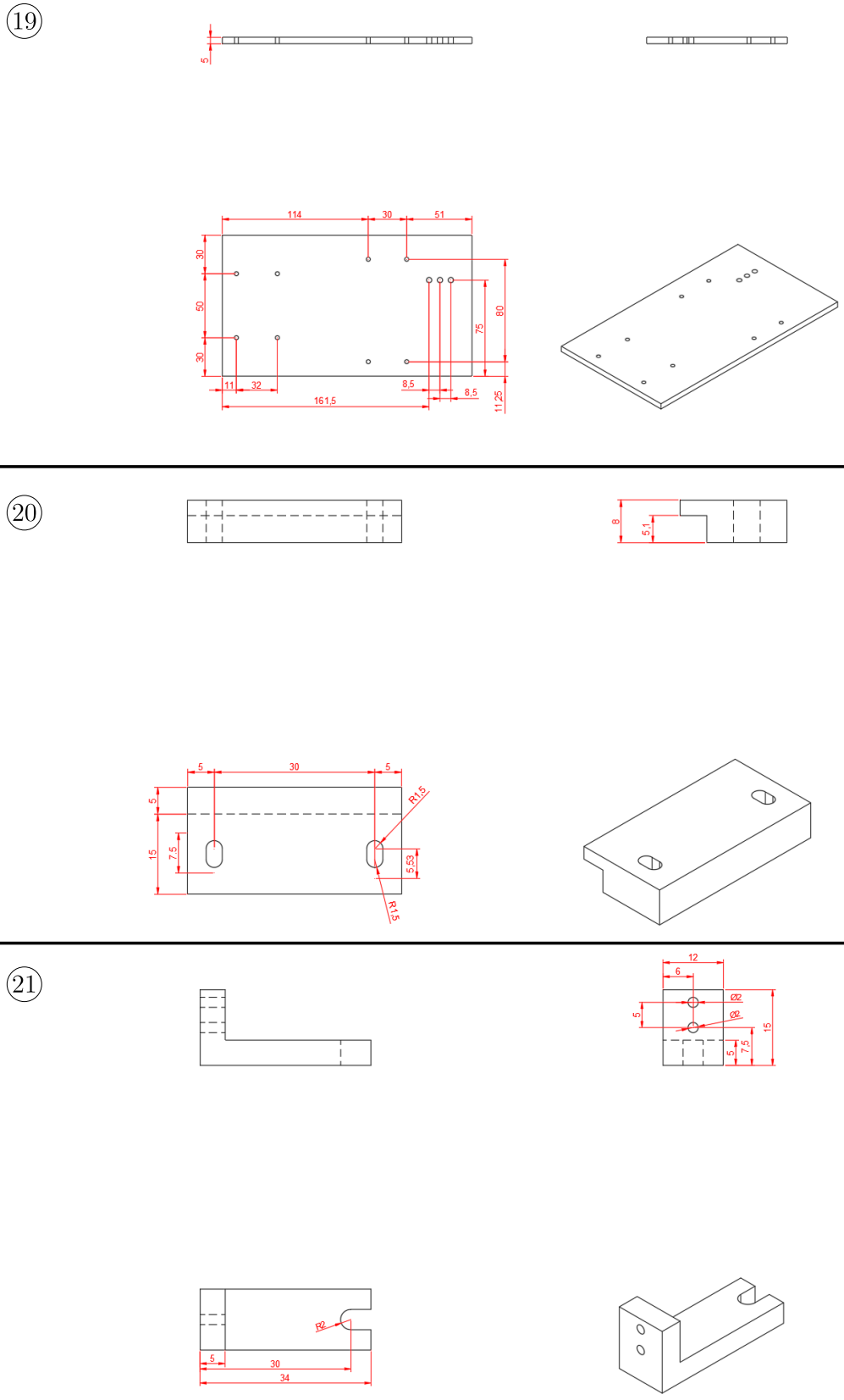

Figure C.9: Mechanical drawings of the of the components 19, 20 and 21.

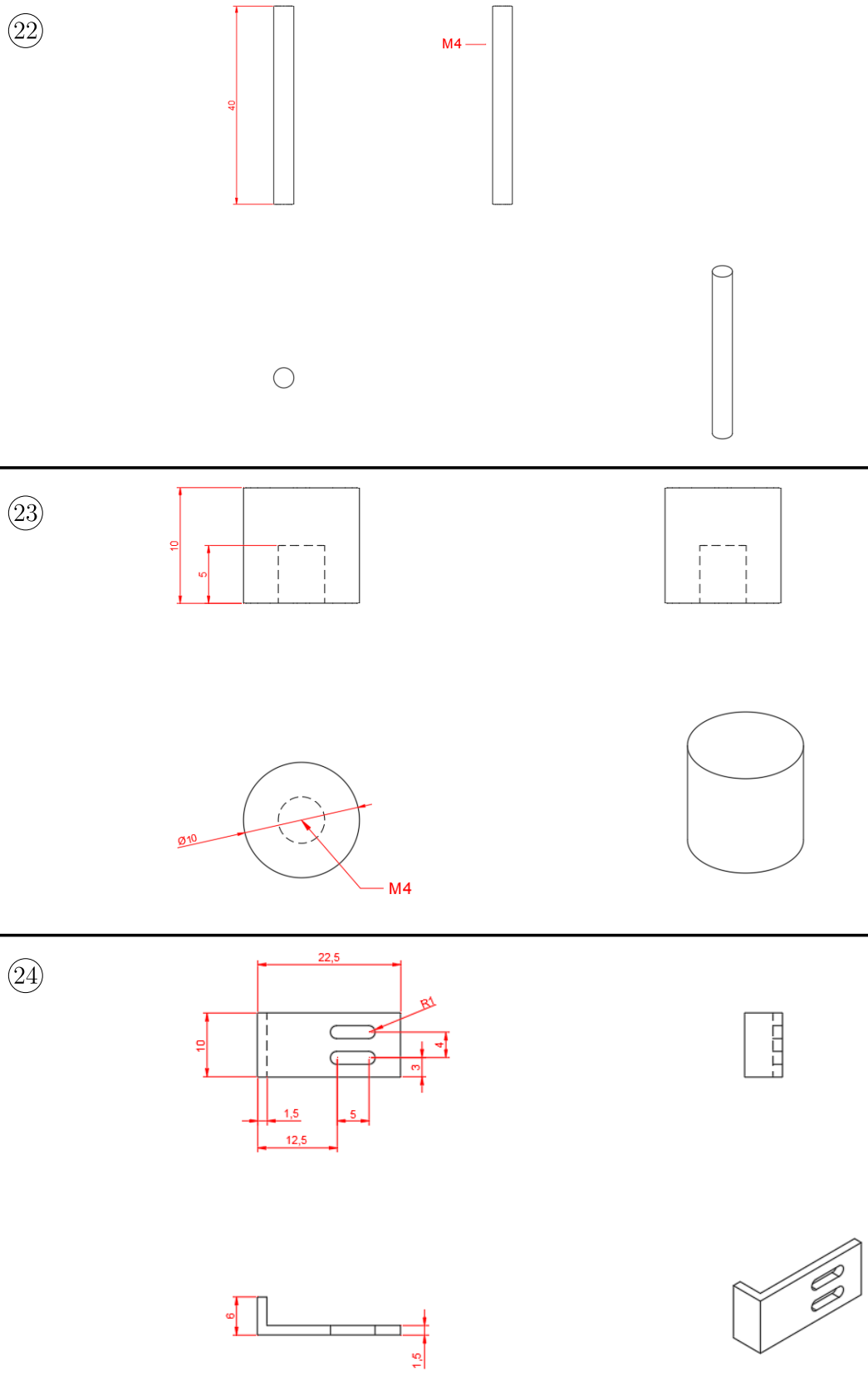

Figure C.10: Mechanical drawings of the of the components 22, 23 and 24.

25

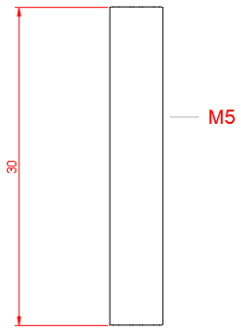

26

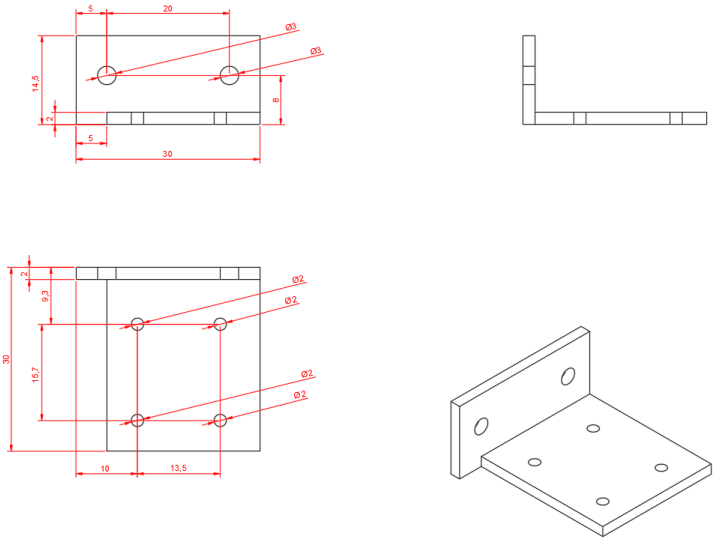

27

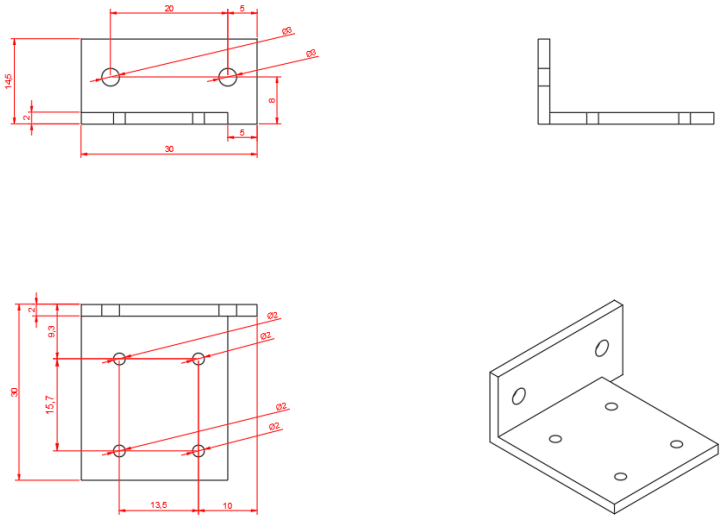

Figure C.11: Mechanical drawings of the of the components 25, 26 and 27.

C.1.2 Mechanical parts manufactured in Permaglas

These mechanical parts were manufactured by the company *Resarm engineering plastics*.

(a)

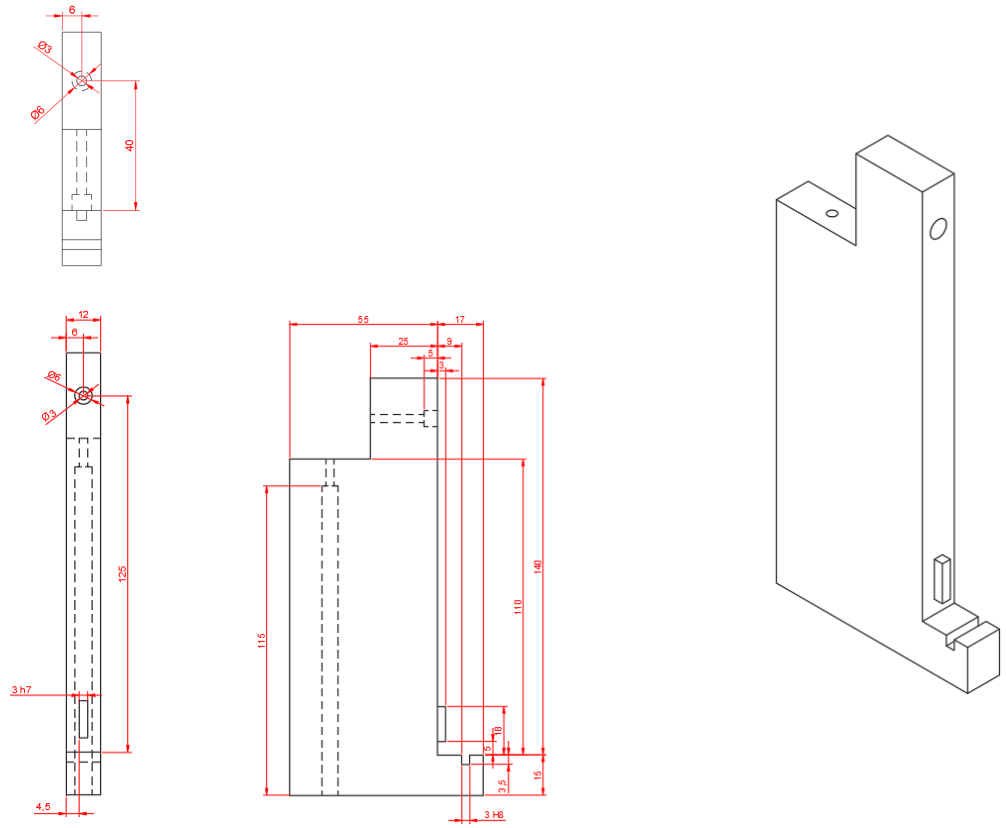

(b)

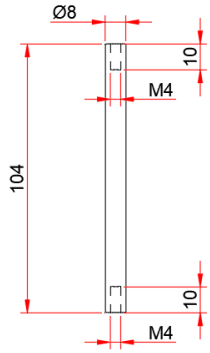

Figure C.12: Mechanical drawings of the of the components manufactured in Permaglas. (a) Sample mounting frame; (b) Manipulation rod.

C.2 Bespoke PPMS insertion instrument

All the mechanical parts were manufactured in aluminium at the mechanical workshop of the physics department at the University of Liege. The numbering used is presented in Figure C.13. Note that parts number ⑨ and ⑪ are not visible in that Figure. Those components consist of protection tubes added for cable management.

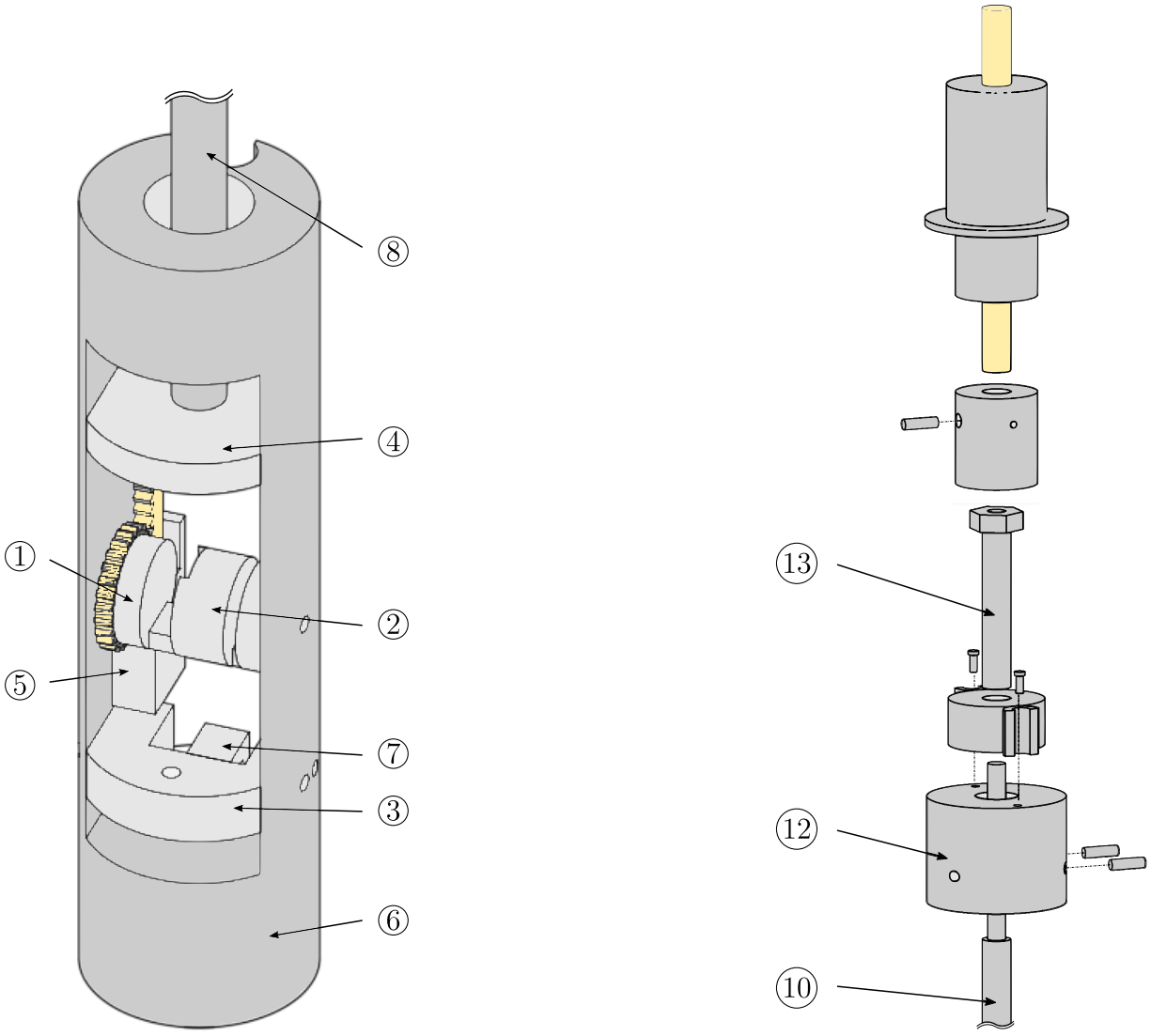

Figure C.13: Numbering of the mechanical part manufactured for the PPMS insertion instrument.

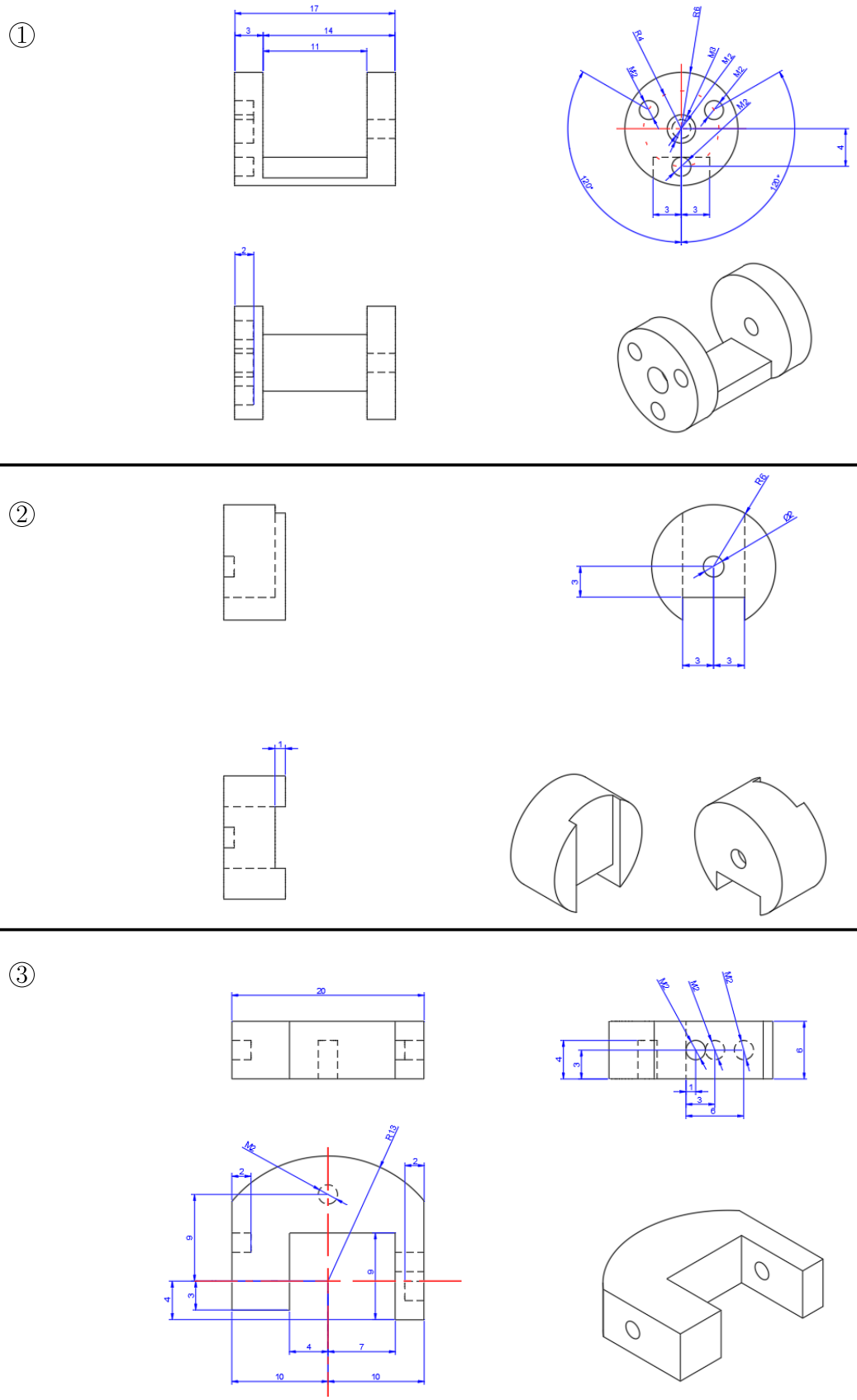

Figure C.14: Mechanical drawings of the components numbered 1, 2 and 3.

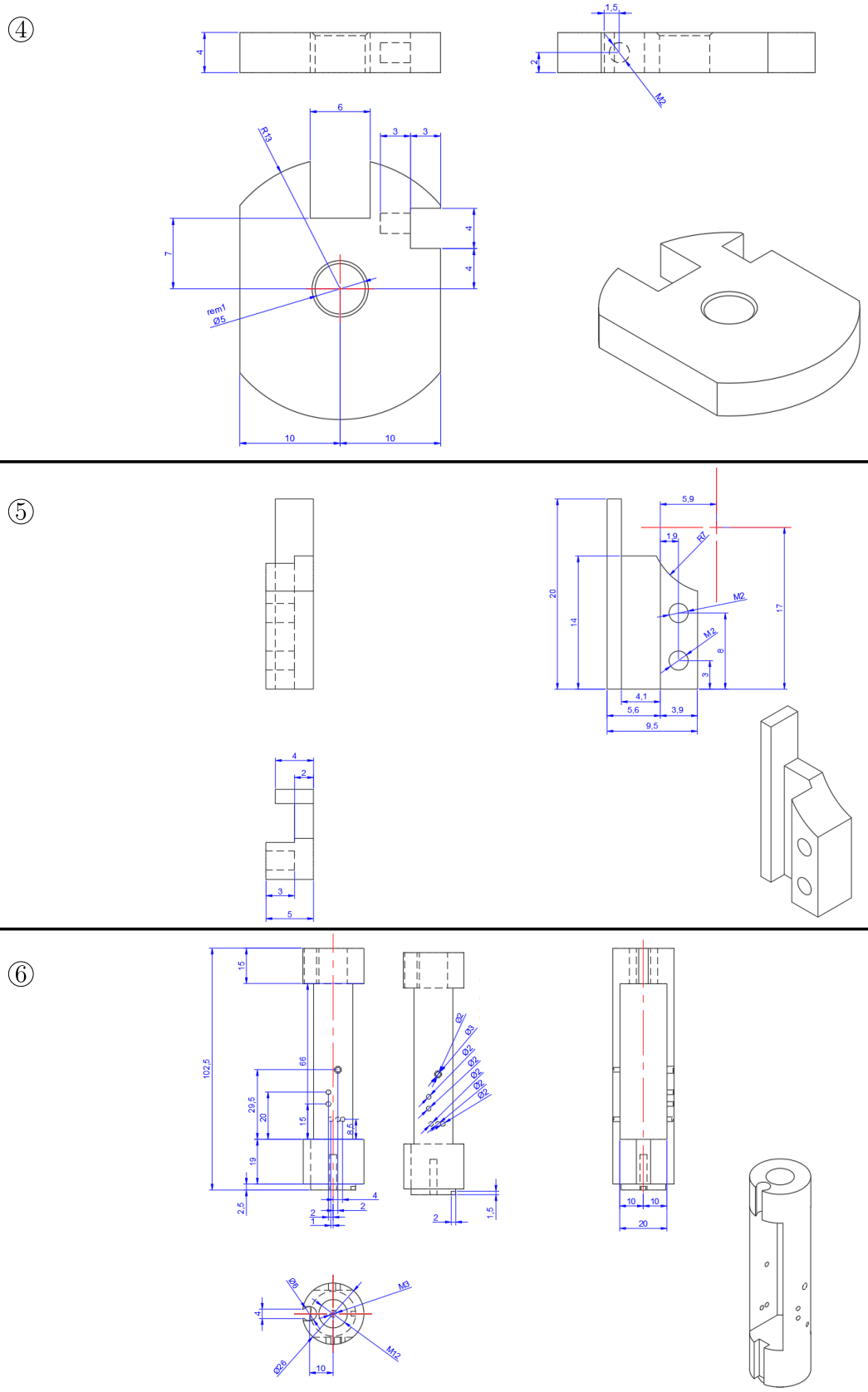

Figure C.15: Mechanical drawings of the components numbered 4, 5 and 6.

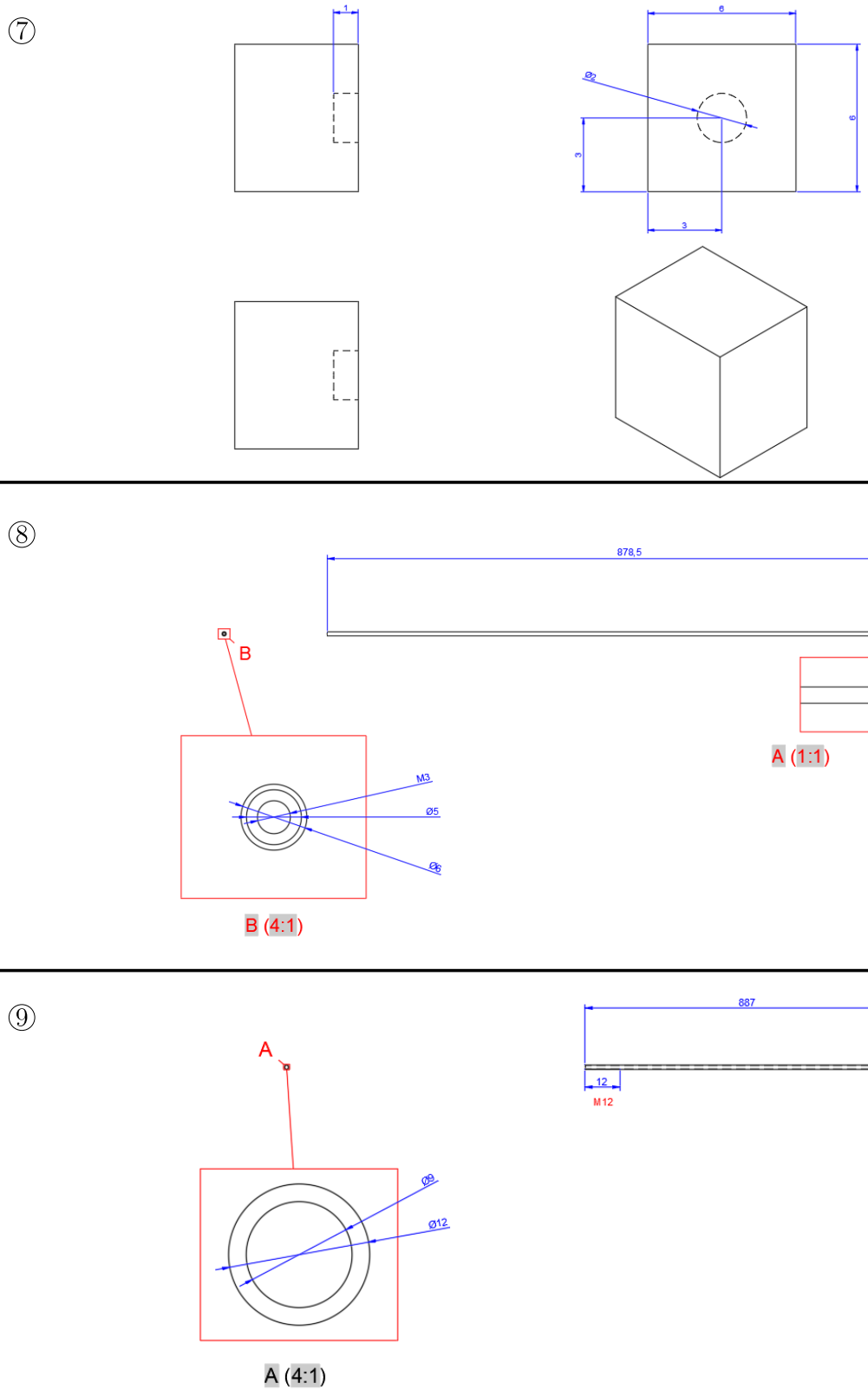

Figure C.16: Mechanical drawings of the components numbered 7, 8 and 9.

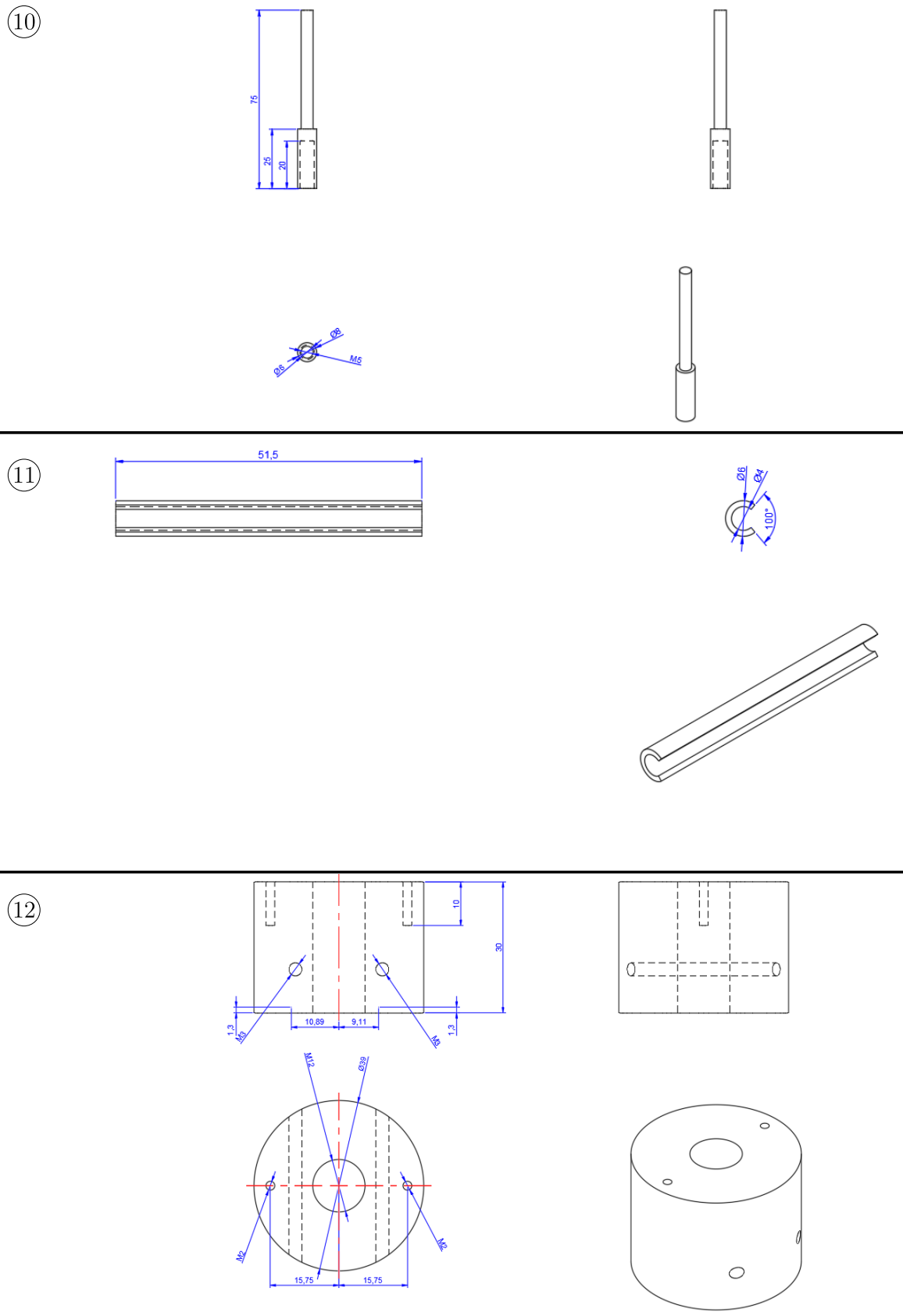

Figure C.17: Mechanical drawings of the components numbered 10, 11 and 12.

13

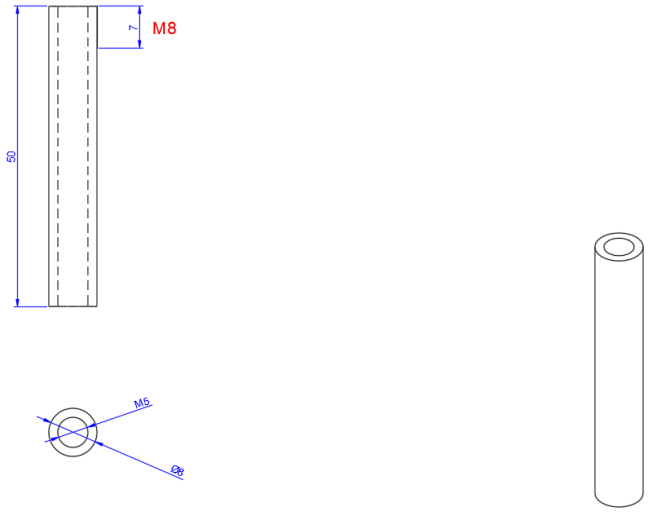

Figure C.18: Mechanical drawings of the component numbered 13.

Bibliography

[1] W. Ge, A. Encinas, E. Araujo, and S. Song. Magnetic matrices used in high gradient magnetic separation (HGMS): A review. *Results in Physics*, 7:4278–4286, 2017.

[2] J. H. Durrell, M. D. Ainslie D. Zhou, P. Vanderbemden, T. Bradshaw, S. Speller, M. Filipenko, and D. A. Cardwell. Bulk superconductors: a roadmap to applications. *Supercond. Sci. Technol.*, 31:103501, 2018.

[3] F. N. Werfel, U. Floegel-Delor, R. Rothfeld, T. Riedel, B. Goebel, D. Wippich, and P. Schirrmeister. Superconducting bearings, flywheels and transportation. *Supercond. Sci. Technol.*, 25:014007, 2012.

[4] K. S. Haran, S. Kalsi, T. Arndt, H. Karmaker, R. Badcock, B. Buckley, T. Haugan, M. Izumi, D. Loder, J. W. Bray, P. Masson, and E. W. Stautner. High power density superconducting rotating machines-development status and technology roadmap. *Supercond. Sci. Technol.*, 30:123002, 2017.

[5] C. C. T. Chow, M. D. Ainslie, and K. T. Chau. High temperature superconducting rotating electrical machines: An overview. *Energy Rep.*, 9:1124–1156, 2023.

[6] S. Senapati, A. K. Mahanta, S. Kumar, and P. Maiti. Controlled drug delivery vehicles for cancer treatment and their performance. *Signal Transduct. Target. Ther.*, 3:7, 2018.

[7] Q. A. Pankhurst, J. Connolly, S. K. Jones, and J. Dobson. Applications of magnetic nanoparticles in biomedicine. *J. Phys. D: Appl. Phys.*, 36:R167, 2003.

[8] W. F. Brown. Thermal fluctuations of a single-domain particle. *Phys. Rev.*, 130:1677–1686, 1963.

[9] S. Martel. Advantages and Limitations of the Various Magnetic Manipulation Methods of Untethered Agents in the Human Body. *Proc. IEEE/ASME Int. Conf. Adv. Intell. Mechatron.*, pages 13–18, 2014.

[10] M. Gao, C. Hu, Z. Chen, H. Zhang, and S. Liu. Design and Fabrication of a Magnetic Propulsion System for Self-Propelled Capsule Endoscope. *IEEE Trans. Biomed. Eng.*, 57:2891–2902, 2010.

[11] S. Tognarelli. Magnetic propulsion and ultrasound tracking of endovascular devices. *J. Robot. Surg.*, 6:5–12, 2012.

[12] A. W. Mahoney, and J.J. Abbott. Five-degree-of-freedom manipulation of an untethered magnetic device in fluid using a single permanent magnet with application in stomach capsule endoscopy. *Int. J. Robot. Res.*, 35:129–147, 2015.

[13] O. Baun, and P. Blumler. Permanent magnet system to guide superparamagnetic particles. *J. Magn. Magn. Mater.*, 439:294–304, 2017.

[14] L. C. Barnsley, D. Carugo, and E. Stride. Optimized shapes of magnetic arrays for drug targeting applications. *J. Phys. D: Appl. Phys.*, 49:225501, 2016.

[15] H. Kee, H. Lee, and S. Park. Optimized Halbach array for focused magnetic drug targeting. *J. Magn. Magn. Mater.*, 514:167180, 2020.

[16] A. Omelyanchik, G. Lamura, D. Peddis, and F. Canepa. Optimization of a NdFeB permanent magnet configuration for in-vivo drug delivery experiments. *J. Magn. Magn. Mater.*, 522:167491, 2021.

[17] H. A. Shute, J. C. Mallinson, D. T. Wilton, and D. J. Mapps. One-Sided Fluxes in Planar, Cylindrical, and Spherical Magnetized Structures. *IEEE Trans. Magn.*, 36:440–450, 2000.

[18] H. A. Leupold, and E. Potenziana. Novel high-field permanent-magnet flux sources. *IEEE Trans. Magn.*, 23:3628–3629, 1987.

[19] H. A. Leupold, A. Tilak, and E. Potenziana. Doubly augmented magic spheres. *IEEE Trans. Magn.*, 32:5079—5081, 1996.

[20] J. C. Mallinson. One-Sided Fluxes - A Magnetic Curiosity? *IEEE Trans. Magn.*, 9(4):678–682, 1973.

[21] K. Halbach. Design of permanent multipole magnets with oriented rare earth cobalt material. *Nucl. Instrum. Methods*, 169:1–10, 1980.

[22] K. Halbach. Physical and Optical Properties of Rare Earth Cobalt Magnets. *Nucl. Instrum. Methods*, 187:109–117, 1981.

[23] K. Halbach. Perturbation Effects in Segmented Rare Earth Cobalt Multipole Magnets. *Nucl. Instrum. Methods*, 198:213–215, 1982.

[24] H.-W. Lee, K.-C. Kim, and J. Lee. Review of Maglev Train Technologies. *IEEE Trans. Magn.*, 42:1917–1925, 2006.

[25] M. J. Bala, D. Roy, and A. Sengupta. The Performance Enhancement of BLDC Motor Using Halbach Array Rotor. *IEEE I.C.C.E.*, pages 405–409, 2020.

[26] R. P. Praveen, M. H. Ravichandran, V. T. Sadasivan Achari, V. P. Jagathy Raj, G. Madhu, and G. R. Bindu. A Novel Slotless Halbach-Array Permanent-Magnet Brushless DC Motor for Spacecraft Applications. *IEEE Trans. Ind. Electron.*, 59:3553–3560, 2012.

[27] S.-M. Jang, S.-S. Jeong, and S.-D. Cha. The Application of Linear Halbach Array to Eddy Current Rail Brake System. *IEEE Trans. Magn.*, 37:2627–2629, 2001.

[28] J. H. Kang, H. Driscoll, M. Super, and D. E. Ingber. Application of a Halbach magnetic array for long-range cell and particle separations in biological samples. *Appl. Phys. Lett.*, 108:213702, 2016.

[29] M. Latulippe, and S. Martel. Dipole Field Navigation for Targeted Drug Delivery. *Proc. IEEE 5th RAS/EMBS Int. Conf. Biomed. Robot. Biomechatronics*, pages 320–325, 2014.

[30] M. Latulippe, and S. Martel. Dipole Field Navigation: Theory and Proof of Concept. *IEEE Trans. Robot.*, 31(6):1353–1363, 2015.

[31] M. Latulippe, O. Felfoul, P. E. Dupont, and S. Martel. Enabling automated magnetic resonance imaging-based targeting assessment during dipole field navigation. *Appl. Phys. Lett.*, 108:062403, 2016.

[32] M. Latulippe, and S. Martel. Evaluation of the Potential of Dipole Field Navigation for the Targeted Delivery of Therapeutic Agents in a Human Vascular Network. *IEEE Trans. Magn.*, 54(2):5600112, 2018.

[33] F. Fohr, and N. Volbers. A high-saturation Fe-27Co material with microalloying additions. *AIP Advances*, 8:047701, 2018.

[34] D. Brown, B.-M. Ma, and Z. Chen. Developments in the processing and properties of NdFeB-type permanent magnets. *J. Magn. Magn. Mater.*, 248(3):432–440, 2002.

[35] F. Fohr, and N. Volbers. A high-saturation Fe-27Co material with microalloying additions. *AIP Advances*, 8:047701, 2018.

[36] H. Kamerlingh Onnes. The superconductivity of mercury. *Comm. Phys. Lab. Univ. Leiden*, 122:122–124, 1911.

[37] W. Meisner, and R. Ochsenfeld. Ein neuer effekt bei eintritt der supraleitfahigkeit. *Naturwissenschaften*, 21:787–788, 1933.

[38] A. A. Abrikosov. The magnetic properties of superconducting alloys. *J. Phys. Chem. Solids*, 2:199–208, 1957.

[39] C. Yao, and Y. Ma. Superconducting materials: Challenges and opportunities for large-scale applications. *Iscience*, 24:102541, 2021.

[40] C. Barth. *High temperature superconductor cable concepts for fusion magnets.* KIT Scientific publishing, 2014.

[41] R.G. Sharma. *Superconductivity: Basics and applications to magnets*, volume 214. Springer Nature, 2021.

[42] Y. Statra, H. Menana, B. Douine, and T. Lubin. Axial-Field Synchronous Machine With HTS Armature Windings: Realization and Preliminary Tests. *IEEE Trans. Appl. Supercond.*, 32:5200405, 2022.

[43] C. Rey. *Superconductors in the power grid: Materials and applications.* Elsevier, 2015.

[44] M. D. Brown, J. Jiang, C. Tarantini, D. Abraimov, G. Bradford, J. Jaroszynski, E. E. Hellstrom, and D. C. Larbalestier. Prediction of the Jc (B) behavior of Bi-2212 wires at high field. *IEEE Trans. Appl. Supercond.*, 29:6400504, 2019.

[45] J. Zhu, S. Chen, and Z. Jin. Progress on second-generation high-temperature superconductor tape targeting resistive fault current limiter application. *Electronics*, 11:11030297, 2022.

[46] M. Sakoda, K. Iida, and M. Naito. Recent progress in thin-film growth of Fe-based superconductors: superior superconductivity achieved by thin films. *Supercond. Sci. Technol.*, 31:093001, 2018.

[47] P. Cayado, J. Hänisch, K. Iida, and Carmine Senatore. Focus on recent advances in superconducting films. *Supercond. Sci. Technol.*, 36:090401, 2023.

[48] J. R. Hull, and M. Murakami. Applications of bulk high-temperature superconductors. *Proc. IEEE*, 92(10):1705–1718, 2004.

[49] M. Murakami. Processing and applications of bulk RE-Ba-Cu-O superconductors. *Int. J. Appl. Ceram. Technol.*, 4(3):225–239, 2007.

[50] M. D. Ainslie, and H. Fujishiro. Modelling of bulk superconductor magnetization. *Supercond. Sci. Technol.*, 28:053002, 2015.

[51] O. Vakaliuk, F. Werfel, J. Jaroszynski, and B. Halbedel. Trapped field potential of commercial Y-Ba-Cu-O bulk superconductors designed for applications. *Supercond. Sci. Technol.*, 33:095005, 2020.

[52] J. H. Durrell, A. R. Dennis, J. Jaroszynski, M. D. Ainslie, K. G. B. Palmer, Y. Shi, A. M. Campbell, J. Hull, M. Strasik, E. E. Hellstrom, and D. A. Cardwell. A trapped field of 17.6T in melt-processed, bulkk Gd-Ba-Cu-O reinforced with shrink-fit steel. *Supercond. Sci. Technol.*, 27:082001, 2014.

[53] A. Patel, A. Baskys, T. Mitchell-Williams, A. McCaul, W. Coniglio, J. Hänisch, M. Lao, and B. A. Glowacki. A trapped field of 17.7 T in a stack of high temperature superconducting tape. *Supercond. Sci. Technol.*, 31:09LT01, 2018.

[54] S. Tumanski. *Handbook of magnetic measurements.* CRC Press, 2011.

[55] T. P. Orlando, and K. A. Delin. *Foundation of applied superconductivity.* Addison-Wesly Publishing Company, 1991.

[56] C. Navau, N. Del-Valle, and A. Sanchez. Macroscopic modeling of magnetization and levitation of hard type-II superconductors: The critical-state model. *IEEE Trans. Appl. Supercond.*, 23:8201023, 2013.

[57] J. G. Bednorz, and K. A. Muller. Possible high T_c superconductivity in the Ba-La-Cu-O system. *Zeitschrift für Physik B Condensed Matter*, 64:189–193, 1986.

[58] M.-K. Wu, J. R. Ashbrurn, C. Torng, P.-H. Har, R. L. Meng, L. Gao, Z. J. Huang, Y. Wang, and A. Chu. Superconductivity at 93 K in a new mixed-phase Y-Ba-Cu-O compound system at ambient pressure. *Phys. Rev. Lett.*, 58:908, 1987.

[59] C. Michel, M. Hervieu, M. Borel, A. Grandin, F. Deslandes, J. Provost, and B. Raveau. Superconductivity in the Bi-Sr-Cu-O system. *Zeitschrift für Physik B Condensed Matter*, 68:421–423, 1987.

[60] S. Gotoh, M. Murakami, H. Fujimoto, and N. Koshizuka. Magnetic properties of superconducting $YBa_2Cu_3O_x$ permanent magnets prepared by the melt process. *J. Appl. Phys.*, 72(6):2404–2410, 1992.

[61] F. Sirois, F. Grilli and A. Morandi. Comparison of Constitutive Laws for Modeling High-Temperature Superconductors. *IEEE Trans. Appl. Supercond.*, 29:8000110, 2019.

[62] J. Rhyner. Magnetic properties and AC-losses of superconductors with power law current—voltage characteristics. *Physica C Supercond.*, 212:292–300, 1993.

[63] E. Zeldov, N. M. Amer, G. Koren, A. Gupta, M. W. McElfresh, and R. J. Gambino. Flux creep characteristics in high temperature superconductors. *Appl. Phys. Lett.*, 56(7):680–682, 1990.

[64] E. Zeldov. Flux creep and vortex potential well structure in high-temperature superconductors. *Physica A*, 168:260–267, 1990.

[65] P.W. Anderson. Theory of Flux Creep in Hard Superconductors. *Phys. Rev. Lett.*, 9:309–311, 1962.

[66] C. P. Bean. Magnetization of hard superconductors. *Phys. Rev. Lett.*, 8(6):250–253, 1962.

[67] B. Douine, F. Sirois, J. Lévêque, K. Berger, C.-H. Bonnar, T.-C. Hoang, and S. Mezani. A New Direct Magnetic Method for Determining Jc in Bulk Superconductors from Magnetic Field Diffusion Measurements. *IEEE Trans. Appl. Supercond.*, 22:9001604, 2012.

[68] B. Douine, K. Berger, C.-H. Bonnard, F. Sirois, A. Kameni, and J. Lévêque. Improved Method for Determining the n-Value of HTS Bulks. *IEEE Trans. Appl. Supercond.*, 26:6800704, 2016.

[69] B. Douine, J. Lévêque, and S. Mezani. JC(B) Determination Method With the Help of the Virgin Magnetization Curve of a Superconducting Cylinder. *IEEE Trans. Appl. Supercond.*, 20:82–86, 2010.

[70] B. Douine, C.-H. Bonnard, F. Sirois, K. Berger, A. Kameni, and J. Lévêque. Determination of JC and n-Value of HTS Pellets by Measurement and Simulation of Magnetic Field Penetration. *IEEE Trans. Appl. Supercond.*, 25:8001008, 2015.

[71] X. Zhang, Z. Zhong, J. Geng, B. Shen, J. Ma, C. Li, H. Zhang, Q. Dong, and T. Coombs. Study of critical current and n-values of 2g hts tapes: Their magnetic field-angular dependence. *J. Supercond. Novel Magn.*, 31:3847–3854, 2004.

[72] H. Yamasaki, and Y. Mawatari. Current-voltage characteristics and flux creep in melt-textured $YBa_2Cu_3O_7$. *Supercond. Sci. Technol.*, 13(2):202–208, 2000.

[73] J. Z. Sun, C. B. Eom, B. Lairson, J. C. Bravman, and T. H. Geballe. Magnetic relaxation, current-voltage characteristics, and possible dissipation mechanisms for high-T_c superconducting the films of Y-Ba-Cu-O. *Phys. Rev. B*, 43(4):3002–3008, 1991.

[74] P. Monk. *Finite Element Methods for Maxwell's Equations*. Clarendon, 2003.

[75] J. Dular, C. Geuzaine, and B. Vanderheyden. Finite-Element Formulations for Systems With High-Temperature Superconductors. *IEEE Trans. Appl. Supercond.*, 30(3):8200113, 2020.

[76] J. Dular, K. Berger, C. Geuzaine, and B. Vanderheyden. What Formulation Should One Choose for Modeling a 3-D HTS Motor Pole With Ferromagnetic Materials? *IEEE Trans. Magn.*, 58:8205204, 2022.

[77] Life-HTS. `http://www.life-hts.uliege.be/`.

[78] Nonlinear solvers. `https://gitlab.onelab.info/getdp/getdp/-/wikis/Nonlinear-solvers`.

[79] J. Rhyner. Magnetic properties and AC-losses of superconductors with power law current—voltage characteristics. *Phys. C: Supercond.*, 212:292–300, 1993.

[80] O. Biro. Edge element formulations of eddy current problems. *Comput. Methods Appl. Mech. Eng.*, 169:391–405, 1999.

[81] R. Brambilla, F. Grilli, L. Martini, M. Bocchi, and G. Angeli. A Finite-Element Method Framework for Modeling Rotating Machines With Superconducting Windings. *IEEE Trans. Appl. Supercond.*, 28:5207511, 2018.

[82] A. Arsenault, F. Sirois, and F. Grilli. Efficient Modeling of High-Temperature Superconductors Surrounded by Magnetic Components Using a Reduced H–ϕ Formulation. *IEEE Trans. Appl. Supercond.*, 31:6800609, 2021.

[83] A. Arsenault, B. d. S. Alves, G. Giard, and F. Sirois. Magnetodynamic H–ϕ Formulation for Improving the Convergence and Speed of Numerical Simulations of Superconducting Materials. *IEEE Trans. Appl. Supercond.*, 33:6801306, 2023.

[84] F. Sass, G. G. Sotelo, R. de Andrade Junior, and F. Sirois. H-formulation for simulating levitation forces acting on HTS bulks and stacks of 2G coated conductors. *Supercond. Sci. Technol.*, 28:125012, 2015.

[85] F. Grilli, R. Brambilla, F. Sirois, A. Stenvall, and S. Memiaghe. Development of a three-dimensional finite-element model for high-temperature superconductors based on the H-formulation. *Cryogenics*, 53:142–147, 2013.

[86] A. Creusé, P. Dular, and S. Nicaise. About the gauge conditions arising in Finite Element magnetostatic problems. *Comput. Math. Appl.*, 77:1563–1582, 2019.

[87] G. P. Lousberg, M. Ausloos, C. Geuzaine, P. Dular, P. Vanderbemden, and B. Vanderheyden. Numerical simulation of the magnetization of high-temperature superconductors: a 3D finite element method using a single time-step iteration. *Supercond. Sci. Technol.*, 22:055005, 2009.

[88] A. Bossavit. Whitney forms: A class of finite elements for three-dimensional computations in electromagnetism. *IEE: Proc. Sci. Meas. Tech.*, 135:493–500, 1988.

[89] P. Dular, J.-Y. Hody, A. Nicolet, A. Genon, and W. Legros. Mixed finite elements associated with a collection of tetrahedra, hexahedra and prisms. *IEEE Trans. Magn.*, 30:2980–2983, 1994.

[90] J. Lohi and L. Kettunen. Whitney forms and their extensions. *J. Comput. Appl. Math.*, 393:113520, 2021.

[91] A. Bossavit. A rationale for edge-elements in 3D fields computations. *IEEE Trans. Magn.*, 24:74–79, 1988.

[92] P. Dular. The benefits of nodal and edge elements coupling for discretizing global constraints in dual magnetodynamic formulations. *J. Comput. Appl. Math.*, 168:165–178, 2004.

[93] P. Dular, C. Geuzaine, and W. Legros. A Natural Method for Coupling Magnetodynamic H-Formulations and Circuit Equations. *IEEE Trans. Magn.*, 35:1626–1629, 1999.

[94] D. F. Griffiths and D. J. Higham. *Numerical Methods for Ordinary Differential Equations: Initial Value Problems*. Springer, London, 2010.

[95] A. Nicolet and F. Delincé. Implicit Runge-Kutta methods for transient magnetic field computation. *IEEE Trans. Magn.*, 32:1405–1408, 1996.

[96] K. Yamazaki. Eddy current analysis using mixed moving coordinate systems for electrical machines including conductors moving at different velocities. *EEJ*, 118:111–120, 1997.

[97] K. Yamazaki and T. Sogawa. Finite element analysis of a canned motor. *Proc. of ISEL-Seoul*, 285, 1994.

[98] K. Muramatsu, T. Nakata, N. Takahashi, and K. Fujiwarta. Comparison of coordinate systems for eddy current analysis in moving conductors. *IEEE Trans. Magn.*, 28:1186–1189, 1992.

[99] V. Leconte. *The finite element method for electromagnetic modeling*. Gérard Meunier, 2008.

[100] K. Yamazaki. 3D Eddy current formulation for moving conductors with variable velocity of coordinate system using edge finite elements. *IEEE Trans. Magn.*, 35:1594–1597, 1999.

[101] M. Houbart, J.-F. Fagnard, A. R. Dennis, D. K. Namburi, Y. Shi, J. H. Durrell, and P. Vanderbemden. Trapped magnetic field distribution above two magnetized bulk superconductors close to each other. *Supercond. Sci. Technol.*, 33:064003, 2020.

[102] E. Durand. *Magnetostatique*. Masson et Cie, 1968.

[103] I. G. Chen, J. Liu, R. Weinstein, and K. Lau. Characterization of $YBa_2Cu_3O_7$, including critical current density J_c, by trapped magnetic field. *J. Appl. Phys.*, 72(3):1013–1020, 1992.

[104] C. Alexiou, D. Diehl, P. Henninger, H. Iro, R. Röckelein, W. Schmidt, and H. Weber. A High Field Gradient Magnet for Magnetic Drug Targeting. *IEEE Trans. Appl. Supercond.*, 16:1527–1530, 2006.

[105] B. Gleich, N. Hellwig, H. Bridell, R. Jurgons, C. Seliger, C. Alexiou, B. Wolf, and T. Weyh. Design and Evaluation of Magnetic Fields for Nanoparticle Drug Targeting in Cancer. *IEEE Trans. Nanotechnol.*, 6:164–170, 2007.

[106] A. D. Grief, and G. Richardson. Mathematical modelling of magnetically targeted drug delivery. *J. Magn. Magn. Mater.*, 293:455–463, 2005.

[107] C. F. Driscoll, R. M. Morris, A. E. Senyei, K. J. Widder, and G. S. Heller. Magnetic targeting of microspheres in blood flow. *Microvasc. Res.*, 27:353–369, 1984.

[108] BK Precision, Multi-Range Programmable DC Power Supplies. `https://bkpmedia.s3.us-west-1.amazonaws.com/downloads/datasheets/en-us/9115_Series_datasheet.pdf`.

[109] Thorlabs, Compact Motorized Translation Stage. `https://www.thorlabs.de/newgrouppage9.cfm?objectgroup_id=3002`.

[110] D. K. Namburi, Y. Shi, W. Zhai, A. R. Dennis, J. H. Durrell, and D. A. Cardwell. Buffer pellets for high-yield, top-seeded melt growth of large grain Y-Ba-Cu-O superconductors. *Cryst. Growth Des.*, 15:1472–1480, 2015.

[111] S. Nariki, H. Teshima, and M. Morita. Performance and applications of quench melt-growth bulk magnets. *Supercond. Sci. Technol.*, 29:034002, 2016.

[112] G. P. Lousberg, J.-F. Fagnard, X. Chaud, M. Ausloos, P. Vanderbemden, and B. Vanderheyden. Magnetic properties of drilled bulk high-temperature superconductors filled with a ferromagnetic powder. *Supercond. Sci. Technol.*, 24:035008, 2010.

[113] D. K. Namburi, Y. Shi, K. G. Palmer, A. R. Dennis, J. H. Durrell, and D. A. Cardwel. An improved top seeded infiltration growth method for the fabrication of Y–Ba–Cu–O bulk superconductors. *J. Eur. Ceram. Soc.*, 36:615–624, 2016.

[114] D. K. Namburi, Y. Shi, K. G. Palmer, A. R. Dennis, J. H. Durrell, and D. A. Cardwel. Control of Y-211 content in bulk YBCO superconductors fabricated by a buffer-aided, top seeded infiltration and growth melt process. *Supercond. Sci. Technol.*, 29:034007, 2016.

[115] D. K. Namburi, Y. Shi, K. G. Palmer, A. R. Dennis, J. H. Durrell, and D. A. Cardwel. Novel methods to characterize bulk RE-BCO superconductors. *Physica C Supercond.*, 426-431:625–631, 2005.

[116] A. Patel, A. Usoskin, A. Baskys, S. C. Hopkins, and B. A. Glowacki. Trapped field profiles for 40-mm wide superconducting tape pieces. *J. Supercond. Novel. Magn.*, 28:397–401, 2015.

[117] K. Selva and G. Majkic. Trapped magnetic field profiles of arrays of (Gd,Y)$Ba_2Cu_3O_x$ superconductor tape in different stacking configurations. *Supercond. Sci. Technol.*, 26:115006, 2013.

[118] T. B. Mitchell-Williams, A. Patel, A. Baskys, S. C. Hopkins, A. Kario, W. Goldacker, and B. A. Glowacki. Toward Uniform Trapped Field Magnets Using a Stack of Roebel Cable Offcuts. *IEEE Trans. Appl. Supercond.*, 26:6800404, 2016.

[119] N. Rotheudt, J.-F. Fagnard, P. Harmeling, and P. Vanderbemden. Adapting a commercial integrated circuit 3-axis Hall sensor for measurements at low temperatures: Mapping the three components of B in superconducting applications. *Cryogenics*, 133:103715, 2023.

[120] High Linearity Hall Probes for Room and Cryogenic Temperatures. https://www.google.com/url?sa=t&rct=j&q=&esrc=s&source=web&cd=&ved=2ahUKEwi7je7u-IaDAxVDwAIHHZGyCFMQFnoECBQQAQ&url=https%3A%2F%2Fcdck-file-uploads-europe1.s3.dualstack.eu-west-1.amazonaws.com%2Farduino%2Foriginal%2F3X%2Fd%2F5%2Fd559e0faeb022f01c157e000a41182b28a1e0d99.pdf&usg=AOvVaw3LwBtcfLA3M4kCp3Wh2cYn&opi=89978449.

[121] R. Egan, M. Philippe, L. Wera, J.-F. Fagnard, B. Vanderheyden, A. R. Dennis, Y. Shi, D. A. Cardwell, and P. Vanderbemden. A flux extraction device to measure the magnetic moment of large samples; application to bulk superconductors. *Rev. Sci. Instrum.*, 86(2):025107, 2015.

[122] Properties of solid materials from cryogenic- to room-temperatures. https://trc.nist.gov/cryogenics/materials/materialproperties.htm.

[123] Trapezoidal lead screw drylin®, double pitch, stainless steel 304. https://www.igus.ch/product/918?L=fr&artNr=PTGSG-10X2-01-R%2FL-1000-ES.

[124] Bronze cylindrical nut. https://shop.hpceurope.com/fr/produit.asp?prid=1262.

[125] PZ12 - Linear Motion Position Sensor. https://www.variohm.com/products/linear-position-sensors-/linear-potentiometers/pz12---linear-motion-position-sensor#:~:text=This%20PZ12%20mini%20position%20transducer,Pulling%20Rod%20Type.

[126] Igarashi gear motor. https://www.conrad.fr/fr/p/igarashi-motoreducteur-c-c-33gn2738-132-gv-5125-1-\protect\penalty\z@33gn2738-132-gv-5125-1-12-0-v-dc-0-35-a-637-nmm-36-tr-min-diametre-de-\protect\penalty\z@1711490.html.

[127] Data sheet of item W-12-N. https://www.supermagnete.fr/data_sheet_W-12-N.pdf.

[128] D. A. Cardwell. Processing and properties of large grain (RE)BCO. *Mater. Sci. Eng. B Solid State Mater. Adv. Technol.*, 53:1–10, 1998.

[129] Y. Shi, D. K. Namburi, W. Zhao, J. H. Durrell, A. R. Dennis, and D. A. Cardwell. The use of buffer pellets to pseudo hot seed (RE)-Ba-Cu-O-(Ag) single grain bulk superconductors. *Supercond. Sci. Technol.*, 29:015010, 2016.

[130] D. K. Namburi, Y. Shi, and D. A. Cardwell. The processing and properties of bulk (RE)BCO high temperature superconductors: current status and future perspectives. *Supercond. Sci. Technol.*, 34:053002, 2021.

[131] Quantum Design. `http://qdusa.com/products/ppms.html`.

[132] P. Vanderbemden, B. Rivas-Murias, V. Lovchinov, and B. Vertruyen. Measurement of dielectric properties at low temperatures: application to the study of magnetoresistive manganite/ insulating oxide bulk composites. *Supercond. Sci. Technol.*, 253:012006, 2010.

[133] P. Vanderbemden, Z. Hong, T. A. Coombs, S. Denis, M. Ausloos, J. Schwartz, I. B. Rutel, N. Hari Babu, D. A. Cardwell, and A. M. Campbell. Behavior of bulk high-temperature superconductors of finite thickness subjected to crossed magnetic fields: Experiment and model. *Phys. Rev. B*, 75:174515, 2007.

[134] M. P. Philippe, J.-F. Fagnard, S. Kirsch, Z. Xu, A. R. Dennis, Y. Shi, D. A. Cardwell, B. Vanderheyden, and P. Vanderbemden. Magnetic characterisation of large grain, bulk Y–Ba–Cu–O superconductor–soft ferromagnetic alloy hybrid structures. *Physica C Supercond.*, 502:20–30, 2014.

[135] M. P. Philippe, J.-F. Fagnard, L. Wéra, M. Morita, S. Nariki, H. Teshima, H. Caps, B. Vanderheyden, and P. Vanderbemden. Influence of crossed fields in structures combining large grain, bulk (RE)BCO superconductors and soft ferromagnetic discs. *J. Phys. Conf. Ser.*, 695:012003, 2016.

[136] J.-F. Fagnard, M. Morita, S. Nariki, H. Teshima, H. Caps, B. Vanderheyden, and P. Vanderbemden. Magnetic moment and local magnetic induction of superconducting/ferromagnetic structures subjected to crossed fields: experiments on GdBCo and modelling. *Supercond. Sci. Technol.*, 29(12), 2016.

[137] *Quantum Design - Physical Property Measurement System Brochure.*

[138] *Quantum Design - Physical Property Measurement System - Hardware Manual.*

[139] AC Measurement System (ACMS) Option User's Manual. `https://web.njit.edu/~tyson/PPMS_Documents/PPMS_Manual/1084-100%20C1%20ACMS%20manual.pdf`.

[140] S. Debois. *Réalisation d'un système cryogénique de mesure de l'anisotropie des propriétés magnétiques d'aimants supraconducteurs.* Master thesis, University of Liege, 2014.

[141] Physical Property Measurement System (PPMS) – Horizontal Rotator (HR). `https://www.ccmr.cornell.edu/wp-content/uploads/sites/2/2015/11/PPMS-SOP-Rotator-V3.pdf`.

[142] Straight cylindrical brass gear. `https://www.michaud-chailly.fr/fr/roue-cylindrique-droite-laiton-module-0-5-largeur-denture-2mm-a1-263/`.

[143] Brass rack. https://www.michaud-chailly.fr/fr/cremaillere-laiton-module-0-3-1-a1-573/.

[144] Rotary Feedthroughs ISO-KF. https://www.leyboldproducts.fr/en/products/feedthroughs/rotary-linear-motion-feedthroughs/481/rotary-feedthroughs-iso-kf?countryswitch=FR.

[145] Kurt J. Lesker Company. https://www.lesker.com/.

[146] Nema 14 bipolar gearless stepper. https://www.active-robots.com/3323-0-35sth36-nema-14-bipolar-gearless-stepper.html.

[147] Optical Rotary Encoder HKT22. https://www.eztronics.nl/webshop2/catalog/index.php?route=product/product&product_id=468.

[148] PhidgetEncoder HighSpeed (1057 3B). https://www.eztronics.nl/webshop2/catalog/index.php?route=product/product&product_id=202.

[149] Model HGT-2101 Magnetic Field Sensor. https://www.lakeshore.com/docs/default-source/product-downloads/literature/hgt_2100_to_hgt_2101_comparison.pdf?sfvrsn=67c39bb5_1.

[150] PPMS Physical Property measurement system-Integrated measurement applications. http://www.lao.cz/data/ke-stazeni/Bro%C5%BEura%20PPMS-d573.pdf.

[151] Instrumentation Feedthrough. https://www.lesker.com/feedthroughs/instrument-feedthroughs-mpc-singleend/part/iftrg197018b?highlight=IFTRG197018B.

[152] B. Douine, K. Berger, F. Trillaud, M. Elbaa, and E. H. Ailam. Determination of the Complete Penetration Magnetic Field of a HTS Pellet From the Measurements of the Magnetic Field at Its Top-Center Surface. *IEEE Trans. Appl. Supercond.*, 28:8800104, 2018.

[153] J. Duron, F. Grilli, L. Antognazza, M. Decroux, B. Dutoit, and O. Fischer. Finite-element modelling of YBCO fault current limiter with temperature dependent parameters. *J. Supercond. Novel Magn.*, 20:338, 2007.

[154] S. R. Curras, J. Vina, M. Ruibal, M. T. Gonzalez, M. R. Osorio, J. Maza, J. A. Veira, and F. Vidal. Normal-state resistivity versus critical current in YBaCuO thin films at high current densities. *Physica C Supercond.*, 372:1095–1096, 2002.

[155] E. J. Cukauskas and L. H. Allen. Critical current characteristics of composite thin films of Au and $YBa_2Cu_3O_7$. *Physica C Supercond.*, 313:11–20, 1999.

[156] L. C. Barnsley, D. Carugo, J. Owen, and E. Stride. Halbach arrays consisting of cubic elements optimised for high field gradients in magnetic drug targeting applications. *Phys. Med. Biol.*, 60:8303–8327, 2015.

[157] M. Tomita, and M. Murakami. High temperature superconductor bulk magnets can trap magnetic fields of over 17 tesla at 29 K. *Letters to Nature*, 421(30):517–520, 2003.

[158] Y. Shi, A. R. Dennis, J. H. Durrell, and D. A. cardwell. The effect of size and aspect ratio on the trapped field properties of single grain, Y–Ba–Cu–O bulk superconductors. *Supercond. Sci. Technol.*, 32:025005, 2019.

[159] Y. Shi, M. D. Ainslie, A. R. Dennis, J. H. Durrell, and D. A. Cardell. Optimisation of stacked, bulk high temperature superconductors for trapped-field magnet applications. *Supercond. Sci. Technol.*, 36:085018, 2023.

[160] N. Saho, N. Nishijima, H. Tanaka, and A. Sasaki. Development of portable superconducting bulk magnet system. *Physica C Supercond.*, 469:1286–1289, 2009.

[161] T. Nakamura, D. Tamada, Y. Yanagi, Y. Itoh, T. Nemeto, H. Utumi, and K. Kose. Development of a superconducting bulk magnet for NMR and MRI. *J. Magn. Reson.*, 259:68–75, 2015.

[162] M. D. Ainslie, A. George, R. Shaw, L. Dawson, A. Winfield, M. Steketee, and S. Stockley. Design and market considerations for axial flux superconducting electric machine design. *J. Phys. Conf. Ser.*, 507:032002, 2014.

[163] D. Zhou, M. Izumi, M. Miki, B. Felder, T. Ida, and M. Kitano. An overview of rotating machine systems with high temperature bulk superconductors. *Supercond. Sci. Technol.*, 25:103001, 2012.

[164] F. Mishima, S.-I. Takeda, Y. Izumi, and S. Nishijima. Three dimensional motion control system of ferromagnetic particles for magnetically targeted drug delivery systems. *IEEE Trans. Appl. Supercond.*, 16(2):367–371, 2006.

[165] Y. Zhang, D. Zhou, T. Ida, M. Miki, and M. Izumi. Melt-growth bulk superconductors and application to an axial-gap-type rotating machine. *Supercond. Sci. Technol.*, 29:044005, 2016.

[166] S.-I. Takeda, F. Mishima, S. Fujimoto, Y. Izumi, and S. Nishijima. Development of magnetically targeted drug delivery system using superconducting magnet. *J. Magn. Magn. Mater.*, 311:367–371, 2007.

[167] F. Mishima, S.-I. Takeda, Y. Izumi, and S. Nishijima. Development of magnetic field control for magnetically targeted drug delivery system using a superconducting magnet. *IEEE Trans. Appl. Supercond.*, 17:2303–2306, 2007.

[168] S. Nishijima, S.-I. Takeda, F. Mishima, Y. Tabata, M. Yamamoto, J.-I. Joh, H. Iseki, Y. Muragaki, A. Sasaki, K. Jun, and N. Saho. A study of magnetic drug delivery system using bulk high temperature superconducting magnet. *IEEE Trans. Appl. Supercond.*, 18:874–877, 2008.

[169] M. Chuzawa, F. Mishima, Y. Akiyama, and S. Nishijima. Drug accumulation by means of noninvasive magnetic drug delivery system. *Physica C Supercond.*, 471:1538–1542, 2011.

[170] T. Terada, S. Fudui, F. Mishima, Y. Akiyama, Y. Izumi, and S. Nishijima. Development of magnetic drug delivery system using HTS bulk magnet. *Physica C Supercond.*, 468:2133–2136, 2008.

[171] S. B. Kim, I. Eritate, T. Abe, M. Takashashi, S. Shima, and A. Nakashima . Development of magnetic field control system using HTS bulks and HTS coil for MDDS. *IEEE Trans. Appl. Supercond.*, 25:4602704, 2015.

[172] K. Funaki, and K. Yamafuji. Abnormal transverse field effects in nonideal type II superconductors I. A linear array of monofilamentary wires. *Jpn. J. Appl. Phys.*, 21(2):299–304, 1982.

[173] A. M. Campbell, M. Baghdadi, A. Patel, D. Zhou, K. Y. Huang, Y. Shi, and T. A. Coombs. Demagnetisation by crossed fields in superconductors. *Supercond. Sci. Technol.*, 30:034005, 2017.

[174] Z. Hong, P. Vanderbemden, R. Pei, Y. Jiang, A. M. Campbell, and T. A. Coombs. The numerical modeling and measurement of demagnetization in bulk YBCO superconductors subjected to transverse field. *IEEE Trans. Appl. Supercond.*, 18(2):1561–1564, 2008.

[175] L. M. Fisher, A. V. Kalinov, S. E. Savel'ev, I. F. Voloshin, V. A. Yampol'skii, M. A. R. Leblanc, and S. Hirscher. Collapse of the magnetic moment in hard superconductor under the action of a transverse ac magnetic field. *Physica C Supercond.*, 278:169–179, 1997.

[176] J. Srpcic, F. Perez, K. Y. Huang, Y. Shi, M. D. Ainslie, A. R. Dennis, M. Filipenko, M. Boll, D. A. Cardwell, and J. H. Durell. Penetration depth of shielding currents due to crossed magnetic fields in bulk (RE)-Ba-Cu-O superconductors. *Supercond. Sci. Technol.*, 32:035010, 2019.

[177] J. Luzuriaga, A. Badía-Majós, G. Nieva, C. López, A. Serquis, and G. Serrano. Magnetic relaxation induced by transverse flux shaking in MgB_2 superconductors. *Supercond. Sci. Technol.*, 22:015021, 2009.

[178] M. Kapolka, J. Srpcic, D. Zhou, M. D. Ainslie, E. Pardo, and A. R. Dennis. Demagnetization of cubic Gd-Ba-Cu-O bulk superconductor by crossed-fields: measurements and 3D modelling. *IEEE Trans. Appl. Supercond.*, 28:6801405, 2018.

[179] T. Oka, Y. Takahashi, S. Yaginuma, J. Ogawa, S. Fukui, T. Sato, K. Yokoyama, and T. Nakamura. Uniform magnetic field between face-to-face HTS bulk magnets combining concave and convex magnetic field distribution. *Phys. Procedia*, 81:45–48, 2016.

[180] K. Yang, T. Zhang, J. He, Q. Zhang, C. Zhang, D. Zhou, and C. Cai. Pulsed Field Magnetization of $YBa_2Cu_3O_{7-\delta}$ Bulk Assembly for Motor Application. *IEEE Trans. Appl. Supercond.*, 32:5200205, 2022.

[181] D. Zhou, Y. Shi, A. R. Dennis, D. A. Cardwell, and J. H. Durrell. Flux jumps in ring-shaped and assembled bulk superconductors during pulsed field magnetization. *Supercond. Sci. Technol.*, 33:034001, 2020.

[182] R. Kinjo, K. Mishima, Y. W. Choi, M. Omer, K. Yoshida, H. Negm, K. Torgasin, M. Shibata, K. Shimahashi, H. imon, K. Okumura, M. Inukai, H. Zen, T. Kii, K. Masuda, K. Nagasaki, and H. Ohgaki. Magnetic property of a staggered-array undulator using a bulk high-temperature superconductor. *Phys. Rev. Accel. Beams*, 17:022401, 2014.

[183] T. Kii, R. Kinjo, N. Kimura, M. Shibata, M. A. Bakr, Y. W. Choi, M. Omer, K. Yoshida, K. Ishida, T. Komai, K. Shimahashi, T. Sonobe, H. Zen, K. Masuda, and H. Ohgaki. Low-temperature operation of a bulk HTSC staggered array undulator. *IEEE Trans. Appl. Supercond.*, 22:4100904, 2012.

[184] S. D. Chen, C. S. Hwang, C. M. Yang, and I. G. Chen. Feasibility and features of a staggered undulator constructed with HTS YBCO bulks. *IEEE Trans. Appl. Supercond.*, 24:4603005, 2014.

[185] M. Calvi, M. D. Ainslie, A. Dennis, J. H. Durrell, S. Hellman, C. Kittel, D. A. Moseley, T. Schmidt, Y. Shi, and K. Zhang. A GdBCO bulk staggered array undulator. *Supercond. Sci. Technol.*, 33:014004, 2020.

[186] K. Zhang, A. Pirotta, X. Liang, S. Hellman, M. Bartkowiak, T. Schmidt, A. R. Dennis, M. D. Ainslie, J. H. Durrell, and M. Calvi. Record field in a 10 mm-period bulk high-temperature superconducting undulator. *Supercond. Sci. Technol.*, 36:05LT01, 2023.

[187] M. Calvi, S. Hellman, E. Prat, T. Schmidt, K. Zhang, A. R. Dennis, J. H. Durrell, and M. D. Ainslie. GdBCO bulk superconducting helical undulator for x-ray free-electron lasers. *Phys. Rev. Res.*, 5:L032020, 2023.

[188] S. Choi, J.-H. Yoon, B.-S. Lee, M.-S. Won, J.-W. Ok, Z. Y. Zhang, T Kiyoshi, S. Matsumoto, and S.-H. Lee. Magnetic lens effect using Gd-Ba-Cu-O bulk superconductor in very high magnetic field. *J. Appl. Phys.*, 111:07E728, 2012.

[189] K. Takahashi, H. Fujishiro, and M. D. Ainslie. A new concept of a hybrid trapped field magnet lens. *Supercond. Sci. Technol.*, 31(2):044005, 2018.

[190] J. R. Hull. Trapped-flux internal-dipole superconducting motor/generator. *IEEE Trans. Appl. Supercond.*, 9(1229):ASC98, 1999.

[191] M. Katter. Angular dependance of the demagnetization stability of sintered Nd-Fe-B magnets. *IEEE Trans. Magn.*, 41:3853 – 3855, 2005.

[192] C. D. Dewhurst, W. Lo, Y. Shi, and D. A. Cardwell. Homogeneity of superconducting properties in $SmBa_2Cu_3O_{7-\delta}$-seeded melt processed YBCO. *Mat. Sci Eng. B*, 53:169–173, 1998.

[193] T. Nakashima, J. Shimoyama, M. Honzumi, Y. Tazaki, S. Horii, and K. Kishio. Relationship between critical current properties and microstructure in cylindrical RE123 melt-solidified bulks . *Physica C Supercond.*, 426-431:720–725, 2005.

[194] P. Yang, J.-F. Fagnard, P. Vanderbemden, and W. Yang. Magnetic shielding of a short thick GdBCO tube fabricated by the buffer aided top-seeded infiltration and growth method. *Supercond. Sci. Technol.*, 32:115015, 2019.

[195] P. Vanderbemden, A. D. Bradley, R. A. Doyle, W. Lo, D. M. Astill, D. A. Cardwell, and A. M. Campbell. Superconducting properties of natural and artificial grain boundaries in bulk melt-textured YBCO. *Physica C Supercond.*, 302:257–270, 1998.

[196] E. M. Gyorgy, R. B. Van Dover, K. A. Jackson, L. F. Schneemeyer, and J. V. Waszczak. Anisotropic critical currents in $Ba_2YCu_3O_7$ analyzed using an extended Bean model. *Appl. Phys. Lett.*, 55:283–285, 1989.

[197] A. Patel, K. Filar, V. I. Nizhankovskii, S. C. Hopkins, and B. A. Glowacki. Trapped fields greater than 7 T in a 12 mm square stack of commercial high-temperature superconducting tape. *Appl. Phys. Lett.*, 102:102601, 2013.

[198] T. Tamegai, T. Hirai, Y. Sun, and S. Pyon. Trapping a magnetic field of 7.9 T using a bulk magnet fabricated from stack of coated conductors. *Phys. C: Supercond.*, 530:20–23, 2016.

[199] M. Baghdadi, H. S. Ruiz, and T. A. Coombs. Crossed-magnetic-field experiments on stacked second generation superconducting tapes: Reduction of the demagnetization effects. *Appl. Phys. Lett.*, 104:232602, 2014.

[200] M. Baghdadi, H. S. Ruiz, and T. A. Coombs. Nature of the low magnetization decay on stacks of second generation superconducting tapes under crossed and rotating magnetic field experiments. *Scientific Reports*, 8:1342, 2018.

[201] A. Baskys, A. Patel, and B. A. Glowacki. Measurements of crossed-field demagnetisation rate of trapped field magnets at high frequencies and below 77 K. *Supercond. Sci. Technol.*, 31:065011, 2018.

[202] M. Kapolka, E. Pardo, F. Grilli, A. Baskys, V. Climente-Alarcon, A. Dadhich, and B. A. Glowacki. Cross-field demagnetization of stacks of tapes: 3D modeling and measurements. *Supercond. Sci. Technol.*, 33:044019, 2020.

[203] A. I. Podlivaev, I. A. Rudnev, and N. P. Shabanova. Magnetic-Field Dependence of the Local Critical Current Density in the Second-Generation HTSC Tapes. *Bull. Lebedev Phys. Inst.*, 41:351–354, 2014.

[204] I. A. Rudnev, and A. I. Podlivaev. Magnetic Response of the Stacks of HTS Tapes. *IEEE Trans. Appl. Supercond.*, 26:8200104, 2016.

[205] I. Rudnev, D. Abin, M. Osipov, S. Pokrovskiy, Y. Ermolaev, and N. Mineev. Magnetic Properties of the Stack of HTSC Tapes in a Wide Temperature Range. *Phys. Procedia*, 65:141–144, 2015.

[206] D.-X. Chen, and R. N. Goldfarb. Kim model for magnetization of type-II superconductors. *J. Appl. Phys.*, 66:2489–2500, 1989.

[207] E. H. Brandt. Superconductor disks and cylinders in an axial magnetic field. I. Flux penetration and magnetization curves. *Phys. Rev. B*, 58:6506–6522, 1998.

[208] D.-X. Chen, A. Sanchez, and J. S. Munoz. Exponential critical-state model for magnetization of hard superconductors. *J. Appl. Phys.*, 67:3430–3437, 1990.

[209] T. H. Johansen, M. R. Koblischka, H. Bratsberg, and P. O. Hetland. Critical-state model with a secondary high-field peak in Jc(B). *Phys. Rev. B*, 56:11273–11278, 1997.

[210] M. R. Koblishka, A. J. J. Van Dalen, T. Higuchi, K. Sawada, S. I. Yoo, and M. Murakami. Observation of multiple peaks in the magnetization curves of NdBa2Cu3O7 single crystals. *Phys. Rev. B*, 54:R6893, 1996.

[211] M. Jirsa, L. Pust, and D. Dlouhy. Fishtail shape in the magnetic hysteresis loop for superconductors: Interplay between different pinning mechanisms. *Phys. Rev. B*, 55:3276–3284, 1997.

[212] Y. Abulafia, A. Shaulov, Y. Wolfus, R. Prozorov, L. Burlachkov, Y. Yeshurun, D. Majer, E. Zeldov, H. Wuhl, V. B. Geshkendein, and V. M. Vinokur. Fishtail shape in the magnetic hysteresis loop for superconductors: Interplay between different pinning mechanisms. *Phys. Rev. Lett.*, 77:1596–1599, 1996.

[213] A. A. Zhukov, H. Kupfer, G. Perkins, L. F. Cohen, A. D. Caplin, S. A. Klestov, H. Claus, V. I. Voronkova, T. Wolf, and H. Wuhl. Influence of oxygen stoichiometry on the irreversible magnetization and flux creep in $RBa_2Cu_3Q_{7-\delta}$ (R =Y,Tm) single crystals. *Phys. Rev. B*, 51:12704–12714, 1995.

[214] L. Civale, A. D. Marwick, T. K. Worthington, M. A. Kirk, J. R. Thompson, L. Krusin-Elbaum, Y. Sun, J. R. Clem, and F. Holtzberg. Vortex Confinement by Columnar Defects in $YBa_2Cu_30_7$ Crystals: Enhanced Pinning at High Fields and Temperatures. *Phys. Rev. Lett.*, 67:648–651, 1991.

[215] P. Vanderbemden, Z. Hong, T. A. Coombs, M. Ausloos, N. Hari Babu, D. A. Cardwell, and A. M. Campbell. Remagnetization of bulk high-temperature superconductors subjected to crossed and rotating magnetic fields. *Supercond. Sci. Technol.*, 20:S174–S183, 2007.

[216] A. Arsenault, and F. Sirois. Simulation of remote force generated by high temperature superconducting bulks for magnetic drug delivery. *IEEE Trans. Appl. Supercond.*, 33:4401409, 2023.

[217] S. Martel, J.-B. Mathieu, O. Felfoul, A. Chan, E. Aboussouan, S. Tamaz, P. Pouponneau, L. Yahia, G. Beaudoin, G. Soulez, and M. Mankiewicz. Automatic navigation of an untethered device in the artery of a living animal using a conventional clinical magnetic resonance imaging system. *Appl. Phys. Lett.*, 90:114105, 2007.

[218] N. Li, Y. Jiang, R. Plantefeve, F. Michaud, Z. Nosrati, C. Tremblay, K. Saatchi, U. O. Hafeli, S. Kadoury, G. Moran, F. Joly, S. Martel, and G. Soulez. Magnetic Resonance Navigation for Targeted Embolization in a Two-Level Bifurcation Phantom. *Ann. Biomed. Eng.*, 47:2402–2415, 2019.

[219] N. Li, C. Tous, I. P. Dimov, C. Cadoret, P. Fei, Y. Majedi, S. Lessard, Z. Nosrati, K. Saatchi, U. O. Hafeli, A. Tang, S. Kadoury, S. Martel, and G. Soulez. Quantification and 3D Localization of Magnetically Navigated Superparamagnetic Particles Using MRI in Phantom and Swine Chemoembolization Models. *IEEE Trans. Biomed. Eng.*, 69:2616–2627, 2022.

[220] J.-B. Mathieu, and S. Martel. Magnetic microparticle steering within the constraints of an MRI system: proof of concept of a novel targeting approach. *Biomed. Microdevices*, 9:801–808, 2007.

[221] J.-B. Mathieu, G. Beaudoin, and S. Martel. Method of propulsion of a ferromagnetic core in the cardiovascular system through magnetic gradients generated by an MRI system. *IEEE Trans. Biomed. Eng.*, 53:292–299, 2006.

[222] O. Felfoul, A. T. Becker, G. Fagogenis, and P. E. Dupont. Simultaneous steering and imaging of magnetic particles using MRI toward delivery of therapeutics. *Sci. Rep.*, 6:33567, 2016.